SESSION

SIMULATION AND COMPUTATIONAL MODELING METHODS + NOVEL APPLICATIONS AND RELATED ISSUES

Chair(s)

TBA

ISBN: 1-60132-430-8, CSREA Press ©

ISBN: 1-60132-430-8, CSREA Press ©

The Case for N-Body Simulations in Rust

A. Hansen, M. C. Lewis
Department of Computer Science, Trinity University, San Antonio, Texas, United States

Abstract— *In this paper we explain the various features of Rust in the context of an n-body simulation, with the purpose of making a strong case for the usage of Rust in numerical simulation programming. Our n-body simulation involved calculating gravitational forces among many bodies. We implemented a large simulation and observed how these features can benefit or harm the programmer. Covering topics such as the type system, slice types, the Borrow Checker, mutability, and the potential for parallelism, we show that Rust's guarantees about safety are useful and practical in simulation programming, and can save time in the development process.*

Keywords: Rust, kD-tree, n-body, simulations, memory safety

1. Introduction

The field of programming and application development has shifted dramatically in the last two decades with the rise of the web and the web application. New projects are often done using dynamically typed scripting languages that are far removed from the hardware they run on. This is not only a result of the rise of the web, but also due to the separation between available computer power and the tasks that most people perform. There are still some areas, like systems programming and numerical simulation, where people actually need to get the full performance of their machine without the language doing things that get in the way. For the most part, that means that these applications are written in C, C++, or even Fortran. Of these, only C++ has really kept up with advances in modern programming languages. While many new languages have been developed in the last 30 years, almost none of them, with the exception of D, have been aimed at system level programming. Rust aims to bring many of the advances of modern languages to this space.

In C/C++, maintenance issues can arise in long-term projects stemming from memory leaks or bugs related to a lack of "safety" of code. This issue as been addressed in many ways, but is often not entirely avoidable. Rust prevents these conditions as a feature of the design, therefore they can not be a problem. This allows the programmer to focus on designing and improving the code.

2. What is Rust?

Rust is a relatively new programming language with guarantees about safety[1] and statically guaranteed memory safety[6]. The compiler for Rust checks for potential errors and insecurities through the usage of something called the "Borrow Checker"[1]. The design of the language, that being the blocks it is defined upon (to be defined later), is also integral to these guarantees. Since all of the guarantees come from the compiler and design, and not runtime checks, Rust claims to have performance comparable to C/C++, the current standards in fast simulation coding. It aims to be a safer alternative to these languages.

The Borrow Checker supplements the design of the language by ensuring that there is never more than one binding to a resource on the heap. As soon as the binding, which is on the stack, to that resource, on the heap, goes out of scope, both the binding and the resource are deallocated. The Borrow Checker enforces the rule that only one binding to a resource is permissible at a time, so this deallocation will never result in "null pointers". Consider the following code.

```
let first_binding = vec!['a', 'b', 'c'];
let second_binding = first_binding;
let a = first_binding[0];
```

This code will not compile, stating that the value held by `first_binding` was moved to `second_binding`. Using `first_binding` at all after this relocation is a safety violation and is therefore non-permissible. Either the data itself must be cloned manually, or the programmer must make a design change using borrowing. By borrowing, I mean using references to treat data in an immutable manner.

The "building blocks" of this language are devised from some core principles. In order to guarantee that no memory can become unreachable without deallocation and that non-allocated memory values can never be read, Rust asserts that all memory must have a unique binding responsible for it. When this binding goes out of scope, so does the memory. A binding can be transferred from one variable to another, but there can never be more than one. Rust then asserts that memory can never be in a mutable state and aliased via multiple pointers. Safe aliasing is done using borrowing, the idea of temporarily lending a value through references. While these building blocks are formally safe,

[1]While this has not been formally proven, the "building blocks" of the language are formally safe and the language is specifically designed to be safe as well [5]

the combination of them has yet to be proven equivalently safe, although that is the design idea of the language[6].

3. Our Project

Our project was to test the speed claims made by Rust by re-implementing a numerical simulation previously written in C++ and determine how it impacts the design process. As the second part of the goal is inherently non-objective, we will present observations without interpretation of them being good or bad. We also were learning more about Rust while we were programming the simulation. Since this is a situation most Rust programmers are in right now (very few people program Rust professionally), we feel that it is fair to present our observations of learning and implementing large scale, efficient Rust code. Currently, our Rust implementation is slower than our C++ implementation, but we believe it is premature to say this is because of Rust's inherent speed, rather we haven't fully optimized it. We hope to follow this paper up with a more formal paper on the speed capabilities of Rust, once we feel we have sufficiently optimized the program that we can conclude the achived speed is reflective of the language capabilities.

3.1 Our Simulation

The simulation is an n-body simulation that calculates gravitational forces and applied them. We used a kD-tree to store the particles. This structure allows major optimizations when calculating gravitational forces among the bodies. The kD-tree is a binary tree at its core, where each node splits upon a single axis in k-dimensions. In our case, as this was a three-dimensional particle space, we used a three-dimensional tree. Each node splits an axis at its median, x, y, or z, (whichever has the greatest range) and then stores the particles with a lesser value on the split axis to the left and a greater value on the split axis to the right. This pattern continues until each node contains fewer than some specified number of particles. For most of our work, each node contained three particles. This means that all of the particle data is actually stored in the leaves of the tree, and all internal nodes serve only for organizational purposes, optimizing certain calculations.

Gravity calculations are done by a few functions. The first function, `particle_gravity` takes two particles, a and b, and returns the gravitational force they exert on each other. The second function, `get_gravitational_acceleration` takes a particle and calls `particle_gravity` on (almost) all other particles in the tree. Finally, a function called `tree_gravity` takes a kD-tree of particles and calculates all of the accelerations by calling `get_gravitational_acceleration` on every particle. This is the overall flow of our implementation.

Gravitational calculations require that each particle feel the force of all other particles. By default, this is an $O(n^2)$ operation, which makes it intractable for large systems. One of the most common ways of improving on this is to use a spatial tree [2]. These methods calculate interactions over longer distances between single particles and mass distributions of groups of particles. The original work by [2] used an octree with the monopole moment of the mass distribution. More recent implementations use other trees, like the kD-tree, and go up to hexadecapole moments [7]. As was mentioned above, this work uses a kD-tree, but considers only monopole moments to keep the code simpler. These codes use a constant value θ that represents the opening angle between the particle and a node that is used to determine if an interaction can be done with the collective mass distribution or if the recursion needs to descend to the children. This effectively sets the accuracy we are willing to sacrifice to gain efficiency. The following inequality determines whether or not we treat a node as a mass distribution, which one can view as one giant particle given the limit to a monopole expansion. If it evaluates to true, then we treat the node as a large particle, a process to be explained later, and if it is false, then we recurse to its child nodes, if it is not a leaf, and do the same calculation. If it is a leaf, then we go ahead and calculate the gravitational forces from every particle it contains.

Let $dist$ be the distance from particle $part$ to the center of mass of node $node$. Let max_di be the maximum range of particle coordinates along any dimension for particles in the leaves that are descendants of the node.

$$dist * \theta^2 > max\_di^2$$

In order to convert a node into a "giant particle", we treat the center of mass coordinates as the position value and the mass as the total mass of all particles that node represents. This is all we need for gravity calculations.

4. Why Rust?

Rust is often spoken of as the answer to unsafe code. For this reason, it seems like it would be a very good candidate for projects that could very quickly become large in terms of length of code. Tracking down issues such as memory leaks and segmentation faults can take weeks of development time, if a situation is particularly bad, and if one uses standard Rust style, this will not be an issue.

4.1 Advantages of Rust in Simulation Programming

The most imperative requirement in large-scale simulation programming is that of speed. A language's performance on certain benchmarks can be vital to its usability in large-scale simulations. As Rust performs as well or better than C++ in many benchmarks[3], this seems like it would lend itself to simulations rather well.

A language that is practical for simulation programming should also allow the user to focus on the mathematics and

logic of the simulation over the computer's most safe and efficient methods of operating. Rust's guarantees of safety should allow this to be attained, preventing the programmer from having to concern himself with issues like null pointers. We will investigate how difficult it is to actually access this speed.

The next requirement would be ease-of-use. This is where many people complain about the status quo and seek to move to "better" languages. As Rust provides entirely different paradigms for data usage[2], the design process could be impacted greatly. Rust boasts higher-level syntax than most low-level languages, which could make mathematical programming more readable, also providing a motivation for simulation use.

Often, C++ is hard to maintain as memory leaks and type bugs infiltrate a project as it ages. This is something that is, by design, not an issue in Rust. In areas where Rust loses in speed compared to C++, it often makes up for in guaranteed safety where C++ does not[9]. This also is a major benefit to using Rust in large numerical situations. If you program something in Rust, and avoid the use of the unsafe keyword,[3] you can be very confident that your simulation will be safe and have integrity.

Using the "unsafe" word in Rust can be appropriate, but is often avoided. It is used in Foreign Function Interface (FFI), the process of linking functions from other languages into Rust, as any function written in a language other than Rust cannot have the same guarantees. Unsafe can be used either in a function declaration, a trait declaration, a block of code, or a trait implementation. It allows you to have a global `static mut` variable, call other unsafe functions, or dereference a raw pointer[4]. If a programmer can avoid using these three features, then he/she can be confident in the safety of his/her code.

One instance of an error that was caught at compile in Rust that could have potentially taken weeks of time to find otherwise arose from a situation similar to the code below.

```
fn main() {
   let mut x = vec!['a', 'b', 'c'];
   for _ in 0..10 { take_ownership(x); }
}
fn take_ownership(v: Vec<char>) {

}
```

This causes an error, stating that the value previously at `x` was moved to the first calling of the `take_ownership()` function, and once the loop iterates again, that value no longer belongs to the variable `x`. After `take_ownership()` takes ownership of `x`, reassigning it to the variable `v`, `v` goes out of scope, causing the vector data on the heap to become deallocated, as a part of Rust's design. In the simulation code, this would have caused undesirable results as the vector should have been declared inside of the for loop, eliminating the ownership issues.

We hope to show the design differences in Rust and how they behave in real programming situations.

4.2 Disadvantages of Using Rust in Simulation Programming

In simulation programming, it is important to be able to dictate efficiency. That is, the ability to clearly make a more efficient choice against a less efficient choice. While this is inherently dependent upon the programmer's mastery of the language he/she is using, we found that it can sometimes be unintuitive as to which method will be more efficient in Rust, when faced with options. This can sometimes lead to confusion, until someone else points out a more "idiomatic", although sometimes unintuitive in relation to established programming languages, approach and then efficiency is achieved again.

Rust's radically different data schemes behave differently than most programmers are used to, and this can further muddle the line between efficient and not efficient. In the beginning phases of becoming a Rust programmer, struggling to understand the borrow checker is often common. The error messages are helpful, but the guarantees of Rust come with a penalty of restricting what is commonplace in other languages. This can be viewed as a disadvantage if the objective is to get a project written and running in a short period of time.

In Rust, a structure cannot be defined in terms of itself. In order to achieve a recursive structure, one must have a pointer, or in Rust terms, a "box", to another instance of the structure. This creates a pointer to memory on the heap, on the stack. instead of directly creating the structure definition on the stack. This can lead to some unsightly handling of structures. The following structure would not compile, as the structure cannot have itself as a member.

```
struct Node {
   left: Node,
   right: Node,
}
```

However, the following code would compile, as a the child nodes are "boxed".

```
struct Node {
   left:Box<Node>,
   right:Box<Node>,
}
```

Occasionally, a programmer might come across a data type where, in order to maintain safety, he/she must chain together a lot of functions to access members via borrowing. An example of this is below.

[2]These being the "safe blocks" that Rust is built upon

[3]This turns off some of Rust's safety guarantees to let you do things that would otherwise not be allowed by the compiler.

```
let left_mass = root_node.left
                    .as_ref()
                    .expect("")
                    .total_mass;
let right_mass = root_node.right
                     .as_ref()
                     .expect("")
                     .total_mass;
```

The combination of `as_ref()` being required to access a field, requirement that data structures must be defined non-recursively, and that `expect()` takes ownership of a value, causes some occasional unsightly requirements to access fields of a structure without taking ownership of them. This was later minimized by enumerating the node type, but examples similar to this are still easy to find.

5. Implementation

This section will cover the observations we gathered from the development process of the Rust implementation.

5.1 Rust's Appeal to Specifically Numerical Simulations

Rust boasts several convenient performance claims. One is that it is a non-garbage collected language, and yet it does not require manual memory management. While programming in Rust, the programmer will often be aware of the memory he/she is using due to the nature of the Borrow Checker preventing moves and Rust's lack of implicit cloning.

Rust's design was also heavily influenced by the functional programming paradigm. This means that the programmer can take advantage of some high level syntax, including option types that do not hurt performance, a strong type system (that supports type inferencing), and the ability to program with a frame of reference closer to the mathematical problems as opposed to the computational problems. This does not sacrifice the low-level properties of Rust, however, as these constructs can be applied to very low-level types and functions.

The Borrow Checker is very beneficial to numerical simulations. This is because it guarantees that your values will not be mutated while other computations are happening, and it will never be deallocated when you do not expect it. At compile time, anything that could result accessing null/deallocated values will be prevented.

Code that has been written in Rust also provides for an easy transition from a single-threaded simulation into a parallel simulation, as data races and other problems are avoided. In Rust, data safety across threads is achieved via the type system. The type system only allows values to be shared across threads if they implement two traits, `send` and `sync`. These two traits are essentially promises that the data will not mutate while being accessed. The `send` trait means that the type can be sent across threads without issue (immutably), and the `sync`trait means that the type will not mutate internally while being accessed from different threads[8]. This, combined with the concept of ownership applied to threads, prevents data races at compile time. As only one thread can own a variable at a time, and they can only be transferred across threads safely, this combination of the type system and ownership guarantees safe concurrency. This is a great thing to have when writing large simulations.

Lastly, the community of Rust is great and helpful. This was another aspect of Rust that was actually part of the design, as it is stated on Rust's website[4]. The language even has a moderation team and anti-harassment policies, plus beginner-friendly areas. It is not difficult to go online and get code reviews, helpful tips and explanations, or general support and feedback from many sources like Internet Relay Chat, the Rust forums, and other online communities.

5.2 Implementation Details

In Rust, something that is "safe" is something that does not use the "unsafe" keyword.[4] Often, programmers rely on unsafe code to speed up their data structures, thus eliminating the guarantees for minimal gain. We opted to write an entirely safe data structure within the confines of the borrow checker, as recommended, so we could rely on the guarantees of Rust.

Rust's borrow-checking and no-null-pointers guarantees saved the simulation on multiple occasions, as references would go out of scope and the lifetime of the variable would not be long enough. Once aware of this aspect, it was not an issue, however.

5.3 Using Vector Slices

In the C++ implementation, the memory-objective was held by storing indexes of the global particle vector that the tree was based off of to refer to particles. In this way, the vector was never cloned. Originally, the Rust implementation allocated vectors to store almost all of its data. This included in calculations such as those that occur in `get_gravitational_acceleration`.As it turns out, vector allocation was a major bottleneck and still continues to the largest consumer of time in our Rust implementation. In order to get around this issue, the C++ implementation used indexes to refer to particles and never actually populated vectors. If a range of particles was needed from index value 10 to index value 200, it would just store these index values. This saved the C++ implementation from a fair amount of vector allocations as well as memory consumption. In Rust, however, the tree was not based off of an array in the first place. It was based off of a recursively defined node structure. This meant that no global particle index values were available. However, each leaf node had a

[4]This is not always true. Some library functions require inherently unsafe things like manually managing pointers for vector allocation. These things use "unsafe" Rust but are presented as safe, so they do not count.

vector of particles. Rust has a type called a vector slice, the type signature for which is &[T]. 'T' in this case stands for a type, so for us, the signature was &[Particle]. When we compared the speed of the program when it used excessive vector allocations to when we implemented slice usage, we saw great performance increases. By switching to slices, we were able to get the runtime down by a third.[5] The top consumer of time is still memory allocations, however.[6]

5.4 Ending Time

We still have not managed to get the Rust implementation to a point at which we feel it is as fast as possible. Currently, it is slower than the C++ implementation by almost a factor of five. We hope to change this in the near future and include optimized time comparisons in a follow up paper.

Below is a table with time comparisons of our current Rust implementation and C++ implementation. The value n denotes the number of bodies. The times were taken by advancing the simulation five time-steps (a time step constitutes calculating all of the acceleration values and rebuilding the tree once). For both implementations, $\theta = 0.2$. Times were taken as an average of multiple runs.

	C++	Rust
n		
10000	0.768s	9.198s
20000	1.671s	49.273s
50000	4.696s	259.116s

As you can see, our current situation is that the Rust code is much slower. However, with the performance of Rust on common benchmarks[3], we should be able to optimize the implementation much more.

6. Conclusion

The simulation is currently in a state where it could be parallelized without much trouble, thanks to Rust's guarantees. It is currently in a state of optimization, however, which is proving difficult as we have not developed a mastery over the language yet. Once adopting the mentality that the borrow checker provides, however, it becomes easy to write safe and efficient programs. Programming in Rust has a different sort of flow, however. Most of the time programming is spent sorting out compiler errors as opposed to runtime errors and debugging. There are many aspects of Rust not discussed in this paper, such as lifetimes, that did not appear as very relevant in this implementation. Overall, the design of Rust lends itself to extremely effective and safe code, but at the cost of a learning curve. Our development process allowed us to observe how the features of Rust can be used to implement safer code than in competing languages, namely C++, in large numerical simulations. We hope that this paper will serve as an exposition to a follow-up where the runtime of the Rust implementation is comparable to that of the C++ implementation (something that should be possible according to the benchmarks at [3]). We also hope that this paper will foster interest in writing numerical simulations in Rust.

[5] Or, more precisely, a 31.63% average reduction in runtime.

[6] It is very convenient that Rust supports profilers to view its annotated source code. We used Valgrind for this statistic.

References

[1] Ivo Balbaert. *Rust Essentials*. Packt Publishing, 2015.

[2] Josh Barnes and Piet Hut. A hierarchical o (n log n) force-calculation algorithm. *nature*, 324(6096):446–449, 1986.

[3] The Benchmarks Game. http://benchmarksgame.alioth.debian.org.

[4] The Rust Programming Language. https://www.rust-lang.org/.

[5] Nicholas D. Matsakis and Felix S. Klock, II. The rust language. *Ada Lett.*, 34(3):103–104, October 2014.

[6] Eric Reed. Patina: A formalization of the rust programming language. *University of Washington, Department of Computer Science and Engineering, Tech. Rep. UW-CSE-15-03-02*, 2015.

[7] Joachim Stadel, James Wadsley, and Derek C Richardson. High performance computational astrophysics with pkdgrav/gasoline. In *High Performance Computing Systems and Applications*, pages 501–523. Springer US, 2002.

[8] Aaron Turon. http://blog.rust-lang.org, 2015.

[9] Patrick Walton. C++ design goals in the context of rust, 2010.

Simulation/Modeling of Pressure and Torque Pulsation for a Swash-plate Type Piston Motor by Using SimulationX®

Jin Woong Sa [#], Won Jee Chung[#], Young Hwan Yoon [#] , Yong Wook Jeong [#]

[#]School of Mechatronics, Changwon National University
Changwon, 641-773, South Korea

Abstract*— Hydraulic equipment has long been used for construction machinery equipment for the high power density and durability. In particular, pumps and motors have been considered essential equipment and continuously investigated to find proper methods of taking advantage of their characteristics properly. Swash-plate type piston motor has many components such as stroke, pulsation and torque vary with the angles of swash plate, and thus properly designed swash-plate angles lay the foundation for developing low-pulsation, low-noise and high-efficiency motors. This paper will investigate a kinematic analysis of a swash-plate type piston motor model, using the hydraulic analysis program SimulationX® to model the 9 piston motor and to simulate the swash-plate angle for the low-pulsation and high-efficiency performance of the motor. Finally, in tandem with the theoretical consideration over stroke, the effect of changing strokes on pulsation is simulated here to analyse and determine the effects of the pulsation reduction. The optimal swash- plate angle and stroke found here will reduce the trial and error in future design.

Keywords— Swash-plate type piston motor, Pressure pulsation, Torque pulsation, Swash plate angle, Piston stroke, Simulation and modeling, SimulationX®

1 Introduction

In the construction and machinery industry, hydraulic equipment has long been used for construction machinery equipment for the high power density and durability. In particular, pumps and motors have been considered essential equipment and continuously investigated to find proper methods of taking advantage of their characteristics properly. The hydraulic cylinders including motors and rotary motors are collectively called a hydraulic actuator, which uses the fluid energy, that is, hydraulic cylinders for linear motions, and hydraulic motors for rotary motions. Also, as hydraulic motors ensure high durability and high efficiency in the unique environment surrounding the construction equipment, they are in wide use including the swing motors for excavators.[1] Among a wide range of hydraulic motors, this paper analyses the changes in performance and pulsation of the swash-plate type piston motor, whose operation is variable depending on the tilting swash-plate angle and whose variable capacity part with a small moment of inertia allows a high-speed control, in terms of design parameters.

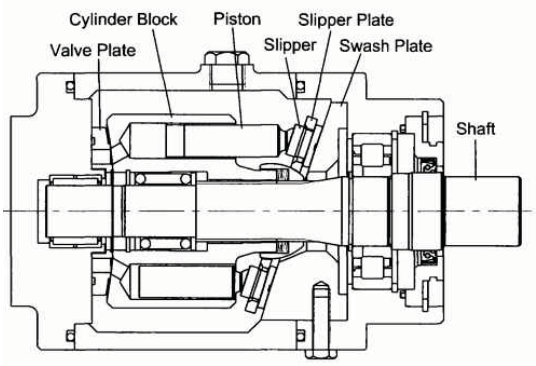

Fig. 1 swash plate type piston motor[2]

As in Fig.1, a swash-plate type piston motor comprises a valve plate, a cylinder block, a swash-plate, a piston, a slipper and a shoe. Lately, research on smaller, lighter, quieter and less pulsating hydraulic systems has been conducted by such industry leaders as Bosch-Rexroth and Kawasaki. In the same vein, the optimization of systems with less noise and pulsation should be considered in designing the foregoing components. To design a safer swash-plate type piston motor with less noise and pulsation, the tilting angle of a swash-plate should be investigated first. Many components such as stroke, pulsation and torque vary with the angles of swash plate, and thus properly designed swash-plate angles lay the foundation for developing low-pulsation, low-noise and high-efficiency motors.

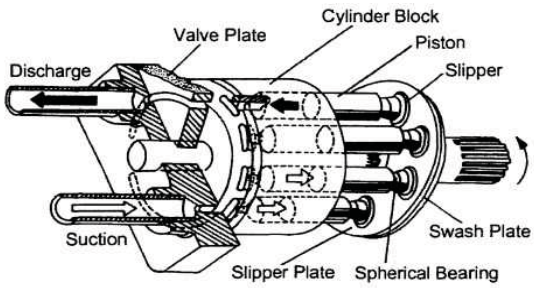

Fig. 2 Swash plate piston pump and motor of performance property [3]

Bae, *et al.* [3] explored the pressure and flow pulsation in view of the valve-plate notch shapes of swash-plate type piston pumps. However, Bae focused on reducing the pulsation of swash-plate type piston pumps without discussing the motor-related torque stabilization, strokes and swash-plate angles. As in Fig. 2, pumps and motors are similar in structure and differ in whether the suction and discharge generate the rotational force or vice versa. Yet, the differences in pulsation reduction and motor efficiency depending on piston displacement and swash-plate angles are significant, which needs further research on pumps as well as motors. Therefore, the present paper highlights a kinematic analysis of a swash-plate type piston motor model, using the hydraulic analysis program SimulationX® to model the single piston motor and to simulate the swash-plate angle for the low-pulsation and high-efficiency performance of the motor. Finally, in tandem with the theoretical consideration over stroke, the effect of changing strokes on pulsation is simulated here to analyse and determine the effects of the pulsation reduction.

2 Angle of Swash Plate Piston Motor

In general, the piston motor works in the following way: when the swash plate is tilted by α degree, the pressure fluid goes through the valve plate and then flows into the suction port of the cylinder block before it pushes the piston. Then, on the tilted swash plate, the piston and the piston shoe do the sliding motion followed by rotational and reciprocating motions, which in turn get the cylinder block and the principal axis connected to the spline to rotate and generate some mechanical energy.[1] The swash plate tilted by α is designed as in Fig.3. The rotation velocity, efficiency and pressure pulsation vary with the angle. Thus, in designing the swash-plate type piston motor, the α of the swash plate is very important.

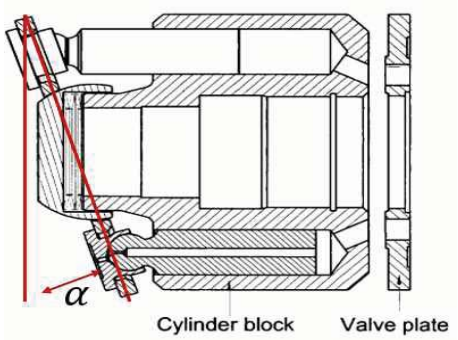

Fig. 3 The swash plate angle 'α'[4]

To simulate the change of motor rotation velocity, the change of efficiency and the change of pressure pulsation in line with the varying swash plate angle, α, the present paper applies angles in the range of 14 ~ 18 degrees to the swash plate and determines the resultant characteristics. As in Table 1, the flow analysis program, SimulationX® is used to model the varying motor performance in line with the different swash-plate angles in cases 1~3 and analyse the results.

Table 1 Paramaters of the swash plate angle

Case	Swash plate angle
1	14
2	16
3	18

3 Application at SimulationX® and Simulation Result

To design a single piston motor using the SimulationX®, a kinematic analysis of the piston motor model is needed. Figure 4 shows a schematic diagram used to design the swash-plate type piston pump model. The fixed angle frame method is used to get the same results as those reported by Jang, *et al.* [5]. The same value of design component is used for the motor and the pump. In Fig.4, *R* denotes the pitch circle diameter. α denotes the swash plate angle. φ denotes the rotational angle of the cylinder block.

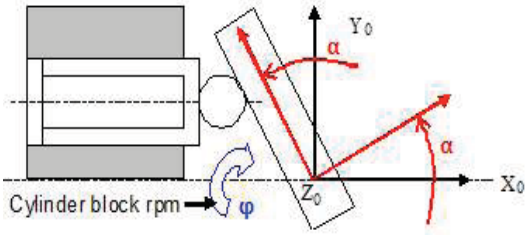

Fig. 4 Coordinate system in piston and swash plate[5]

$$XO_{PL} = -R \cdot sin\alpha \cdot cos \qquad (1)[5]$$

Figure 5 shows the single piston motor model based on the foregoing kinematic analysis. In this model, not only the swash plate but also many parameters, *e.g.*, the notch shape, suction pressure and piston weight, can be manipulated. In this section, the variation and characteristics of motor performance depending on the swash-plate angles are simulated. The other parameter values are shown in Table 2. Here, 3 cases (case 1 ~ 3) are analysed.

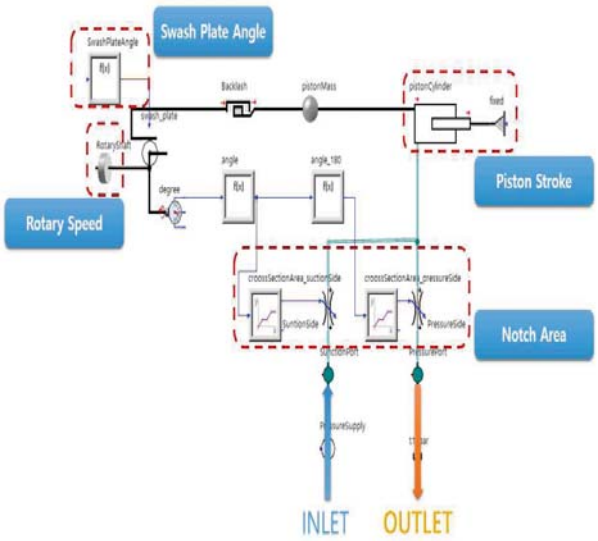

Fig. 5 Single piston motor modelling using SimulationX®

Table 2 Parameters of the model

Variable	Value
pressure supply (bar)	100
Piston diameter (mm), d	16.5
Stroke (mm), L	2 R tanα
Pitch circle diameter (mm), R	37
Piston mass (g)	100

To find out the pulsation and performance of the motor depending on the varying swash-plate angles only, the open area of shapeless notches is applied to all analysis models.[6] The open area orbit is shown in Fig.6. First, although the analysis of the single piston motor model is intended to find out the performance of the motor and the effects of less pulsation depending on the swash-plate angles, the single piston motor model does not provide a consistent RPM (Revolutions Per Mininute) value as below but repeats + and – as shown in Fig.7.

Fig. 6 The opening area without notch

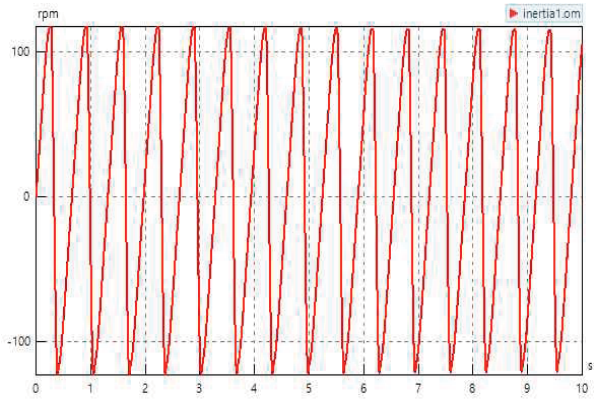

Fig. 7 The rotary speed at single piston motor

As the hydraulic motor generates the rotational force by pressure, to see a constant RPM or pressure pulsation, at least three pistons need to be used for the configuration and analysis. Therefore, this paper configures the well-known structurally stable and most widely used nine-piston motor to simulate the motor performance and pressure pulsation varying with the swash-plate angles. Instead of a single piston motor, a 9-piston motor is configured as in Fig.8. In Fig. 8, the dynamic design parameter of the rotation part need be designated in the 9-piston motor. The rotational inertia of the rotational moment of inertia on the motor is 0.01$kg \cdot m^2$ with the other parameters designated as shown in Table 3.

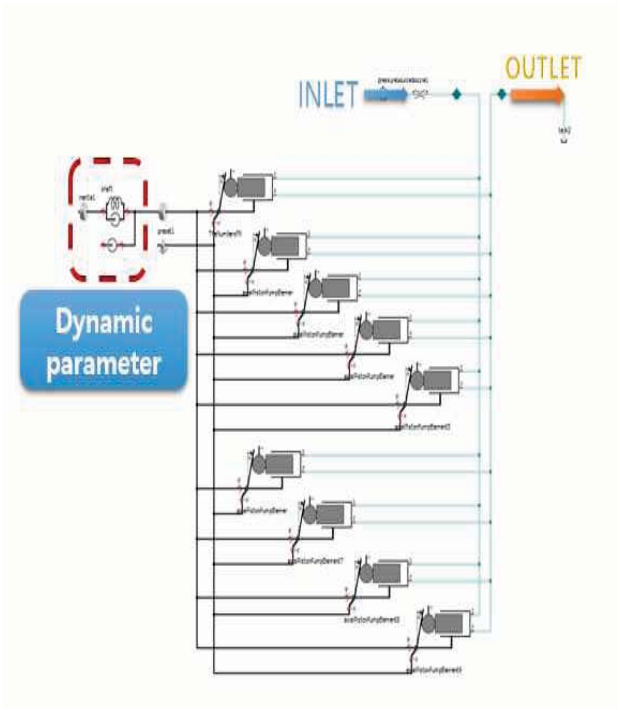

Fig. 8 9 piston motor modelling using SimulationX®

Table 3 Parameters of the model

Variable	Value
Moment of inertia(kgm^2)	0.01
Piston number	9
Stiffness of contact(N·m/rad)	500000
Damper(N·m·s/rad)	0.001

Although the shape of the valve-plate notch can reduce the pressure pulsation, the notch-less open area orbit is used to determine the motor performance in line with the swash-plate angles without affecting the other design components as in the single piston motor. This is the same as Fig.6. Also, to represent the suction and discharge parts of the valve plate, a variable orifice is used. That is, the role of the valve plate is represented by entering the function values that keep the discharge orifice from flowing when suction is needed and keep the suction orifice from flowing when discharge is needed.[7] The simulation of the cases 1~3 under the same condition provides the following results of the rotary speed, pressure pulsation, and torque pulsation. As for the rotary speed, the early reaction rate increases in proportion to the size of the swash-plate angle, whereas the RPM decreases as the swash-plate angle remains constant as in Fig. 9. The enlarged part shows the characteristics more clearly. It takes 0.4, 0.33 and 0.32 seconds (so-called stable time) to reach a steady rotary speed in cases 1, 2 and 3, respectively. Also, the rotary speed fell to 1966 RPM, 1833 RPM and 1707 RPM in cases 1, 2 and 3, respectively. These results indicate that motor performance can be improved with the swash-plate angle only as the condition for the 9-piston motor based on the suction pressure. Table 4 shows the results.

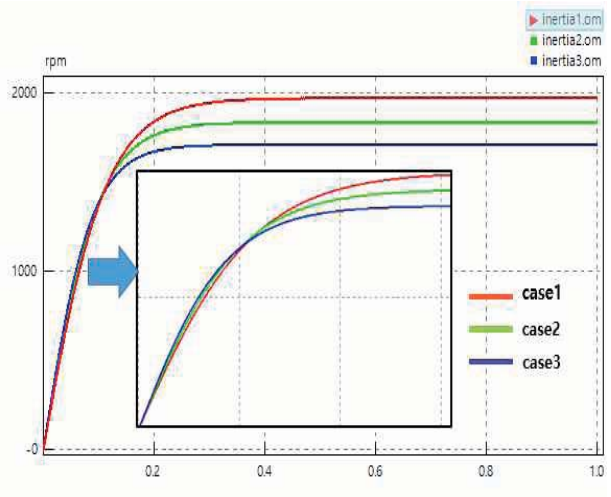

Fig. 9 Rotary speed according to swash plate angle

Table 4 Rotary speed & stable time

Case	Time (s)	Rotary speed (RPM)
Case1	0.4	1966
Case2	0.32	1833
Case3	0.33	1707

The volume per rotation, as in Eq. (2), is influenced by the number of pistons (z), the cross-sectional area of pistons (A), and the diameters of pistons(d). Also, the volume (V) varies with the swash- plate angles.

$$V = z \cdot A \cdot H = z \cdot \frac{\pi d^2}{2} \cdot \tan \alpha \quad (2)[1]$$

Therefore, as the flow increases with the swash plate angles, the pulsation on the valve plate also increases. Figure 10 shows the pressure increases with the growing flow. Also, the enlarged part shows the pulsation increases as well.

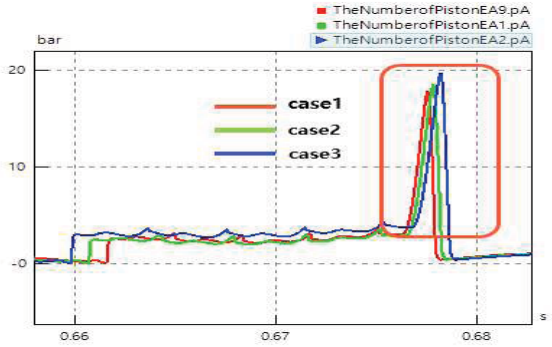

Fig. 10 The pressure pulsation at cylinder according to swash plate angle

Thus, the findings suggest that the excessive increase in the swash plate angles exerts great effects on the noise due to pulsation and resistance and that it is important to choose appropriate angles. Moreover, the torque pulsation is affected by Eq. (3).

$$T_t = \frac{Z}{2\pi} \int_0^{2\pi/z} T' * d\emptyset = \frac{d^2}{4} ZPR \tan \alpha \quad (3)[7]$$

As in Eq. (3), the torque pulsation is influenced by the swash-plate angles. As in Fig. 11, the simulation proves that the torque pulsation and the torque value increase in proportion to the swash-plate angles. Here, the value (δ) of torque pulsation of the motor is given y Eq. (4).

$$\delta = \frac{T_{max} - T_{min}}{T_t} \quad (4)[7]$$

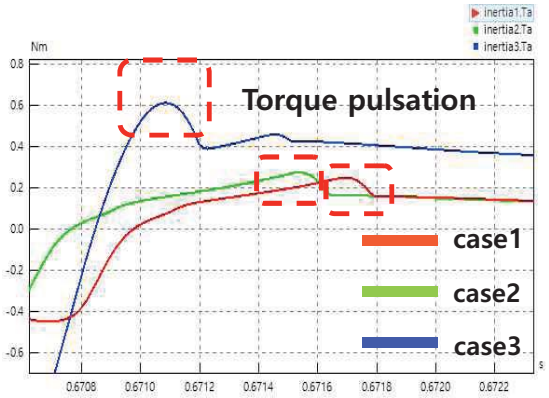

Fig. 11 Torque pulsation at shaft according to swash plate angle

4 Stroke Simulation at SimulatonX®

To lower the pulsation of the swash-plate type piston motor, it is very important to find out the design components through a theoretical approach where instant pulsation occurs. Figure 13 shows the rotary part excluding the valve plate of the swash-plate type piston motor. d_p denotes the piston diameter. $H_k$denotes the maximum stroke of the piston. $D_z$denotes the PCD (Pitch Circle Diameter). This paper aims to theoretically prove the effects of the maximum stroke value of a piston on pulsation, and the pulsation reduction effects of H_k using SimulationX®.

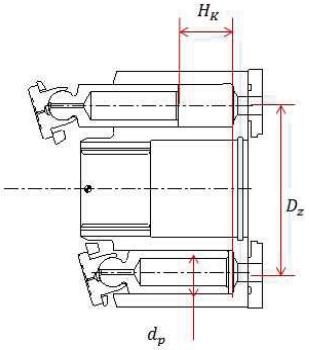

Fig. 13 Section diagram of 'H_k' -1 [8]

First, α and φ denote the swash-plate angle and the rotation angle of the cylinder block, respectively, in Fig. 14. Here, Eq. (8) calculates the displacement of the piston, where H_k is the maximum displacement of the piston.

$$y = R \cdot \tan\alpha \quad (5)[1]$$

$$b = R \cdot \cos\varphi \cdot \tan\alpha \quad (6)[1]$$

$$S_k = y - b = R \cdot \tan\alpha \quad (7)[1]$$

$$H_k = 2 \cdot R \cdot \tan\alpha \quad (8)[1]$$

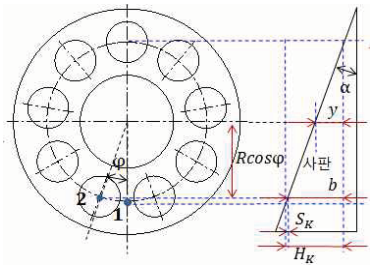

Fig. 14 Section diagram of 'H_k' -2 [8]

The flow pulsation (Q) of the motor instantly gained from the pump is Eq. (9)

$$Q = \sum_{i=1}^{z_0} A_p v_i = A_p \frac{H_k \omega}{2} \sum_{i=1}^{z_0} \sin\{\theta + (i-1)\frac{2\pi}{z}\} \quad (9)[1]$$

Here, v is given by Eq. (10).

$$v = \frac{H_k}{2} \cdot \omega \cdot \sin\theta \quad (10)[1]$$

The frequency of flow pulsation is higher and the flow pulsation rate is lower for the unit time when the number of pistons is an odd number in comparison to an even number. Therefore, this paper selects a nine-piston motor, and the formula for an odd-number flow pulsation is as follows.

$$Q = \frac{A_p H_k \omega}{2} \cdot \cos\frac{\pi}{2z} \cdot \cos(\theta - \frac{\pi}{2z}) / \sin\frac{\pi}{z} = \frac{A_p H_k \omega}{2} \cdot \cos(\theta - \frac{\pi}{2z}) / \sin\frac{\pi}{2z} \quad (11)[1]$$

As per Eq. (11), the values of H_k are varied (20mm, 25mm 30mm and the theoretically calculated 17.5mm) to analyze the effects of H_k values on the flow pulsation (Q) of the swash-plate-type piston port. How to set up the piston stroke at SimulationX® is illustrated as shown in Fig. 15.[9]

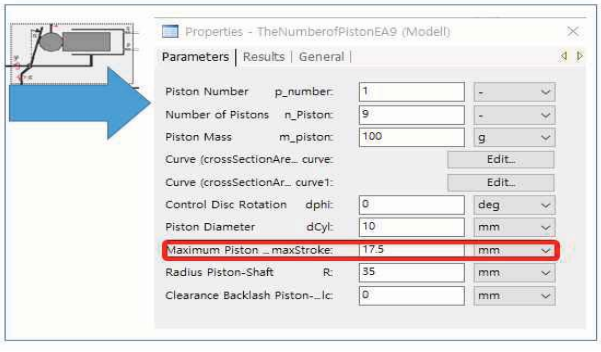

Fig. 15. Setting a value of 'H_k' at SimulationX®

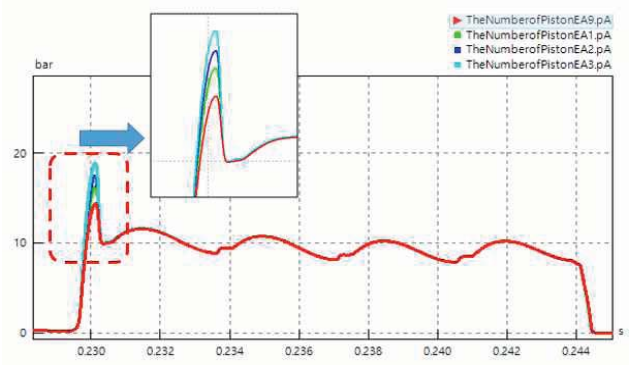

Fig. 16. The flow pulsation at cylinder according to 'H_k'

The results are shown in Fig. 16, where the pulsation is lowest at 17.5mm calculated for the parameter value of the motor, whereas the pulsation within the cylinder is high in a motor whose stroke is too short or too long. As in Table.5, the least pulsation is found in the theoretically calculated piston stroke in case 1. Thus this means that, in designing the piston motor, the stroke should be set based on the theoretical design.

Table 5 Value of 'H_k' and flow pulsation

Case	H_k (mm)	Maximum flow pulsation (bar)
Case1	17.5	14
Case2	20	16
Case3	25	17.5
Case4	30	18.8

5 Conclusions

The present paper investigates the design of the swash-plate angle and stroke of the swash-plate type piston motor with high power and rotary speed used for the swing motor of construction machinery, and **simulates** the impacts of the swash-plate angles and stroke on motor performance and pulsation using the hydraulic analysis program SimulationX®. The results of **simulation** shed light on the following. First, the swash-plate angles in the range of 14~18 degrees are used. Optimal angles exist for the parameter values of a motor. The motor used in this paper shows the highest motor performance and stable pulsation at 14 degree. Second, the design components impacting on the pulsation are theoretically proved. In particular, the effects of the piston stroke on pulsation are proved using **simulation**.

Conclusively, this paper **simulates** the swash-plate angle and stroke for the purpose of high- performance and high-resistance of the swash-plate-type piston motor. The optimal swash- plate angle and stroke found here will reduce the trial and error in future design. Future work will delve int the design of valve-plate notches to develop an evolved high-performance and high-durability piston motor.

6 References

[1] Y. Y. Lee, "Hydraulic Engineering", 2012

[2] J. G. Kim, "Performance Characteristics with Valve Plate Shapes in Swash Plate Type Oil Piston Pumps", Ph.D thesis of Chonbuk National University, 2003

[3] J. H. Bae, W. J. Chung, S B. Kim, "Application of SimulationX based Simulation Technique to the Design of opening Area for a Valve Plate of Swash Plate type piston Pump", Journal of The 2015

[4] J. H. Jang, W. J. Chung, S. W. Jeong, "A study of efficiency for Variable Swash Plate Type Piston Pump, Journal of The 2012 Korean Society Of Precision Engineering, 2012.

[5] J. H. Jang, W. J. Chung, D. S. Lee, Y. H. Yoon, "Application of SimulationX based Simulation Technique to Notch Shape Optimization for a Variable Swash Plate Type Piston Pump, Journal of The 2013 International Conference on Scientific Computing, 2013

[6] D. K. Noh, and J. S. Jang, "Shape Design Sensitivity analysis of the Valves installed in the Hydraulic Driving Motor" Journal of The Korea Society for Fluid Power and Construction Equipments KSFC, 2012

[7] Y. W. Jeong, "A Study on the Design of Rotary parts in a Fixed Displacement Swash Plate Type Piston Motor", Changwon National University, 2015.6

[8] SimulationX user manual and library manual, ITI GmbH, 2011

[9] L. L. Liu, J. S. Jang, "Characteristics Analysis of the Hydraulic Motor Design Variables", Journal of the 2013 Korean Society Of Automotive Engineers, 2013.7

Data Deduplication for Firmware Files

Noboru Takeuchi, Mayuko Hirose, Matrazali Noorafiza,
Satoshi Takano, Itaru Koike, Toshiyuki Kinoshita

Graduate School of Computer Science, Tokyo University of Technology
1404-1 Katakura, Hachioji Tokyo, 192-0982, Japan

Abstract *The firmware is installed in many kinds of equipment, and is built-in the inner memory of hardware, so it can be considered as a part of hardware. Recently it has been able to be recorded on the rewritable flash memory and be updatable through the network. The firmware file size has increased because the memory size for the firmware has grown up and the firmware has realized more functions. Therefore, it is important to reduce the firmware file size. Then, we consider making the firmware file size smaller by data deduplication technique. Almost all the firmware keeps multiple versions and the newest version is activated and used. In this study, we analyzed the efficiency of deduplication applied for the firmware files, especially how does the version management of the firmware files affect the effect of deduplication.*

Experimental results show that the deduplication rates for the newest & previous versions and the deduplication rates for all versions are much higher, while the deduplication rates for only the newest version and the reduce rates of compression are lower. It is very important for deduplication for the firmware to perform the deduplication among multiple versions of the firmware

Keywords *data deduplication, firmware, multiple versions*

1. Introduction

Recently, there exist many kinds of electronic equipment, such as PC, smart phone, tablet device, and game machine, etc., and the electronic equipment consists of several kinds of elements; hardware, firmware, and software. Hardware is devices or parts of the equipment. Firmware is a built-in program in the inner memory of hardware to control basic hardware such as processor, memory, and HDD devices, etc., and cannot be usually rewritten. Software is a program that is loaded in main memory, executes on the processor and realizes the system functions. Application software achieves the function for end-users such as spreadsheet, Web-browser, or graphic software, etc. System software (basic software) controls the hardware and makes the application software utilize the hardware function easily. Although the system software and the firmware have similar functions, the firmware is built-in the inner memory of hardware, so it can be considered as a part of hardware, and can be hardly rewritten, while the system software can be repeatedly installed and version-up. Therefore, the former is called "firmware" ("firm" means hard, fixation).

Formerly the firmware file size had been very small because the memory size for the firmware had been so small. Lately the firmware file size has increased because the memory size for the firmware has grown up and the firmware realizes more functions. Moreover, although the firmware had been recorded on the inner memory of hardware, called a mask ROM, recently it has been able to be recorded on the rewritable flash memory. Moreover, since the number of equipment connected with the network has increased, the firmware can be updatable through the network. However,

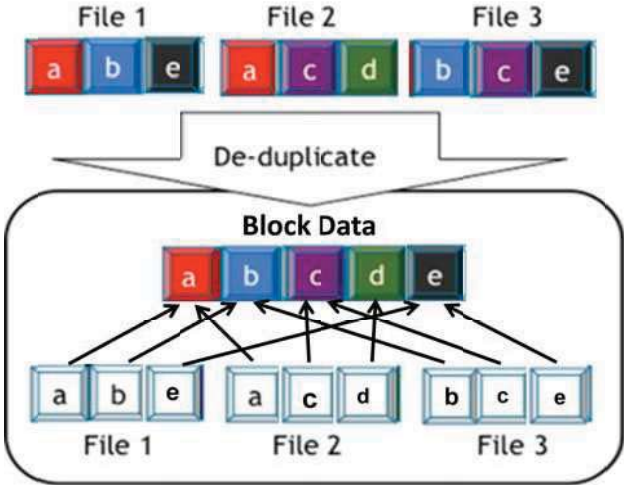

Fig.1 Concept of data deduplication

if the firmware is repeatedly sent whenever updating, the network resource can be much wasted. Therefore, it is important to reduce the firmware file size. Then, we consider making the firmware file size smaller by data deduplication technique.

Data deduplication is a process that tests the similarity in record pairs and merges them if similarity is detected. It can reduce a huge amount of data by eliminating overlapping data (redundant data) in large-scale servers or data storage. Using data deduplication, only one representative of two or more overlapping data is preserved as block data, while the overlapping data is replaced with links that point to the representative data (as shown in Fig. 1). By replacing multiple overlapping data with links, data storage size can be extremely reduced. As a result, the efficiency of data storage can be highly improved and cost in data maintenance and storage can be also decreased.

2. Data deduplication

2.1 Two types of block

In the data deduplication technique, the target files are divided into several parts (each part is called a block) and any duplicate blocks are eliminated. By dividing the files into blocks and finding the duplicate part by the blocks, files are not required to be strictly same and high deduplication efficiency can be achieved.

There are two types of block; one is fixed-length block whose length is constant and the other is variable-length block whose length can be changed. In the fixed-length block method, when some data are inserted into the file and the blocks after inserted position are shifted, they cannot be recognized as duplicate blocks in the original data (Fig. 2 (a)). On the other hand, in the variable-length block method, even if some data are inserted into the file, by adjusting the block length for the insertion, the blocks after inserted position can be recognized as duplicate blocks and be applied for deduplication (Fig. 2 (b)). Thus, in the variable-length block method, the effect of deduplication can be maintained even if some data have been inserted or deleted.

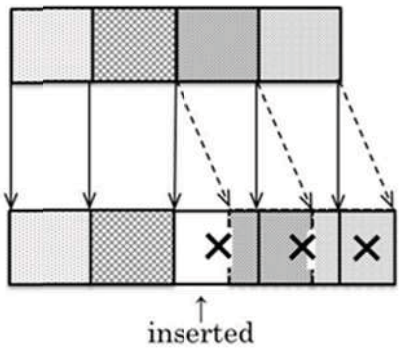

(a) Fixed-length block

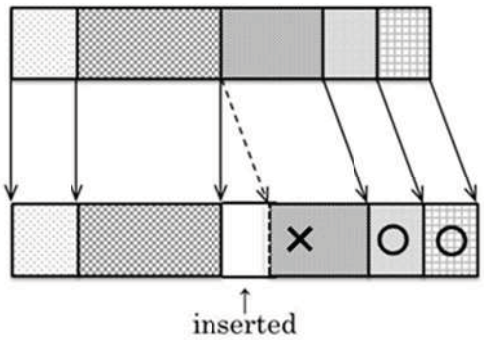

(b) Variable-length block

Fig. 2 Tow types of block

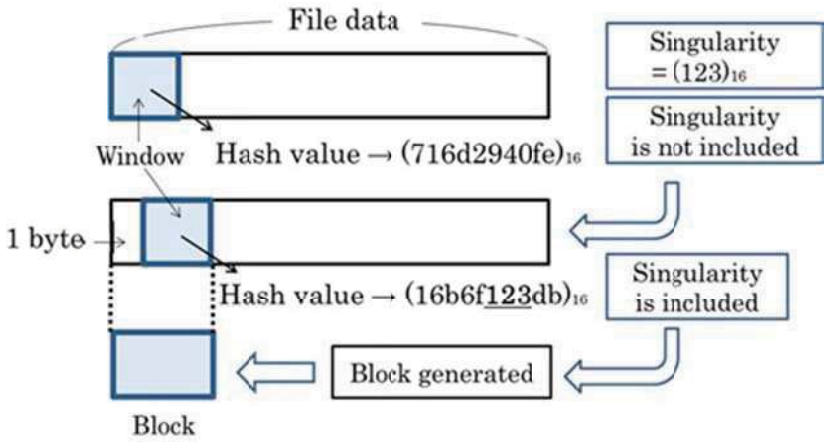

Fig.3 Breakpoint search

Fig. 3 shows how to detect the break point of valuable-blocks efficiently. Firstly the hash value of a

small part with constant length, that is called a window, is calculated. The window indicates the candidate of the breakpoint of the block. When a particular bit-pattern, that is called a singularity, is included in the hash value of the window, the candidate becomes a real breakpoint of the block. When the singularity is not included in the hash value, the candidate does not become a breakpoint. The effect of deduplication can be affected by the singularity; especially by the singularity size. In our previous works [5][6], we found that the optimum singularity size is 15 bits and the optimum window size is around 32 bytes. In this study, we also used these parameters.

2.2. Variable-length block

The Rabin-Karp string search algorithm is used for finding the singularity in the hash value of the window. The following parameters are used in the algorithm.

(1) Minimum file size (default is 40 bytes)
Files that are smaller than this size will not be targeted for deduplication.
(2) Minimum block length (default is 4,000 bytes)
(3) Maximum block length (default is 16,000 bytes)
(4) Window size (default is 32 bytes)
Window is a unit for calculating a hash value.
(5) Singularity
When the singularity is included in the bit-pattern of the hash value of the window, a breakpoint is found and a block is generated at this position.

For a file whose size is between the minimum file size and the minimum block length, the whole file is generated as a block. When a file is larger than the minimum block length, a breakpoint will be determined. As shown in Fig. 3, in searching for the breakpoint, a hash value is first created for the window at the location of the minimum length block, and is checked up if it includes the singularity, or not. When the hash value includes the singularity, a breakpoint is found and a block is generated at this position. When the hash value does not include the singularity, the window is shifted one byte and the breakpoint search is repeated. When the breakpoint is not found until the maximum block length, a maximum length block is generated at this position.

In the variable-length block method, the block length can be changed, and the maximum and minimum block length is set not to generate an extremely large or small block. The effect of deduplication is also affected by this maximum / minimum block length.

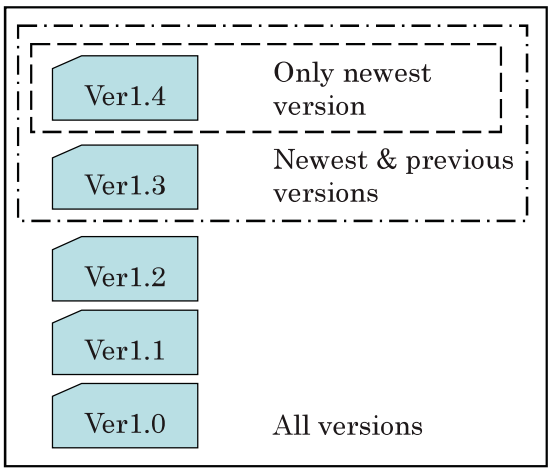

Fig.4 Multi-versions of firmware

3. Related Works

The effect of deduplication in the fixed-length block method when the block length is set to 4 ~ 16 K bytes was investigated in [1] and the efficiency of the variable-length method was discussed in [3]. The differences of the effects of deduplication between in the variable-length block method and in the fixed-length block method when the block length is larger than 4 K bytes were reported in [2] and when the block length is smaller than 4 K bytes were discussed in [4]. These studies have investigated the relationship between the block length and the effect of deduplication. In [5], the double layered deduplication method that combines the fixed-length method and valuable-length method is proposed. In our previous work [6][7], we analyzed the relationship between the singularity size and the deduplication rate. In this study, we analyzed the efficiency of deduplication applied for the firmware files, especially how does the version management of the firmware files affect the effect of deduplication.

4. Version management

When we apply the deduplication technique to the firmware, the version management is very important. There are three types of version-up. In the major version-up, the program is much changed. In the minor version-up, the program is not so much changed. In the maintenance version-up, some light changes such as easy troubles are performed. As the major version-up is rarely performed and the minor version-up is not also often performed on the firmware file, almost all version-up of the firmware is the maintenance version-

Table 1 Deduplication for firmware

		HDD Case	Access Point A	Access Point B	Wi-Fi Router
Deduplication	File size (Byte)	1,139,174	5,425,572	48,005,836	4,055,042
	Number of versions	3	6	4	6
	Dedup. in only newest version	0 (0.00%)	0 (0.00%)	1,884,160 (3.92%)	128,000 (3.16%)
	Dedup. in newest & previous versions	45,811 (4.02%)	429,267 (7.91%)	1,917,070 (3.99%)	356,987 (8.80%)
	Dedup. in all versions	45,811 (4.02%)	466,459 (8.60%)	1,925,262 (4.01%)	801,279 (19.76%)
Compression (Zip)	Reduce rate	1.93%	0.00%	8.14%	0.22%
		Upper line: dedup. size (Byte) Lower line: dedup. rate (%)			

		Mobile Router	Router A	Router B	Router C
Deduplication	File size (Byte)	5,685,644	5,765,296	4,686,212	4,903,460
	Number of versions	3	6	5	16
	Dedup. in only newest version	0 (0.00%)	0 (0.00%)	0 (0.00%)	0 (0.00%)
	Dedup. in newest & previous versions	2,222,232 (39.08%)	833,770 (14.46%)	120,946 (2.58%)	268,416 (5.47%)
	Dedup. in all versions	2,226,581 (39.16%)	968,025 (16.79%)	292,755 (6.25%)	332,333 (6.60%)
Compression (Zip)	Reduce rate	3.99%	2.56%	3.20%	2.45%
		Upper line: dedup. size (Byte) Lower line: dedup. rate (%)			

up. Therefore, the block data management of each version of the firmware is important.

In this study, we performed experiments for three patterns of block data; block data of only present version, block data of present and previous versions, and block data of all versions (Fig. 4). Since there is only a few updates in a maintenance version-up, the high deduplication rate can be expected between two or more versions of the firmware files. Moreover, in a version-up of the firmware, the block data can be easily obtained since we have both firmware file before and after version-up.

5. Firmware deduplication

5.1 Experiment environment

For the experiments, we prepared 8 kinds of firmware; 1 hardware controller, 2 access points, 1 mobile router, 1 Wi-Fi router, 3 network routers. For comparison, we have the compression rate of Zip as an ordinary compression program. The evaluation indexes are deduplication size, deduplication rate that is the ratio of the deduplication size to the original file size, and compression rate by Zip.

5.2 Experiment results

Table 1 and Fig. 5 show the results of deduplication and compression for the firmware files. On the whole, we can see that the deduplication rates for the newest version only are zero except two cases, Access point B and Wi-Fi router, and the deduplication rates for these two cases are also low even though not zero. This means that the effects of the deduplication within only one version are quiet limited. On the other hand, the deduplication rates for the newest & previous versions and the deduplication rates for all versions are 4 ~ 39%

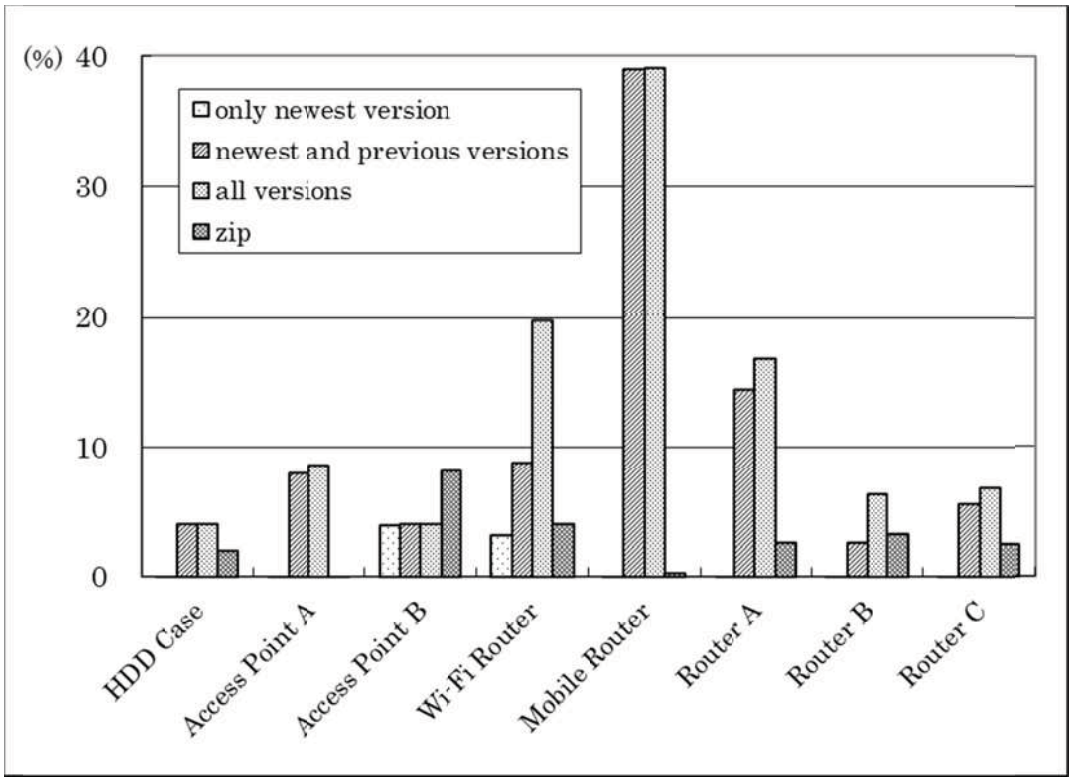

Fig.5 Deduplication rate & Reduce rate

and the effects of the deduplication are quiet improved. This means that the version management of the firmware significantly affects the efficiency of the deduplication.

Table 1 also shows that the reduce rates of the compression are 0 ~ 8% and the effects of the compression can be generally lower than the effects of the deduplication among the multi-versions of the firmware. Here we can see that the version management of the firmware is very important again.

6. Conclusion

The efficiency of deduplication applied for the firmware files was analyzed. As many versions are maintained in the firmware files, we clarified that the efficiency of the deduplication is much improved by performing the deduplication among the multi-versions of the firmware.

As our future work, we will analyze how the difference of file types affects the efficiency of the deduplication.

References

[1] Q. He, Z. Li, X. Zhang, "Data deduplication techniques," Future Information Technology and Management Engineering (FITME) 2010, vol. 1, pp. 430-433, Oct. 2010

[2] C. Constantinescu, J. Glider, D. Chambliss , "Mixing Deduplication and Compression on Active Data Sets," Data Compression Conference (DCC) 2011, pp. 393-402, March 2011

[3] A.N. Yasa, P.C. Nagesh, "Space savings and design considerations in variable length deduplication," ACM SIGOPS Operating Systems Review, Vol. 46 Issue 3, pp. 57-64, Dec. 2012

[4] M. Noorafiza, I. Koike, H. Yamasaki, A. Rizalhasrin, T. Kinoshita, "Block Length Optimization in Data Deduplication Technique," Proceedings of the 10th International Conference on Scientific Computing (CSC2013), pp.216-220, July 2013

[5] H. Yamasaki, I. Koike, T. Kinoshita, "Analysis of double layered deduplication efficiency," IPSJ SIGMPS Technical Report, Vol. 2014-MPS-97 No. 9, March 2014 (in Japanese)

[6] M. Ogiwara, M. Takaya, T. Kasuya, I. Koike, T. Kinoshita, "Singularity Size Optimization in Data Deduplication Technique," Proceedings of the International Parallel and Distributed Processing Techniques and Applications 2014, (PDPTA2014), pp.171-175, July 2014
[7] M. Noorafiza, M. Hirose, M. Takaya, I. Koike, T. Kinoshita, "Optimum Singularity Size in Data Deduplication Technique", Proceedings of the 2015 International Conference on Scientific Computing (CSC2015), pp.101-105, July 2015

ISBN: 1-60132-430-8, CSREA Press ©

SESSION

COMPUTATIONAL SCIENCE: GRAPH BASED ALGORITHMS + OPTIMIZATION METHODS AND FUZZY LOGIC

Chair(s)

TBA

ISBN: 1-60132-430-8, CSREA Press ©

ISBN: 1-60132-430-8, CSREA Press ©

Dominating Effect on Spinodal Structure Behaviour of the Giant Component Cluster in Simulations of the Kawasaki Diffusion Model

K. A. Hawick
Computer Science, University of Hull, Cottingham Road, Hull HU6 7RX, UK.
Email: k.a.hawick@hull.ac.uk
Tel: +44 01482 465181 Fax: +44 01482 466666

March 2016

ABSTRACT

The Kawasaki diffusion model model provides a foundation for understanding phase separation in various physical and model systems including alloys. We use a graph component labelling technique to identify and analyse the clusters formed in Monte Carlo simulations of the Kawasaki model in three dimensions after long simulation times. We provide some visually rendered snapshots of the system over its phase diagram. We find that the giant component cluster dominates the behaviour through formation of percolating string-like spinodal structures over a remarkably wide range of concentrations and quench temperatures. We discuss the emergence of this complex spatial structure and its variations in thickness, density and energy over this range.

KEY WORDS
computational modelling; Monte Carlo simulation; computational physics; complex systems; visualisation.

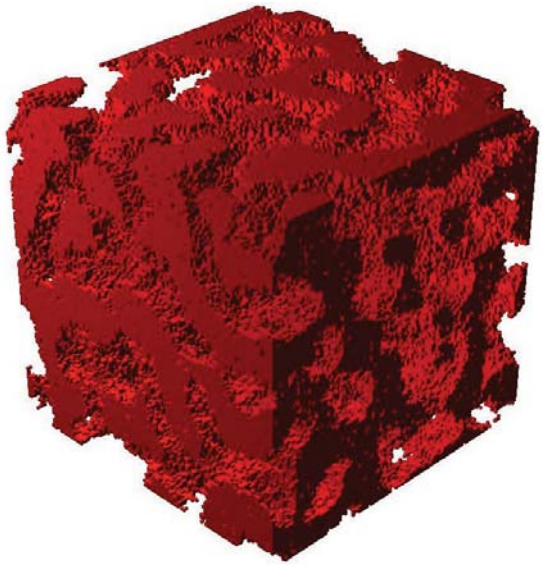

Figure 1: Largest Cluster - showing fully spinodal structure - of 2 State Kawasaki model run for 32,768 steps at 50% concentration and quench temperature of 3.0.

1 Introduction

Understanding complex systems and spatially emergent behaviour remains an important general use for computer simulation models. Materials such as alloys and other mixtures can be studied using the behaviour of models such as the Kawasaki diffusion model [27–29] as a baseline. Some properties of the Kawasaki system such as the nucleation of particles in it following a quench and its phase separation behaviour [30] have been studied extensively, but a systematic study of connected components in large scale realisations of this model have been difficult due to limits on computational memory and speed performance of the simulation model itself [40, 41] and also the component analysis techniques [21], until recently.

We have simulated large scale Kawasaki systems over long simulation times to obtain model configurations that are representative of the long time-scale behaviour of this model. We have used graph connected-component labelling to identify and measure various properties of the system to explore whether a single giant component is always formed and what effect it has on the overall behaviour of the system. We have found that over a remarkably wide range of temperatures and concentrations, a single giant cluster does form and completely dominates the bulk behaviour of the systems properties such as the energy. This spinodal decomposition mechanism [1, 15] has been widely studied using simulations and real experiments using microscopy and neutron scattering on real alloys. We are not aware of any extensive work studying simulation microscopic details using graph component labelling before however.

In addition to its use as model for binary alloys [24] and materials science mixtures, the Kawasaki base line model has been used to study a diverse range of applied systems including: coastal erosion [17]; non-Newtonian fluid layering [22]; pair annihilation and multi species screening [16]; photobioreactors [18]; and art systems such as falling sand pictures [35]. It forms the basis for transport [26] and diffusional behaviour in more generalised agent-based models [13]. Its general properties can be analysed theoretically [32], but much of its complex spatial behaviour is still difficult to analyse and indeed characterise without recourse to computer simulation and visualisation.

Gaining insights into simulation model such as the Kawasaki system are quite difficult in dimensions higher than two [38]. Looking inside three dimensional systems is difficult and only to some limited extent do graphical renderings help this endeavour [20]. We present some renderings of the three dimensional model over a range of concentrations and temperatures, giving a visual representation of phenomena over a large part of its phase diagram.

Figure 1 shows the largest fully connected cluster in a Kawasaki model, aged for 32,768 Metropolis steps at temperature of 3.0 and concentration of 50%. The structure is a full spinodal or interconnected single component, percolating the periodic lattice of 128^3 sites completely.

There are a number of features of the Kawasaki model that we do not explore including the many variations of simulation dynamics using various dynamical schemes [36] and these have been well studied before [23]. For this present work we focus on use of the simplest Metropolis Monte Carlo dynamical mechanism [2, 3] for our studies here.

Graph component labelling [7] is a computationally demanding for the large system sizes [39] we report on here. Recent work with Graphical processing Units (GPUs) has allowed array parallelism to speed up some of these calculations considerably [19]. We outline our generally approach in this present article but defer details of component labelling optimisation to [19].

Our article is structured as follows: In Section 2 we outline the Kawasaki model and its formulation for simulation purposes. In Section 3 we outline our method for identifying spatial connected components in model configurations. We present a range of visual and quantitative results in Section 4 and a discussion of our observations of the giant component cluster behaviour in Section 5. We offer some conclusions and areas for further work in Section 6.

2 Kawasaki Exchange Model

In formulating the Kawasaki model we first consider a two component substitutional alloy consisting of a single crystal or lattice of material. We restrict the model to just two atomic species.There are only two chemical species occupying the sites of a regular lattice. While they will oscillate about some mean positions, the bulk material retains its structure and the average positions do not change, and so there are no interstitial atoms permitted. We take there to be N atoms on the lattice and subdivided by chemical species into N_A of species A and N_B of species B so that $N = N_A + N_B$. Focusing our attention on species A the number of possible arrangements W of the N_A atoms of species A is simply given by:

$$W = \frac{N!}{N_A!(N - N_A)!} = \frac{N!}{N_A!(N_B)!} \tag{1}$$

given that the A-species atoms are individually indistinguishable. The micro-structure produced by the set of atomic arrangements constitutes a microstate of the model alloy and to make the model able to simulate the dynamics of an alloy, it is necessary to impose a dynamical scheme whereby the system can explore all its microstates.

We need a model for the interactions between the species and the simplest model Hamiltonian ($\mathcal{H}$) consists of an assignment of pair-wise bonds or interactions between neighbouring atoms. We formulate this in terms of a local concentration variable c_i for each lattice site which has the value 1 for A-sites and value 0 for B-sites. The Hamiltonian can then be written in terms of coupling constants $V_{ij}^{c_i - c_j}$ between sites i and j.

The Kawasaki model Hamiltonian or the energy functional for a binary alloy of the two species "A" and "B" is thus written:

$$\begin{aligned}\mathcal{H}_{\text{Alloy}} = \mathcal{H}^0 + \quad \sum_{i \neq j} \quad & V_{ij}^{\mathbf{A-A}} c_i c_j + \\ & V_{ij}^{\mathbf{A-B}} c_i (1 - c_j) + \\ & V_{ij}^{\mathbf{B-A}} (1 - c_i) c_j + \\ & V_{ij}^{\mathbf{B-B}} (1 - c_i)(1 - c_j)\end{aligned} \tag{2}$$

in terms of the potential terms V. All these parameters used in the Hamiltonian can be specified explicitly, or we can limit the model to nearest neighbour uniformly isotropic interactions, so that only one parameter V^{A-A} is retained. For simulation purposes we can focus on a V between like-like species. By so expressing this one parameter in Boltzmann units of $k_b T$, we are implicitly specifying the temperature T of the system which can be used in a quench experiment.

This Hamiltonian does not have an explicit dynamical scheme, and so one must be imposed artificially using standard Monte Carlo techniques to make the model system evolve between different microstate configurations "X" along a trajectory in state space that is physically realistic and which will reflect useful growth properties.

This form of Hamiltonian can in fact be shown to be isomorphic to that of the Ising model for a spin-$\frac{1}{2}$ magnet in a magnetic field [31] and was first employed by Bragg and Williams to study order-disorder processes in alloys [4], and by Cernuschi and Eyring as a model for lattice gases [6].The Hamiltonian can then be written in the form:

$$\mathcal{H}_{Ising} = -\sum_{i \neq j} \mathcal{J}_{ij} s_i s_j + H \sum_i s_i \tag{3}$$

where the Ising spins s_i take the values $s_i = \pm 1$ and are given by the transformation:

$$s_i = 2c_i - 1 \tag{4}$$

$$c_i = \frac{s_i + 1}{2} \tag{5}$$

In our present work we use the simplest case of this, where the interactions are short range nearest neighbour in fact The Ising coupling parameter $\mathcal{J}_{ij}$ can be written as $\mathcal{J}$ and taken outside of the summation. This allows the Ising coupling $\mathcal{J}$ and magnetic field strength H to be written as:

$$\mathcal{J}_{ij} = \frac{1}{4}\{(V^{\mathbf{A-A}} + V^{\mathbf{B-B}}) - (V^{\mathbf{A-B}} + V^{\mathbf{B-A}})\} \tag{6}$$

$$H = -\frac{1}{2} \triangle \mu^{\mathbf{A-B}} \tag{7}$$

This only leaves two free parameters, and the alloy Hamiltonian is thus expressed in terms of only $V^{\mathbf{A-A}}$ and $\triangle\mu^{\mathbf{A-B}}$. The binary alloy can be thought of as just the A-species in a background of B. The lattice gas picture merely involves treating the B sites as "vacancies". It is possible to reduce the parameters involved to one, by operating with zero chemical potential, as described in the dynamical scheme below.

Both the alloy and Ising Hamiltonians as expressed above do not give rise to their own dynamical equation so it is necessary to introduce a stochastic mechanism for the system to explore its microstates. Focusing attention on the A-particles we require a mechanism for the particles to change position and explore the lattice but keeping the number of particles present (N_A) constant. We need to operate with a constant chemical potential $\mu^{\mathbf{A-B}}$ without increasing or decreasing the particle population. This is know as 'spin-exchange' or Kawasaki dynamics [27] and is used for a canonical thermodynamical simulation of the alloy model whereupon neighbouring site variables c_i and $c_{i\pm1}$ are exchanged. The exchanges must be performed with a carefully specified probability if our system is to have valid thermodynamic properties.

Recognizing that for a Boltzmann statistical weighting of the microstates, the probabilities $P(\mathbf{X}$ can be expressed in terms of the Hamiltonians $\mathcal{H}(\mathbf{X})$.

$$P(\mathbf{X}) = Ae^{-\frac{\mathcal{H}(\mathbf{X})}{k_bT}} \tag{8}$$

Where A is a normalising constant, k_b is Boltzmann's constant and T the temperature. This gives:

$$\frac{W_{\mathbf{X}'\to\mathbf{X}}}{W_{\mathbf{X}\to\mathbf{X}'}} = e^{-\frac{\{\mathcal{H}(\mathbf{X})-\mathcal{H}(\mathbf{X}')\}}{k_bT}} \tag{9}$$

This does not have a unique solution but the two most commonly used are [10, 33] and for the purposes of the work reported here we use the conventional Metropolis solution:

$$W_{\mathbf{X}\to\mathbf{X}'} = \begin{array}{ll} \frac{1}{\tau}e^{-\frac{\triangle\mathcal{H}}{k_bT}}, & \triangle\mathcal{H} > 0 \\ \frac{1}{\tau}, & \triangle\mathcal{H} \leq 0 \end{array} \tag{10}$$

The simulation time can then be defined in units of 'an average of one Metropolis update attempt per site'. It is obviously important to include every site in this definition of the time-step. Without such a universal definition, it becomes impossible to compare other works in the literature and on other different models, in terms of their dynamical properties. The problem remains that this is an artificially constructed time. It is also noticeable that for deep quench experiments, there is little thermal activity below the phase transition temperature and the system evolves very slowly. This effect is generally known as hydro-dynamic slowing down.

The subject of whether the stochastic time variable in a Monte-Carlo simulation bears any resemblance to a *real* time remains controversial [3, 34]. In general it does not, but it is thought that for certain models it can be scaled to a real time, at least in the long-time limit. There is strong evidence that the Monte-Carlo time *is* scalable to real aging time. We do not address this controversy in our present work and simply use the Metropolis update scheme.

3 Cluster Component Labelling

In the context of general graphs and graph theory [11] graph labelling is a well known problem with relatively easy to understand serial algorithms [8]. More generally, graph component labelling is a subset problem of the wider graph colouring problems [5] with a number of known algorithmic variations [9].

A useful perspective on the problem is in terms of equivalence classes and the popular formulation in Numerical Recipes books [37] shows how a predicate function that specifies equivalence or "connected-ness" can be used to iteratively sweep across all pairs of graph nodes to identify clusters or equivalence classes. In the case of simulations or applications involving fixed graphs or meshes, we often know the adjacency lists in advance and it is not necessary to conduct sweeps over all-pairs of nodes. In our work, we assume this is the case, and that the lattice nearest neighbour data structure specifies the subset of nodes that are considered adjacent to a particular node.

Algorithm 1 Simple Component Labelling of Lattice sites

```
for all sites k, ∈ [0..N − 1] do
   initialise site labels l_k ← k
end for
repeat
   for all sites k do
      for all sites j neighbouring k do
         if species s_k = s_j and label l_j < l_k then
            l_k ← l_j
            note changes still occurring
         end if
      end for
   end for
until no further changes
```

Algorithm 1 shows an elementary way of doing a breadth-first-search sweep through the sites of the lattice, propagating component labels according to connected species of the same site. Various optimisations and conditions can be added to this simple outline algorithm, such as a predicate to count only connected component clusters of a particular species. Doing bi-directional assignment of the minimum label so that all connected neighbours of site k take on the minimum label at once or adding global check operations when a particular label is overwritten can also speed up what is otherwise an $\mathcal{O}(\mathcal{N}^{\in})$ complexity algorithm.

The component labelling problem for a d-dimensional rectilinear image is relatively straightforward to formulate. It is required that each vertex be coloured or labelled with each component having a unique integer label. Arbitrary graph vertices can be indexed explicitly by some integer k but even in the case of a hyper-cubic mesh, image or lattice, these indices can usefully encode the spatial dimensions $(x_1, x_2, ..., x_d)$ in some order of significance [14].

An initial labelling of individual vertices is often the slowest algorithmic component as it may involve sweeping through the adjacency information iteratively. To make use of the correctly

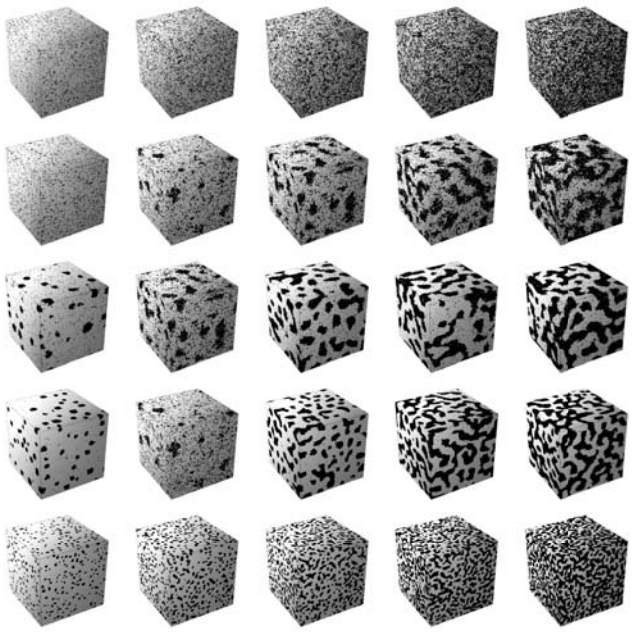

Figure 2: 2 State Kawasaki model Phase Diagram, showing Concentrations horizontally (10%, 20%, 30%, 40%, 50%), and Temperatures (5,4, 3, 2, 1) vertically downwards.

labelled component information however, an application may subsequently need to carry out some "book-keeping" operations to tidy up the label information into another structure - such as a mapping - whereby subsequent iterations over each component cluster can be made - for example to compute cluster moments or average properties such as the energy we compute for clusters in this present article.

Sequential algorithms for component labelling will typically be implemented as a sweep through all the graph nodes, adjusting their component "colours" according to adjacency information until each component has a single and unique colour - usually in the form of an integer label. The sweep is usually organised as a breadth first tree search, with various accelerating heuristics, depending upon properties of the data. Some formats lend themselves particularly well to various heuristics and also to parallel algorithms. Data-parallel GPUs are well-suited to carrying out the operations of component labelling and the hosting CPU can usefully be employed fairly easily to carry out the book-keeping support operations serially, and usually with more ordinary or global memory available than the dedicated memory available on the GPU card [19].

4 Simulation Results

We carried out a range of computer simulations of the Kawasaki model and measured the bulk system and component cluster properties. Figure 2 shows a tableaux of renderings of the 2-species Kawasaki exchange model simulated on a three dimensional cubic lattice of size 128^3 for $32,768 = 2^{15}$ Metropolis time steps. The concentration parameter is shown horizontally and the temperature vertically with "hot" at the top.

The critical temperature for this model is known to be around 4.5 for a 50% system and we observe structures on all length scales available at $C = 50, T = 4$ (right column, second from top) and with coarser "cleaner" structures at temperatures colder and noisier structures at higher temperatures. Lower concentrations still allow a percolating spinodal structure to form albeit requiring quite long simulation times as we have applied, to allow it to properly form at lower concentrations.

As can be seen the size and shape of the structures formed varies considerably. It is difficult to "see inside" the structures and interestingly when we study the size and shape of the largest cluster formed we find that it percolates or fully spans the whole lattice even across the range of concentrations and temperatures shown.

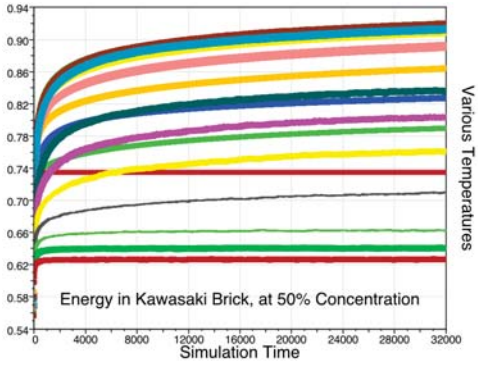

Figure 3: Whole system energy plotted against simulation times with curves showing different temperatures for a fixed concentration of 50%. There is a cross over in the T curves.

Figure 3 shows the time evolution of the energy function of the whole bulk system as it evolves over time. We are primarily interested only in the long term behaviour of the system. Inherently the system starts after a random initialisation representing an effectively infinite temperature and is quenched to a finite temperature as characterised by our parameter T. The system is inherently far from equilibrium, but does gradually converge towards a representative state in the long term and in fact slows down with the changes in behaviour becoming effectively on a logarithmic scale. The figure suggests that there is a cross over in temperature.

It is interesting to vary T and C and observe various metrics, including the energy. We summarise these behaviours in the surface plots below.

Figure 4 shows how the whole Kawasaki system energy (in terms of like-like species bonds) varies with both concentration C and temperature T. A saddle point structure is observed in the surface plot showing how the system remains stuck at low temperatures.

We are interested in how the component clusters formed in the model affect its bulk behaviour and in Figure 5 we plot the size of the largest component cluster formed in the system at various concentrations and temperatures. The plot varies almost linearly with concentration as one =might expect, but with two anomalies. The first is a crease in the surface around the critical

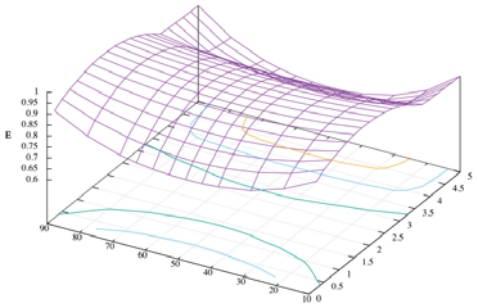

Figure 4: Energy of 128^3 Kawasaki system after 2^{15} Metropolis steps, as a function of percentage Concentration $C \in [0, 100]$ and Temperature $T \in [0, 5]$.

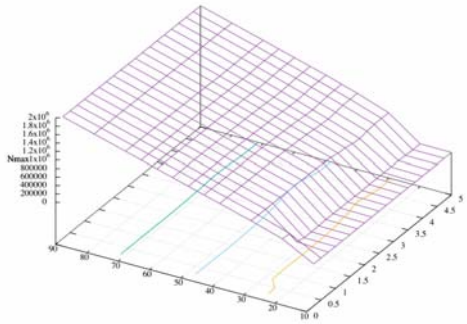

Figure 5: Number of Cells N_{max} in largest cluster in 128^3 Kawasaki system after 2^{15} Metropolis steps, as a function of percentage Concentration $C \in [0, 100]$ and Temperature $T \in [0, 5]$.

temperature of $T \approx 4$ and another at very low concentrations where the fully connected spinodal structure is not fully formed.

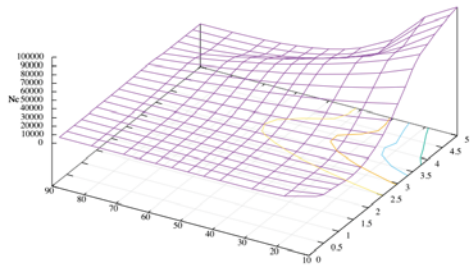

Figure 6: Number of Component Clusters N_c in 128^3 Kawasaki system after 2^{15} Metropolis steps, as a function of percentage Concentration $C \in [0, 100]$ and Temperature $T \in [0, 5]$.

Figure 6 shows the number of independent component clusters in the model and illustrates a relatively smooth surface variation with both concentration and temperature. Large number of components form at high temperatures when the system is noisy and at low concentrations when it is unable to fully join up into one giant component.

It is interesting to look beyond just the number of components and to focus on the number of monomers in the system. Since

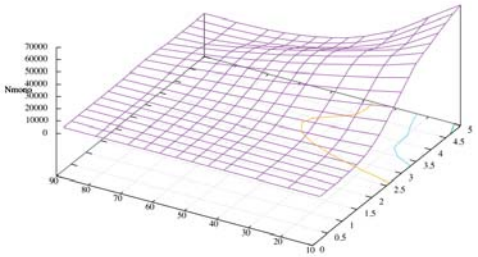

Figure 7: Number of Monomers N_{mono} in 128^3 Kawasaki system after 2^{15} Metropolis steps, as a function of percentage Concentration $C \in [0, 100]$ and Temperature $T \in [0, 5]$.

the Kawasaki dynamics is manifested through the exchange/diffusion of single particle monomers, we expect them to have a dominant effect. In fact as Figure 7 shows, the monomer variation is very similar in structural form to that of the number of other components, although the scale is significantly different. There is a variation at high temperature and low concentration, but otherwise the monomer count surface is similar.

5 Discussion

Close examination of the energy plots from Figure 3 on a log-log scale suggests that there are likely two regimes (early [12] and late stage [25]) as shown in Figure 8 where we fit straight lines to the early and late stages of the curves.

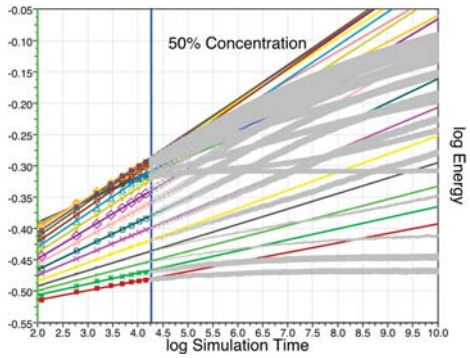

Figure 8: Energy-vs-time on log-log scale for 50% system.

The log-log plot implies that: $E \approx t^{\alpha}$ where the power can be determined from the slope of the straight lines that are least-squares fitted to the early and late stages of the log-log curves shown in Figure 8.

Figure 9 shows plots of α_{early} as they vary with temperature for various key values of the concentration. We observe that the curves have a peak that occurs at around half the critical temperature for the 50% system, with corresponding diminution as critical temperature lowers with C.

Figure 10 shows plots of α_{late} as they vary over the same range of C and T. The behaviour is more complicated displaying a flattish plateau region that stars near the critical temperature and extends down to temperatures of around 1 with a ringing peak

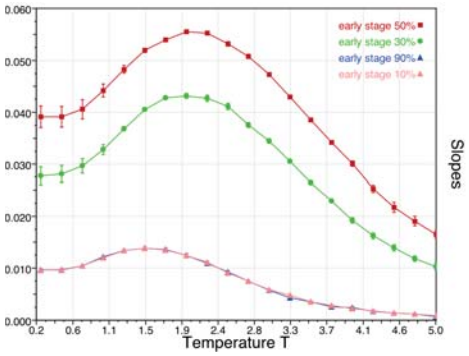

Figure 9: Early-stage E-slopes

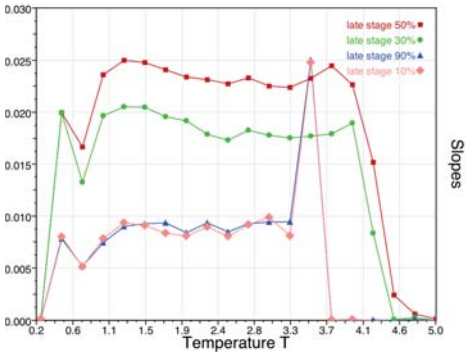

Figure 10: Late-stage E-slopes

near the critical temperature itself that is more pronounced at the extreme concentrations of 10 and 90 percent. The system has a symmetry of course, so that we would expect that 10 and 90 percent systems would be essentially mirror images of one another, and similarly $20/80$ and $80/20$ and so forth. We might hypothesize that at low temperatures the system has not had enough time to reach a representative state of its long term behaviour.

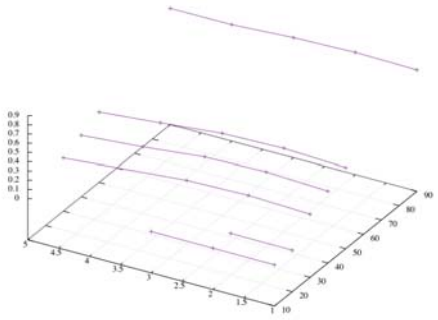

Figure 11: Energy (like-like links) of the largest component cluster.

Examination of the energy of the biggest cluster as seen in Figure 11 indicates that it varies remarkably little with temperature, but varies smoothly and systemically with concentration. This suggests that even at relatively low concentrations, the system is still dominated by the spinodal behaviour of the largest component cluster, and that at high temperature, although there are more monomers and other clusters of various sizes present, the spinodal giant cluster still dominates.

We have focused on the 2-species Kawasaki system but it would be feasible to investigate intermingling effects of more separate species in a variation of the Q-State Potts model, but using Kawasaki dynamics. We might anticipate tangling of separate spinodal structures might give rise to interesting and complex inter-facial energy effects.

In this work, we have restricted our work here to three dimensional systems. Two dimensional system have been studied elsewhere, but the model would extend in principle to higher dimensions such as 4 or 5. While these would no longer be "physical" systems, for some models, examining higher, non-physical dimensional systems can give insights into whether there are critical dimensions in the fundamental model itself.

We have used the simple periodic boundary case model nd have kept each length in each dimension the same length. There is scope to examine whether finite size effects or non-periodic boundaries would result in different ways for the material to form structures and whether this would affect the symmetry of the spinodal structures significantly.

6 Conclusion

We have simulated the 2-state Kawasaki diffusion model on a relatively large model lattice size and for long annealing simulation times. We have studied the energy and component cluster behaviours and have found that the largest component cluster dominates the long term behaviour of the model system even at relatively low concentrations as low as 10%, and for all the temperatures below the critical temperature.

The spinodal structures form and eventually percolate and dominate the system, although they vary in their ability to thicken and coarsen at different rates depending upon the concentration. Generally at higher temperatures, spinodals still form and vary their thickness rate of formation according to concentration but can continue to exist with more noise - bubble incursions and so forth into both species' territory.

It is surprising and interesting to find just how dominant the giant component cluster is in a model like the Kawasaki system over such a wide range of concentrations and temperatures. There is scope to extend the model and analysis for systems of more than two species present, which may give further insights into internal structures of more complex alloys.

References

[1] Ball, R., Essery, R.: Spinodal decomposition and pattern formation near surfaces. J. Phys. Condensed Matter 2, 10303–10320 (1990)

[2] Binder, K.: The Monte-Carlo method for the study of Phase Transitions: A review of some recent progress. J. Comp. Phys. 59, 1–55 (1985)

[3] Binder, K. (ed.): Monte Carlo Methods in Statistical Physics. Topics in Current Physics, Springer-Verlag, 2 edn. (1986), number 7

[4] Bragg, W.L., Williams, E.J.: The effect of thermal agitation on

atomic arrangement in alloys I. Proc. Roy. Soc. A 145, 699–730 (1934), bakerian lecture 1934

[5] Brelaz, D.: New methods to color the vertices of a graph. Communications of the ACM 22(4), 251–256 (April 1979)

[6] Cernuschi, F., Eyring, H.: An elementary theory of condensation. J. Chem. Phys. 7, 547–551 (Jul 1939)

[7] Choudhary, A., Thakur, R.: Connected component labeling on coarse grain parallel computers: An experimental study. Journal of Parallel and Distributed Computing 20, 78–83 (1994)

[8] Cormen, T.H., Leiserson, C.E., Rivest, R.L., Stein, C.: Introduction To Algorithms. MIT Press, 2 edn. (2001)

[9] Gallian, J.A.: A dynamic survey of graph labeling. The Electronic Journal of Combinatoris 16, DS6 (December 2005)

[10] Glauber, R.: Time dependent statistics of the Ising Model. J. Math. Phys. 4(2), 294–307 (1963)

[11] Gould, R.: Graph Theory. The Benjamin/Cummings Publishing Company (1988)

[12] Grant, M.S., Miguel, M.S., , J.Vinals, Gunton, J.D.: Theory for the early stages of phase separation: The long range force limit. Phys. Rev. B 31(5), 3027–3039 (Mar 1985)

[13] Hawick, K.A.: An agent model formulation of the ising model. Tech. rep., Information and Mathematical Sciences, Massey University, Albany, North Shore 102-904, Auckland, New Zealand (November 2003)

[14] Hawick, K.A.: Multi-party and spatial influence effects on opinion formation models. In: Proc. IASTED International Conference on Modelling and Simulation (MS 2010). pp. 235–240. No. 696-035, IASTED, Banff, Canada (15-17 July 2010)

[15] Hawick, K.A.: Analysing spinodal decomposition using image morphology with thinning, edge detection and graph methods. In: Proc. IASTED International Conference on Signal and Image Processing (SIP 2013). pp. 804–040. No. CSTN-176, IASTED, Banff, Canada (17-19 July 2013)

[16] Hawick, K.A.: Multi-species screening in anti-ferromagnetic pair-annihilation model simulations. In: Proc. 10th International Conference on Scientific Computing (CSC'13). p. CSC3420. No. CSTN-191, WorldComp, Las Vegas, USA (22-25 July 2013)

[17] Hawick, K.A.: Modelling flood incursion and coastal erosion using cellular automata simulations. In: IASTED International Conference on Environmental Management and Engineering. pp. 1–8. IASTED, Banff, Canada (16-18 July 2014), http://www.hull.ac.uk/php/466990/csi/reports/0007/csi-0007.html

[18] Hawick, K.A., Husselmann, A.V.: Photo-penetration depth growth dependence in an agent-based photobioreactor model. In: Proc. 14th International Conference on Bioinformatics and Computational Biology (BIOCOMP'13). p. BIC4051. No. CSTN-204, WorldComp, Las Vegas, USA (22-25 July 2013)

[19] Hawick, K.A., Leist, A., Playne, D.P.: Parallel Graph Component Labelling with GPUs and CUDA. Parallel Computing 36(12), 655–678 (December 2010), www.elsevier.com/locate/parco

[20] Hawick, K.A., Odiam, L.F., Stockwell, L.: 3d printing for visualisation of the complex physical structures of agent-based simulation models on lattices. In: Arabnia, H. (ed.) Proc. Int. Conf. Modeling, Simulation and Visualization Methods. pp. 1–7. No. MSV3215, WorldComp, Las Vegas, USA (25-28 July 2016)

[21] Hawick, K.A., Playne, D.P.: Parallel algorithms for hybrid multicore cpu-gpu implementations of component labelling in critical phase models. In: Proc. Int. Conf. on Parallel and Distributed Processing Techniques and Applications (PDPTA'13). p. PDP3297. No. CSTN-177, WorldComp, Las Vegas, USA (22-25 July 2013)

[22] Hawick, K.: Visualising multi-phase lattice gas fluid layering simulations. In: Proc. International Conference on Modeling, Simulation and Visualization Methods (MSV'11). pp. 3–9. CSREA, Las Vegas, USA (18-21 July 2011)

[23] Hawick, K.A.: Domain Growth in Alloys. Ph.D. thesis, Edinburgh University (1991)

[24] Hetherington, M.G., Hyde, J.M., Miller, M.K.: The measurement of composition during the early stages of the spinodal decomposition of FeCr alloys (Oct 1990), proc. 37 IFES, Albuquerque, 1990, to appear in Surface Science, 1991

[25] Huse, D.A.: Corrections to late stage behaviour in spinodal decomposition: Lifshitz-Slyozov scaling and Monte-Carlo simulations. Phys. Rev. B 34(11), 7845–7850 (Dec 1986)

[26] Kadanoff, L.P., Swift, J.: Transport coefficients near the critical point: A master equation approach. Phys. Rev. 165(1), 310–322 (Jan 1968)

[27] Kawasaki, K.: Diffusion constants near the critical point for time dependent Ising model I. Phys. Rev. 145(1), 224–230 (1966)

[28] Kawasaki, K.: Diffusion constants near the critical point for time-dependent ising models. ii. Physical Review 148(1), 375–381 (1966)

[29] Kawasaki, K.: Diffusion constants near the critical point for time-dependent ising models. iii. self-diffusion constant. Physical Review 150(1), 285–290 (1966)

[30] Lebowitz, J.L., Marro, J., Kalos, M.H.: Kinetics of Phase Segregation: A Review of Some Recent Results. Comments Solid State Physics 10(6), 201–217 (1983)

[31] Lee, T.D., Yang, C.N.: Statistical theory of equations of state and phase transitions. II Lattice Gas and Ising model. Phys. Rev. 87(3), 410–419 (Aug 1952)

[32] Marro, J., Valles, J.L.: Relevance of the Cahn-Hilliard-Cook Theory at early times in spinodal decomposition. Phys.Lett. A 95, 443–446 (1983)

[33] Metropolis, N., Rosenbluth, A.W., Rosenbluth, M.N., Teller, A.H., Teller, E.: Equation of state calculations by fast computing machines. J. Chem. Phys. 21(6), 1087–1092 (Jun 1953)

[34] Muller-Krumbhaar, H., Binder, K.: Dynamic properties of the Monte Carlo Method in Statistical Physics. J. Stat. Phys. 8(1), 1–24 (1973)

[35] Pearce, B.T., Hawick, K.A.: Interactive simulation and visualisation of falling sand pictures on tablet computers. In: Proc. 10th International Conference on Modeling, Simulation and Visualization Methods)MSV'13). p. MSV2341. No. CSTN-196, WorldComp, Las Vegas, USA (22-25 July 2013)

[36] Penrose, O.: A mean field equation of motion for the dynamic ising model. J.Stat.Phys. 63(5/6), 975–986 (1991)

[37] Press, W., Flannery, B., Teukolsky, S., Vetterling, W.: Numerical Recipes in C, chap. 12, pp. 252–254. Cambridge University Press (1988), determination of Equivalence Classes

[38] Sadiq, A., Binder, K.: Dynamics of the formation of two dimensional ordered structures. J.Stat.Phys. 35(5), 517–586 (1984)

[39] Suzuki, K., Horiba, I., Sugie, N.: Fast connected-component labeling based on sequential local operations in the course of forward raster scan followed by backward raster scan. In: Proc. 15th International Conference on Pattern Recognition (ICPR'00). vol. 2, pp. 434–437 (2000)

[40] Wang, J.S., Binder, K., Lebowitz, J.L.: Computer simulation of driven diffusive systems with exchanges. J.Stat.Phys 56(5), 783–819 (1989)

[41] Zhang, M.Q.: A fast vectorised multispin coding algorithm for 3d Monte Carlo simulations using Kawasaki spin-exchange dynamics. J.Stat.Phys 56(5), 939–950 (1989)

Optimization of the Solar Energy Harvesting Using Statistical Optimization

Z. Almusaied, B. Asiabanpour, N. Hawkes, K. Rainosek, S. Aslan
Ingram School of Engineering, Texas State University, San Marcos, Texas, USA

Abstract – *This research intends to improve the performance of the solar panels by identifying and optimizing the affecting factors. A design of experiments and response surface methodology were used to investigate the impact of these factors on the yield response as well as the output optimization.*

Keywords: Solar Energy, Optimization, Solar Panel Orientation and Direction

1 Introduction

Solar energy is now estimated for one-third of the United States new generating capacity in 2014, surpassing both wind energy and coal for the second year in a row [1 and 2]. However the current Photovoltaic (PV) panels are not highly efficient. The sources of inefficiency in solar panels are related to built in material deficiency (i.e., manufacturer spec.), power conversion (DC to AC), environment effects (e.g., high temperature), and Status of the solar panel (e.g., Orientation and tilting and Cleanness) [3-9]. This research intends to improve the performance of the solar panels by identifying and optimizing the affecting controllable factors.

2 Response Surface Methodology

2.1 Background

The experiment was designed using Response Surface Methodology (RSM). The selection of the method was based on both the objective of the experiment and the number of factors and levels. RSM can be defined as a combination of mathematical and statistical techniques effective for establishing, refining, and optimizing processes. It can be also used for the design and creation of new products as well as improving current ones [10]. The RSM inputs are the identified independent variables and the output will be the yield response which represents the performance measure of the process. The unknown response can be approximated to a first, second or third order model. The most used model is the second order model (Quadratic) especially if curvature in the response is suspected. In this model main effects and interaction between factors can be identified. In general, the second-order model is:

$$\eta = \beta_0 + \sum_{j=1}^{k} \beta_j x_j + \sum_{j=1}^{k} \beta_{jj} x_j^2 + \sum_{i<j} \sum \beta_{ij} x_i x_j$$

Where:

x_j : Variable j

$\beta_0, \beta_j, \beta_{jj}$: Parameters of second-order model

η : Model response

Variables (x_j) usually are coded variables transformed from natural variables. The independent variables are called natural variables when they are expressed with natural units. "…Natural Variables can be transformed to coded variables who are dimensionless with mean zero and the same spread or standard deviation" (Myers & Montgomery, 2002, p.3).

An experiment, as described by Montgomery (1997), is a test or sequence of tests where deliberate adjustments are made to the input variables of a system so that we may detect and distinguish the causes for the changes in the output response. Designed experiments are used in many disciplines and their impacts can be seen in almost every aspect of our lives. They help to build our knowledge about certain processes and systems which give us insight to enhance and improve performance. Engineering fields are one of the biggest venues where design of experiment is used. Lower costs, new ideas, new processes, new products, and new systems are invented due to the practice of design of experiments.

2.2 Factors Identification

The first stage of the Response Surface Methodology is to identify the important factors and their levels. They should have significant impact on the yield response. In this experiment independent variables with multi levels are identified with a goal to study their effect on the response yield and to find the optimum setting of the factors' levels. A model of typical process is applied with input, independent variables, uncontrollable factors, and output. The photovoltaic effect is considered as the process. Two PV panels are used as the input materials. The irradiance is considered another input to the process. The Date, time, and location were also considered as inputs to the process. The temperature of the PV panels and the ambient temperature, though measured, were considered as uncontrollable factors. General weather conditions were considered as uncontrollable factors including the clouds and humidity. Tilt angle, Azimuth angle, Wind

intensity, and Solar panel cleanness were considered as the controllable factors.

2.3 Factors Levels in Feasible Ranges

For four independent variables three levels in the feasible ranges were identified: A-tilt angle with three levels of 0º, 30º, and 60º from the horizon; B- azimuth angle with three levels of 0º, 45º, and -45º from the south; C- the wind with three levels of 0, 5.5, and 10 Km/h. The wind factor has been achieved through the use of a fan with multiple speeds. The speed of the fan was measured through the use of a wind sensor. The fan placed in front of the panel with two feet distance from the center of the PV panel. The fan was set to oscillate to make the air waves cover the entire PV panel. Finally, D- the cleanness of the PV panels with three levels. Talc was used to emulate the cleanness of the PV panels. Three levels of cleanness were determined based on the amount of the talc scattered randomly on the surface of the PV panel. The levels were absent of talc as 0 gram, ten shakes of talc which equal 20 grams as second level. The third level of cleanness was twenty shakes of talc which is equal to 40 grams.

The two PV panels used in the experiment were identical. One panel was placed on the dual axis mechanical system while the other was flat on the ground. The rheostats loads that were used in the electrical system were identical. To overcome the minor discrepancy of the initial output power of the two PV panels, a small calibration was applied to them with R1=7.1Ω and R2= 7.4Ω. The irradiance of the flat PV panel was determined as the input of the process and it was measured through the use of an irradiance sensor placed flat beside the flat PV panel. Another irradiance sensor was attached to the mechanical system and it was subjected to only two factors which were tilt and azimuth angles (orientation of the PV panel), and their three levels. The second sensor was recording the irradiance changes due to the changes in the tilt angles and the azimuth angels. The yield response of the process was determined to be the recorded power differences between the two PV panels. The Selection of the power difference as an output was to minimize the effect of the variation of the irradiance during the experiment on the process. The four factors were selected with high, mid, and low levels.

TABLE I. The four uncoded factors with their three levels.

level	A=Tilt angle	B=Azimuth angle	C=wind	D=Panel Cleanness
Low	0	-45	0	0
Mid	30	0	5.5	20
High	60	45	10	40

2.4 Design of Experiments

Experimental design has been implemented to characterize the process in terms of how input parameters affect the power output. The main two kinds of designs of Response Surface are Central Composite designs and Box-Behnken designs. The selection of the type of Response Surface design is the second stage. In this experiment Box- Behnken was used. The advantages of using Box-Behnken designs are to have less design points than Central Composite designs which will make it less costly. High efficiency to estimate the first and second order model coefficients. The disadvantages are the incapability to use runs from a factorial experiments, the limitation of three levels per factor while the Central Composite can have up to five, and finally they cannot to have runs with the extreme value of the factors.

The software used for the design of experiment and to analyze the result is Minitab. The setting included the selection of three replications and randomization to reduce the bias. The software generated the following 81 uncoded runs.

2.5 Conducting the Experiment

The experiment was conducted on 17th and the 18th of December 2015. The readings were collected from the data aquization system and were inputed to the runs' charts.These runs were later compared to the data saved in the system to guarentee the accuracy.

Figure 1. The PV panel with levels of treatments. The tilt at 60º, the panel toward the south, the wind at 0, and low level of cleanness.

2.6 Data Analysis

The next stage of the RSM is to analyze the data and find the RSM coefficients. Minitab is used to perform the aforementioned tasks. The confidence level used during the analsysis was 95%, and it was two sided.

The normal probabiltity plot on the top left of figure 2 shows normal distrbution of the residuals. The histogram plot in the same fgure shows the frequency of the residual. The highest residual frequency is around zero. Unusual high residuals (-60) can be seen with low frequency. The residuals versus fits plot shows no pattern which support the regression model. The residual versus observation order shows randamizaton which support the independence assumption.

Table II. The analysis of the data using Minitab.

Response Surface Regression: Power Difference versus A, B, C, D

Analysis of Variance

Source	DF	Adj SS	Adj MS	F-Value	P-Value
Model	14	117742	8410.2	16.19	0.000
Linear	4	102326	25581.4	49.24	0.000
A	1	45412	45411.6	87.42	0.000
B	1	2604	2604.4	5.01	0.029
C	1	91	90.6	0.17	0.678
D	1	54219	54219.1	104.37	0.000
Square	4	9361	2340.2	4.50	0.003
A*A	1	2188	2188.2	4.21	0.044
B*B	1	2071	2071.3	3.99	0.050
C*C	1	254	253.7	0.49	0.487
D*D	1	2327	2327.0	4.48	0.038
2-Way Interaction	6	6056	1009.3	1.94	0.087
A*B	1	2033	2033.2	3.91	0.052
A*C	1	377	377.4	0.73	0.397
A*D	1	161	160.6	0.31	0.580
B*C	1	2617	2616.7	5.04	0.028
B*D	1	4	4.1	0.01	0.930
C*D	1	864	863.6	1.66	0.202
Error	66	34286	519.5		
Lack-of-Fit	10	7254	725.4	1.50	0.163
Pure Error	56	27032	482.7		
Total	80	152028			

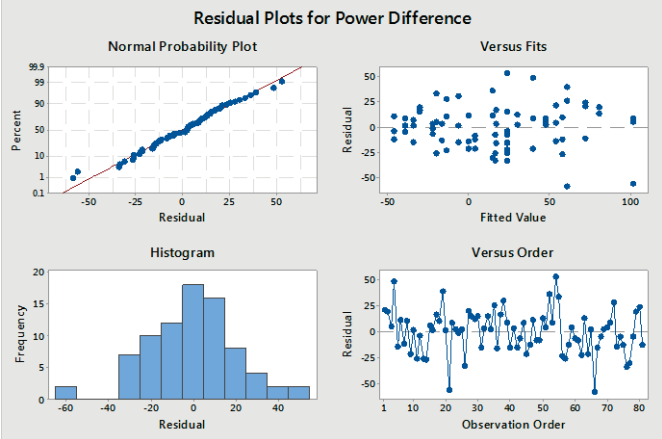

Figure 2. Four-in-one residual plot generated by Minitab.

The calculated P-values through the ANOVA indicate the significance of the factors and their interactions on the yield response. Some of the factors have a high P-value and they were removed from the edited equation (higher than 0.05). These factors or their interactions are: C, C², AC, AD, BD, and CD. Some of the second order parameters have a critical P-value and are kept in the final equation. These include BB and AB with a P-value equal to 0.05 and 0.052 respectively. The wind factor and its interactions showed insignificant impact on the response except the interaction with the azimuth angle (orientation) of the PV panel. This might be due to uncontrollable natural wind occurred during the experiment. The final equations are

Regression Equation in Uncoded Units

$$Power\ Difference = 4.1 + 2.272\,A + 0.241\,B - 50.8\,D - 0.01299\,A^2 - 0.00562\,B^2 + 12.06\,D^2 + 0.00964\,AB - 0.328BC$$

2.7 Optimization

The opimization of the response was determined through the use of Mintab. The software generated the optimum settings of the factors to maximize the yield response.

The following setting and figure show the Minitab generated optimum results.

Multiple Response Prediction

Variable	Setting
A	60
B	45
C	0
D	0

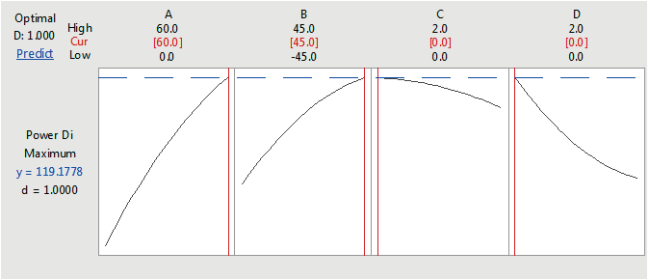

Figure 3. The optimization graph generated by Minitab. The four factors and their optimum setting is shown in red.

The Minitab calculations shows the optimum settings to maximize the power difference are achieved when the tilt of the PV panel is 60º and the PV panel is oriented toward the west and there is no wind and dirt on the surface of the panel.

2.8 Validation

The PV panel was subjected the founded optimum levels of treatments on the 26th of February. A sample of the data was collected from 27th record and result were close to the predicted value in the model (119 W).

Table III. Validation sample of data. A sample of data from the 27th of February 2016 with the optimum settings of 60º, 45 º from the south, 0 wind and 0 talc.

Date and time	Power1	Power2	Power difference	Irrediance1	Irrediance2
Feb 27	169.8W	60.5W	109.31W	1000.8W	394.25W

3 Discussion and Conclusion

- The research used design of experiments and response surface methodology to plan, analyze, and optimize the experiments.
- The three out of four factors investigated in this research to optimize the performance of the PV panels have significant impacts on the power output.

- In addition to these factors, other variables such as the date/time and the location of the PV panels affect the performance of the PV panels as well.

4 Acknowledgement

This work has been completed with funding from the Department of Education-MSEIP program (grant number P120A140065). The authors would like to thank the Department of Education and Texas State University for providing funding and access to infrastructure and laboratories. Sponsors are not responsible to the content and accuracy of this article.

5 References

1- Solar Energy Industrial Application (SEIA), "U.S. Solar Market Insight", Retrieved on March 1, 2015. http://www.seia.org/research-resources/us-solar-market-insight

2- EcoWatch Transforming Green, "U.S. Solar Energy Industry Achieves Record-Shattering Year", Retrieved on March 1, 2015. http://ecowatch.com/2015/03/10/rhone-resch-solar-shattering-year/

3- Central Electricity Regulatory Commission. (2011). Performance of Solar Power Plants in India, New Delhi, India: http://www.cercind.gov.in

4- Almusaied, Z., Asiabanpour, B., Salamy, H., Jimenez, J., Aslan, S., "Solar Energy Generation: Roadblocks and Their Economically Viable Remedies", IERC2015, TN, 2015.

5- Haan, J. Den. (2009). Solar Panel Information. Retrieved from: http://www.solarpower2day.net/solar-panels/

6- Jaiganesh, K. & Duraiswamy, K, (2013). "Improving the Power Generation from Solar PV Panel Combined with Solar Thermal System for Indian Climatic Condition." International Journal of Applied Environmental Sciences (ISSN 0973-6077). Volume, Number 6.

7- Dorobantu, L., Popescu, M. O., Popescu, C., Craciunescu, A, (2011). "The Effect of surface Impurities on Photovoltaic Panels," International Conference on Renewable Energy and Power Quality.

8- Honsberg, C. & Bowden, S. (N. D.). Degradation and Failure Modes. Retrieved from: http://pveducation.org/pvcdrom/modules/degradation-and-failure-modes

9- Jordan, D. C., & Kurtz, S. R. (2013). Photovoltaic Degradation Rates-an Analytical Review. Progress In Photovoltaics, 21(1), 12-29. doi:10.1002/pip.1182

10- Myers, R. H., & Montgomery, D. C. (2002). Response surface methodology: process and product optimization using designed experiments. New York: J. Wiley, c2002.

Optimal Tuning and Comparison of Different Power System Stabilizers Using Different Performance Indices Via Jaya Algorithm

H. Shayeghi [1,2]*, H. A. Shayanfar [1], S. Asefi[2], A. Younesi[2]
[1] Center of Excellence for Power System Automation and Operation, School of Electrical Engineering, Iran University of Science & Technology, Tehran, Iran
[2] Electrical Engineering Department, University of Mohaghegh Ardabili, Ardabil, Iran
hshayeghi@gmail.com, hashayanfar@gmail.com, Sajjad.asefi1992@gmail.com, a.younesi@ieee.org

Abstract - In this paper, a powerful optimization algorithm is used for optimal tuning of different types of PSS to stabilize a synchronous machine connected to an infinite bus. The robustness of each controller has been evaluated via four different types of error criteria and the coefficients optimized by the Jaya algorithm which provides reasonable solution. By analyzing the results based on the solutions given by Jaya algorithm, the excellency of this algorithm in solving such problem are obvious. The capability of each controller for damping, when acting alone, may be matter of concern, too. Finally results obtained for each controller due to different criteria, have been compared to show the operational results of each controller.

Keywords: Fractional Order PID (FOPID), Jaya Algorithm, PID, Power System Stabilizer

1 Introduction

Service continuity is one of the most important features of a power system. This means that the power system must remain a reliable power source even after being subjected to a disturbance or occurrence of a fault [1]. The main reasons which cause instability in a power system are local oscillations between generators exist in the same power plant, oscillations caused by neighboring power plants and global oscillations of unstable generators connected to the same grid. It's obvious that these oscillations (even at low frequency) have negative effects on power transferred in transmission lines. Disturbances such as sudden load changes or faults lead to an imbalance between electrical power delivered by the generator and the mechanical power being produced by the turbine. The imbalance results in a shaft torque with an accelerating or decelerating effect on the shaft line. So considering the problem of transient stability which concerns maintaining synchronism between generators in the case of a severe disturbance, is necessary [2].

The basic role of a Power System Stabilizer (PSS) is damping of such power oscillations, by producing electrical torque using the excitation system. Lead-Lag, PID and Fractional Order PID (FOPID), are different types of PSSs, to name a few. One of the commonly used PSS is lead-lag compensator. Although new types may operate better in real-world, i.e. industrial applications, but they show robust performances for various operating conditions and are easy to implement [3]. Beyond choosing one type of PSS, tuning its parameters can be considered as a problem, too. From this point of view there has been so many works provided in the literature about tuning PSS parameters. Approaches differ from modern control theory [2,4-6], to random heuristic methods, such as Tabu search, genetic algorithms, chaotic optimization algorithm, rule based bacteria foraging and particle swarm optimization, teaching and learning based optimization and bat optimization for achieving the optimal PSS parameters which give us the optimal recovery condition of a power system after a disturbance [7-11].

Despite the significant number of recently proposed algorithms that have been used for optimizing the PSS parameters, there might be a fundamental question about using and testing different algorithms. For answering to this question we refer to the so-called No Free Lunch (NFL) theorem [12]. This theorem challenges the ability of a single algorithm for solving the optimization problem. So, success of an algorithm in solving a specific set of problems does not guarantee solving all optimization problems with different type and nature. In this regard, we have used Jaya algorithm to optimize the parameters of the applied PPS in the system. Jaya is a simple and powerful optimization algorithm which have the ability to solve whether constrained or unconstrained optimization problems. The fundamental concept of algorithm is that the solution obtained for a problem should move towards the best solution and should avoid the worst solution. This does not need any algorithm-specific control parameters except common control parameters [13]. Furthermore, we have used three types of PSS, Lead-Lag, PID and FOPID for our system and after optimization the results have been compared regarding different error criteria, including Integral Absolute Error (IAE), Integral Squared Error (ISE), Integral of the Time-Weighted Absolute Error (ITAE) and Integral of Time multiplied by the Squared Error (ITSE).

*Corresponding Author, H. Shayeghi, hshayeghi@gmail.com

2 Power system modelling and PSS design

In the next two sections presented below, we have provided the model of the power system and its complete block diagram which can be used for simulations.

2.1 Power system model

For the stability analysis a Single Machine connected to an Infinite Bus (SMIB) through transmission line has been adopted. The system includes synchronous generator which is connected to a power grid (infinite bus) via a transmission line. Exciter Automatic Voltage Regulator (AVR) is one of the equipment used in generator [14]. Figure 1 shows a schematic diagram for the test system. System data are given in Ref. [15].

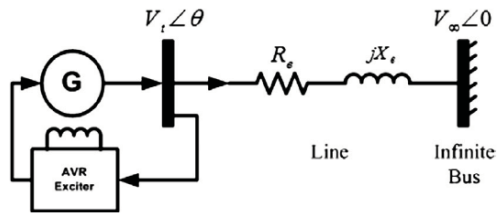

Fig. 1. Single line diagram of SMIB

2.2 Block diagram of Simulink model

We have considered synchronous generator by model 1.1, i.e. containing field circuit and one equivalent damper winding on the q axis (4th - order model). Due to linearizing the nonlinear model for an operating condition, a linear dynamic model can be obtianed. Block diagram of the linearized dynamic model of the SMIB power system with PSS is shown in Fig. 2. *K1*, *K2*,… *K6*, are Heffron-Phillips constants that can be easily obtained by data presented in Ref. [15].

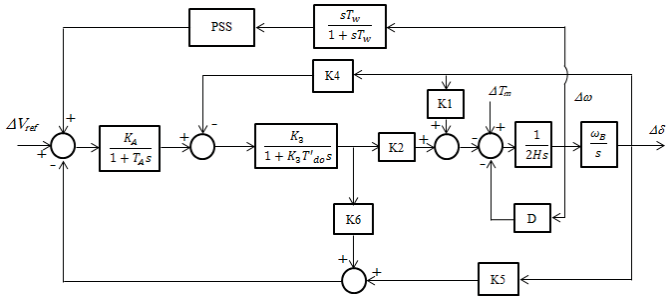

Fig. 2. Block diagram of the linearized dynamic model of the SMIB

The linearized equations can be rewritten in the state space form as follows:

$$\Delta\dot{x} = A\Delta x + B\Delta u \tag{1}$$

$$y = C\Delta x \tag{2}$$

Where, A, B and C are the system, input and measurement matrices, respectively. The overall linearized state-space model of the power system (SMIB including PSS) has been developed using the state-space equations and is provided in [15]. Note that, as *D* is a zero matrix, it has not been mentioned in the above equation.

3 Proposed stabilizers

Here, three kind of power system stabilizers which have been used in this investigation, are discussed.

3.1 Lead-Lag power system stabilizer

The transfer function of commonly used structure of the PSS that implemented in this study is given by the relationship below. It comprises of a block of K_{PSS} gain followed by a high-pass filter (so called washout filter) of time constant T_w and lead-lag structured phase compensation blocks with time constants T_1 and T_2. It is to be noted that the reduction of the power system oscillations after a wide perturbation in order to enhance the stability of power system is one of the reasons for suggesting stabilizers designation. The output of stabilizer is a voltage signal that adds supplementary control loops to the generator AVR, i.e. input voltage signal of the exciter system. The input signal of such a structure is usually the deviation of the synchronous speed $\Delta\omega$ [16-18].

$$U(s) = K_{PSS}\left(\frac{1+sT_1}{1+sT_2}\right)\Delta\omega(s) \tag{3}$$

It is worth noting that in this study, the time constant T_w is considered as 10.0 s.

3.2 PID type power system stabilizer

The main application of a PID type power system stabilizer is to create a proper torque on the rotor of the generator in order to compensate the phase lag between the machine electrical torque and the exciter input. The transfer function of the PID-PSS is given by:

$$U(s) = \left[K_P + \frac{K_i}{s} + K_d s\right]\Delta\omega(s) \tag{4}$$

3.3 FOPID type power system stabilizer

To improve the robustness and performance of PID control systems, Podlubny has proposed an extension to the PID controllers, which can be called $PI^{\lambda}D^{\mu}$ (FOPID) controller because of involving a differentiator of order μ and integrator of order λ. Many applications have been provided for this controller and detailed information about it is presented in the literature [19]. The commonly used concept for the fractional differintegral, is the Riemann-Liouville (RL) definition. The transfer function of FOPID can be written as follows:

$$G(s) = K_P + K_i s^{-\lambda} + K_d s^{\mu} \tag{5}$$

In this work, a comparison based on the different types of PSS and either $PI^{\lambda}D^{\mu}$ controller is considered in order to see which one can prove greater damping of power system. To assess the robustness of each controller we have not combined them together and same signal washout filter is used for all of them.

The transfer function of the FOPID-PSS to modulate the excitation voltage is given by:

$$U(s) = \left[K_P + K_i s^{-\lambda} + K_d s^{\mu}\right]\Delta\omega(s) \quad (6)$$

Below you can see Simulink implementation of FOPID, in which coefficient "a" and "b" represent "λ" and "μ", respectively.

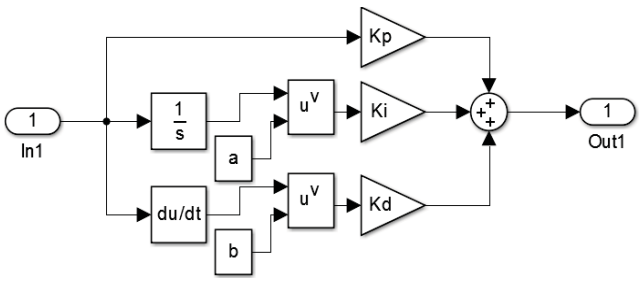

Fig. 3. Simulink implementation of FOPID

4 Objective function

In this article, we used performance indices including Integral Absolute Error (IAE), Integral Squared Error (ISE), Integral of the Time-weighted Absolute Error (ITAE), Integral of Time multiplied by the Squared Error (ITSE), to minimize the error signal; in other terms minimize the overshoots and settling time in power system oscillations, and compare them to find the best suitable one, where, Jaya algorithm has been applied to minimize the values provided by the objective functions of the system that is given by:

$$IAE = \int_0^{ts} |e(t)|dt \quad (7)$$

$$ITAE = \int_0^{ts} t \times |e(t)|dt \quad (8)$$

$$ISE = \int_0^{ts} e(t)^2 dt \quad (9)$$

$$ITSE = \int_0^{ts} t \times e(t)^2 dt \quad (10)$$

Where, t_s is total simulation time.

5 Proposed algorithm

Regarding to success of the TLBO algorithm, another algorithm-specific parameter-less algorithm is proposed in this paper [14]. As we remember from TLBO algorithm, there are two phases, one is teacher phase and the other is learner phase. But, Jaya algorithm has only one phase and it is very easy to use, whether the problem is constrained or unconstrained. Thus, the working of the proposed algorithm is much different from that of the TLBO algorithm.

Imagine $f(x)$ as the objective function to be minimized, with four error criteria (*i.e.* IAE, ITAE, ISE, ITSE). At any iteration i, 'm' indicates the number of design variables (i.e. j=1,2,…,m) and 'n' indicates the number of candidate solutions (i.e. population size, k=1,2,…,n). Amongst the entire candidate solutions, best candidate *best* obtains the best value of $f(x)$ (i.e. $f(x)_{best}$) and the worst candidate *worst* obtains the worst value of $f(x)$ (i.e. $f(x)_{worst}$). If $X_{j,k,i}$ is the value of the jth variable for the kth candidate during the ith iteration, then the modification of its value will be done by Eq. (11).

$$X'_{j,k,i} = X_{j,k,i} + r_{1,j,i}\,(X_{j,best,i} - |X_{j,k,i}|) - r_{2,j,i}\,(X_{j,worst,i} - |X_{j,k,i}|) \quad (11)$$

where, $X_{j,best,i}$ and $X_{j,worst,i}$ show the value of the variable j for the *best* and *worst* candidate, respectively. $X'_{j,k,i}$ is the updated value of $X_{j,k,i}$ while $r_{1,j,i}$ and $r_{2,j,i}$ are the two random numbers for the jth variable during the ith iteration in the range [0, 1]. The term "$r_{1,j,i}$ (($X_{j,best,i}$ - $|X_{j,k,i}|$)" indicates the willing of the solution to move closer to the best solution and the term "-$r_{2,j,i}$ ($X_{j,worst,i}$- $|X_{j,k,i}|$)" indicates the willing of the solution to avoid the worst solution. $X'_{j,k,i}$ is accepted if it gives better function value. All the accepted function values at the end of iteration are maintained and these values become the input to the next iteration. The flowchart of the proposed algorithm can be seen in Fig. 4. The main idea behind the name of Jaya algorithm is the fact that, the algorithm has the willing get closer to success (i.e. obtaining the best solution) and tries to move away from failure (i.e. avoiding the worst solution). Reaching the best solution somehow considered as achiving victory and hence it is named as **Jaya** (a Sanskrit word meaning **victory**).

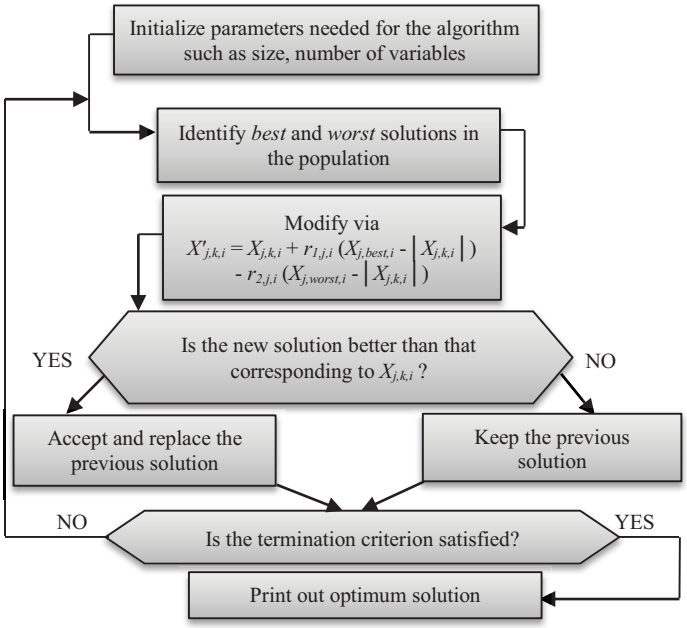

Fig. 4. The Flowchart of the proposed algorithm

6 Results and discussions

By simulating system using the data provided here, it can be seen that the system is in a stable condition. In another word, system will regain its stability after being subjected to a change in T_m. Results are obtained after 0.01 p.u. change in T_m and by using different kinds of controllers and objective functions. Robustness of each controller is compared due to different objective functions. It is to be noted that each criterion has its

own feature (lower or higher overshoot and settling time). Therefore, choosing a controller depends on the needs we want to meet, i.e. we should try to reach to an equilibrium point regarding so called cost and benefit of our system. As there are many works available in the area of these controllers in the literature, for the sake of brevity, we just provided a comparison of this controller due to different scenarios.

Figure 5 shows rotor speed deviation of lead-lag power system stabilizer simulation results which compare 4 types of objective function for this kind of PSS. In Table 1 the coefficients obtained via the algorithm for lead-lag PSS and the result of objective function (cost) using these coefficients is provided. Consider that the lower and upper limits of coefficient which specified in the algorithm are as follows:

$0.001 < K_{PSS} < 15$
$0.001 < T_1 < 10$
$0.001 < T_2 < 10$

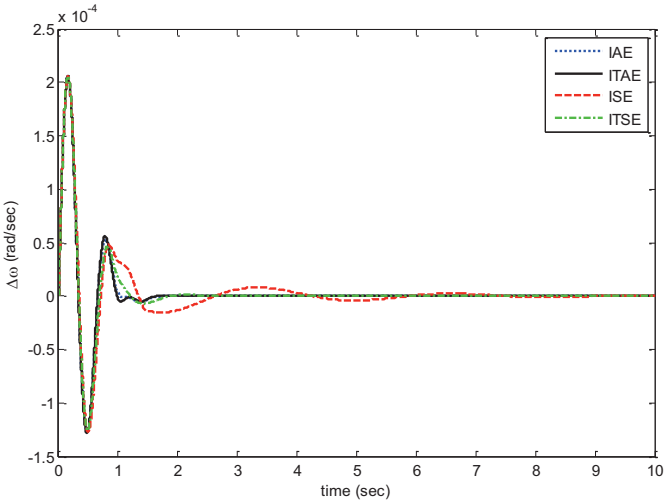

Fig. 5. Comparison of lead-lag PSS evaluated by different criteria

As it can be seen from Fig. 5 the lowest overshoot and settling time belongs to ISE and ITAE criterion, respectively.

Table 1. Coefficients obtained via the algorithm and cost for lead-lag PSS

Coef. / Criteria	K_{PSS}	T_1	T_2	Cost
IAE	15	0.4017	0.0147	3.47E-05
ITAE	15	0.3669	0.0189	8.24E-06
ISE	15	4.7905	0.001	1.76E-09
ITSE	15	0.5411	0.001	4.80E-10

Figure 6 shows PID type power system stabilizer rotor speed deviation simulation results, comparing 4 types of objective function for this kind of PSS. In Table 2 the coefficients obtained via the algorithm for PID PSS and the result of objective function (cost) using these coefficients is provided. Consider that the lower and upper limits of coefficient which specified in the algorithm are as follows:

$0.001 < K_P < 15$
$0.001 < K_I < 15$
$0.001 < K_D < 15$

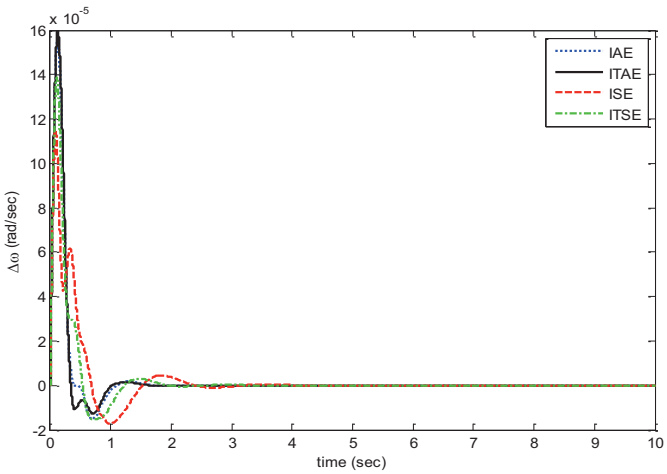

Fig. 6. Comparison of PID PSS evaluated by different criteria

Figure 6 shows that the lowest overshoot and settling time belongs to ISE and ITAE criterion, respectively.

Table 2. Coefficients obtained via the algorithm and cost for PID PSS

Coef. / Criteria	K_P	K_I	K_D	Cost
IAE	15	1.4409	5.8991	3.50E-05
ITAE	15	1.4475	5.2364	8.55E-06
ISE	15	15	15	2.23E-09
ITSE	15	15	8.6846	4.46E-10

Figure 7 shows FOPID power system stabilizer simulation results, comparing 4 type of objective function for this kind of PSS. In Table 3 the coefficients obtained via the algorithm for FOPID PSS and the result of objective function (cost) using these coefficients is provided. Consider that the lower and upper limits of coefficient which specified in the algorithm are as follows:

$1 < K_P < 15$
$1 < K_I < 15$
$1 < K_D < 15$
$0.1 < \lambda < 1$
$0.1 < \mu < 1$

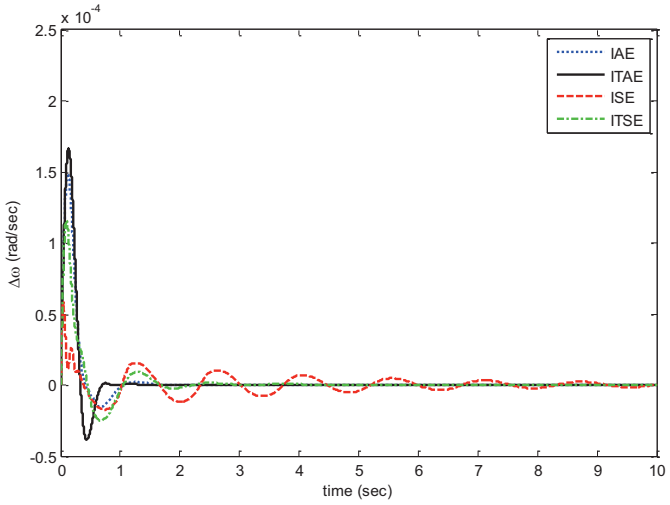

Fig. 7. Comparison of FOPID PSS evaluated by different criteria

Table 3. Coefficients obtained via the algorithm and cost for FOPID PSS

Criteria / Coef.	IAE	ITAE	ISE	ITSE
K_P	1	15	11.19941	1
K_I	5.9468	1.4608	11.11323	1
K_D	6.3655	3.9173	14.1983	14.6111
λ	0.4042	1	0.4311	0.3033
μ	0.3326	1	0.4343	0.4495

To completely consider different aspects of our controllers, Figures 8-11 compares different controllers due to different performance indices.

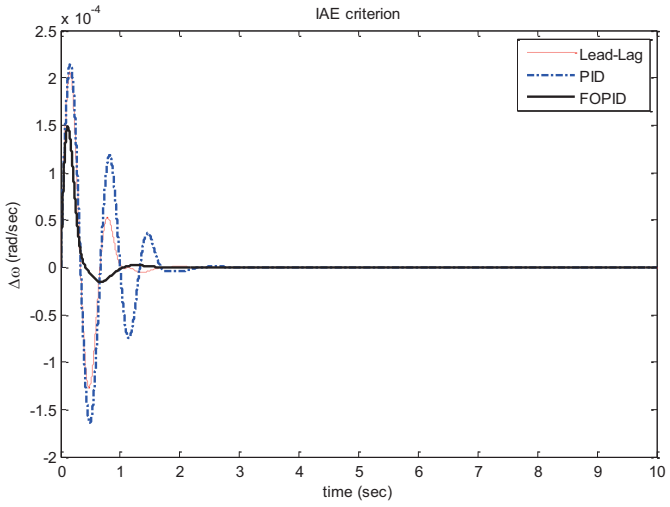

Fig. 8. Considering IAE criterion

From Fig. 8 it can be seen that PID and lead-lag controllers perform in the same manner. But, the FOPID shows a different manner that we see a decrease in overshoot by a factor of about 8 while the settling time increases in contrast.

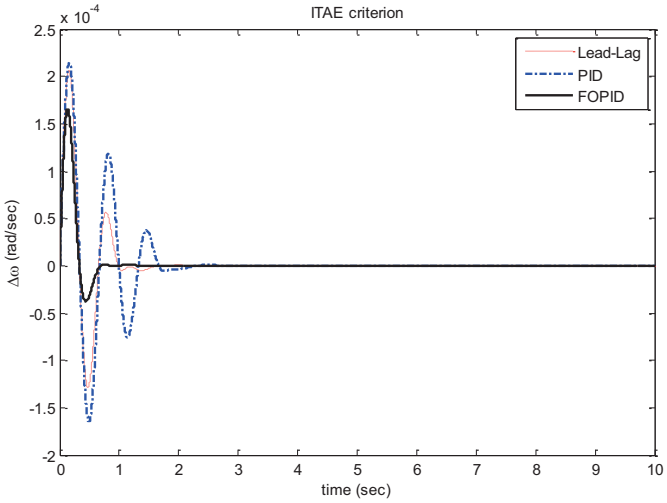

Fig. 9. Considering ITAE criterion

It's clearly obvious from Fig. 9 that the three applied controller have same overshoot but FOPID damps the power oscillations faster than other two controllers.

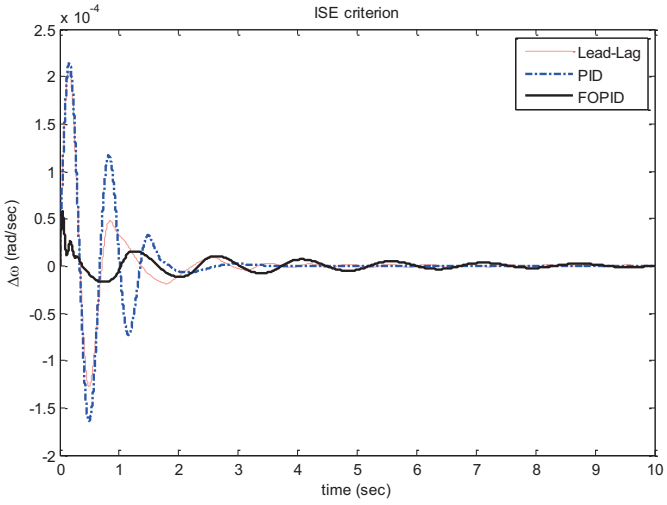

Fig. 10. Considering ISE criterion

As Fig. 10 shows, PID controller has the highest overshoot and the lowest settling time belongs to this controller, too. Lead-Lag controller lowers the overshoot by a factor of 3 but its settling time increases. Although the FOPID controller has the least overshoot but it has the most settling time among others. Finally in Fig. 11, while PID and lead-lag controllers have the same overshoot, FOPID decreases the overshoot by a factor of 7. In contrast lower overshoot and its settling time is increased.

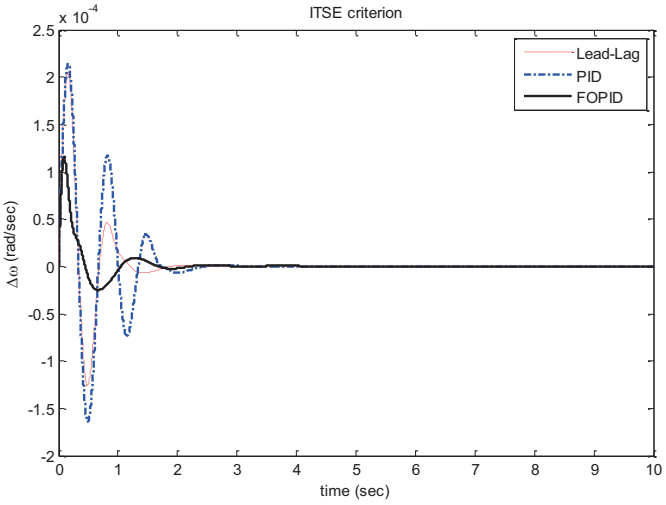

Fig. 11. Considering ITSE criterion

7 Conclusion

In this article, we have applied a newly presented optimization algorithm named Jaya, to determine and compare robustness of commonly used and newly presented power system stabilizers using performance indices (PI) including IAE, ISE, ITAE and ITSE. The coefficients and the results of objective functions which obtained using algorithm are presented in Tables 1-3 and the deviation of rotor speed regarding 0.01 p.u. change in T_m with the given system data are shown in Figs. 5-11. It is clearly obvious that the algorithm works well in solving our stability problem by providing reasonable coefficients. Thus, regarding to the needed criteria (i.e. lower rise time, smaller over shoot and etc.), one can choose the appropriate controller. In addition, the newly proposed FOPID controller shows high capability in damping. Further study can be made on practical implementation of these controllers and comparing simulational results with real-world.

References

[1] P. Anderson and A. Fouad, *Power system control and stability*. Piscataway, N.J.: IEEE Press, 2003.

[2] P. Kundur, N. Balu and M. Lauby, *Power system stability and control*. New York: McGraw-Hill, 1994.

[3] H. Shayeghi and B. Esmaeilnezhad, "PID controller design for power system stabilization", *Proc. Of the 7th International Conference on Technical and Physical Problems of Engineering, Lefkosa, TR Northern Cyprus*, pp. 252-256, July 2011.

[4] Y. Hsu and C. Hsu, "Design of a proportional-integral power system stabilizer", *IEEE Trans. Power Syst.*, vol. 1, no. 2, pp. 46-52, 1986.

[5] P. Kundur, M. Klein, G. Rogers and M. Zywno, "Application of power system stabilizers for enhancement of overall system stability", *IEEE Trans. Power Syst.*, vol. 4, no. 2, pp. 614-626, 1989.

[6] M. Gibbard, "Robust design of fixed-parameter power system stabilisers over a wide range of operating conditions", *IEEE Trans. Power Syst.*, vol. 6, no. 2, pp. 794-800, 1991.

[7] E. Bayat and H. Delavari, "Performance evaluation of power system stabilizers using teaching learning based optimization of a multi-machine system", *Cumhuriyet Science Journal*, vol.36, no. 3, pp. 2405-2411, 2015.

[8] Abdelghani, Choucha, Chaib Lakhdar, Arif Salem, Bougrine Med Djameleddine, and Mokrani Lakhdar. "Robust design of fractional order PID sliding mode based power system stabilizer in a power system via a new metaheuristic Bat algorithm." In *Recent Advances in Sliding Modes (RASM), 2015 International Workshop on*, pp. 1-5. IEEE, 2015.

[9] Y. Abdel-Magid and M. Abido, "Optimal multiobjective design of robust power system stabilizers using genetic algorithms", *IEEE Trans. Power Syst.*, vol. 18, no. 3, pp. 1125-1132, 2003.

[10] H. Shayeghi, H.A. Shayanfar, S. Jalilzadeh and A. Safari, "Multi-machine power system stabilizers design using chaotic optimization algorithm", *Energy Conversion and Management*, vol. 51, no. 7, pp. 1572-1580, 2010.

[11] S. Mishra, M. Tripathy and J. Nanda, "Multi-machine power system stabilizer design by rule based bacteria foraging", *Electric Power Systems Research*, vol. 77, no. 12, pp. 1595-1607, 2007.

[12] S. Mirjalili, "SCA: A sine cosine algorithm for solving optimization problems",*Knowledge-Based Systems*, vol. 96, pp. 120-133, 2016.

[13] R. Venkata Rao, "Jaya: A simple and new optimization algorithm for solving constrained and unconstrained optimization problems", *International Journal of Industrial Engineering Computations*, vol. 7, no.1, pp. 19-34, 2016.

[14] Lee, D. C., D. H. Baker, and K. C. Bess, "IEEE recommended practice for excitation system models for power system stability studies." *IEEE Standard* 421, pp. 5-92, 1992.

[15] K. Ellithy, S. Said and O. Kahlout, "Design of power system stabilizers based on μ-controller for power system stability enhancement", *International Journal of Electrical Power & Energy Systems*, vol. 63, pp. 933-939, 2014.

[16] Mazlumi, Kazem, M. Darabian, and M. Azari. "Adaptive fuzzy synergetic PSS design to damp power system oscillations", *Journal of Operation and Automation in Power Engineering*, vol. 1, no. 1, 2013.

[17] H. Shayeghi, and A. Ghasemi, "Improved time variant PSO based design of multiple power system stabilizer", *International Review of Electrical Engineering*, vol. 22, 2011.

[18] H. Shayeghi, H. A. Shayanfar, A. Akbarimajd and A. Ghasemi," PSS design for a single-machine power system using honey bee mating optimization", *In: Proceedings of the International Conference on Artificial Intelligence*, *Las Vegas, USA*, pp. 210-216, 2011.

[19] I. Podlubny, "Fractional-order systems and PID-controllers", *IEEE Trans Autom Control*, vol. 44, no. 1, pp. 208-214, 1999.

Biographies

Heidar Ali Shayanfar received the B.S. and M.S.E. degrees in Electrical Engineering in 1973 and 1979, respectively. He received his Ph.D. degree in Electrical Engineering from Michigan State University, U.S.A., in 1981. Currently, he is a Full Professor in Electrical Engineering Department of Iran University of Science and Technology, Tehran, Iran. His research Interests are in the Area of Application of Artificial Intelligence to Power System Control Design, Dynamic Load Modeling, Power System Observability Studies, Voltage Collapse, Congestion Management in a Restructured Power System, Reliability Improvement in Distribution Systems, Reactive Pricing in Deregulated Power Systems and Smart Grids. He has published more than 220 papers in international journals and 300 papers in conference proceedings. He is a member of the Iranian Association of Electrical and Electronic Engineers and IEEE.

Hossein Shayeghi received the B.S. and M.S.E. degrees in Electrical and Control Engineering in 1996 and 1998, respectively. He re ceived his Ph.D. degree in Electrical Engineering from Iran University of Science and Technology, Tehran, Iran in 2006. Currently, he is a full Professor in Technical Engineering Department of University of Mohaghegh Ardabili, Ardabil, Iran. His research interests are in the application of robust control, artificial intelligence and heuristic optimization methods to power system control design, operation and planning, power system restructuring and smart grids. He has authored and co-authored of 5 books in Electrical Engineering area all in Farsi, one book and two book chapters in international publishers and more than 330 papers in international journals and conference proceedings. Also, he collaborates with several international journals as reviewer boards and works as editorial committee of three international journals. He has served on several other committees and panels in governmental, industrial, and technical conferences. He was selected as distinguished researcher of the University of Mohaghegh Ardabili several times. In 2007 and 2010 he was also elected as distinguished researcher in engineering field in Ardabil province of Iran. Furthermore, he has been included in the Thomson Reuters' list of the top one percent of most-cited technical Engineering scientists in 2015 and 2016, respectively. Also, he is a member of Iranian Association of Electrical and Electronic Engineers (IAEEE) and senior member of IEEE.

Abdollah Younesi received B.S and M.S.E degrees both in Electrical Engineering from Faculty of Technical Eng. Department of the Mohaghegh Ardabili University, Ardabil, Iran in 2012 and 2015, respectively. Currently He is a PhD. student in Technical Eng. Department of the University of Mohaghegh Ardabili, Ardabil, Iran. His area of interest are application of artificial intelligence in power system automation and control, application of Reinforcement Learning to power system control, Fuzzy Systems, Heuristic optimization in power system control. He is a student member of Iranian Association of Electrical and Electronic Engineers (IAEEE) and IEEE.

Sajjad Asefi received B.S degree in Electrical Engineering from Faculty of Technical Eng. Department of the Guilan University, Rasht, Iran in 2015. Currently, he is a M.S.E. student in Technical Eng. Department of the University of Mohaghegh Ardabili, Ardabil, Iran. His areas of interest are application of PSSs in bulk power system, Heuristic optimization in power system control, Power system reliability, Renewable Energies and their application in distribution system.

Intelligent Disease Outbreak System Based Swarm Algorithm for Epidemiologists

Naser El-Bathy
North Carolina A&T State University
nielbath@ncat.edu

Ghassan Azar
Lawrence Technological University
gazar@ltu.edu

Ali Tariq Bhatti
North Carolina A&T State University
atbhatti@aggies.ncat.edu

Israa Alothman
North Carolina A&T State University
Greensboro, NC, USA
eaalothm@aggies.ncat.edu

Abstract—**During a disease outbreak or environmental exposure, fast and accurate prediction of outbreak clusters saves lives. This year's measles outbreak is an example with immediate impacts. As the measles is spreading, patients move and create new measles clusters. Time is of the essence in detecting these unforeseen clusters. This research, as reported in this paper, focuses on creating an Environmental Exposure Surveillance Model (E^2SM) for Epidemiologists using Intelligent Swarm Algorithm. The purpose of the model is to develop a computerized prediction system that is superior to others in terms of speed and accuracy. It will track the measles outbreak and predict future outbreaks. Because of the new technologies used this system is faster and more accurate than previous and current approaches. By analyzing social media it detects and tracks diseases as they spread. The measles outbreak is used as a model, but it will also work on future outbreaks. Epidemiologists will be able to more efficiently and effectively determine the locations of disease outbreaks as they occur. They do not have to rely on the illnesses being directly reported, so they will know about diseases much sooner. This model is efficient, it saves money, and it saves lives. A prototype is created and examined in order to validate the concepts.**

I. INTRODUCTION

The source and development characteristics of a disease is a major challenge that epidemiologists face in order to study causes and transmission of disease within a population. Epidemiology of Escherichia coli O157:H7 Outbreaks reported to Centers for Disease Control and Prevention (CDC) that Escherichia coli O157:H7 causes 73,000 illnesses and an estimated 2,100 hospitalizations annually in the United States [1]. It is a result of eating an infected food. Such Contamination is the reason for hemorrhagic diarrhea, and kidney failure [2]. Spread passes through fecal-oral route and transmission of poisoned green vegetables and lightly cooked meat [3][4].

The study of this research improves on current epidemiological surveillance of disease outbreaks by applying an evolutionary computation algorithm such as social swarms to track and forecast diseases. This new concept integrates this swarm algorithm approach with established techniques in search methodologies, intelligent information retrieval, clustering, and intelligent agents in a Service-Oriented Architecture (SOA) environment. Similar algorithmic approaches to outbreak prediction are proven to be effective and established science [5].

The project of this study will both create a prototype to apply a swarm algorithm to measles epidemiology and analyze the prototype to ensure it improves over older approaches. This is valuable and feasible because proven technologies are being combined in a novel way and applied to real disease emergence.

The remaining material of this paper is structured as follow: In Section II, the problem statement and research question are defined. In Section III, related work is presented. In Section IV, the research significance is identified. In Section V, the model is described. In Section VI, a comparison of extended genetic algorithm and swarm algorithm is developed. In Section VII, the prototype is created for research validation. Finally, the results and conclusion are given in Sections VIII and IX.

ISBN: 1-60132-430-8, CSREA Press ©

II. PROBLEM STATEMENT AND RESEARCH QUESTION

The origin of this research problem is lack of applications that if defined will allow Epidemiologists to more efficiently and effectively determine the locations of disease outbreaks much sooner as they occur. The reasons for the research problem are inefficient access to epidemiology of outbreaks reports, reports contradiction, irrelevant reports, delays, redundancy, and poor interface [6]. The research problem focuses on the development of environmental exposure surveillance model for epidemiologists using intelligent swarm algorithm. In this paper, the problem of clustering the cities of disease outbreaks as they occur has been analyzed and the need for an optimal surveillance model is justified.

One specific research question which arises is: How does the environmental exposure surveillance model using intelligent swarm algorithm help epidemiologists determine the locations of disease outbreaks as they occur. Fig. 1 describes the environmental exposure surveillance model (E^2SM) that forms the major components needed for answering the research question.

III. RELATED WORK

Similar approaches to outbreak prediction are proven to be effective and established science. Bioterrorism is a form of outbreak of disease. It means that the risk evaluation and development of plan for health policies require predictive tools such as an agent based tools along with visualization tools are used to examine and observe a disease outbreak [7].

The Centers for Disease Control and Prevention's sentinel physicians-surveillance network produced a detection of several natural disease outbreaks and introduced an analysis of retrospective data throughout the influenza time. It discovered a drastically analogous curving to the proportion of patients tilted with a respiratory illness [8].

An odds ratio-based binary particle swarm optimization (OR-BPSO) method has been proposed to assess the possibility of breast cancer. This method produces SNP barcodes which is a mixture of SNPs and its genotype with the maximal difference of occurrence between control and breast cancer groups. Amongst seven SNP mixture in the space of one minute, OR-BPSO method has discovered certain SNP barcode with an optimized fitness value. These barcodes has the best function to protect breast from cancer. A statistical analysis of odds ratio for quantitative measurement proved that these SNP barcodes can be an efficient high-speed method to evaluate SNP–SNP relations for breast cancer [9].

In this paper, we develop a project that will both create a prototype to apply a swarm algorithm to measles epidemiology and analyze the prototype to ensure it improves over older approaches. This is valuable and feasible because proven technologies are being combined in a novel way and applied to real disease emergence.

IV. RESEARCH SIGNIFICANCE

This study of disease outbreak (including technology employed, product scope, user-outcomes orientation, and range of public health needs served) is significant for three main reasons. First, the study of this research is a new theoretical development that improves support for strategic decision making in public health. The user outcome is improved standards for fast and accurate prediction for epidemiologists. Second, this study accelerates information retrieval processing time and reduces the cost of automated disease outbreak prediction. Third, technologies employed combine Particle Swarm Optimization (PSO) with SOA and social media surveillance approaches. This is an innovative Information Technology (IT) solution that provides more effective and efficient yields. This IT solution is inimitable and allows public health organizations to meet strategic, tactical and operational needs quickly.

This concept and approach is novel in a broad sense and specifically new to public health informatics. The translation of these findings will accelerate public health action. This study will test the advantage of Particle Swarm Optimization over the Genetic Algorithm (GA) and its algorithmic simplicity [10][11]. Swarm Algorithm is very easy to implement, simple in concept, and computationally efficient. It works well for contagion surveillance because it has roots for artificial life and evolutionary computation. Clusters predicted by PSO have a higher quality and a higher accuracy than GA. Put simply, PSO is a much better technique for clustering cities based on diseases.

V. THE MODEL

This research combines three components into one public health monitoring solution. Fig. 1 describes the model.

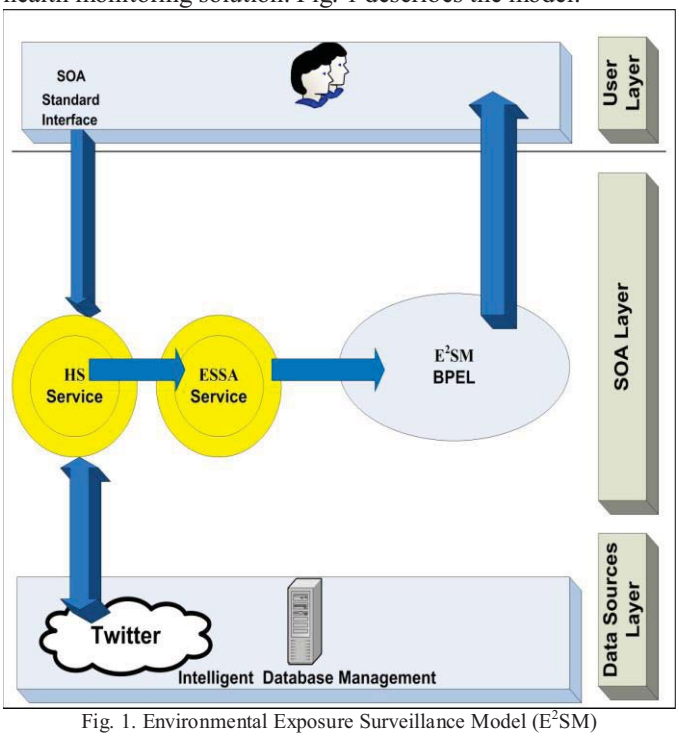

Fig. 1. Environmental Exposure Surveillance Model (E^2SM)

The first component is an Epidemiological Surveillance Disease Outbreak-Based Evolutionary Social Swarms Algorithm (ESSA). This improved automated concept accelerates information retrieval processing time and reduces costs. The second is infrastructural component uses SOA, which allows dynamic change and provides established benefits in terms of agility [12]. The third component is indirect health surveillance (HS) through social-media-based informatics. It uses public (and only public) social media posts or Tweets to detect and track diseases as they spread. Using Tweets as data sources answers challenges about immediacy in disease surveillance, providing data long before hospital-based surveillance can be communicated generally[13]. The algorithmic approach analyzes this data, verifies, adapts, and uses it to predict future outbreaks.

Service-Oriented Architecture is a paradigm that enables development of the technical solution of this research based on web services [14][15]. Reducing development time of this solution is a major SOA benefit [16][17]. Therefore, it is a central part of the concept that is proposed in the research. In this paper, SOA middleware is deployed as a suite consisting of:

A. Web Services (WS)

A web service is a process of two steps. Publication step makes web service available to consumers (clients/users). Composition or orchestration step organizes multiple services within end-to-end business flows [15][16]. The study solution of this research mainly publishes and consumes two web services to perform operations that are required for developing the solution. They mutually exchange information with each other. Exchange of information includes simple data passing from a browser to a web server [17][18]. Data that is passed from a browser is a query string. It is a list of cities. The output of first web service is a query string identifier. This output is input of the second web service. Output of second web service is a list of clustered common diseases in one or more cities.

Searching Twitter for current data regarding diseases at first seems like a very simple task. The technical solution searches for tweets within the area of the location input for the past day, and determine a frequency count of each disease mentioned.

The "Location" is an operation of a user defined Java web service (HS Service) that reads "uscities.txt" and displays the states and cities in the application's home page. The "Search" is another operation of the HS Service as well. It receives the user request, processes it by importing " twitter4j" classes, and returns the search results in the form of 3 top diseases.

The approach taken to retrieve the data uses a series of queries, one for each disease, combining the key phrases associated with each disease into a single query for each disease.

This approach proved to be successful at finding tweets relevant to the diseases the program was looking for. It is also used in the current application. Fig. 2 illustrates the sequence of the data processes.

B. E²SM Business Process Execution Language (BPEL)

The orchestration of web services is supported by Business Process Execution Language (BPEL) [19][20]. In the study solution of this research, the process is simply designed, deployed, monitored, and administered within a framework provided by Oracle BPEL Process Manager.

BPEL enables linking two or more services as one piece of a process [20]. Fig. 3 describes the data flow.

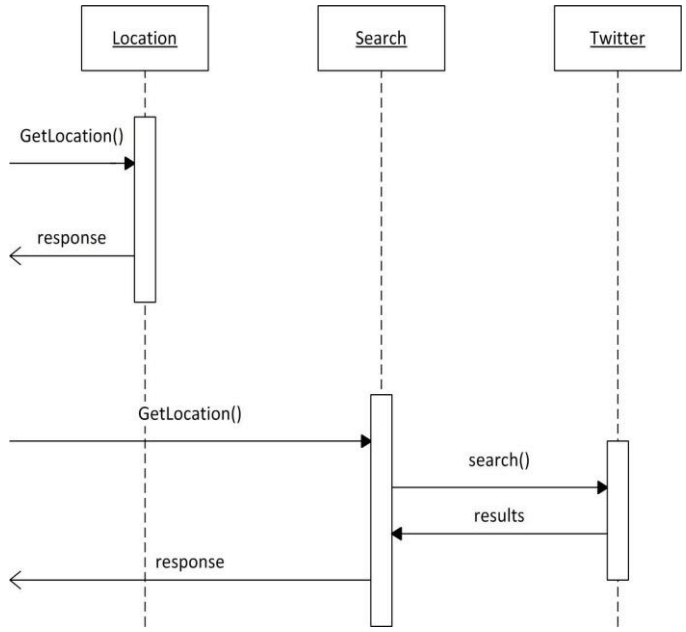

Fig. 2. Sequence of Processes

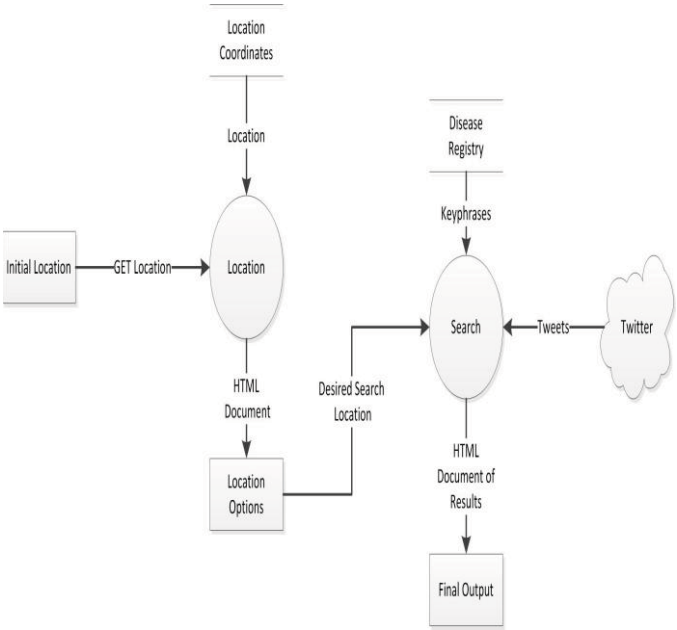

Fig. 3. The Data Flow

The initial request is one or a list of locations. These are cities that are available for searching for the user. The cities chosen by the user are transmitted to web service Search operation, which then communicates with Twitter's servers to retrieve the results of the required searches.

VI. PSO ALGORITHM AND EXTENDED GA ALGORITHM

As a heuristic method for complex problems solving, Particle Swarm Optimization algorithm and genetic algorithm are intelligent optimization techniques. Swarm Algorithm generates a population of particles that adjusts its particle position and velocity in the search space according to a set of mathematical formulas to locate the best solution.

This algorithm is an iterative algorithm. At each iteration, every particle gets a chance to move. The particle moves by the magnitude of their velocity. If the velocity is very high, the particle will take bigger steps, and if the velocity is very small, the particle will take smaller steps closer to the target in the search space [10].

Fig. 4 explains 50 particles (diseases) in a regional search space as they are assigned with the initial particle position and velocity. The region space is specified with the minimum and maximum range values. In each iteration, particle is searching for the city. The black color is the target (city) for the disease. The other color shows fitness values of how far the particles within different boundary near to the target (city). At every iteration, particle calculate their fitness values and therefore, each individual fitness value is the Personal best(local best) Best value and the particle individual value closest to the target indicates the Global best(gBest) values. This way, they have their minimum and maximum fitness values. Once, the personal best and global best values are achieved, particle velocity is calculated the and the particle position is updated. They keep tracking for the target in the search regional space.

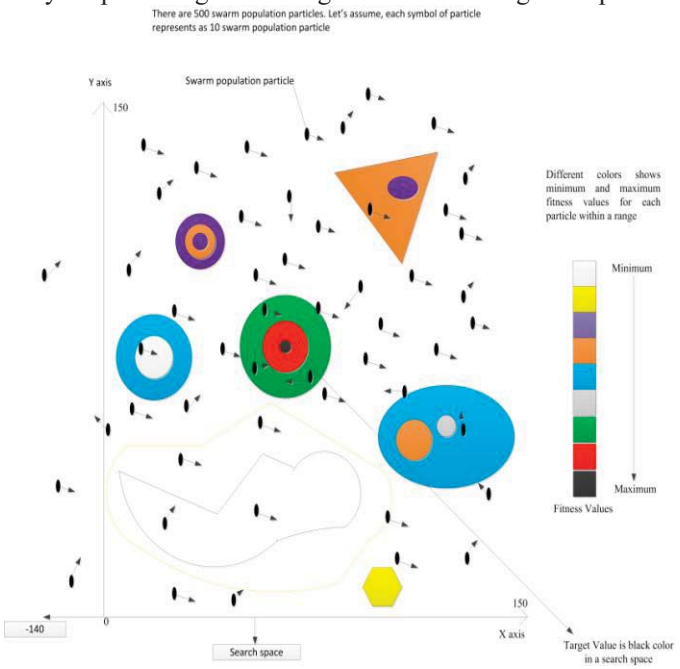

Fig. 4. Swarm population of 500 particles in search space

Any particles can have maximum fitness value closest to the target. Once particles achieved the target, they need to know its location. So, particles get the target based on their pBest and gBest values. Once the target achieved with the location, so algorithm stops otherwise it will be keep on searching for the target until the last iteration.

Swarm algorithm involves the following steps:

1. Initialize the swarm form the solution space
2. Evaluate the fitness of each particle
3. Update local
4. Update global bests
5. Update velocity and position of each particle
6. Go to step2, and repeat until termination condition

The advantages of PSO algorithm are calculation is easy to perform, small number of parameters to adjust, and high efficiency in global searching.

On the other hand, extended genetic algorithm finds an ideal clustering solution instead of a more mathematical method. This key difference allows for more adaptive behavior within our clustering method. This paper builds a utility-based intelligent agent that implements a faster extended genetic algorithm with greater efficiency than the original algorithm.

Chromosomes are encoded to represent an extended genetic algorithm and to be parsed into tree structures, which prevents syntax crossovers and allows for mutation stages. The EGA algorithm used one type of mutation. This type is known as a one-point mutation. Either a single city's position is moved through the chromosome, switching its place in the clusters with another city, or the point at which a cluster is organized is moved. Through the repeated use of these two types of mutations, the study can create a generation consisting of a multitude of clustering possibilities.

To further increase the genetic diversity present in each generation of the EGA, the algorithm includes a step where a new individual is added to the population. This individual is randomly generated with each generation iterated, to create additional diversity, even without the crossover step's inclusion in the algorithm.

In this study, crossover step is eliminated although it is a key part of numerous genetic algorithms. Crossover affects the efficiency of the study solution. It would build new chromosomes out of sections from two different chromosomes, creating new generations with greater diversity. The lesser number of generations required comes with a cost in the form of a drop in efficiency. Currently, our genetic algorithm stores each chromosome as a sequence of characters representing the city. The order of the characters in our chromosomes is of great importance and no repeats are allowed. Traditional genetic algorithms use a series of bits which represent in turn a series of operations and values [21-23].

Rewriting our genetic algorithm code to use crossovers could lower the efficiency of the algorithm more than it would lower the amount of generations required. With just our current generation loop utilizing only varying degrees of mutations, we are likely creating the same chromosomes which would result from crossovers. The EGA algorithm is simply a way to go

through a vast number of possible solutions with greater speed and efficiency than other strategies.

The fitness of an individual is computed based on the "distances" between the words or other tracked items appearing within a city. The items are compared by their weights, meaning the ratio of their appearances to the total sum of words in the city. These weights are then treated as if they were coordinated for the city's point on an n-dimensional grid, where n is the number of different words appearing within the set of cities being clustered by the EGA. In the solution's EGA, an individual with a lower fitness value actually represents a solution of greater quality than one with a greater fitness value. This is because the quality of the clustering solution is the closeness of the items being clustered. Only the most individual fit is passed on to the next generation.

Once proper algorithms are put in place, the desired service item from the web part can be requested. Upon this initial request, the first generation of information retrieval is randomly generated, which can lead to a slight decrease of efficiency.

What makes up for this initial sacrifice in performance is that as the workflow processes information, the algorithm creates a new generation of logic and the results are assessed based on goodness of fit to results.

As new logic workflows are developed, they can be selected and mutated to produce better results. As this process continues, eventually the service can be provided in such a way to enable increased efficiencies over time.

Upon delivery of the user request, the generation cycle is terminated. The EGA algorithm does not have a normalization step as it does not use centroids to define the clusters like the traditional clustering method. Fig. 5 describes Extended Genetic Algorithm (EGA). The algorithm input: diseases, cities. Output: disease's ID, city's ID, and clusters names.

1. Create initial random population P of N individuals
2. i ← 0
3. If i is equal to the number of desired generations,
   return the best individual of the most recent generatic
4. P_{i+1} ← empty set
5. B ← the most fit individual of the previous generatic
6. Add B to P_{i+1}
7. Insert into P_{i+1} mutate(B)
8. Repeat 7 until P_{i+1} has N individuals
9. Evaluate the fitness for all individuals from P
10. i ← i + 1
11. Goto 3

Fig. 5. The EGA Algorithm

VII. RESEARCH PROTOTYPE

The study of this research implements Architected Rapid Application Development (ARAD) prototype model [24-26]. In this research, the prototype system is an Environmental Exposure Surveillance Model (E^2SM). It generates a list of cities. Once the user selects a state or a county, a list of cities that are available for searching are displayed so that the user can select city or cities.

In its final form, the prototype system web-based application made up of two web services. The first service, HS, searches twitter for locations diseases. The second service includes the required operations for clustering cities based on diseases using swarm algorithm.

VIII. EXPERIMENTAL RESULTS

The following are preliminary results:

- The comparison of different results on various population particles using Swarm and Extended Genetic algorithm shows that swarm is better and faster in a search space in terms of iteration and execution time.
- Table 1 explains population size of 500 particles with different target values of iterations set to 100 for Swarm and Genetic algorithm with respect to its execution time(ms) and iterations within minimum (-140) and maximum range values (150) in a search space. Swarm inputs which are twenty basically used to add twenty random values to get the minimum or maximum fitness value. Swarm iterations becoming lower and lower because swarm input are more than three or four times lesser than swarm population particle. The table's columns from left to right are number of swarm inputs, number of particles, target, execution of swarm algorithm, number of iteration, execution of extended GA, number of iteration, #of epochs.
- The techniques of walkthrough are approved as experimental assessment approaches to evaluate system application usability. The walkthrough method evaluates the different phases of the research process. During the system evaluation phase, the examiners evaluated the interfaces that are related to real roles and real users [26]. The walkthrough examiners of this study are professors, researchers, and SOA engineers in North Carolina and Michigan States in the United States of America.

Table 1
Comparison of PSO and EGA

S	P	T	SA (ms)	I	EGA (ms)	I	# E
20	20	50	6.056	19	2.799	6	100
20	20	40	3.732	92	1.4	5	100
20	20	30	4.199	23	1.866	9	100
20	20	20	3.732	26	2.333	2	100
20	20	10	3.732	20	1.399	1	100

They identified different types of problems. These types include design, development, testing, usability, and maintenance problems. They verified that the prototype satisfies requirements of this research. Also, the prototype is evidence that proves the new concept is valid, the solution is conceptualized, and the findings answer the research question and solve the research problem.

IX. CONCLUSION

An Environmental Exposure Surveillance Model (E^2SM) for Epidemiologists using Intelligent Swarm Algorithm is a computerized prediction system that tracks the measles outbreak and predict future outbreaks.

This model is a new theoretical development that improves support for strategic decision making in public health. The outcome is improved standards for fast and accurate prediction for epidemiologists.

Particle Swarm Optimization algorithm is faster, simpler, and more accurate comparing to Extended Genetic Algorithm.

DEDICATION

The primary author of this paper, Dr. Naser El-Bathy, has dedicated this research to the Egyptian writer, Ibrahim El-Bathy, who passed away in 1979. His methods in writing and dedication to the publishing and newspaper industries are what drove him to choose this concentration for this research. His interest in the field of medicine whether it was personally helping a patient or raising awareness for new medical techniques being researched sparked an interest and embedded the idea for this research in Dr. Naser El-Bathy. Ibrahim El-Bathy's achievements in the field of medicine, publishing and newspaper industries are reported in several Arabic newspapers and magazines during his life and after his death.

REFERENCES

[1] J. Rangel, P. Sparling, C. Crowe, P. Griffin, and D. Swerdlow. "Epidemiology of Escherichia coli O157:H7 Outbreaks, United States, " 1982–2002. *University of Nebraska - Lincoln,Public Health Resource*, 2005.

[2] H. Karch, P. Tarr, and M. Bielaszewska. "Enterohaemorrhagic Escherichia coli in human medicine," *Int J Med Microbiol* 295 (6–7): 405–18, 2005.

[3] A. O'Brien, J. Newland, S. Miller, R. Holmes, and H. Smith. "Shiga-like toxin-converting phages from Escherichia coli strains that cause hemorrhagic colitis or infantile diarrhea," *Science* 226 (4675): 694–6, 1984.

[4] Reports of Selected E. coli Outbreak Investigations. *Centers for Disease Control and Prevention (CDC) http://www.cdc.gov/ecoli/outbreaks.html*. Accessed March 2015.

[5] N. El-Bathy, C. Gloster, G. Azar, M. El-Bathy, and G. Stein. "Intelligent Optimization Models for Disease Diagnosis Using A Service-Oriented Architecture and Management Science," *Proceeding of IEEE, Electro/Information Technology Conference at Indianapolis, IN*, 2012.

[6] N. Ehrenkranza1, M. Shultza, and I. Emily. "Recorded Criteria as a "Gold Standard" for Sensitivity and Specificity Estimates of Surveillance of Nosocomial Infection: A Novel Method to Measure Job Performance," *Infection Control* , V. 16, pp. 697-702, 1995.

[7] R. Thomas. "Agent Based Systems for Prediction and Prevention of Infectious diseases," *University of Windsor,* 2010.

[8] M. Lewis, J. Pavlin, J. Mansfield, S. O'Brien, and L. Boomsma. "Disease outbreak detection system using syndromic data in the greater Washington DC area," *American Journal of Preventive Medicine* , V. 23, pp. 180-186, 2002.

[9] C. Yang, H. Chang, Y. Cheng, and L. Cheuang. "Novel generating protective single nucleotide polymorphism barcode for breast cancer using particle swarm optimization," *The International Journal for Cancer Epidemiology, Detection and Prevention,* V. 33, pp147–154, 2009.

[10] J. Kennedy and R. Eberhart. "Particle Swarm Optimization," Proc. the 1995 IEEE Int. Conf. Neural Networks (Perth, Australia), vol. IV, pp. 1942-1948, 1995.

[11] N. El-Bathy, C. Gloster, and G. Azar. "Intelligent Internet Search Technology using A Novel Genetic Algorithm and A Service-Oriented Architecture," *American Journal of Intelligent Systems*, V. 3, No. 2, pp. 83-92, 2013.

[12] N. El-Bathy, C. Gloster, G. Azar, and M. El-Bathy. "Intelligent Search Lifecycle Architecture for Mass Media Using SOA," *Architecture Research Journal*, V. 2, No. 4, pp. 36 – 41, 2012.

[13] State of the Twittersphere - Q4 2008 Report.
http://blog.hubspot.com/blog/tabid/6307/bid/4439/State-of-the-Twittersphere-Q4-2008-Report.aspx. Accessed February 2015.

[14] D. Vladimir, "Development of applications with service-oriented architecture for grid," *ACM New York*, Vol. 374, 2008.

[15] D. Steiner, "Oracle SOA Suite Quick Start Guide 10g (10.1.3.1.0)," *Oracle*, pp. 7 – 11,2006.

[16] A. Dan, R. Johnson, and A. Arsanjani, "Information as a service: modeling and realization," *International Workshop on Systems Development in SOA Environments, IEEE*, 2007.

[17] N. El-Bathy and G. Azar, "Intelligent Information Retrieval and Web Mining Architecture Applying Service-Oriented Architecture," KG. Saarbrücken, Germany: *LAP LAMBERT Academic Publishing AG & Co*. 2010.

[18] D. Krafzig, K. Banke, and D. Slame, "Enterprise SOA Service-Oriented Architecture Best Practices," *NJ: Prentice Hall*, 2005.

[19] N. El-Bathy, C. Gloster, G. Azar, M. El-Bathy, G. Stein, and R. Stevenson. "Intelligent Teaching Models for STEM Related Careers Using A Service-Oriented Architecture and Management Science," *Proceeding of IEEE, Electro/Information Technology Conference at Indianapolis, IN*, May 2012.

[20] N. El-Bathy, P. Chang, G. Azar, and and R. Abrahiem , "An Intelligent Search of Lifecycle Architecture for Modern Publishing and Newspaper Industries Using SOA," *IEEE, Electro/Information Technology, Normal, IL, United States*, pp. 1-7, 2010.

[21] N. El-Bathy, G. Azar, M. El-Bathy, and G. Stein, "Intelligent Extended Clustering Genetic Algorithm," *IEEE, Electro/Information Technology, Mankato, MN, United States*, pp. 1-5, 2011.

[22] B. Coppin, "Artificial intelligence illuminated," *Sudbury, Massachusetts: John and Bartlett Publishers*, 2004.

[23] N. Chaiyaratiia and A. M. S . Zalzala, "Recent developments in evolutionary and genetic algorithms: theory and applications," Genetic Algorithms in Engineering Systems: Innovations and Applications," *GALESIA 97. Second International Conference On (Conf. Publ. No. 446)*, pp. 270 – 277, 1997.

[24] N. El-Bathy, C. Gloster, G. Azar, C. Seay, M. El-Bathy, I. Kateeb, R. Agrawal, A. Baset. Open Source Software Engineering Theory: Intelligent Educational Tool Increases Placement of Graduates in STEM Related Careers. *Proceeding of American Society for Engineering Education Conference at San Antonio, Texas*, 2012.

[25] D. E. Rowley and D. G. Rhoades, "The cognitive jogthrough: a fast-paced user interface evaluation procedure," *CHI '92 Proceedings of the SIGCHI conference on Human factors in computing systems, ACM, New York*, 1992.

[26] D. Pinelle and C. Gutwin, "Groupware walkthrough: Adding context to groupware usability evaluation," *CHI '02 Proceedings of the SIGCHI conference on Human factors in computing systems: Changing our world, changing ourselves, ACM, New York*, 2002.

Complexity Analysis for Initial Graph in Volumetric Segmentation Method

Dumitru Dan Burdescu, Marius Brezovan, Liana Stănescu,
Cosmin Stoica Spahiu, Daniel Costin Ebâncă
Computers and Information Technology Department,
Faculty of Automatics, Computers and Electronics,
University of Craiova, Dolj, Romania

ABSTRACT - *The purpose in this article is to present a method to detect visual objects from color digital images by volumetric segmentation and to discuss the complexity of algorithms for visual computing. The problem of partitioning images into homogenous regions or semantic entities is a basic problem for identifying relevant objects. The presented method is a general-purpose volumetric segmentation method and it produces results from two different perspectives: (a) from the perspective of perceptual grouping of regions from the images and also (b) from the perspective of determining regions if the input spatial images contain visual objects. We present an unified framework for volumetric image segmentation and prism cells used in the first run into volumetric segmentation methods. The major concept used in graph-based volumetric segmentation method is the concept of homogeneity of volumes and thus the edge weights are based on color distance. Our original algorithm for volumetric segmentation is linear.*

Keywords : Graph-based Segmentation; Color Segmentation; Syntactic Segmentation; Dissimilarity.

1 Introduction and related works

Visual is related to some semantic concepts because certain parts of a scene are pre-attentively distinctive and have a greater significance than other parts. However, many real images contain multiple structures and most of the structure may not be unambiguous defined. As a consequence, we consider that a volumetric segmentation method can detect visual objects from images if it can detect at least the most objects. We develop a visual method which uses a virtual spatial graph constructed on cells of prisms with tree-hexagonal structure containing less than half of the image voxels in order to determine representing visual objects. Thus, the volumetric segmentation is treated as a spatial graph partitioning problem.

Some methods for planar pictures [1], [2] are using an adaptive criterion that depends on local properties rather than global ones. In contrast with the simple graph-based methods, cut-criterion methods capture the non-local cuts in a graph and are designed to minimize the similarity between pixels that are being split [3] [4]. The normalized cut criterion [4] takes into consideration self similarities of regions. For example in [5] the quality of each cycle is normalized in a way that is closely related to the normalized cuts approach. The methods [6] use a measure of uniformity of a region. In contrast, [1] and [2] are using a pair-wise region comparison rather than applying a uniformity criterion to each individual region. Complex grouping phenomena can emerge from simple computation on these local cues [7]. A number of approaches to segmentation are based on finding compact clusters in some feature space [8], [11]. A recent technique using feature space clustering [9] [10] first transforms the data by smoothing it in a way that preserves boundaries between regions.

Previous works for planar images [12], [13] are related to the works in [14] and [15] in the sense of pair-wise comparison of region similarity.

In addition, our volumetric segmentation algorithm produces results from both the perspective of perceptual grouping and also from the perspective of determining homogeneous in the input images. Based on number of the tree-edges of the input spatial graph G = (V, E) of the color-based algorithm, and the number of the vertices of input graph we say and prove that the time of volumetric segmentation algorithm is linear.

2 Constructing a virtual tree-hexagonal structure

The low-level system for volumetric image segmentation and boundary extraction of visual objects described in this section can be designed to be integrated in a general framework of indexing and semantic digital image processing. The framework uses color and geometric features of image volumes in order to: (a) determine visual objects and their volumetric surface, and also (b) to extract specific color and geometric information from these objects to be further used into a higher-level digital image processing system.

The segmentation modules are used over the initial RGB spatial image in order to obtain regions and visual objects [14], [15]. Then the segmentation modules create virtual prism cells with tree-hexagonal structure defined on the set of image voxels of the input digital image and a spatial grid

graph having tree-hexagons as vertices. However, we intent to use some of the advantages of the spatial hexagonal grid such as uniform connectivity. As a consequence we construct a virtual structure over the voxels of an input image, as presented in Figure 1.

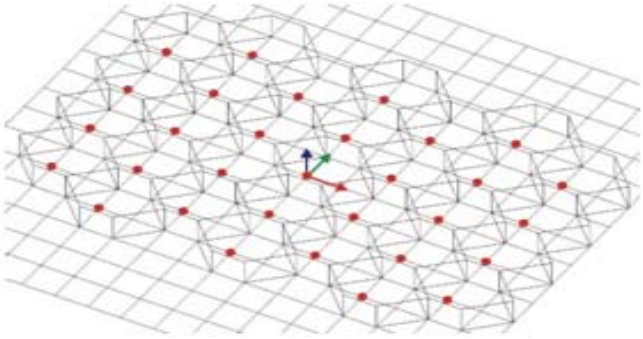

Fig. 1. Virtual tree-hexagonal structure constructed on the digital image voxels.

Let I be a spatial initial image having the dimension h × w × z (e.g. a matrix having 'h' rows, 'w' columns and 'z' deep of matrix voxels). In order to construct a tree-hexagonal grid on these voxels we retain an eventually smaller image with

$$h' = h - (h - 1) \bmod 2,$$
$$w' = w - w \bmod 4,$$
$$z' = z. \quad (1)$$

In the reduced image at most the last line of voxels and at most the last three columns and deep of matrix of voxels are lost, assuming that for the initial image h > 3 and w > 4 and z ≥ 1, that is a convenient restriction for input images.

Each tree-hexagon from the tree-hexagonal grid contains sixteen voxels: twelve voxels from the frontier and four interior frontiers voxels. Because tree-hexagons voxels from an image have integer values as coordinates we always select the left up voxel from the four interior voxels to represent with approximation the gravity center of the tree-hexagon, denoted by the pseudo-gravity center. Each tree-hexagon (prism cell) represents an elementary item and the entire virtual tree-hexagonal structure represents a spatial grid graph, G = (V; E), where each tree-hexagon H in this structure has a corresponding vertex v ∈ V. The set E of edges is constructed by connecting tree-hexagons that are neighbors in 8-connected sense. The vertices of this graph correspond to the pseudo-gravity centers of the hexagons from the tree-hexagonal grid and the edges are straight lines connecting the pseudo-gravity centers of the neighboring hexagons, as presented in Figure 2.

Let h × w × z be the three dimensions of the initial volumetric image verifying the previous restriction. Given the coordinates ⟨l; c; d⟩ of a voxel 'p' from the input volumetric image, we use the linear function

$$ip_{h;w;z}(l; c; d) = (l - 1) \times w \times z + (c - 1) \times z + d; \quad (2)$$

in order to determine an unique index for the voxel.

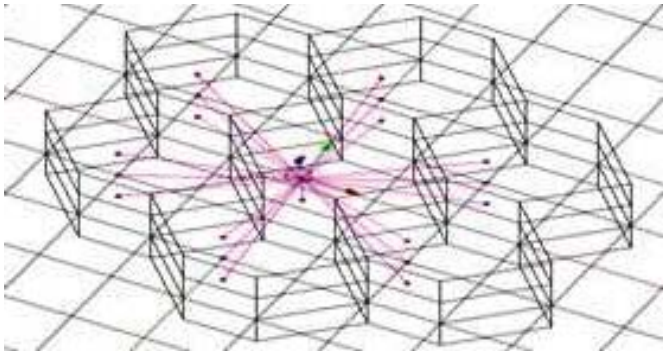

Fig. 2. The grid graph constructed on the pseudo-gravity centers of the tree-hexagonal grid.

It is easy to verify that the function 'ip' defined by the Equation (2) is bijective.

These relations allow us to uniquely determine the coordinates of the voxel representing the pseudo-gravity center of a tree-hexagon specified by its index (its address). In addition, these relations allow us to determine the sequence of coordinates of all sixteen voxels contained into a tree-hexagon with an address 'k'.

The vertices of this spatial graph correspond to the pseudo-gravity centers of the hexagons from the tree-hexagonal grid and the edges are straight lines connecting the pseudo-gravity centers of the neighboring hexagons, as presented in Figure 2.

We associate to each tree-hexagon 'H' from V two important attributes representing its dominant color and the coordinates of its pseudo-gravity center, denoted by g(h). The dominant color of a tree-hexagon is denoted by c(h) and it represents the color of the voxel of the tree-hexagon which has the minimum sum of color distance to the other twenty voxels. Each tree- hexagon 'H' in the tree-hexagonal grid is thus represented by a single point, g(h), having the color c(h).

3 Volumetric segmentation algorithm

Let $V = \{h_1, \ldots, h_{|V|}\}$ be the virtual set of tree-hexagons constructed on the spatial image voxels as presented in previous section and G = (V, E) be the undirected spatial grid-graph, with E containing pairs of tree-hexagons that are neighbors in a 8-connected sense. Components of an input image represent compact regions containing voxels with similar properties. Thus the set V of vertices of the spatial graph G is partitioned into disjoint sets, each subset representing a distinct visual object of the initial image. As in other graph-based approaches [10], [15] we use the notion of segmentation of the set V.

A segmentation S, of V is a partition of V such that each component C ∈ S corresponds to a connected component in a spanning sub-graph GS = (V, ES) of G, with ES ⊆ E.

The set of edges (E – ES) that are eliminated connect vertices from distinct components. The common boundary

between two connected components (C′, C″) ∈ S represents the set of edges connecting vertices from the two components:

$$cb(C', C'') = \{(h_i, h_j) \in E \mid h_i \in C', h_j \in C''\}. \quad (3)$$

The set of edges (E – ES) represents the boundary between all components in S. This set is denoted by bound(S) and it is defined as follows:

$$bound(S) = \cup_{C',C'' \in S} cb(C', C''). \quad (4)$$

We use the notions of segmentation too fine and too coarse as defined in [1] that attempt to formalize the human perception of visual objects from an image. A segmentation S is too fine if there is some pair of components (C′, C″) ∈ S for which there is no evidence for a boundary between them. S is too coarse when there is a proper refinement of S that is not too fine. The key element in this definition is the evidence for a boundary between two components.

Definition 1. Let G = (V; E) be the undirected spatial graph constructed on the tree-hexagonal structure of an input digital image, with V = {h_1, . . ., $h_{|V|}$}. A proper segmentation of V, is a partition S of V such that there exists a sequence ⟨S_i; S_{i+1}; : : : ; S_{f-1}; S_f⟩ of segmentations of V for which:

- S_f is the final segmentation and S_i is the initial segmentation,
- S_j is a proper refinement of S_{j+1} (i.e., $S_j \subset S_{j+1}$) for each j = i, ..., f −1,
- segmentation S_j is too fine, for each j = i; : : : ; f − 1,
- any segmentation S_l such that $S_f \subset S_l$, is too coarse,
- segmentation S_f is neither too coarse nor too fine.

The volumetric segmentation algorithm starts with the most refined segmentation, S_0 = {{h_1}. . . . . {$h_{|V|}$}} and it constructs a sequence of segmentations until a proper segmentation is achieved. Each segmentation S_j is obtained from the segmentation S_{j-1} by merging two or more connected components for which there is no evidence for a boundary between them [15]. When starting, for a certain number of segmentation components the only considered feature is the color of the volumes associated to the components and in this case we use a color based region model. When the components become complex and contain too much tree-hexagons, the color model is not sufficient and geometric features together with color information are taken into consideration. In this case, we use a syntactic based region with a color-based region model for volumes. In addition, syntactic features bring supplementary information for merging similar volumes in order to determine objects.

In the color of graph-based model, the volumes are modeled by a vector in the RGB color space.

The segmentation S is too fine in the color-based region model if there is a pair of components (C'; C'') ∈ S for which *adjacent(C'; C'') = true* and

$$ExtVar(C'; C'') = IntVar(C'; C'') + tresh(C'; C'') \quad (5)$$

where the adaptive and efficient threshold *tresh*(C'; C'') is given by

$$tresh(C'; C'') = tresh/(min(|C'|; |C''|). \quad (6)$$

The threshold 'tresh' is a global adaptive value defined by using a statistical model.

The maximum internal contrast between two components, (C'; C'') ∈ S is defined as follows:

$$IntVar(C'; C'') = max\{IntVar(C'); IntV\ ar(C'')\}. \quad (7)$$

We decided to use the RGB color space because it is efficient and no conversion is required. Although it also suffers from the non-uniformity problem where the same distance between two color points within the color space may be perceptually quite different in different parts of the space, within a certain color threshold it is still definable in terms of color consistency. We use the perceptual Euclidean distance with weight-coefficients as the distance between two colors

Let G = (V; E) be the initial spatial graph constructed on the tree-hexagonal structure of a volumetric input image. The proposed segmentation algorithm will produce a proper segmentation of V according to the Definition 1.

The color-based sequence of segmentations, S, and its associated sequence of forests will be generated by using the color-based region model and a maximum spanning tree construction method based on a modified of the Kruskal's algorithm [16].

The syntactic-based sequence of segmentations, S and its associated sequence of forests will be generated by using the syntactic-based model and a minimum spanning tree construction method based on a modified form of the Boruvka's algorithm.

Let G = (V; E) be the initial graph constructed on the tree-hexagonal structure of a volumetric input image. The proposed segmentation algorithm will produce a proper segmentation of V according to the Definition 1.

Algorithm 1 Volumestric Segmentation Algorithm
1: ****Procedure** SEGMENTATION(l, c, d, P, H, Comp)
2: **Input** l, c, d, P
3: **Output** H, Comp
4: H ← *CREATEHEXAGONALSTRUCTURE(l, c, d, P)
5: G ← *CREATEINITIALGRAPH(l, c, d, P, H)
6: *CREATECOLORPARTITION(G, H, Bound)
7: G′ ← *EXTRACTGRAPH(G, Bound, th^{kg})
8: *CREATESYNTACTICPARTITION(G, G′, th^{kg})
9: Comp ← *EXTRACTFINALCOMPONENTS(G′)
10: **end procedure**

The input parameters represent the image resulted after the operation: the array P of the spatial image voxels structured in 'l' lines, 'c' columns and 'd' depths. The output parameters of the segmentation procedure will be used by the contour extraction procedure: the tree-hexagonal grid stored in the array of tree-hexagons H, and the array *Comp* representing the set of determined components associated to the objects in

the input spatial image. The global parameter th^{kg} is the threshold.

The color-based segmentation and the syntactic-based segmentation are determined by the procedures CREATECOLORPARTITION and CREATESYNTACTICPARTITION respectively.

The color-based and syntactic-based segmentation algorithms use the tree-hexagonal structure H created by the function CREATEHEXAGONALSTRUCTURE over the voxels of the initial spatial image and the initial triangular grid graph G created by the function CREATEINITIALGRAPH. Because the syntactic-based segmentation algorithm uses a graph contraction procedure, CREATESYNTACTICPARTITION uses a different graph, G', extracted by the procedure EXTRACTGRAPH after the color-based segmentation finishes.

The procedure EXTRACTFINALCOMPONENTS determines for each determined component C of Comp, the set sa(C) of tree-hexagons belonging to the component, the set sp(C) of tree-hexagons belonging to the frontier and the dominant color c(C) of the component.

Overall running time is T(CREATECOLORPARTITION) = O(n*logn) and T(CREATESYNTACTICPARTITION) = O(n*logn) where 'n' is n = |V|.

4 Complexity Analysis for Initial Graph

Let 'np' be the number of the voxels of the initial image structured in 'l' lines, 'c' columns and 'd' in depth, then np = l × c × d. In order to realize the tree-hexagonal structure as presented in Figure 1 the (1) condition must hold. With these new values only few voxels from the initial image will be lost: at most the last line at the bottom of image and the last three columns at the right of the image.

Denoting by V the set of the hexagons belonging to the tree-hexagonal structure constructed on the image voxels a grid graph having as vertexes the tree-hexagons of the set V can be constructed as presented in Figure 2. The cardinality of V can determined as follows:

$$|V| = 2 \times l_1 \times c_1 - l_1 - c_1 + d + 1 \quad (8)$$

where $l_1 = (l - 1)/2$, and $c_1 = c/4$.

The procedure CREATEHEXAGONALSTRUCTURE creates the tree-hexagonal structure and it initializes the variable V which is an array implementing the set of tree-hexagons of the grid graph. It is easy to determine the cardinality of the set E:

$$|E| = 6 \times l_1 \times c_1 - 7 \times l_1 - 5 \times c_1 + d + 6. \quad (9)$$

One can observe that the initial graph G is a simple, unconnected and spatial graph. The verification of the spatiality criterion,

$$|E| \leq 3 \times |V| - 6, \text{ if } |V| \geq 3, \quad (10)$$

follows from the following relation:

$$|E| = 6 \times l_1 \times c_1 - 7 \times l_1 - 5 \times c_1 + d + 6 = \\ = 3 \times (2 \times l_1 \times c_1 - l_1 - c_1 + 1) - 6 - (4 \times l_1 + 2 \times c_1 - 9) + d = \\ = |V| - 6 - (4 \times l_1 + 2 \times c_1 - 9) + d, \quad (11)$$

with $4 \times l_1 + 2c_1 - 9 \geq 0$, for either $c \geq 4, l \geq 7$, or $c \geq 8, l \geq 3$.

The conditions $c \geq 4, l \geq 7$, or $c \geq 8, l \geq 3$ are satisfied from the assumption $|V| \geq 3$ (the image contains at least three cells).

From the relation (10) it follows that the spatial graph G is also a sparse graph, with |E| = O(|V|). The properties of spatial graph and sparse graph are useful when discussing the running times of the segmentation algorithms.

The assertion that the number of the resulted tree-hexagons is always less than np/4 follows from the following relation:

$$|V| = 2 \times (l - 1)/2 \times c/4 - (l - 1)/2 - c/4 + d + 1 = \\ = (l \times c - 2 \times l - 2 \times c + d + 6)/4 = \\ = (np - 2 \times l - 2 \times c + d + 6), \quad (12)$$

where $np = l \times c \times d$, and $2 \times l + 2 \times c + d - 6 \geq 0$, for $l + c + d \geq 3$.

Denoting by 'n' the number of the resulted tree-hexagons (i.e., n = |V|, the number of the vertices of the spatial graph G), the time needed to build the tree-hexagonal grid is

$$T(CREATEHEXAGONALSTRUCTURE) = O(n), \quad (13)$$

because $O(n) = O(np)$ from the relation (12).

The time needed to the function CREATEINITIALGRAPH to build the initial graph G is also

$$T(CREATEINITIALGRAPH) = O(n), \quad (14)$$

because O(n) = O(np) and CREATEINITIALGRAPH performs a traversal of the array V and, at each iteration, operations can be accomplished in constant time.

5 Segmentation results and quantitative evaluation

Volumetric segmentation remains a difficult problem to tackle due to the complex nature of the topology of volumetric objects, the huge amount of data to be processed and the complexity of the algorithms that scale with the new added dimension [17]. Martin thesis [18] states that human segmentation can be used as the ground-truth reference in benchmarking segmentations produced by different methods. For image segmentation algorithms, Martin D. proposes a method that outputs Precision-Recall curves as a mean to evaluate segmentation consistency.

In pattern recognition and information retrieval, Precision-Recall method has received a world-wide

acceptance and it's considered as a standard measure because it offers good results for relevance [19]. Generally, precision (or confidence) is defined as the fraction of retrieved cases that are relevant, while recall (or sensitivity) is the fraction of relevant cases that are retrieved. In other words, in the context of classification, the precision for a class is equivalent with the true positives accuracy which is the number of true positives (i.e. the number of cases that are correctly labeled as belonging to that class) divided by the total number of cases labeled as belonging to that class (including false positives, which are cases that were incorrectly labeled as belonging to the class).

$$Precision = TP/(TP + FP) \quad (15)$$

Also in this context, recall is equivalent with the true positives rate which is defined as the number of true positives divided by the total number of cases that actually belong to the positive class (i.e. the sum of true positives and false negatives, which are cases that were not labeled as belonging to the positive class but should have been).

$$Recall = TP/(TP + FN), \quad (16)$$

where - true positives (TP), true negatives (TN), false positives (FP) and false negatives (FN) compare the classifier's prediction against apriority external information that is considered as the ground truth (observation).

The curve offers a rich descriptor where both axes are sensitive and intuitive and the inherent trade-off between these two quantities can be easily analyzed.

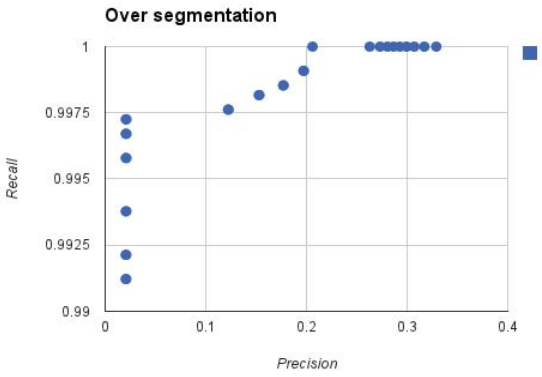

Fig. 3. Experimental results.

The segmentation method used for the experimental results is based on simple hysteresis threshold. All voxels with the density within a specified threshold 'tresh' will be treated as boundary voxels while the others as empty space. The results are as expected: the over-segmented volume has high recall and low precision (see Figure 3), while the under-segmented image has low recall because it fails to find salient features for the volume, and also low precision (since because many boundary pixels remain unmatched).

6 Conclusions

It is used a priori information that includes shape, topology and appearance model of the category of images to be segmented which is getting more popularity. The problems of volumetric image segmentation and grouping remain great challenges for computer vision.

A graph-based theoretic framework is taken into consideration by modeling digital image segmentation as a graph partitioning and optimization problem using input spatial graph. We have introduced an algorithm for volumetric segmentation based on virtual tree-hexagonal structure (prisms) constructed on the image voxels. We have presented the efficient algorithm of volumetric segmentation methods and virtual tree-hexagonal structure (prisms) used in the first run in volumetric segmentation algorithm. The key to the whole algorithms of volumetric segmentation method is the prism cells. Our algorithm for color-based segmentation is linear.

Enhancement and generalization of this method is possible in several further directions. First, it could be modified to handle open curves for the purpose of medical diagnosis. Second research direction is the using of composed shape indexing for both semantic and geometric image reasoning. Incorporation of the fuzzy set theory into graph based frameworks can achieve enhanced segmentation performances.

7 References

[1] Felzenszwalb, P., Huttenlocher, W.. Efficient graph-based image segmentation. International Journal of Computer Vision, 59(2), 167–181, (2004).

[2] Guigues, L., Herve, L., Cocquerez, L.P.. The hierarchy of the cocoons of a graph and its application to image segmentation. Pattern Recognition Letters, 24(8), 1059–1066, (2003).

[3] Gdalyahu, Y., Weinshall, D., Werman, M.. Self-organization in vision: stochastic clustering for image segmentation, perceptual grouping, and image database organization. IEEE Transactions on Pattern Analysis and Machine Intelligence, 23(10), 1053–1074, (2001).

[4] Shi, J., Malik, J.. Normalized cuts and image segmentation. IEEE Transactions on Pattern Analysis and Machine Intelligence, 22(8), 885–905, (2000).

[5] Jermyn, I., Ishikawa, H.. Globally optimal regions and boundaries as minimum ratio weight cycles. IEEE Transactions on Pattern Analysis and Machine Intelligence, 23(8), 1075–1088, (2001).

[6] Cooper, M.. The tractibility of segmentation and scene analysis. International Journal of Computer Vision, 30(1), 27–42, (1998).

[7] Malik, J., Belongie, S., Leung, T., Shi, J.. Contour and texture analysis for image segmentation. International Journal of Computer Vision, 43(1), 7–27, (2001).

[8] Comaniciu, D., Meer, P.. Robust analysis of feature spaces: color image segmentation. IEEE Transactions on Pattern Analysis and Machine Intelligence, 24(5), 603–619, (2002).

[9] Daniel Weinlanda, Remi Ronfardb, Edmond Boyerc. A survey of vision-based methods for action representation, segmentation and recognition, in Computer Vision and Image Understanding, Vol. 115(2), pp. 224–241, (2011).

[10] A. Alonso-González, Valero, S., Chanussot, J., López-Martínez, C., and Salembier, P.. Processing Multidimensional SAR and Hyperspectral Images With Binary Partition Tree, Proceedings of the IEEE, vol. 101, no. 3, pp. 723 – 747, (2013).

[11] P. Arbelaez, Pont-Tuset, J., Barron, J., Marqués, F., and Malik, J.. Multiscale Combinatorial Grouping, in Computer Vision and Pattern Recognition (CVPR), (2014).

[12] Brezovan, M., Burdescu, D., Ganea, E., Stanescu, L.. An Adaptive Method for Efficient Detection of Salient Visual Object from Color Images. In Proceedings of the 20th International Conference on Pattern Recognition, Istambul, Turkey (pp. 2346–2349), (2010).

[13] Burdescu, D., Brezovan, M., Ganea, E., Stanescu, L.. A new method for segmentation of images represented in a HSV color space. Lecture Notes in Computer Science, 5807, pp. 606–616, (2009).

[14] D.Burdescu, L. Stanescu, M. Brezovan, C. Stoica Spahiu. Computational Complexity Analysis of the Graph Extraction Algorithm for 3D Segmentation, in: IEEE Tenth World Congress on Services-SERVICES 2014, pp. 462-470, ISBN-13: 978-1-4799-5069-0, (2014).

[15] Burdescu, D.D., Brezovan, M., Stanescu, L., Stoica-Spahiu, C.. A Spatial Segmentation Method, International Journal of Computer Science and Applications, ©Technomathematics Research Foundation, Vol. 11, No. 1, pp. 75 – 100, (2014).

[16] Cormen, T., Leiserson, C., Rivest, R.. Introduction to algorithms. Cambridge, MA: MIT Press, (1990).

[17] Powers, D.M.. Evaluation: from precision, recall and f-measure to roc, informedness, markedness and correlation. Journal of Machine Learning Technologies 2(1), pp. 37–63, (2011).

[18] Martin, D.. An empirical approach to grouping and segmentation, Ph.D. Thesis, University of Berkeley (2002).

[19] P. Arbelaez, P., C. Fowlkes, C., Martin, D.. The Berkeley segmentation dataset and benchmark, Computer Science Department, Berkeley University. [Online]. Available: http://www.eecs.berkeley.edu/Research/Projects/CS/vision/bsds/.

Frequency Stabilization in Isolated Wind-Diesel System Using ISA-Based PID Controller

H. Shayeghi *[1] , H. A. Shayanfar[2] , A. Younesi[1],
[1]Electrical Engineering Department, University of Mohaghegh Ardabili, Ardabil, Iran
[2] Center of Excellence for Power System Automation and Operation, School of Electrical Engineering, Iran University of Science & Technology, Tehran, Iran
hshayeghi@gmail.com, hashayanfar@gmail.com, a.younesi@ieee.org

Abstract – *In this paper a PID controller designed for frequency stabilizing in an isolated wind-diesel power system. tuning of PID controller gains, formulated as an optimization problem and solved using Interior Search Algorithm (ISA). In order to prove the performance of proposed method, four case of simulations are assumed, step change in load of diesel side, step change in wind speed, random changing of the diesel side load, and random changing of the wind speed. Also, performance indices like overshoot, undershoot, settling time, ITAE and ISTSE are calculated and compared with Bee Colony (BC) algorithm. Results show that the proposed method is very robust and effective.*

Keywords: Interior Search Algorithm, PID Controller, Wind-Diesel System,

1 Introduction

In the entire world, electricity is one of the most demanding forms of energy in every one's daily life. There are groups of people that do not have access to the grid electricity, they are located in either remote or isolated communities, where grid connectivity is not at all neither economical nor viable. For this group of people, electricity is mainly supplied by small diesel-based power generation that it is very harmful for the environment [1]. Therefore, renewable energy sources are used to reduce the dependency of this power generation systems to the fuel and as a result reduce the harmful effect of this systems to the environment. However, renewable energy sources are mostly intermittent, so they can't supply quality power constantly. This problem solved by combining more renewable energy sources together with non-renewable or storage devices [2-5]. The oscillations of wind speed and load demand lead to mismatch between the power generation and load demand resulting in mismatch in system frequency (f) and power (*P*) from their nominal values.

In the past, many researches have proposed for control the oscillations of the frequency in hybrid power system generations. This controller are include control of pitch in wind side and governor in diesel side.

Many control strategies have been proposed in the literature. In [6-7], optimization of controller parameters proposed. Also, in [8-9] PI controller, in [10-12] variable structure control and in [13-14] energy storage controller have been reported.

The Proportional-Integral-Derivative (PID) controller has its widespread acceptance in the industrial processes due to its simplicity in understanding and its applicability to a large class of process having different dynamics [15]. Thus, in this paper two PID controllers designed simultaneously, one for diesel side and another for pitch control of wind side.

It is shown that the appropriate selection of PID controller parameters results in satisfactory performance during system upsets. Therefore, the optimal tuning of a PID gains is required to get the desired level of robust performance. Since optimal setting of PID controller gains is a multimodal optimization problem (i.e., there exists more than one local optimum) and more complex due to nonlinearity, complexity and time-variability of the real world power systems operation. Hence, local optimization techniques, which are well elaborated upon, are not suitable for such a problem. For this reason, a new metaheuristic algorithm based on interior design and decoration metaphor called Interior Search Algorithm (ISA) are used [16].

In this paper, optimal PID controller design for the frequency oscillation damping of a wind-diesel hybrid system, is formulated as an optimization problem and solved using Interior Search Algorithm (ISA). The results of the proposed method is compared with the Bee Colony (BC) algorithm. Simulation results show that the ISA-based PID controller (ISA-PID) has better performance in compared with BC-based PID controller (BC-PID) from the perspective of the response to step change in load demand of diesel side, step change in wind speed. Also, two performance indices according to the system defined and with overshoot, undershoot, and settling time calculated for both ISA-PID and BC-PID controllers, which proves that the proposed ISA-PID controller is very effective and robust compare to BC-PID controller.

* Corresponding Author, H. Shayeghi (hshayeghi@gmail.com)

2 System Modeling

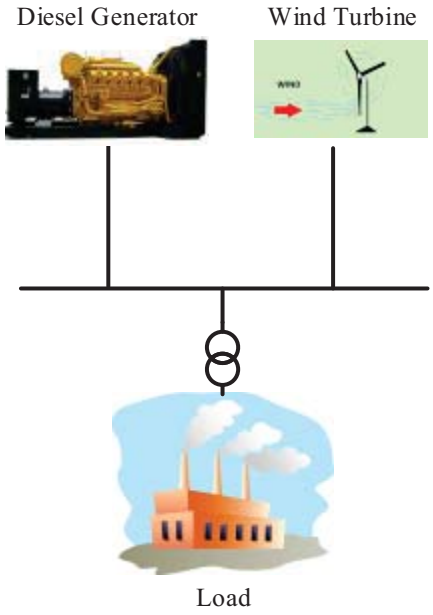

Fig. 1. Configuration of a hybrid wind-diesel isolated power system

Fig.1 shows the configuration of the hybrid wind-diesel isolated power system. Also, transfer function model of this system is shown in Fig. 2 [17]. Parameters of this system are given in [9].

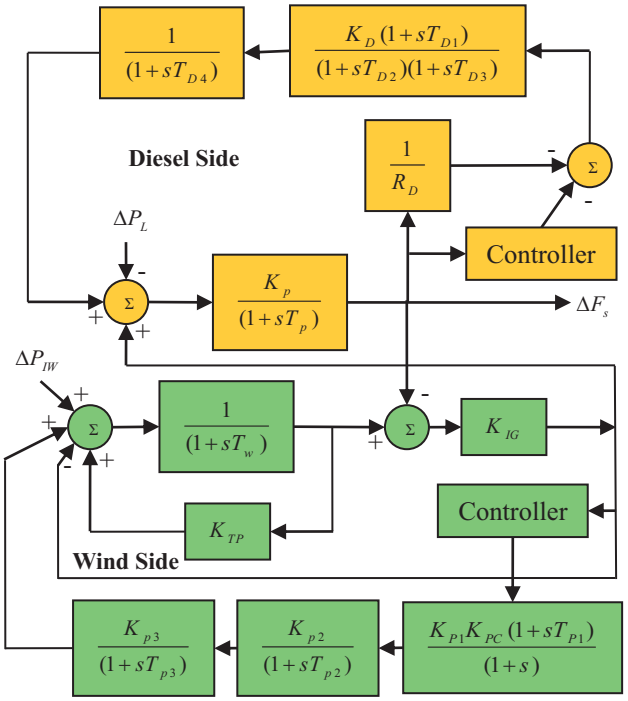

Fig. 2. Transfer function model of hybrid wind-diesel system

3 Interior Search Algorithm (ISA)

The ISA is inspired by to important architectural process, composition design and mirror work. The interior design procedure follows a coordinated and systematic methodology. In this process, a designer changes the composition of elements to find a more beautiful view and environment. A mirror worker uses different mirrors to produce a more decorative environment. An important part of this process is that mirrors are placed near the most beautiful elements to emphasize their prettiness. In ISA, the elements are divided into two groups with the exception of the fittest element. In one of these groups, called the composition group, the composition of elements is changed to find a more beautiful view. In the other one, called mirror group, mirrors are placed between these elements and the fittest element to find better views. The detailed algorithm is described below [16]:

1. Randomly generate the locations of elements between Lower Bounds (***LB***) and Upper Bounds (***UB***), and compute their fitness values.

2. Find the fittest element (for a minimization problem this element has the minimum objective function) in the j^{th} iteration, xgb^j, which is called the global best.

3. Randomly divide the other elements into two groups, the composition group and the mirror group, using two parameters each is in the range 0 to 1. A threshold value α and random variables $r1$. Elements with $r1 \leq \alpha$ go to the mirror group; otherwise, they go to the composition group. α is the only parameter of the ISA and it should be tuned carefully. In this paper α changes from 0.1 to 0.9 linearly.

4. For the global best, it is advantageous to slightly change its location using the random walk for local search around the global best. It can be formulated as:

$$x_{gb}^{j} = x_{gb}^{j-1} + r_n \times \lambda \quad (1)$$

Where r_n is a vector of normally distributed random numbers, and λ is a scale factor equal to 0.01 × (***UB-LB***).

5. For the composition group, the composition of each element is randomly changed. For this group of element boundary conditions (upper bounds and lower bounds) are changed, which can be formulated as:

$$x_i^j = LB^j + (UB^j - LB^j) \times r_2 \quad (2)$$

where, r_2 is a random value between 0 to 1; x_i^j is the i^{th} element in the j^{th} iteration; LB^j and UB^j are respectively lower and upper bounds of the elements in j^{th} iteration.

6. For the elements of the mirror group, a mirror is randomly placed between each element and the fittest element (global best). The location of a mirror for the i^{th} element in the j^{th} iteration is formulated as follows:

$$x_{m,i}^{j} = r_3 \times x_i^{j-1} + (1 - r_3) \times x_{gb}^{j} \quad (3)$$

Where, r_3 is a random value between 0 and 1. The location of the image or virtual location of the element depends on the mirror location, and can be formulated as follows:

$$x_i^{j} = 2x_{m,i}^{j} - x_i^{j-1} \quad (4)$$

7. The fitness values of the new locations of the elements and virtual elements are calculated. Each location is updated if its fitness is improved. For a minimization problem, this can be expressed as:

$$x_i^{j} = \begin{cases} x_i^{j} & f(x_i^{j}) < f(x_i^{j-1}) \\ x_i^{j-1} & Else \end{cases} \quad (5)$$

8. If any of the stop criteria are not satisfied, repeat from 2.

The simplified pseudo code of the ISA is presented in Table 1 [16].

Table 1. The simplified pseudo code of the ISA

```
Initialization
While any stop criteria are not reached
    find the x_gb^j
    for i = 1 to n
        if x_gb
                Apply Eq. (1)
        else if r_1 > α
                Apply Eq. (2)
        else
                Apply Eq. (3)
                Apply Eq. (4)
        end if
        Check the boundaries except for decomposition elements.
    end for
    for i = 1 to n
                Evaluate f(x_i^j)
                Apply Eq. (5)
    end for
end while
```

4 Problem Formulation

PID controllers are being extensively used by industries today due to their simplicity. Its main duty in this paper is to eliminate the steady state error and improvement of dynamic response. The structure of PID controller that is used in this paper shown in Fig. 3. It has three parameters, K_{PN}, K_{IN}, and K_{DN}. Where, N can be D or W, for diesel side and wind sides, respectively.

In the proposed system, there are two PID controllers, one for diesel side that its parameters denoted by K_{PD}, K_{ID}, and K_{DD}, and another for wind side that its parameters denoted by K_{PW}, K_{IW}, and K_{DW}. Therefore, there are six parameters that have to be well tuned. To increase frequency stabilization, a time based objective function is considered as follows:

$$J = \int_0^5 t \left| \Delta F_s \right| dt \quad (6)$$

Where, ΔF_s is the frequency deviation, and t is the simulation time. In the optimization process, it is aimed to minimize J in order to damp frequency oscillations.

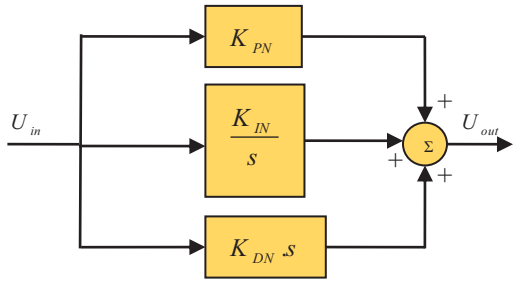

Fig. 3. PID controller structure

The design problem can be formulated as the following constrained optimization problem, where the constraints are the PID gains.

Minimize J Subject to:

$$\begin{aligned} 0 \le K_{PD} &\le 300 \\ 0 \le K_{ID} &\le 300 \\ 0 \le K_{DD} &\le 300 \\ 0 \le K_{PW} &\le 300 \\ 0 \le K_{IW} &\le 300 \\ 0 \le K_{DW} &\le 300 \end{aligned} \quad (7)$$

Results of the PID parameters based on the objective function J, solved using the proposed ISA and BC algorithm (see Ref. [17] for more details) are given in Table 2. Fig. 4 shows the minimum fitness functions evaluating process.

Table 2. Optimal PID gains

Algorithm	K_{PD}	K_{ID}	K_{DD}	K_{PW}	K_{IW}	K_{DW}
ISA	289.28	201.3	89.75	159.3	0.439	265
BC	240.36	55.67	0.326	38.69	0.779	9.08

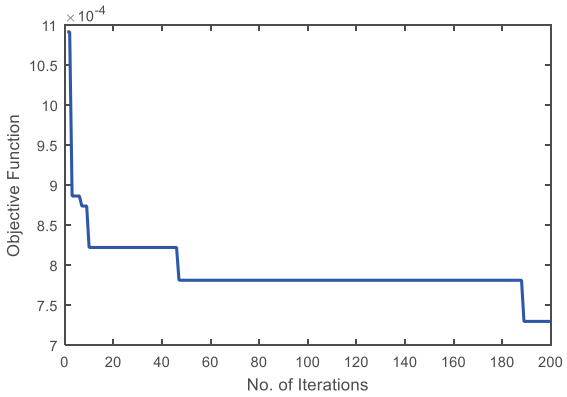

Fig. 4. Fitness convergence of the ISA

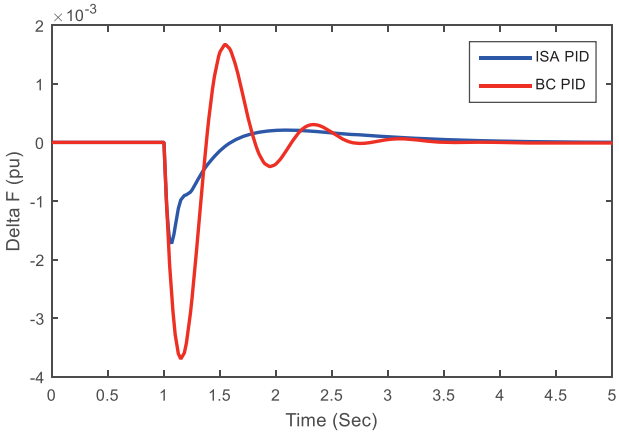

Fig. 5. Frequency response under load increase in diesel side

5 Simulation Results

In order to show the effectiveness of the proposed algorithm four case of simulations are considered.

Case 1. Step change in load demand of the diesel side

In this case of the simulations it's assumed that in t = 1 sec, a step change (ΔP_L=0.01 pu) occurred in diesel side load. Fig. 5 shows the frequency response of the system with ISA-PID and BC-PID controllers.

Also, performance indices like overshoot, undershoot, settling time, ITAE, and ISASE are calculated and shown in Table 3.

Table 3. Comparison of performance indices of two controllers for case 1

Algorithm	OS[%]	US[%]	T_s[sec]	ITAE	ISTSE
ISA	0.0206	0.1726	1.325	1.1804	7.5225
BC	0.1670	0.3697	1.5784	2.2281	50.77

ITAE and ISTSE based on the system performance characteristics are defined as:

$$ITAE = 1000 \times \int_0^{\text{Upper limit}} t\,|\Delta f_s|\,dt \tag{8}$$

$$ISTSE = 10^6 \times \int_0^{\text{Upper limit}} t^2 \Delta f_s{}^2\,dt \tag{9}$$

As Fig. 5 and data of Table 3 show, the proposed ISA-PID controller is very effective in compared with BC-PID controller.

Case 2. Step change in wind speed

In this case of the simulations it's assumed that in t = 1 sec, a step change (ΔP_{IW}=0.01 pu) occurred in wind speed. Fig. 6 shows the frequency response of the system with ISA-PID and BC-PID controllers.

Also, performance indices like overshoot, undershoot, settling time, ITAE, and ISASE are calculated and shown in Table 4.

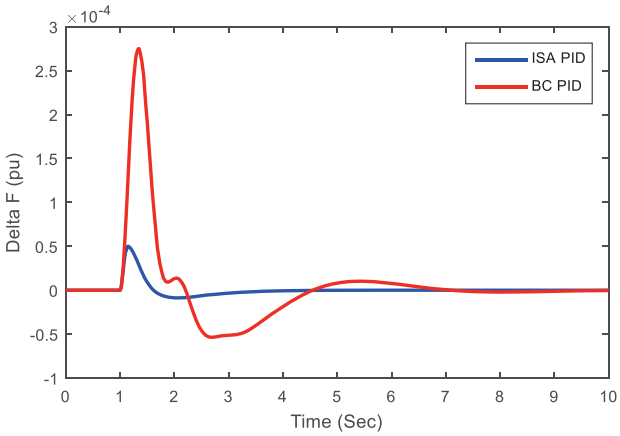

Fig. 6. Frequency response under wind speed increase

Table 4. Comparison of performance indices of two controllers for case 2

Algorithm	OS[%]	US[%]	Ts[sec]	ITAE	ISTSE
ISA	0.0050	0.0009	2.7678	0.0465	0.0119
BC	0.0275	0.0054	5.2911	0.5247	0.7844

Data of Table 4, and Fig. 6 proves the results of case 1 of simulations.

Case 3. Random change in load of diesel side

In this case of simulations, assume that random load change shown in Fig. 7 applied to the system. Fig. 8 shows that the control effect on the system frequency deviation of the ISA-PID controller is superior to that of the BC-PID controller.

Case 4. Random change in wind speed

Same as case 3, in this case of simulations, assume that random wind speed shown in Fig. 9 applied to the system. Fig. 10 shows that the control effect on system frequency deviation of the ISA-PID controller is superior to that of the BC-PID controller.

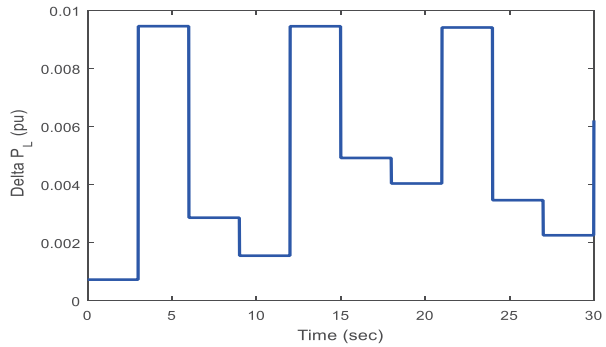

Fig. 7. Random load change

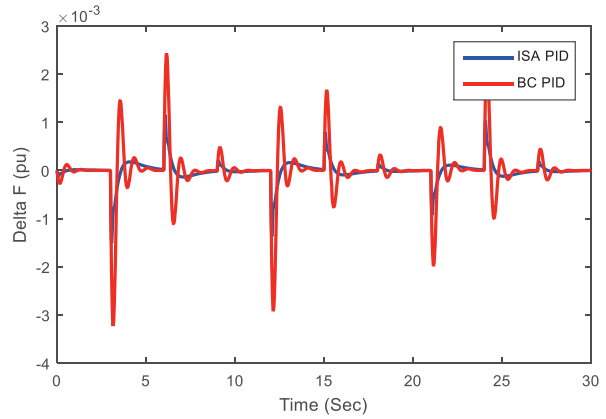

Fig. 8. System frequency response under random change in load of diesel side

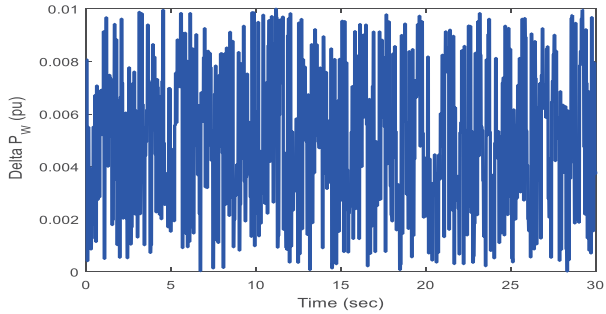

Fig. 9. Random change of wind side power (wind speed)

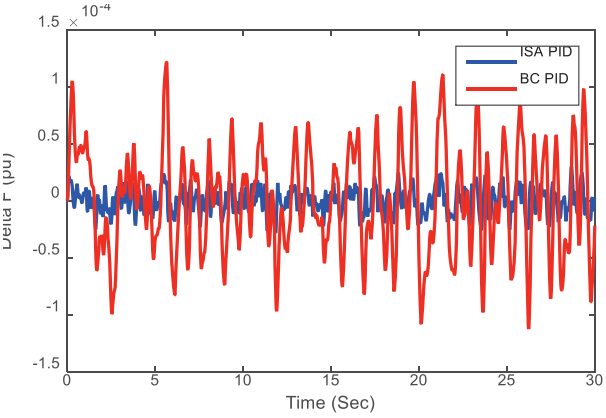

Fig. 10. System frequency response under random change in wind side power

6 Conclusion

In this paper, optimal PID controller design for the frequency control of a wind-diesel hybrid system, is formulated as an optimization problem and solved using Interior Search Algorithm (ISA). The results of the proposed method compared with Bee Colony algorithm. In order to prove the performance of proposed method, simulation carried out in four cases, step change in load of diesel side, step change in wind speed, random changing of the diesel side load, and random changing of the wind speed. Simulation results show that the ISA-based PID controller (ISA-PID) has better performance in compared with BC-based PID controller (BC-PID) from the perspective of the response to step change in load demand of diesel side, step change in wind speed. Also, two performance indices according to system defined and with overshoot, undershoot, and settling time calculated for both ISA-PID and BC-PID controllers, which proves that the proposed ISA-PID controller is very effective and robust compare to BC-PID controller.

References

[1] D. Hayashi, T. Senjyu, R. Sakamoto, N. Urasaki, T. Funabashi and H. Sekine, "Generating power leveling of renewable energy for small power system in isolated island," in *Intelligent Syst Application to Power Syst Conf*, Arlington, VA, 2005.

[2] M. Carmeli, F. C. Dezza, M. Mauri, G. Marchegini and D. Rosati, "Control strategies and configurations of hybrid distributed generation systems," *Renew Energy,* vol. 41, pp. 294-305, 2012.

[3] R. B. Bagen, "Evaluation of different operating strategies in small standalone power systems," *IEEE Trans Energy Convers,* vol. 20, no. 3, pp. 654-60, 2005.

[4] C. Wang and H. Nehrir, "Power management of a stand-alone wind/photovoltaic/fuel cell energy system," *IEEE Trans Energy Conv,* vol. 23, no. 3, pp. 957-967, 2008.

[5] R. Pena, R. Cardenas, J. Proboste, J. Clare and G. Asher, "Wind-diesel generation using doubly fed induction machines," *IEEE Trans. on Energ. Conv.,* vol. 23, no. 1, pp. 202-2014, 2008.

[6] V. Singh, S. Mohanty, N. Kishor and P. Ray, "Robust H-infinity load frequency control in hybrid distributed generation system," *Int J Electr Power Energy Syst,* vol. 46, pp. 294-305, 2013.

[7] A. Perera, R. Attalage, K. Perera and V. Dassanayake, "A hybrid tool to combine multi-objective optimization and multi-criterion decision making in designing standalone hybrid energy systems," *Appl Energy,* vol. 107, pp. 412-425, 2013.

[8] C. Nandar, "Robust PI control of smart controllable load for frequency stabilization of microgrid power system," *Renew Energy,* vol. 56, pp. 16-23, 2013.

[9] T. S. Bhatti, A. A. F. Al-Ademi and N. K. Bansal, "Load frequency control of isolated wind diesel hybrid power systems," *Energy Conversion and Management,* vol. 38, no. 9, pp. 829-837, 1997.

[10] W. Gu, W. Liu, C. Shen and Z. Wu, "Multi-stage under frequency load shedding for islanded microgrid with equivalent inertia constant analysis," *Int J Electr Power Energy Syst,* vol. 46, pp. 36-49, 2013.

[11] N. Mendis and K. Muttaqi, "An integrated control approach for standalone operation of a hybridised wind turbine generating system with maximum power," *Int J Electr Power Energy Syst,* vol. 49, pp. 339-348, 2013.

[12] R. Hooshmand and M. Moazzami, "Optimal design of adaptive under frequency load shedding using artificial neural networks in isolated power system," *Int J Electr Power Energy Syst,* vol. 42, no. 1, pp. 220-238, 2012.

[13] Y. Wang, F. Ronilaya, X. Chen and A. Roskilly, "Modelling and simulation of a distributed power generation system with energy storage to meet dynamic household electricity demand," *Appl Thermal Eng,* vol. 50, no. 1, pp. 523-535, 2013.

[14] I. Ngamroo, "Robust coordinated control of electrolyzer and PSS for stabilization of microgrid based on PID-based mixed H2/H$_\infty$ control," *Renew Energy,* vol. 45, pp. 16-23, 2012.

[15] M. N. Anwar and S. Pan, "A frequency response model matching method for PID controller design for processes with dead-time," *ISA Transactions,* vol. 55, pp. 175-187, 2015.

[16] Amir H. Gandomi, "Interior search algorithm (ISA): A novel approach for global optimization," *ISA Transactions,* vol. 53, pp. 1168-1183, 2014.

[17] T. Chayatman, I. Ngamroo, S. Pothiya and S. Vachirasricirikul, "Design of optimal fuzzy logic-PID controller using bee colony optimization for frequency control in an isolated wind-diesel system," in *Transmission & Distribution Conference & Exposition: Asia and Pacific*, Seoul, 2009.

Biographies

Hossein Shayeghi received the B.S. and M.S.E. degrees in Electrical and Control Engineering in 1996 and 1998, respectively. He re ceived his Ph.D. degree in Electrical Engineering from Iran University of Science and Technology, Tehran, Iran in 2006. Currently, he is a full Professor in Technical Engineering Department of University of Mohaghegh Ardabili, Ardabil, Iran. His research interests are in the application of robust control, artificial intelligence and heuristic optimization methods to power system control design, operation and planning and power system restructuring. He has authored and co-authored of 5 books in Electrical Engineering area all in Farsi, one book and two book chapters in international publishers and more than 330 papers in international journals and conference proceedings. Also, he collaborates with several international journals as reviewer boards and works as editorial committee of three international journals. He has served on several other committees and panels in governmental, industrial, and technical conferences. He was selected as distinguished researcher of the University of Mohaghegh Ardabili several times. In 2007 and 2010 he was also elected as distinguished researcher in engineering field in Ardabil province of Iran. Furthermore, he has been included in the Thomson Reuters' list of the top one percent of most-cited technical Engineering scientists in 2015 and 2016, respectively. Also, he is a member of Iranian Association of Electrical and Electronic Engineers (IAEEE) and senior member of IEEE.

Heidar Ali Shayanfar received the B.S. and M.S.E. degrees in electrical engineering in 1973 and 1979, respectively. He received the Ph.D. degree in electrical engineering from Michigan State University, East Lansing, MI, USA, in 1981. Currently, he is a Full Professor with the Department of Electrical Engineering, Iran University of Science and Technology, Tehran, Iran. His research interests are in the application of artificial intelligence to power system control design, dynamic load modeling, power system observability studies, voltage collapse, congestion management in a restructured power system, reliability improvement in distribution systems, smart grids and reactive pricing in deregulated power systems. He has published more than 520 technical papers in the international journals and conferences proceedings.
Dr. Shayanfar is a member of the Iranian Association of Electrical and Electronic Engineers
.

Abdollah Younesi received B.S and M.S.E degrees both in Electrical Engineering from Faculty of Technical Eng. Department of the Mohaghegh Ardabili University, Ardabil, Iran in 2012 and 2015 respectively. Currently He is a PhD. student in Technical Eng. Department of the University of Mohaghegh Ardabili, Ardabil, Iran. His area of interest are application of artificial intelligence in power system automation and control, application of Reinforcement Learning to power system control, Fuzzy Systems, Heuristic optimization in power system control. He is a student member of Iranian Association of Electrical and Electronic Engineers (IAEEE) and IEEE.

GA-based MATLAB® Simulation to the Design Optimization of a New Overboarding Prototype with 2-DOF Mechanism including a Parallelogram Link

A. Seonk Hak Park[1], **B. Won Jee Chung**[2], **C. Hyo Gon Kim**[2]
[1]School of Mechatronics, Changwon National University, Changwon, The Republic of Korea
[2]Field Robotics R&D Division, Korea Institute of Robot and Convergence, Pohang, The Republic of Korea

Abstract *- Cranes are used in general to lift or load equipment or materials. The present paper delves into a tool used for drop/lift the sonar system for undersea exploration. This paper deals with a GA-based MATLAB® simulation to the design optimization of a new overboarding prototype with 2-DOF mechanism including a parallelogram link which is efficient in operation and maintenance of the sonar system. An active/passive sonar system consists of 1) a transmitter towing cable for adjusting the depth of the transmitter towed body, 2) a receiving array for measuring sound waves, 3) a transmitter towed body for transforming sound waves and 4) an array cable for connecting a receiving array to a transmitter towed body. There is a need to develop an automated equipment to drop the active/passive sonar system into the deep sea from the surface ship and then lift it, since this consists of a cable with a length of over 1000m, a transmitter towed body, etc. With the research on the active/passive sonar system, a variety of mechanisms of the overboarding unit suitable for the limited environments have been developed. First, we analyzes the strengths and weaknesses of the existing overboarding mechanisms, and then suggest a new mechanism to improve these problems. For the proposed mechanism, we will treat with the GA-based MATLAB® simulation technique to optimize the link length and the actuator length for the mechanism not to interfere in the hull's internal environment, to satisfy work ROM (Range of Motion) and to have good torque-angle properties. Our approach will be helpful for calculating the maximized output torque of the actuator for the actual application of a similar type of the proposed mechanism in practice.*

Keywords: GA (Genetic Algorithm)-based MATLAB® Simulation, Drop/Lift of Sonar System, Overboarding Mechanism, Parallelogram Link, ROM (Range Of Motion), Optimization.

1 Introduction

Cranes are used in general to lift or load equipment or materials. On construction, ship-building, container loading, underwater robot deployment/refloating sites, cranes are used for diverse purposes. The present paper delves into a tool used for deploying/refloating the sonar system for undersea exploration.

After the Second World War, the reexamination of surface ship's sonar for anti-submarine operation execution began and thereby the research and development of low-frequency active/passive sonar has been continued for the past 20 years. Submarine attempts an attack by approaching a surface ship, based on its high concealable capability and approaches a surface ship using the shadow zone which sound waves are not properly transmitted, operating in the deep sea. To deal with this situation, not a hull-mounted sonar, an active/passive variable depth sonar of a surface ship is being researched and developed for capturing submarines in the shadow zone. Starting with the development of ATAS (Active Towed Array Sonar) by British Aerospace, England in 1982, this type of sonar is being researched and developed in Germany, France and the U.S. [1].

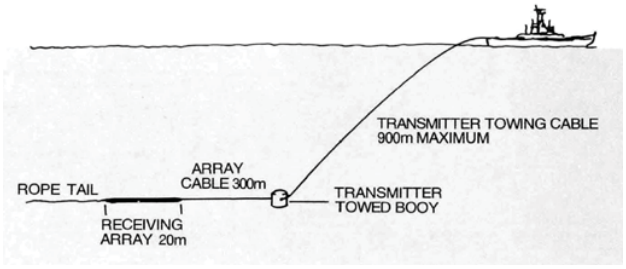

Fig. 1 Structure of the active/passive sonar system [1]

An active/passive sonar system consists of 1) a *transmitter towing cable* for adjusting the depth of the transmitter towed body, 2) a *receiving array* for measuring sound waves, 3) a *transmitter towed body* for transforming sound waves and 4) an *array cable* for connecting a receiving array to a transmitter towed body, as shown in Fig. 1 [1]. There is a need to develop an *automated equipment* to drop the active/passive sonar system into the deep sea from the surface ship and then lift it, since this consists of a cable with a length of over 1000m, a transmitter towed body, *etc*. A drop/lift automated equipment of the active/passive sonar system consists of a winch for coiling a transmitter towing cable, a rope tail, a receiving array, a winch for coiling an array cable and an overboarding unit for dropping and lifting a transmitter towed body.

With the research on the active/passive sonar system, a variety of mechanisms of the overboarding unit suitable for the limited environments have been developed. But the

existing overboarding mechanisms should be installed outside the hull. Moreover their operation and maintenance is hard, because they use a number of actuators within their complex structure. This paper suggests a new overboarding mechanism which is efficient in operation and maintenance of the sonar system. First, section 2 analyzes the strengths and weaknesses of the existing overboarding mechanisms, and section 3 suggests a new mechanism to improve these problems. Section 4 deals with the GA (Genetic Algorithm) - based method where MATLAB® is used to optimize the lengths of links and actuators with a view to gaining good torque-angle characteristics whilst meeting the ROM (Range of Motion) without interfering with the interior environment of the hull based on the proposed mechanism.

2 Overboarding mechanisms

Figure 2 expresses the ship's indoor space to install the overboarding unit (or mechanism), considering its operation. The indoor space is 4m (width) × 6m (depth) × 2.2m (height) where the height from the deck to the sea surface is 1.8m. ACTAS [2], CAPTAS [3] and ALOFTS [4] are representative (existing) overboarding units.

ACTAS unit is a *1 link type with 4-bar linkage*, so there are a small number of actuator powerpacks and controls by using only one actuator for operating a link structure. Especially none of singular configurations (or *singularities*) occurs, since the link structure is designed to operate within an angle of 180 degrees using a 4-bar linkage. Though there is no limitation in height, since this unit is installed outdoors, its installed height from the sea surface varies depending on the kinds of ships, In particular, for a high surface ship, the link of ACTAS overboarding mechanism needs to be lengthened to lower down the sonar system to the sea surface using only one link. Besides, connecting the cable to the towed body is quite dangerous, because the sonar system doesn't come inside the ship.

CAPTAS unit can be characterized as a 1 link installed on a sliding mechanism. As shown in Fig. 4, the sliding unit has an additional space for the link structure to come inside the ship. Thus it is possible to connect the array cable to the towed body safely inside the ship. Even though this unit is installed indoors, there is no limitation in height because the actuator for operating the link structure works like a *lever*. Besides, similarly as ACTAS, none of singular configurations (or *singularities*) occurs because the link structure is designed to operate within an angle of 90 degrees. But the link needs to be lengthened in order to reach the sea surface, as well as the number of controls being increased, compared to ACTAS type, since there is a need to control the sliding unit, in addition to the actuator. ALOFTS unit is upgraded as a *2 link type* to overcome the weakness to lengthen the link of ACTAS mechanism. Therefore, this is free from the height limit. But two actuators are required to operate two links, which means the number of controls increases and for cutting load while multi-joints are used, remodeling including digging a deck is needed.

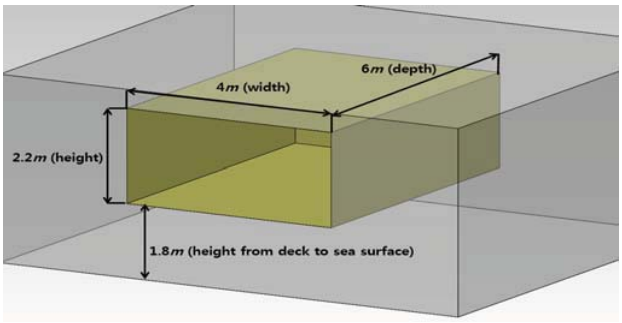

Fig. 2 Installation space of the overboarding mechanism


Fig. 3 Overboarding unit of ACTAS [2]


Fig. 4 Overboarding unit of CAPTAS [3]

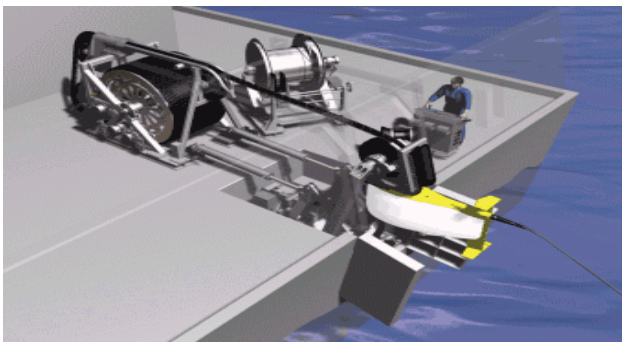
Fig. 5 Overboarding unit of ALOFTS [4]

3 Design of new proposed mechanism

The efficient operation and maintenance of the sonar system can be significantly improved by developing an overboarding unit that can be installed inside without altering the hull structure and can store the sonar system in its entirety. This paper proposes a mechanism featuring the foregoing advantages as in Fig. 6.

The proposed overboarding unit is based on the mechanism using a parallelogram-link and designed to send down the equipment to the maximum extent possible without tampering with the ceiling inside the hull. Two actuators are used to drive the proposed unit. As the existing 2-link mechanism of ALOFTS [4] is based on two actuators, this can be subject to the ceiling height limits. For ALOFTS's mechanism, the second link should be pulled backward to store the towed body inside the hull once the towed body is refloated. To fully store the sonar equipment including the towed body by pulling the second link backward, the ROM that the second link needs to meet should increase. If the ROM increases too much, it may be impossible to fully store the sonar equipment. *To make up for the foregoing drawback, the parallelogram-link is designed to fully store the sonar equipment by extending the sub-actuator and thus having the sub-links cross and go inside instead of pulling the second link backward after refloating.*

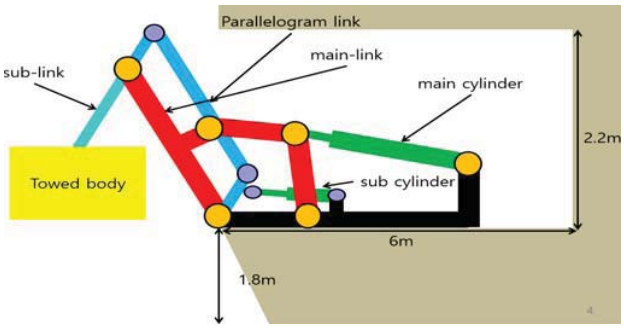

Fig. 6 Simple model of new overboarding mechanism

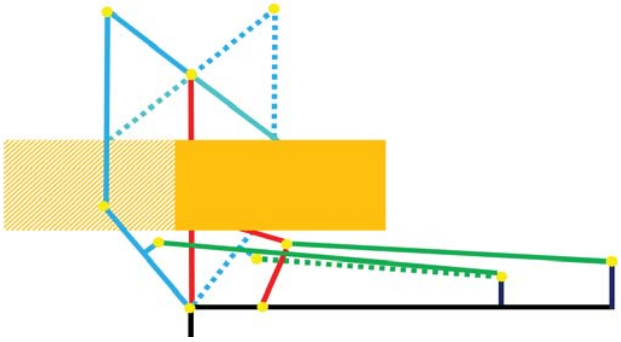

Fig. 7 Configuration of Mechanism in which parallelogram-link and main-link intersect at 90º

For the proposed 2-DOF (Degrees of Freedom) mechanism with a parallelogram, the sub-link in Fig. 6 intersects as shown in Fig. 7 while the main-link is pulled up and held at $\theta_1 = 90^\circ$ (θ_1 is indicated Fig. 8.) In this figure, the solid lines denote the configuration of the mechanism just before intersecting, while the dotted lines denote the configuration of the mechanism just after intersecting. The parallel link connected to the sub-cylinder measures 0.5m. To meet the ceiling height of 2.2m, the main-link measures 1.7m in length (when the main-link is pulled up and held at 90º, the length of main-link (1.7m) comes from the fact : the ceiling height (2.2m) – the parallel link length (0.5m)). Also, when the towed body measures 1.1m in height, its sub-link measures 0.6m in length (the length of sub- link = the length of main-link (1.7m) - the height of the towed body (1.1m)).

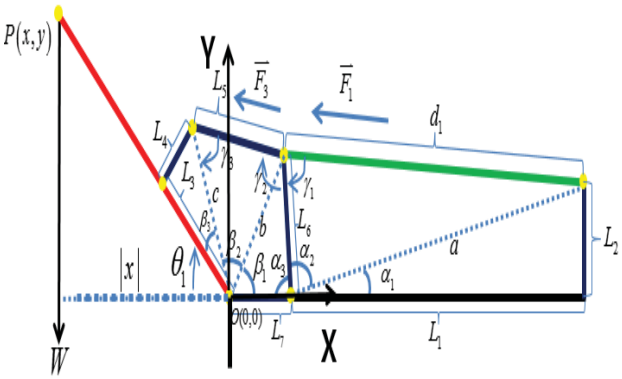

Fig. 8 Schematic drawing and kinematic parameters of main-link

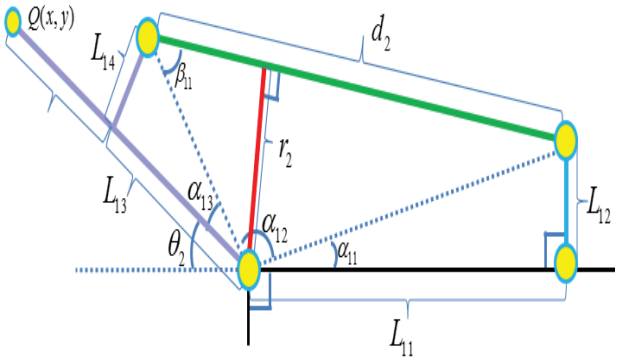

Fig. 9 Schematic drawing and kinematic parameters of parallelogram-link

Figures 8 and 9 are generalized schematic diagrams for kinematic analysis of the main-link in the new mechanism and the parallelogram-link, respectively. In Figs. 8 and 9, *d* denotes the length of the *hydraulic actuator*.

3.1 Kinematic analysis of main-link

The angle θ_1 of the link mechanism depending on the change of d_1, given by Eq. (1), is shown in Fig. 8.

$$\theta_1 = \frac{3}{2}\pi - \beta_1 - \beta_2 - \beta_3 \quad (1)$$

where

$$\beta_1 = \cos^{-1}\left(\frac{a^2 + L_7^2 - L_6^2}{2aL_7}\right)$$

$$\beta_2 = \cos^{-1}\left(\frac{a^2 + L_3^2 + L_4^2 - L_5^2}{2a\sqrt{L_3^2 + L_4^2}}\right)$$

$$\beta_3 = \tan^{-1}\left(\frac{L_4}{L_3}\right)$$

wherein

$$a = \sqrt{L_6^2 + L_7^2 - (2L_6L_7)\cos\alpha_3}$$

$$\alpha_3 = 180 - \alpha_1 - \alpha_2$$

$$\alpha_1 = \tan^{-1}\left(\frac{L_2}{L_1}\right)$$

$$\alpha_2 = \cos^{-1}\left(\frac{L_1^2 + L_2^2 + L_6^2 - d_1^2}{2L_6\sqrt{L_1^2 + L_2^2}}\right)$$

The torque arm regarding the actuator length is shown by Eq. (2) :

$$r_1 = \frac{c\sin\gamma_1\sin\gamma_3}{\sin\gamma_2} \quad (2)$$

where

$$\gamma_1 = \cos^{-1}\left(\frac{d_1^2 + L_6^2 - a^2}{2d_1L_6}\right)$$

$$\gamma_2 = 360 - \alpha_3 - \beta_1 - \beta_2 - \gamma_3$$

$$\gamma_3 = \cos^{-1}\left(\frac{L_5^2 + c^2 - b^2}{2cL_5}\right)$$

Then the output torque (τ_1) of the main-actuator is given as follows:

$$\tau_1 = W \cdot r_1 \quad (3)$$

where W denotes the weight of the towed body. Now the installation position of the towed body, $P(x,y)$, with respect to the Cartesian coordinates (X, Y) (of which origin is located at O) in Fig. 8, can be obatined as follows:

$$P(x) = -(1.7)\cos\theta_1 \quad (4a)$$

$$P(y) = (1.7)\sin\theta_1 \quad (4b)$$

3.2 Kinematic analysis of parallelogram-link

In Fig. 9, the angle of the parallel link (θ_2) relative to the changing length of d_2 is expressed by the following Eq. (5).

$$\theta_2 = \pi - \alpha_{11} - \alpha_{12} - \alpha_{13} \quad (5)$$

where

$$\alpha_{11} = \tan^{-1}\left(\frac{L_{12}}{L_{11}}\right)$$

$$\alpha_{12} = \cos^{-1}\left(\frac{L_{11}^2 + L_{12}^2 + L_{13}^2 + L_{14}^2 - d_2^2}{2\sqrt{L_{11}^2 + L_{12}^2}\sqrt{L_{13}^2 + L_{14}^2}}\right)$$

$$\alpha_{13} = \tan^{-1}\left(\frac{L_{14}}{L_{13}}\right)$$

Notice that L_{11}, L_{12}, L_{13}, L_{14}, and d_2 are indicated in Fig. 9. The torque arm regarding the actuator length is shown by Eq. (6) :

$$r_2 = \sqrt{L_{13}^2 + L_{14}^2}\sin\beta_{11} \quad (6)$$

where

$$\beta_{11} = \cos^{-1}\left(\frac{L_{13}^2 + L_{14}^2 + d_2^2 - L_{11}^2 - L_{12}^2}{2d_2\sqrt{L_{13}^2 + L_{14}^2}}\right)$$

Then the output torque (τ_2) of the sub-actuator is given as follows:

$$\tau_2 = W \cdot r_2 \quad (7)$$

Figures 10 and 11 show the angles the parallelogram-link should meet. Fig. 10 shows the angle of the parallel link (δ) for $d_{1\max}$ (when the equipment is sent down to the sea level). Fig. 11 shows the angle of the parallel link (ζ) for $d_{1\min}$ (when the equipment is sent into the hull). The angle of the parallelogram-link is found by optimizing the length of the main-link. $R(x, y)$ is expressed in Eq. (8) to yield δ, while $S(x, y)$ is expressed in Eq. (9) to yield ζ :

$$R(x) = P_x - (0.6)\cos(\delta) \quad (8a)$$

$$R(y) = P_y - (0.6)\sin(\delta) \quad (8a)$$

$$S(x) = P_x + (0.6)\cos(\zeta) \quad (9a)$$

$$S(y) = P_y - (0.6)\sin(\zeta) \quad (9a)$$

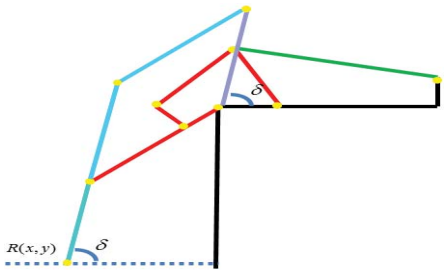

Fig. 10 The angle of parallelogram-link when the equipment is sent down to the sea level

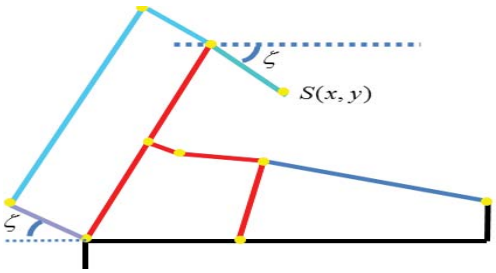

Fig. 11 The angle of parallelogram-link when the equipment is sent into the hull

4 Optimizing simulation of proposed mechanism

4.1 Simulation of main-link optimization

The link lengths (L_1, L_2, L_3, L_4, L_5, L_6, L_7, δ, ζ) and the actuator rod length (d_1) should be optimized for the proposed machanism not to interfere with the hull's internal environment, so as to satisfy work ROM and to have good torque-angle properties. The design variables of the proposed mechanism are as follows:

$$V = \{L_1, L_2, L_3, L_4, L_5, L_6, L_7, \delta, \zeta, S_1\} \tag{10}$$

Here, S indicates a value of the actuator stroke. When the absolute value of x given by Eq. (4a) is maximized, the load torque depending on the weight of the towed body reaches the maximum value. Now the torque arm (r_1) of the actuator can be set as an objective function, as shown in Eq. (11), in order to induce the maximized output torque (τ_1) of the main-actuator.

$$f = r_1\{L_1, L_2, L_3, L_4, L_5, L_6, L_7, \delta, \zeta, d_1\} \tag{11}$$

where

$$d_1 = d_1(\max(|x|))$$

Here, $d_1(\max(|x|))$ means the variable d_1 which maximizes the absolute value of x. More specific, d can be a function of S (the stroke length of the actuator). Especially the minimum value of d, *i.e.*, $d_{\min}$, and the maximum value of d, *i.e.*, $d_{\max}$, can be assigned by Eq. (12). Here the constant C_b was set at 0.3m as a default value not to be included in S.

$$\begin{aligned} d_{\min} &= S + C_b \\ d_{\max} &= 2S + C_b \end{aligned} \tag{12}$$

To avoid interference with the hull as well as satisfying the required drop/lift jobs of the towed body assuming the indoor placement of the proposed mechanism, a constraint function can be defined by Eqs. (13) to (17). Especially the height from the inner deck to the ceiling, the distance from the inner deck to the sea surface and the sideview (X × Y) size of the towed body were set at 2.2m, 1.8m and (2.0m × 1.1m), respectively. In detail, the equality constraint function for the towed body to reach the sea surface is shown in Eq. (13).

$$C_{eq} = R(y) = -1.8 \tag{13}$$

where

$$d_1 = d_{1\max}$$

The equality constraint function for the towed body to enter the hull is as in the Eq. (14) :

$$C_{eq} = S(x) = 1.1 \tag{14}$$

where

$$d_1 = d_{1\min}$$

The equality constraint function to place the towed body on the floor inside the hull for refloating is as in Eq. (15) :

$$C_{eq} = S(y) = 1.1 \tag{15}$$

where

$$d_1 = d_{1\min}$$

The inequality constraint function to prevent the deployed towed body from touching the hull is as in Eq. (16) :

$$C_{ineq} = R(x) < -1.1 \tag{16}$$

where

$$d_1 = d_{1\max}$$

Finally, the inequality constraint function to prevent the main-link from touching the hull once the towed body is deployed is as in Eq. (17) :

$$C_{ineq} = P(x) < 0 \tag{17}$$

where

$$d_1 = d_{1\max}$$

Using MATLAB® genetic algorithm (GA) method [5], 10 design variables of V given by Eq. (11) are optimized. In comparison to the existing method [6] to find the optimum value by relying on the starting point, the GA method has a high possibility of finding the global optimum value [7]. The optimized design variables are obtained as shown in TABLE I When the optimized design variables listed in TABLE I are applied to Eqs. (2), (4a) & (4b), (8a) & (8b) and (9a) & (9b), the results are shown in Figs. 12, 13, and 14, respectively. Figure 12 shows the changing position of P, which is the end-effector of the main cylinder, relative to the changing length of the cylinder load. For $d_{1\max}$, P(x) is -1.7m, which meets the constraint Eq. (17). The torque arm relative to the load arm is plotted on the graph of Fig.13, where the maximum torque arm is 0.44m, which can be used for calculating the maximized output torque of the actuator by using Eq. (3). Figure 14 shows the end-points when the towed body is sent down and pulled up. When it is sent down to the sea level, the

value of x is -1.385m, which meets Eq. (16), whilst the value of y is -1.8m, which meets the formula (13). When it is pulled up inside the hull, the value of x is 1.1m, which meets the Eq. (14), whilst the value of y is 1.1m, which meets the Eq. (15).

Table I Optimized degign variables of main-link using GA

Design variables	Optimal value
L_1 (m)	1.83
L_2 (m)	0.46
L_3 (m)	0.31
L_4 (m)	0.17
L_5 (m)	0.69
L_6 (m)	0.63
L_7 (m)	0.39
ζ (rad)	1.18 (67°)
δ (rad)	0.84 (48°)
S_1 (m)	0.96

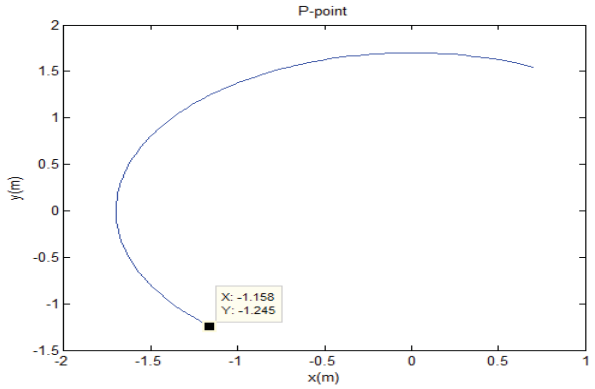

Fig. 12 Position changes of $P(x,y)$ point

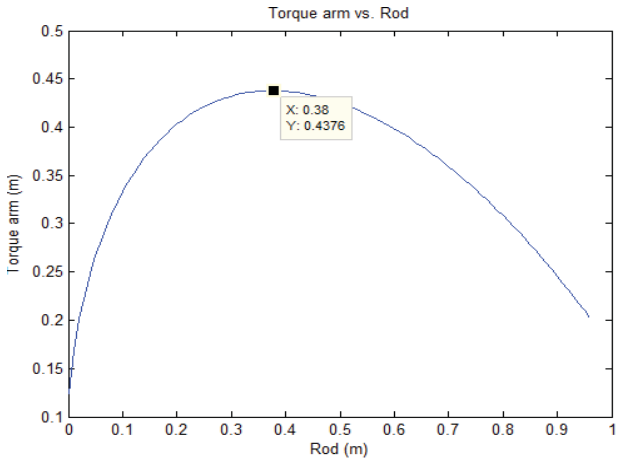

Fig. 13 Torque arm (r) according to actuator length (d)

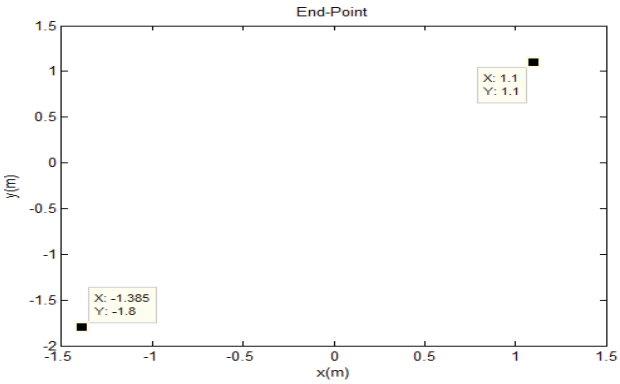

Fig. 14 End point of the mechanism

4.2 Optimization of parallelogram-link

The length of the link and that of the actuator load optimized to operate within ROM ($\delta \sim \zeta$) of the parallelogram-link are yielded in the following. First, the design variables of the link structure are set as follows:

$$V = \{L_{11}, L_{12}, L_{13}, L_{14}, S_2\} \tag{18}$$

When the link structure is maximally unfolded ($d_{2\max}$), the maximum torque occurs, when the torque arm (r_2) is induced to be maximized by applying the objective function in Eq. (19) :

$$f = r_2\{L_{11}, L_{12}, L_{13}, L_{14}, d_2\} \tag{19}$$

where

$$d_2 = d_{2\max}$$

The constraint function for the parallel link to meet the angle δ is as in Eq. (20) :

$$C_{eq} = \theta_2(1) = \pi - \delta = \pi - 1.18(rad) = \pi - 67^\circ = 113^\circ \tag{20}$$

where

$$d_2 = d_{2\min}$$

The constraint function for the parallel link to meet the angle ζ is as in Eq. (21) :

$$C_{eq} = \theta_2(end) = \zeta = 0.84(rad) = 48^\circ \tag{21}$$

where

$$d_2 = d_{2\max}$$

The given 5 design variables are optimized using MATLAB's GA method in Eq. (18), and the results are presented in TABLE II. Figure 15 shows the optimized results applied to the design variables and indicates the torque arm relative to the load arm.

Table I Optimized degign variables of parallelogram-link using GA

Design variables	Optimal value
L_{11} (m)	1.49
L_{12} (m)	0.23
L_{13} (m)	0.49
L_{14} (m)	0.21
S_2 (m)	0.7

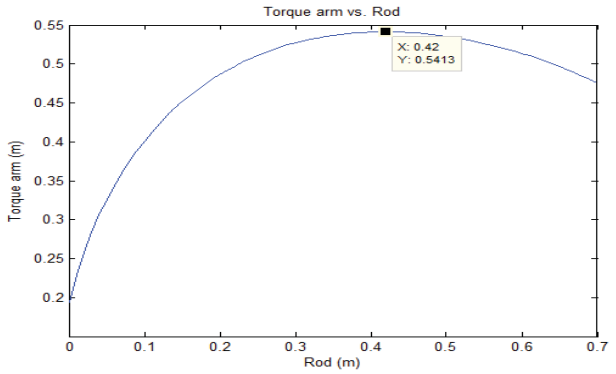

Fig. 15 Torque arm (r) according to actuator length (d)

5 Conclusion

This paper deals with the GA-based MATLAB® *simulation* to the design *optimization* of a new overboarding prototype with 2-DOF mechanism including a parallelogram link, which is an automated equipment to drop the active/passive sonar system into the deep sea from the surface ship and then lift it. First, we have analysed the strengths and weaknesses of the existing overboarding mechanisms about installation location, operating mechanism and ROM. Based on this analysis, we have suggested a new overboarding mechanism which is efficient in operation and maintenance of the sonar system. For the proposed mechanism, using the genetic algorithm (GA), we have optimized the link length and the actuator length not to interfere with the hull's internal environment, to satisfy work ROM and to have good torque-angle properties. The design variables of the proposed overboarding mechanism have satisfited 1) the limited height from the inner deck to the ceiling, 2) the height from inner deck to sea surface, and 3) the condition of the sonar system to come indoors. It is anticipated that applying the presented mechanism would bring a big advantage to sailor's safety, work efficiency, maintenance and production cost, compared to the existing mechanism. Fuerthermore, our approach will be helpful for calculating the maximized output torque of the actuator for the actual application of a similar type of the proposed mechanism in practice.

6 References

[1] U. H. Kim, "An Reality and Development prospect of the Sonar in Surface Ship" Journal of Defence Technology, 1995
[2] http://navaltoday.com/2013/12/20/atlas-elektronik-to-supply-sonar-for-royal-thai-navys-new-frigate/
[3] http://navalanalyses.blogspot.kr/2014/08/bergamini-class-fremm-frigates-of.html
[4] http://www.odimspectrum.com/newsroom.php
[5] http://kr.mathworks.com/help/gads/performing-a-genetic-algorithm-optimization.html
[6] http://kr.mathworks.com/help/optim/ug/fmincon.html
[7] H.G.Kim, S.D.Park and C.S.Han, "Design of novel knee joint for an exoskeleton with good energy efficiency for load-carrying augmentation" Journal of Mechanical Science and Technology 28, 2014
[8] https://www.thalesgroup.com/en/worldwide/defence/naval-forces/underwater-warfare/anti-submarine-warfare-surface-ships/captas-4-variable-depth-sonar
[9] Stormy attaway. "A practical introduction to programming and problem solving", A-jin, 2013
[10] https://www.atlas-elektronik.com/what-we-do/anti-submarine-warfare/actas/

Wind Power Prediction Model based on Hybrid Strategy

H. A. Shayanfar[1] *, O. Abedinia [2], N. Amjady[3], Saman Rajaei[2]
[1]Department of Elec. Engineering, College of Tech. and Engineering, South Tehran Branch, Islamic Azad University, Tehran, Iran
[2]Department of Electric Power Engineering Budapest University of Technology and Economics, Budapest, Hungary
[3]Department of Electrical Engineering, Semnan University, Semnan, Iran

hashayanfar@gmail.com, oveis.abedinia@gmail.com, n_amjady@yahoo.com, saman_persis_rj@yahoo.com

Abstract - *By growing the integration of wind farms into electric power grids based on its uncertain nature an accurate prediction model is demanded for the operation of these power plants. This paper proposed a new forecasting model for wind power prediction. In this model, the Fully Complex valued Wavelet Network (FCWN) for forecasting the wind power generation is proposed. The proposed approach is started by filtering the wind signal through the feature selection. Then, the new forecast engine based on FCWN and an intelligent algorithm predicts the wind power signal. Furthermore, proposed algorithm improves the training mechanism of forecast engine. Finally, the proposed wind power forecasting model is tested with real-world hourly data of wind farms in Spain and Alberta, Canada. In order to demonstrate the validity of the proposed model, it is compared with several other wind speed and power forecast techniques. Obtained results confirm the validity of the developed approach.*

Keywords: Wind Power Forecast, Complex Valued Wavelet Network, Learning Algorithms.

1 Introduction

Along with fire and moving water, wind was one of the first of nature's forces to be harnessed by man. Wind was not just utilized on the water, though. Several centuries after the invention of the sail, vertical-axis windmills (windmills rotating around a vertical line, like a carousel) in Persia began to grind rain and lift water out of streams for irrigation in the 10th century [1]. Recently, wind energy application is growing in Europe, particularly in Denmark and Germany where many European manufacturers were, and still are, important suppliers of wind turbine equipment. While California was the leader in U.S. wind energy until 2006, Texas would overtake it and move on to a commanding lead, with approximately 3 times the connected capacity of California at the end of 2011 [2]. Much of Texas' explosive growth may be attributed to the fortunate circumstance that one of its biggest and most dense wind resource areas is bisected by one of its largest electrical transmission lines.46 Aggressive state programs to build transmission capacity in areas most likely to motivate wind power improvement also attracted development. Similarly, access to transmission and a supportive policy environment have supported Iowa overtake California to become the second largest wind power state in the U.S [3].

According to important role of this energy in operation of power system, an accurate prediction model is demanded. So, recently several prediction models have been proposed. Some of the proposed models can be described as; Auto-Regressive Moving Average (ARMA) models [4, 5], Fractional ARIMA (FARIMA) model [6], Auto-Regressive Integrated Moving Average (ARIMA) model [7], NN-based forecast engine in [8], combination of differential Empirical Mode Decomposition (EMD) and Relevance Vector Machine (RVM) in [9] for prediction of short-term wind power output, two Neural Network (NN) based models in [10], combination of nonparametric and time-varying regression and time-series model, i.e. Holt–Winters and ARMA in [11], and Hybrid Iterative Forecast Method (HIFM) in [12] based on two stage feature selection model. Although the mentioned approaches are simple and strong forecasting methods and can be easily implemented, most of the predictors are linear, however, wind power signal is a no convex and a non-linear signal.

Recently the Complex-Valued Neural Networks (CVNNs) have proved their abilities for the identification of nonlinear systems [13]. They have obtained this ability from that nature of having the possibility of simultaneous modeling and forecasting [13, 14, 15]. The main motivation to use CVNNs is its fast convergence, reduction in learning parameters and ability to learn 2 dimensions motion of signal in complex valued neural network [16]. The nature of the CVNNs obliges the neural network world to divide into two poles, the first use the split complex valued functions. This strategy keeps the complex valued form apparently but the neurons inside the network treat the data as two real valued parallel neurons. In this work, the fully complex valued wavelet network (FCWN) with a new wavelet activation function is proposed to forecast the wind power.

So, the contributions of this paper can be summarized as follows;

- ✓A new feature selection has been presented for selecting the features of wind power features based on high relevancy and low redundancy.

* Correspanding Author: hashayanfar@gmail.com (H. A. Shayanfar)

✓A new prediction model based on fully complex valued wavelet network has been implemented to predict the wind power with high accuracy.

2 The Proposed Feature Selection

2.1 Input Set Structure

First of all, it is very important to recognize the construction and behavior of input signal (here the wind power) in prediction process. Accordingly, a bulk candidate set of input features is structured considering the statistical behavior of the wind signal. Considering such a more set of signal enables us to employ the maximum information value of the available data such that no likely informative and benefit feature is missing. But, the large number of these features cannot be useful directly for using in forecast engine. Hence, these features should be filtered by appropriate filter named feature selection.

As the mentioned this energy can be seen as a nonlinear mapping function of several exogenous meteorological variables as well as their past values. By the past and forecast values of variables, such as wind speed, direction, temperature, and humidity are available at the wind farm place or a weather station near to the wind farm, a set of selected features (inputs), say $S(t)$, can be constructed as:

$S(t) = \{WP(t\text{-}1), \ldots, WP(t\text{-}N_{WP}), WS(t), WS(t\text{-}1), \ldots, WS(t\text{-}N_{WS}), WD(t), WD(t\text{-}1), \ldots, WD(t\text{-}N_{WD}), T(t), T(t\text{-}1), \ldots, T(t\text{-}N_T), H(t), H(t\text{-}1), \ldots, H(t\text{-}N_H)\}$ (1)

Where, $WP(t)$, $WS(t)$, $WD(t)$, $T(t)$ and $H(t)$ define the wind power, speed, direction, temperature and humidity at time interval t, respectively. The time interval belongs the desired forecasting step; for example, in hourly wind prediction, t is scaled based on hour. The selected input features $WP(t\text{-}1), \ldots, WP(t\text{-}N_{WP})$ in (1), are the historical data of wind power. $WS(t)$, is the prediction value of wind speed for time interval t and $WS(t\text{-}1), \ldots, WS(t\text{-}N_{WS})$ are its past amounts, based on this fact that wind speed is an important driver for wind power. Finally, for using the presented signal directly for forecast engine based on filtering the features, a minimum set of the most informative features will be selected based on the proposed feature selection method as described in the following;

2.2 Hybrid Feature Selection

According to the special conditions in SR forecasting problem, occasionally we encounter with many attributes whereas some of them no longer have helpful data and just complex the situation. Hence, feature selection is one of the very critical aspect that has a highly regarded recommendation [17]. This section introduce, a new feature selection which have greater effect on risk and return and appropriate analysis of algorithms results a novel feature selecting method in two stages is established. In this problem we deal with so many features that are either useless or have low information value. So, dealing with these features is time wasting except any good results. Feature selection methods are generally categorized into 3 main groups as: (1) filter methods, (2) wrapper methods, and (3) hybrid methods [18]. In this paper we applied a hybrid method based on mixing the filter and function-based clustering model to extract a set of effective features.

2.3 Filter model

As the mentioned in [17], seven algorithms have been defined as Filter methods of: Info Gain, Gain Ratio, Chi square, Relief-f, One R, consistency and causal feature selection (CFS).

Moreover, Symmetrical Uncertainty and support vector machine (SVM) algorithm are also implemented for weighting the features [17]. In this manuscript, to compare the importance of each feature based on mentioned models, a comprehensive analysis was proposed on the features and eventually the weightings of features are presented.

2.4 Function-based clustering method

After reaching to the features weights by various filter based algorithms we have "n" feature with "m" feature's weight and then a model to determine the important features' clustering is needed which is between these weighted attributes. Consequently, we develop the presented function-based clustering model in [18]. This method is based on hierarchical divisive clustering model which starts with one cluster consisting all objects, ($Xn \times m$).

For the object x1, . . . ,xn, we define the vector of group membership of objects as $z = (z1, \ldots, zn)^T$, where $z \in Z$, and Z is the space of sign vectors denoted as:

$$Z = \left\{ z = (z_1, \ldots, z_n)^T \,|\, z_i = \pm 1 \right\} \quad (2)$$

All objects that are depended with an entry of 1 in z are categorized into one group, whereas the others with an entry of -1 are categorized into the other group. Then by using the method of multivariate analysis of variance denoted as follows:

$$x_i = \mu + z_i \gamma + \varepsilon_i, \qquad i = 1, 2, \ldots, n \quad (3)$$

Where, ε_i is the error vectors and assumed to be normally distributed with a zero mean and a common covariance matrix V, i.e. N(0,V). Additionally, ε_i and ε_i ($i \neq j$) are assumed to be independent. Then by maximum similarity, the clustering problem is presented as a least squares optimization problem as;

$$\min_{\alpha, \beta, z \in Z} \left\{ (z - \alpha 1 - X\beta)^T (z - \alpha 1 - X\beta) \right\} \quad (4)$$

In a same time, the unknown vector of cluster membership and the coefficients of the linear clustering function are approximated. The calculation of the clustering-function-based model will be converted to that of sign analysis [18], and by solving the problem, 2 clusters is obtained. Then, one

of these groups based on higher within-group dispersion matrix is further categorized into two dis-similar sub-groups. The procedure continues till some stopping criterion has been satisfied which is based on within-group dispersion and/or between-group dispersion matrices.

By this method we use the benefits of several filter methods and use these weighting attributes by function-based clustering model to make more accurate decision of effective feature.

3 Proposed Forecast Strategy

In this section the proposed forecast engine has been developed. This model is based on a complex valued function. The proposed function is described as:

$f(z)= u(x,y)+jv(x,y)$ is nonlinear in x and y ,

$f(z)$ is not entire

The partial derivatives $\frac{\partial u}{\partial x},\frac{\partial u}{\partial y},\frac{\partial v}{\partial x}$ and, $\frac{\partial v}{\partial y}$ exist, should be continuous and bounded, $\frac{\partial u}{\partial x}\frac{\partial v}{\partial y}\neq\frac{\partial u}{\partial y}\frac{\partial v}{\partial x}$ except if $\frac{\partial u}{\partial x}=\frac{\partial v}{\partial x}=0$ and $\frac{\partial u}{\partial y}=\frac{\partial v}{\partial y}=0$ $u(x, y)$ and $v(x, y)$ should be bounded, therefore $f(z)$ is bounded.

Furthermore, if the activation function is wavelet basis function, two more conditions should be satisfied: the function should have a finite energy and should be admissible.

In this section, we propose a form of the complex valued Mexican Hat wavelet function that could be obtained using the negative second derivative of the *sech* function. Obtaining that the hyperbolic secant "*sech*" could replace the Gaussian function and it presents the fully complex valued form [16], in addition the 1 real valued Mexican hat wavelet function is the second derivative of the real valued Gaussian function. The negative second derivative of the *sech* function has a solely every ($z= j(2n+1)\pi/2$, $n \in N$), however these types of solely points and discontinuities at nonzero points do not create a problem in training when the domain of interest is bounded within a circle of radius $\pi/2$ [15].

$$f(z)=2\sec h(z)(2\sec h^2(Z)-1) \quad (5)$$

This function proofs the above situations.

In the reviewed literature, there is no work dealing with such particular complex-valued wavelet function at present stage. One can see that both real and imaginary sections and the absolute value of this function have court duration. This should be proof that, this function could be accepted as wavelet function. The complex valued function $f(z)=f(x,y)$, localized in space, must satisfy the admissibility condition [14]:

$$C_f=(2\pi)^2\int_R\int_R\frac{|F(\omega,\xi)|^2}{\omega^2+\xi^2}d\omega d\xi<\infty \quad (6)$$

Where, $F(\omega,\xi)$ is the Fourier transform of $f(z)$ and (ω,ξ) are the two specific frequencies.

Using the geometric series equation of the function $sech(z)$, and make a derivation twice of the provided series, one can find:

$$f(z)=f(x,y)=2\sum_{k=0}^{\infty}(-1)^k(2k+1)^2e^{-(2k+1)x}e^{-j(2k+1)y} \quad (7)$$

The Fourier transform of the function $f(z)$ could be found as follows:

$$F(\omega,\xi)=2\sum_{k=0}^{\infty}(-1)^k(2k+1)^3\frac{\delta(\xi+2k+1)}{\omega^2+(2k+1)^2} \quad (8)$$

In the above equation δ is the Dirac impulse. Also, by the mentioned equation and the proprieties of δ, the integral could be simplified as:

$$C_f=16\pi^2\sum_{k=0}^{\infty}\int_R\left[\frac{(2k+1)}{\omega^2+(2k+1)^2}\right]^3d\omega \quad (9)$$

After evaluating this last integral, the value of C_f is found: $C_f = 0.75\ \pi^5 < \infty$ that means the function $f(z)$ is admissible complicated amount wavelet function. Hence, this function is acceptable as fully complex valued function for the FCWN and as fully complex valued wavelet function as well. Which permits us to construct the FCWN.

3.1 FCWN Model

In literature, wavelet network has deal with a remarkable place. The complex valued wavelet function proposed in the later is used as an activation function to make the FCWN of Fig. 1, where its k_{th} output is described as:

$$\hat{y}_k=\sum_{l=1}^{m}\omega_{kl}\psi(h_1) \quad (10)$$

Where, ω_{kl} shows the complex valued weights among the hidden layer and the output layer. $1 \le l \le m$ is the number of neurons in the hidden layer. $\psi(h_1)$ is the l_{th} hidden layer's output (i.e. f (z)).

Accordingly, $h_1=\sigma^{T}{}_1(z-c_1)$, $z \in C^n$ is the complex amount input vector, $\sigma_1 \in C^n$ is the complex-valued scaling vector of the l_{th} hidden neuron, which shows the dilation values in wavelet functions, and $c_1 \in C^n$ is the complex-valued translation vector of the l_{th} hidden neuron [16].

3.1.1. Learning Algorithm

In this section the objective of proposed structure should be minimized. Where, this minimization leads to find the lower value for error at the output layer which can be defined as;

$$E=\frac{1}{2}e^He=\frac{1}{2}\sum_k e_ke_k^*=\frac{1}{2}\sum_k E_k \quad (11)$$

$$E_k=e_ke_k^*=|e_k|^2 \quad (12)$$

In this equation, $e_k=y_k-\hat{y}_k$ is the k_{th} error among the k_{th} desired output y_k and the k_{th} estimated output $\hat{y}_k$, $k = 1, 2, \ldots$

shows the number of outputs. e_k^* is the error's conjugate of the k_{th} output neuron [15].

The complex valued gradient descent algorithm is widely applied to find the optimal parameters of nonlinear function in complex domain. So, in this paper we used an intelligent algorithm for finding the optimal values of nonlinear function network. In the following the proposed optimization algorithm has been discussed.

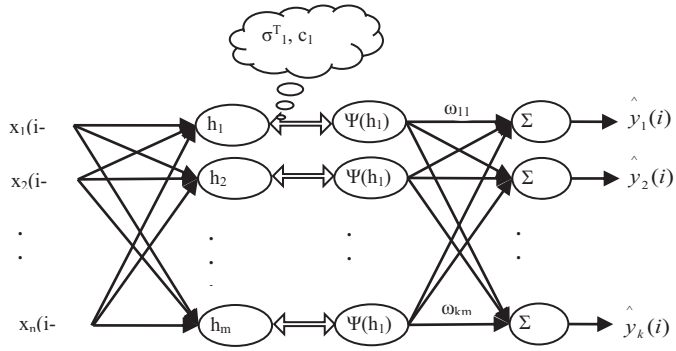

Fig. 1. Fully complex-valued wavelet network model

Also, as combination of this learning method with shark smell optimization algorithm (SSO), this algorithm is applied in this prediction model. As this model is not the novelty of this paper, more details of this algorithm is presented in [19].

4 Numerical Results

Since system operators need hourly wind power forecast a day before real-time operation in order to perform unit commitment and economic dispatch analyses, an accurate hourly wind speed and power forecast is vital for system operators; hence, this paper mainly focuses on hourly prediction. Also, the forecasting horizon of 24 hours ahead is adopted in this paper. Today, with the aid of advanced telemetry, GPS (Global Positioning System), and SCADA (Supervisory Control And Data Acquisition) systems, the required data all over the power grids are synchronously recorded in the control centers such that delay between the recorded data and execution of power application software, such as the forecasting processes, is usually in the range of a few minutes or even less. Moreover, the proposed wind forecasting strategy has a low setup time. Thus, we assume that the historical data up to the previous hour is available and the proposed wind forecasting strategy can be quickly trained with this data. Consequently, the forecast horizon of 1-24 hours ahead is adopted for day-ahead wind prediction in this paper. This forecast horizon has extensively been considered in the other day-ahead wind forecast research works, such as [20,21,22,23]. Moreover, the proposed wind prediction strategy has no limitation for longer forecasting horizons, sine it generates forecasts recursively.

The proposed wind forecasting strategy is tested by the real-world data from wind farms in Spain and Alberta, Canada. Moreover, the test cases include both wind speed and power forecasts. Considering wind speed prediction test case has another advantage that we can also compare our obtained results with some of the relevant existing literature.

4.1. Sotavento Test Case

Sotavento wind farm, located in Galicia, Spain, has 24 wind turbines with the nominal power of 17.56 MW and predicted annual production of 38.5 GWh [24]. Obtained wind speed forecast results from the proposed strategy for this test case are shown in Table 1. Also, the proposed strategy is compared with some other methods presented in our previous work [22]. In this way, the same test conditions, such as the same wind farm and test periods, can be considered to present fair informative comparisons. According to [22], 200 lagged hourly values of wind speed are considered as the candidate inputs, that are selected by the feature selection technique to select a minimum subset of the most informative candidates for the proposed forecasting engine, and 50 days prior to each forecast day are considered as the historical data divided to 49 days as the training set and one day before the forecast day as the validation set. Moreover, the same test periods of [22], including the third week of February, May, August, and November of year 2005 are adopted here for the sake of a fair comparison. For instance, the selected features of the feature selection technique for February 15, 2005, i.e. the first day of the February test week, are as follows:

$X = [x_1,x_2,\ldots,x_m] = [WS(t–1),\ WS(t–2),\ WS(t–3),\ WS(t–6),\ WS(t–12),\ WS(t–24),\ WS(t–16),\ WS(t–121),\ WS(t–132),\ WS(t–124),\ WS(t–192),\ WS(t–69),\ WS(t–112),\ WS(t–115),\ WS(t–49),\ WS(t–149),\ WS(t–59),\ WS(t–63),\ WS(t–72),\ WS(t–167)]$

The above 20 features are selected among the 200 candidate inputs $\{WS(t–1), WS(t–2), \ldots, WS(t–200)\}$.

The error criterion of table 1 is Root Mean Square Error (RMSE) defined as follows:

$$RMSE = \left[\frac{1}{NH}\sum_{t=1}^{NH}\left(S_{ACT(t)} - S_{FOR(t)}\right)^2\right]^{1/2} \quad (13)$$

Where, $S_{ACT(t)}$ and $S_{FOR(t)}$ indicate the actual and forecast values of the signal (wind speed or wind power) for hour t. Also, NH indicates number of hours, which is 168 for test weeks. Note that for day-ahead wind forecasting of this paper, the proposed prediction method proceeds hour by hour along the each day forecast horizon. At the end of each day, when the wind speed/power values of the 24 hours become available, the historical data can be updated once a day to perform day-ahead wind prediction of the next day. Thus, the forecast horizon includes 24 forecast steps. On the other hand, if the historical data is updated hour by hour instead of day by day, hour-ahead wind forecast instead of day-ahead forecast is obtained leading to much shorter forecast horizon of hour-ahead instead of day-ahead. However, one week or 168 hours are considered as the evaluation period for the error criteria of RMSE and MAPE to better evaluate performance of the model over a longer period. Table 1 demonstrates that the RMSE of the wind speed forecast of the proposed method is significantly lower than the RMSE of the other methods based on the proposed forecast engines.

In the next numerical experiment, the proposed forecast strategy is applied to predict wind power of Sotavento wind farm. While an intelligent forecasting engine can construct an effective model for wind power prediction process, more accurate numerical weather predictions can provide more qualified inputs for the wind power forecasting strategy, which effectively improve its accuracy. For this reason, wind speed and temperature, which are highly correlated weather parameters with wind power, are considered as the exogenous variables for wind power prediction process in this paper. In other words, the historical data and forecast values of wind speed and temperature along with the historical data of wind power are used as inputs for the proposed wind power forecasting strategy. Forecast values of wind speed and temperature are separately generated for the next 24 hours by means of the proposed forecasting strategy as the forecast values of meteorological parameters might not be available at wind farm sites. Within the proposed strategy, an effective feature selection technique, based on the information theoretic criterion of mutual information, first filters out the ineffective inputs and selects most informative features for the forecasting engine. The results obtained from the feature selection technique for wind power prediction of different days illustrate that the forecast of wind speed and temperature are usually among the selected features, which indicate their high relevance with the target variable, i.e. wind power. For instance, the selected inputs of the feature selection technique for the Sotavento test case in May 15, 2005, are as follows:
X = [x1,x2,…,xm] = [WP(t–1), WP(t–2), WP(t–3), WP(t–4), WS(t), WS(t–1), WS(t–2), WS(t–12), WS(t–17), WS(t–25), WP(t–28), WP(t–35), WS(t–135), WS(t–167), WP(t–49), Temp(t), Temp(t–1), WS(t–48), Temp(t–183), WP(t–71), WS(t–196), Temp(t–191), WS(t–185)]

Table 1) RMSE results (m/s) for day-ahead wind speed forecast of Sotavento wind farm in the four test weeks of year 2005

Test week	Correlation analysis +HIFM [22]	MI-MR +MLP [22]	MI-MR+HIFM [22]	Proposed method
	RMSE	RMSE	RMSE	RMSE
Feb.	7.56	7.68	5.71	3.78
May	5.82	5.96	4.26	3.22
Aug.	6.93	7.01	5.92	3.86
Nov.	5.97	6.04	4.55	3.54
Average	6.57	6.68	5.11	3.60

Where, WP, WS and Temp represent wind power, wind speed and temperature, respectively. These input features are used for wind power forecast of the next hour, i.e. WP(t). It is seen that 15 out of 23 selected inputs are from WS and Temp, which demonstrate the contribution of wind speed and temperature for wind power prediction. Moreover, prediction of wind speed and temperature, i.e. WS(t) and Temp(t), are among the selected features. Similar feature selection results have been obtained for the other forecast days. Hence, more accurate forecasts for wind speed and temperature can significantly decrease the wind power prediction error. It should be noted that the forecast values of temperature are separately generated by the proposed strategy, similar to those of wind speed, based on 200 lagged hourly values of temperature as the candidate inputs and hourly historical data of one and 49 days as the validation and training sets, respectively.

Furthermore, in the next section effectiveness of the proposed training model is evaluated. Accordingly, the proposed optimization method is replaced with several other well-known stochastic search techniques as mentioned in Table 2. Briefly, in Genetic Algorithm (GA), a population of candidate solutions, called chromosomes, is evolved toward better solutions using techniques inspired by the process of natural evolution such as mutation, selection, and crossover. Particle Swarm Optimization (PSO) optimizes a problem using a population of candidate solutions, called particles, and moving these particles around in the search-space according to simple mathematical formula over the particle's position and velocity. Each particle's movement is influenced by its local best known position and is also guided toward the best known positions among particles. Dynamic Evolutionary (DE) is a population-based evolutionary algorithm which creates new candidate solutions by combining existing ones using mutation and crossover operators. In DE, the difference between two random candidate solutions of the population is calculated in mutation operation to generate a trial solution. Then, the crossover operator generates the offspring from the trial and parent based on random selection. Simulated Annealing (SA) is a heuristic optimization method, based on an analogy taken from thermodynamics and inspired by the annealing process of metal and glass. SA also allows movements to the solutions with objective function values that are worse than the objective function value of the current solution, which is called uphill move. More details about these techniques can be found in [25].

The obtained results from each prediction method are shown in Table 2. Two error criteria are reported for each method in Table 2: Normalized RMSE (NRMSE) which is RMSE error criterion defined in (24) divided by nominal power of the wind farm and Mean Absolute Percentage Error (MAPE), defined as follows:

$$MAPE(\%) = \frac{1}{NH}\sum_{t=1}^{NH}\frac{\left|S_{ACT(t)} - S_{FOR(t)}\right|}{S_{AVE-ACT}} \times 100\,, \qquad S_{AVE-ACT} = \frac{1}{NH}\sum_{t=1}^{NH} S_{ACT(t)} \quad (14)$$

As presented in the numerical results in tables, the proposed model obtained lowest results in comparison with other methods. Sample results of the training strategy including training error and validation error curves for the first day of the winter test week are shown in Fig. 2. The effect of the proposed termination criterion can be seen from this figure such that the training phase of the forecasting engine is terminated in the SSO generation of 41 leading to the minimum validation error, which is expected to yield the maximum generalization capability for the WNN. Also, Fig. 3, represent the measured and the forecasted day ahead for wind power generation in table one in the temporal and the polar plans.

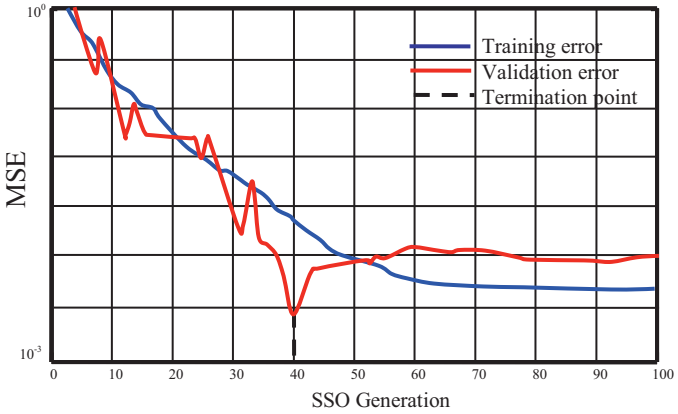

Fig. 2. Training and validation error curves, in terms of MSE, for the first day of the February test week for the Sotavento wind farm

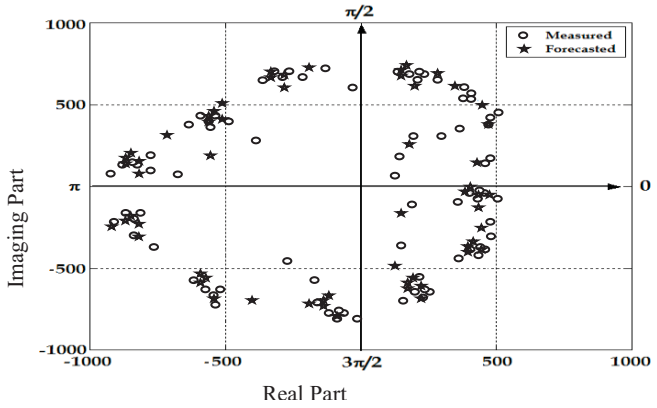

Figure 3. Measured and forecasted five days ahead of daily solar irradiation in the polar representation

Table 2) Comparison of the proposed training strategy, i.e. SSO, with GA, PSO, DE and SA for day-ahead wind power forecast of Sotavento wind farm in the four test weeks of year 2005

Test week	GA		PSO		DE		SA		SSO	
	NRMSE	MAPE	NRMSE	MAPE	NRMSE	MAPE	NRMSE	MAPE	NRMSE (%)	MAPE (%)
Feb.	10.87	40.15	10.47	37.43	10.19	37.01	9.16	33.67	6.90	25.50
May	11.27	40.97	10.87	38.42	10.59	37.87	9.68	35.12	7.36	25.78
Aug.	10.46	38.24	10.13	36.13	9.79	35.77	9.05	33.05	6.06	24.46
Nov.	10.59	37.66	9.85	35.74	9.56	35.23	8.25	32.42	5.75	23.55
Average	10.82	39.25	10.30	36.93	10.02	36.47	8.99	33.56	6.52	24.82

5 Conclusion

In this paper, a new wind prediction strategy is proposed. In this model, the fully complex valued wavelet network for forecasting the wind power generation. In this model, the signal is selected with a feature selection model. After that, the new forecast engine predicts the wind power signal. This model is tested over real-world hourly data of wind farms in Spain and Alberta. Obtained numerical results demonstrate the validity of the proposed model, through the comparison with wind speed and power forecast techniques.

6 References

[1]. S. Fan, et al., "Forecasting the Wind Generation Using a Two-Stage Network Based on Meteorological Information", IEEE Transactions on energy conversion, Vol. 24, No. 2, June 2009.

[2]. M. Lei, L. Shiyan, J. Chuanwen, L. Hongling, and Z. Yan, "A review on the forecasting of wind speed and generated power," Renewab. Sustain. Energy Rev., vol. 13, no. 4, pp. 915–920, May 2009.

[3]. P. Hu, R. Karki, R. Billinton, "Reliability evaluation of generating systems containing wind power and energy storage", IET, Generation, Transmission & Distribution, Volume: 3, Issue: 8, Page(s): 783 – 791, August 2009.

[4]. Corotis RB, Sigl AB, Cohen MP., "Variance analysis of wind characteristics for energy conversion", Journal of Applied Meteorology; 16(11):1149–1157, 1977.

[5]. Daniel AR, Chen AA., "Stochastic simulation and forecasting of hourly average wind speed sequences in Jamaica", Solar Energy; 46(1):1–11, 1991.

[6]. R. G. Kavasseri, K. Seetharaman, "Day-ahead wind speed forecasting using f-ARIMA models", Renewable Energy 34, 1388–1393.

[7]. Milligan M, Schwartz M,Wan Y. Statistical wind power forecasting models: results for U.S. wind farms, NREL-CP-500-33956, May 2003, Available [Online]: http://www.nrel.gov/docs/fy03osti/33956.pdf

[8]. I. Maqsood, M. Riaz-Khan, A. Abraham, An ensemble of neural networks for weather forecasting. Neural Comput Appl., vol. 13, no. 2, pp. 112–122, 2004.

[9]. Y. Bao, H. Wang, B. Wang, Short-term wind power prediction using differential EMD and relevance vector machine, Neural Comput & Applic, vol. 25, no. 2, pp 283-289, August 2014

[10]. A. Khosravi, S. Nahavandi, and D. Creighton, Prediction intervals for short-term wind farm power generation forecasts, IEEE Transactions on Sustainable Energy, vol. 4, no. 3, p. 602-610, July 2013.

[11]. T. Jónsson, P. Pinson, H. A. Nielsen, H.k Madsen, and T. S. Nielsen, Forecasting Electricity Spot Prices Accounting for Wind Power Predictions, IEEE Transactions on Sustainable Energy, vol. 4, no. 1, pp. 210-218, January 2013.

[12]. N. Amjady, F. Keynia, H. Zareipour, "A New Hybrid Iterative Method for Short Term Wind Speed Forecasting," European Transactions on Electrical Power, Vol. 21, No. 1, pp. 581-595, January 2011.

[13]. S.L. Goh, M. Chen, D.H. Popovic, K. Aihara, D. Obradovic, D.P. Mandic, "Complex valued forecasting of wind profile", Renewable Energy, 31, 1733–1750, 2006.
[14]. S. L. Goh and D. P. Mandic, "Nonlinear Adaptive Prediction of Complex-Valued Signals by Complex-Valued PRNN", IEEE TRANSACTIONS ON SIGNAL PROCESSING, VOL. 53, NO. 5, pp.1827-1836, May 2005.
[15]. S. Chen, S. McLaughlin and B. Mulgrew, "Complex-valued radial basis function network, Part II: Application to digital communications channel equalization", Signal Processing, 36, 175-188, 1994.
[16]. B. K. Tripathi, B. Chandra, M. Singh and P. K. Kalra, "Complex generalized-me neuron model and its applications", Applied Soft Computing, vol. 11, 768–777, 2011.
[17]. I. H. Witten, & E. Frank, Data mining: Practical machine learning tools and techniques (3rd ed.). San Francisco: Morgan Kaufmann, 2011.
[18]. B. Li, A new approach to cluster analysis: The clustering-function-based method. Journal of the Royal Statistical Society, Series B (Statistical Methodology), vol. 68, pp. 457–476, 2006.
[19]. O. Abedinia, N. Amjady, A. Ghasemi, A New Meta-heuristic Algorithm Based on Shark Smell Optimization, Complexity Journal (John Wiley), , DOI: 10.1002/cplx.21634, December 2014,.
[20]. R.E. Abdel-Aal, M.A. Elhadidy, S.M. Shaahid, "Modeling and forecasting the mean hourly wind speed time series using GMDH-based abductive networks," Renewable Energy, Vol. 34, pp. 1686-1699, February 2009.
[21]. Maqsood I, Khan MR, Huang GH, Abdalla R, "Application of soft computing models to hourly weather analysis in southern Saskatchewan, Canada", Engineering Applications of Artificial Intelligence; 18(1):115–125, 2005.
[22]. N. Amjady, F. Keynia, H. Zareipour, "A new hybrid iterative method for short-term wind speed forecasting," Euro. Trans. Electr. Power 20:1–15, 2010.
[23]. N. Amjady, F. Keynia, H. Zareipour, "Wind Power Prediction by a New Forecast Engine Composed of Modified Hybrid Neural Network and Enhanced Particle Swarm Optimization", IEEE Transactions on Sustainable Energy, Vol. 2, Issue 3, pp. 265-276, July 2011.
[24]. Sotavento Wind Farm: [Online] www.sotaventogalicia.com
[25]. A. P. Engelbrecht, Computational intelligence: an introduction, 2nd ed. John Wiley & Sons; 2007.

Biographies

Heidar Ali Shayanfar received the B.S. and M.S.E. degrees in Electrical Engineering in 1973 and 1979, respectively. He received his Ph. D. degree in Electrical Engineering from Michigan State University, U.S.A., in 1981. Currently, he is a Full Professor in Electrical Engineering Department of Iran University of Science and Technology, Tehran, Iran. His research interests are in the Application of Artificial Intelligence to Power System Control Design, Dynamic Load Modeling, Power System Observability Studies, Smart Grids, Voltage Collapse, Congestion Management in a Restructured Power System, Reliability Improvement in Distribution Systems and Reactive Pricing in Deregulated Power Systems. He has published more than 520 technical papers in the International Journals and Conferences proceedings. He is a member of Iranian Association of Electrical and Electronic Engineers and IEEE.

Oveis Abedinia received his Ph.D from Semnan University, Semnan, Iran in 2015. At present, he is a postdoctoral researcher and adjunct faculty in Budapest university of Technology and Economics (BME). His major research interests are Application of Artificial Intelligence to Power System and Control Design, Forecasting in power system, Distribution Generation, Restructuring in Power Systems, and Optimization.

Nima Amjady (SM'10) was born in Tehran, Iran, on February 24, 1971. He received the B.Sc., M.Sc., and Ph.D. degrees in electrical engineering from Sharif University of Technology, Tehran, Iran, in 1992, 1994, and 1997, respectively. At present, he is a Professor with the Electrical Engineering Department, Semnan University, Semnan, Iran. He is also a Consultant with the National Dispatching Department of Iran. His research interests include security assessment of power systems, reliability of power networks, load and price forecasting, and artificial intelligence and its applications to the problems of power systems.

Saman Rajaei is a Senior year Bachelor's student of Electrical Engineering and informatics with the specialisation of Power Engineering, at Budapest university of Technology and Economics (BME). He has been living in Hungary for the past 4 years where he pursues his degree and is planning to go Canada for his Master's studies. During his Bachelor's studies he has worked with technology companies and won an award for innovation in Wearable technologies in Munich, Germany. His upcoming diploma work is studying the Impact of Electric Car Charging on Low Voltage Smart Grids.

Building Graphical Fuzzy Inference System in Political Documents

Dr. Sameera Alshayji
Political and Economic Affairs Department, Amiri Diwan, Seif Palace, Kuwait

Abstract - *The synchronization of terrorism in many countries, especially in Arab states, makes it imperative for the leaders to redirect their investment compass in a proper way. This is especially true when considering whether to strengthen bilateral economic relations among nations, as critical decisions are influenced by certain variables that are based on heterogeneous and vague information, such as information found in minutes of meetings held between the heads of state and envoys and other decision makers. In addition, the content in the minutes of meetings suffers from the presence of question marks and exclamation marks. Applying a fuzzy ontology method is one of the possible solutions to address the lack of conceptual clarity. A fuzzy inference system's (FIS) greatest strength lies in its ability to handle imprecise data. This paper will present nonverbal communication's place as an integral part of minutes of meeting thought.*

Keywords: Fuzzy logic, FIS, Ontology, Bilateral meetings

1 Introduction

Political decision makers, in terms of creating and strengthening the economic bilateral relationship with other countries, need to organize different factors and indicators from different domains to support and guide them with expertise knowledge and certain information to make better decisions. This is necessary because decision support systems require large-scale data analysis facilities for making efficient decisions. Making the right decision at the right time with the most up-to-date data is very important for political decision support. The main objective of applying ontology is to help the political decision office retrieve the information it really needs as quickly as possible. Also, analysis of heterogeneous information from internal and external sources will help a political decision maker to know the main factors that affect the promotion of economic relations. Ontology methods can capture information from several different systems to facilitate sharing with different parties and identifying the shared information. The proper decisions in strengthening economic cooperation with other countries are very important for many reasons, such as security, stability, and the prosperity of the country, both locally and globally. Sometimes, the political relationship is excellent, but the investment in the country is not successful. This situation can cause waste and the depletion of state funds. Other times, the political relationship is weak, but the investment in the country is successful. Political decision makers have to keep all data up to date, which may delay the decision-making process and cause heavy financial losses to the state. In either case, political decision makers need to make proper decisions to strengthen economic relationships with friendly nations to achieve successful investments in the right places.

1.1 Overview

Regions may experience complications, especially the Middle East, which has faced complications such as fighting terrorism, striving for peace, and aspiration to lift the economy, particularly in light of the descent of oil prices. All of these challenges force the heads of state to rethink their investment compasses, especially when it comes to strengthening their bilateral economic relationships. The world's increasing interconnectedness and the recent increase in the number of notable regional and international events pose ever-greater challenges for political decision-making processes. Many times, the response of a decision maker is to question the wishes of the other nations that his or her country already has some economic bilateral relations with; thus, the answer becomes a silent thought, or some sentences include question marks or exclamation marks. Such question marks, and exclamation marks at the end of sentences must have scientific logical parameters. Silent thoughts and question marks require someone to analyze them, as the people from the information systems require clear variables to add into the system. This is especially true, for example, Alshayji et al. [9] presented the "MATLAP" system; which has the ability to convert linguistic variables to fix the number by conducting fuzzy logic methodologies. To be more precise, we need to depict these variables in a database rather than in documents.

1.2 Current Challenges

Unfortunately, in reality, most of the concept of political and investment information are a linguistic variable, that is, a variable with values in words rather than numbers. Also, these kinds of concepts, which are located inside the minutes of meeting documents, contain the presence of question marks and exclamation marks. These kinds of information held during the official talks, along with silent thoughts, are unknown information, and we can consider them as vague

information. This makes it extremely difficult for the decision maker to understand the concepts that exist in the documents in the political domain. For example, Alshayji et al. [5] identified some concepts that influence decisions to strengthen economic relationships with other countries, such as the agreements concept [4], the nuclear affairs concept, and the peace in the Middle East concept; these ideas are also presented by Alshayji et al. [7]. The decision-maker who is considering whether to strengthen economic relationships requires structured information. Examples of information that may be assessed in the decision-making process include competency questions such as "What is the result of the bilateral meeting? The types of answers may involve a description such as "strong positive", "positive", "neutral", and "negative". In addition, such as “silent thoughts” or “question marks” and “exclamation marks,” which are included at the end of the sentence, make obstacles for the decision maker to understand the intent of the speech. In this situation, the political decision maker could describe the bilateral relationship between the two nations in several phases, such as "very good" at a specific time, "good" in another time, or "weak" at the current time. Or sometimes the result of the bilateral meeting is unclear in other words, the result of the bilateral meeting is fuzzy at the current time because some answers contain question marks and exclamation marks at the end of some sentences, in addition to the presence of “silent thoughts.” This kind of information obscures the thoughts of the decision-making process

1.3 Problem formulation

A serious problem that the political or investment decision-maker faces is the difficulty of building an efficient political decision support system (DSS) with heterogeneous and vague information in the political and investment domains, especially regarding the decision to strengthen bilateral economic relationships with friendly nations. Typically, these critical decisions are influenced by heterogeneous and vague information from different domains. Most of the political decision maker’s documents use linguistic variables whose values are words rather than numbers and therefore are closer to human intuition. A natural language is needed to describe such information, which requires more human knowledge for interpretation.

1.4 Proposed solutions

A popular way to handle scattered data is to construct the so-called fuzzy ontology as presented by Inyaem et al. [14]. The fuzzy membership value μ is used for the relationship between the objects in question, where $0<\mu<1$ and μ corresponds to fuzzy membership relationships such as "low," "medium," or high" for each object. The purpose of fuzzy control is to influence the behavior of a system by changing the inputs to that system according to the rule or set of rules under which that system operates. The purpose of applying fuzzy systems is to enable one to weigh the consequences (rule conclusions) of certain choices based on vague information.

1.5 Contribution knowledge

The fuzzy inference system contributes to understanding the context and perspectives that are important to the impact of political variables on strengthening bilateral economic relationships. The proposed technique efficiently utilizes algorithms to access, integrate, and manage the contributed information at the international level. Using object paradigm ontology and Protégé-OWL methods to contribute to understanding the domain as well as the relation between objects, the technique also contributed significantly to simplifying the concept by extracting the main variables that affect the decision process [5]. These methods facilitate implementation. In addition, they enhance the clarity of the natural concepts and encourage us to shed light on other, more difficult domains, such as a parliament. Utilizing fuzzy logic contributed to the understanding of linguistic and imprecise data. The utilization of the fuzzy cognitive mapping (FCM) scheme provides insight into the interdependencies variables (vague data). FIS is a high-level technical computing language and interactive environment for algorithm development, data visualization, data analysis, and numeric computing. Its contribution lies in the secret of the calculations that automate dealing with imprecise language and vague information.

2 Methodology

2.1 Proposed ontology

Ontology facilitates the communication between the user and the system, and the success of the information systems is based on integration of information. Different methodological approaches for building ontology have been proposed in the literature [10, 12, 14, 18].

Two approaches are described in this paper. The first is adopted from the ontology modeling approach of Noy and McGuinness [19] and Fernandez-Lopez [13]. The second approach Process of Construction of Fuzzy Ontology is adopted from Inyaem et al. [14]. The main framework is to complete the construction of fuzzy ontology for a specific domain involves the following steps: 1) input unstructured data; 2) specify the definition of related concepts in the domain and their relationships; 3) clarify the generation of domain ontology; 4) extend the domain ontology to fuzzy ontology; and 5) apply the fuzzy ontology to the specific domain.

We will use the same developed model of fuzzy ontology for several reasons: 1) the authors used this model in the terrorism domain, which is considered an integral part of the political domain because terrorism undermines political stability; the model includes political variables such as “stability” and “terrorism” and 2) the author used linguistic

variables and ambiguous concepts that are roughly equivalent to vague variables used in the political domain.

However, more sub-steps (processes) will be added within the main steps used by the Inyaem model [14]. The five new processes (sub-steps) are as following: 1) construct object paradigm (OP) ontology; 2) apply ontology language OWL-editor from the World Wide Web Consortium (W3C); 3) construct fuzzy cognitive map theory (FCM); 4) apply fuzzy causal algebra method; and 5) apply fuzzy inference system (FIS).

2.2 Mechanism for using new sub-steps of fuzzy construction

Alshayji et al. [6] used an object paradigm (OP) ontology to identify important concepts and capture a high level for ontology conceptualization of knowledge to facilitate the work of decision processes [4, 5, 6, 8]. More details of OP were presented by Alasswad et al. [2]. Accordingly, this paper presents the concept of the bilateral meeting concept by using an OP ontology, the OWL editing tools ontology, and then proceed to integrating fuzzy logic with ontology. Alshayji et al. [8, 9] used OWL to present the concept in the political domain [4, 5]. More justification for using Protégé was presented by Alshayji et al. [5], Islam et al. [15], and Noy & Guinness [19]. On the other hand, the third and fourth processes, which involve Fuzzy Cognitive Mapping (FCM) and causal algebra, are especially applicable in the soft knowledge domains (e.g., political science, military science, international relations, and political elections at government levels). Alshayji et al. [7] demonstrated the causal inter-relationship between certain variables in the domain, such as "stability" and "terrorism," in addition the processes of fuzzy ontology construction presented in investment domains and the agreement ontology in political domains, respectively [4, 5, 6, 8].

2.3 Justification for using new sub-steps of fuzzy construction

In this regard, and coinciding with the previously mentioned process, the new sub-steps are added for two key reasons: to accelerate the application process for the construction of fuzzy ontology and to simplify the extraction of the most variables that in some way affect the political decision-making process. Political decision-makers would thus be aided by a system that would allow them to formulate constructive rule conclusions by dealing with vague variables as described and drawing rule conclusions in the form of an IF-THEN statement- an if-antecedent (input) and then-consequent (output). Because of this situation, and along with FCM and causal algebra propagation, the fifth process the "fuzzy inference" includes displaying what is going on in the political mind in the form of a calculation through the use of fuzzy sets and linguistic models consisting of assets of IF-THEN fuzzy rules. Fuzzy systems enable one to weigh the consequences (rule conclusions) of certain choices based on vague information. Rule conclusions follow from rules composed of two parts: the "if" (input) and the "then" (output). Fuzzy logic toolbox graphical user interface (GUI) tools enable us to build a fuzzy inference system (FIS) to aid in decision-making processes. For the purposes of the ontology, we refer the readers to Alshayji et al. [8]. Figure 1 depicts the complete process of the construction of fuzzy ontology. In addition fuzzy uses will be present in the next section.

2.4 Fuzzy logic uses

Fuzzy logic is used to present imprecise information (Jun et al. 2008). More recent work on developing models based on fuzzy logic was presented by Basha and Ameen [11] to identify predictor variables that are significant in the act of purchasing. Alshayji et al. [5] used fuzzy logic to propose bilateral relation domains to help decision processes in the political domain. To begin with, an ontology can be converted into fuzzy ontology, where any relationship is a fuzzy relationship accompanied by its weight as defined in Table 1 by Muhammad and Bulaish [18]

Table 1: Weight associated with linguistic and semantic relation by Muhammad and Bulaish [18].

Interpretation	Relation Name	Weight
Linguistics	Synonym	1.0
	Related Term	0.5
Semantic	Same as	1.0
	Kind-of	0.8
	Part-of	0.7
	Contains	0.5
	Associates	0.3

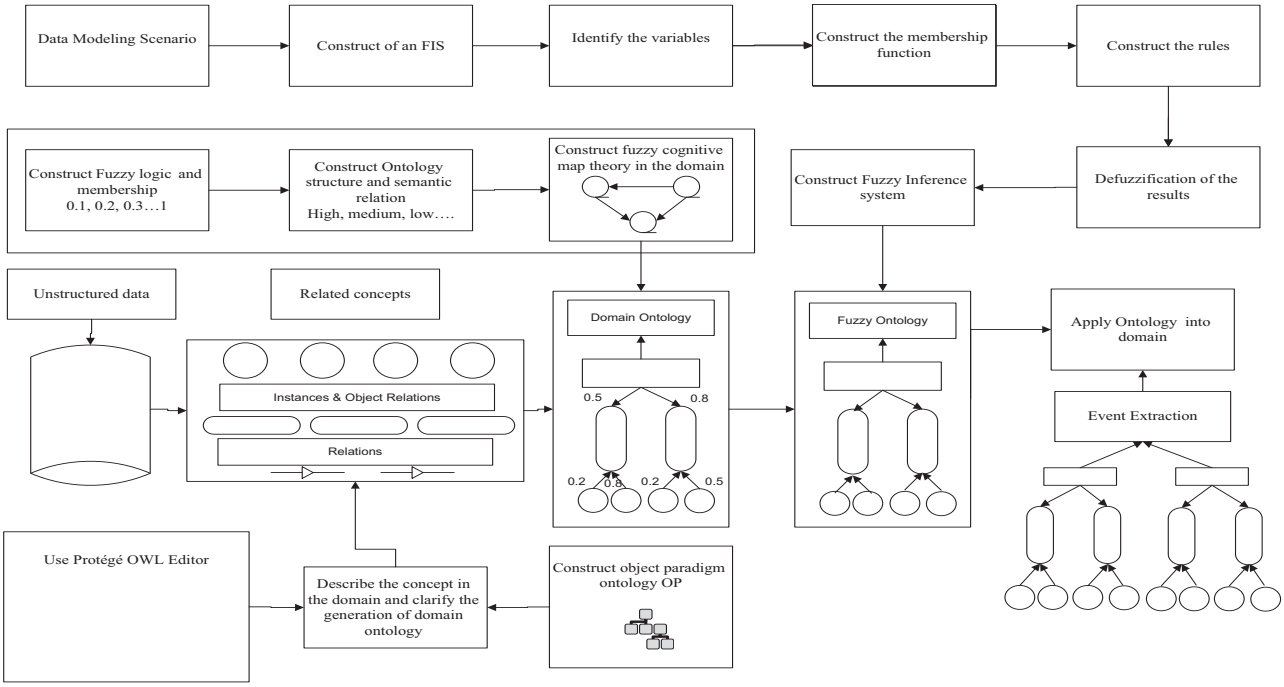

Figure 1: Process of Construction of Fuzzy Ontology with inference system for the Specific Domain

3 Specifying therelated concepts – Illustrative case: meeting documents

Bilateral meetings (minutes of meetings) occur between friendly countries through the meetings of heads of state or envoys, some time minutes of meetings documents contain "question marks," and "exclamation marks"whether the prime minister or the minister of foreign affairs. We consider that it is possible to convert this matter to such a parameter, but most of the time, the terminology is too difficult to analyze and understand. For instance, it is important not to limit the answers to sentence such as "do you expect that the division will happen to the country a!", this question has exclamation marks at the end of the sentence, so we notice here that the content of the concept is to find some information indirectly rather than question." Those sentences create difficult challenges for the programmers and analysts in information systems. such previous sentences must be converted into other parameters and in different degrees so that we can finally get accurate results for the outcome of the final interview. In other words, we can depict the power of the political relationship by understanding such variables. Undoubtedly this change was made for plural agreement with variables. This shed light on the proper planning needed to build and strengthen the investment relationship between nations.

3.1 Specifying the definition of related concepts

In this section we will apply the proper ontology to identify some concepts of "question marks," and "exclamation marks found in bilateral meetings. So we can understand the formal talks between friendly countries. The proper ontology was identified by Alshayji et al. [5], who used the loan as case study, in this section, we will use the bilateral meetings as a case study. To capture all concepts of bilateral meetings, the "result" class is linked to the "negative" class through the "hasWeak" tuple type. In addition, to capture the "positive" result, the "P-strong" class is linked to the "positiveAnswer" class. To be more semantically precise, the engineering process links link with all concepts that related to bilateral meetings.

According to the OP, the process starts with the selection of the concept, followed by the analysis of its spatial and temporal dimensions. The aim is to have a clear conceptualization of the bilateral concept while extracting the concepts that exist within the bilateral meetings document. This is done by considering all official talks in order to create a bilateral meetings ontology. The result of the bilateral meetings concept will be more identified by using OP ontology, through which we will analyze the 'results' concept. Mainly, each result has a different type such as "negative answer," "positive answer," "neutral," etc. In addition, the result is submitted on a specific date. This date requires analysis in order to track change over time, as OP considers the temporal dimension, thus enables changes over time. To monitor minutes results, the "MinutesResult" class is

linked to the "position," "CountryName," and "Title" through the tuple types "hasPositionType," "hasCountryName," and "hasSubject," respectively, as these descriptions can change only if changes happen to the minutes' results. (See Figure 2)

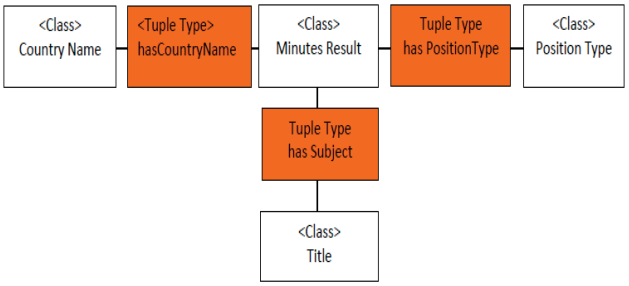

Figure 2: Engineering the result ontology

We considered the important information in the bilateral meetings concept. This information enhances the semantic presentation, and such enhancements may also significantly affect the quality and performance of the implemented software system. Thus, more details enable an ontology to provide a more faithful presentation.

3.2 Using OWL ontology

The construction of the bilateral relation "result" is also presented by the Protégé OWL editing tool in Figure 3.

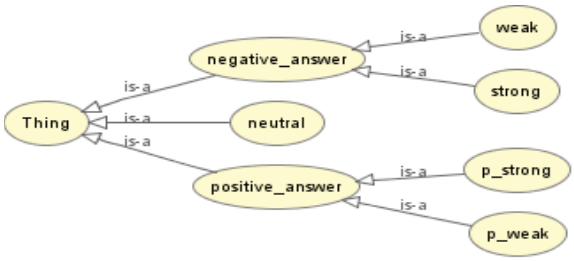

Figure 3: Result of bilateral meetings ontology by Protégé OWL

At this stage we have 1) input unstructured data; 2) specified the definition of related concepts in the domain and their relationships; and 3) clarified the generation of domain ontology. In the next section, we will extend the domain ontology to fuzzy ontology.

4 Extending ontology to fuzzy ontology

At this point, it is important to understand and specify the classes in bilateral meetings domain and generate fuzzy ontology.

4.1 Fuzzy Set and Membership

In this section, we will integrate fuzzy logic in our ontology. Fuzzy logic, as presented by Abulaish & Dey [1] and also Alshayji et al. [5, 8, 9] has different properties. More fuzzy concepts in the same domain have been presented [5]. Integrating information with rich concepts undoubtedly helps political decision-makers make correct decisions. Answering whether to "prevent" or "redirect" the bilateral economic relationships requires also considering the concept of an "investment indicator."

4.2 Fuzzy Cognitive Map Theory

FCM is a fuzzy-graph structure for representing causal reasoning with a fuzzy relationship to a causal concept [7]. Justification for its use is described in subsection 2.3; more justification can found in the literature [7, 17]. Signed fuzzy non-hierarchic digraphs and metrics can be used for further computations, and causal conceptual centrality in cognitive maps can be defined with an adjacency matrix [7, 16].

4.3 Use of Fuzzy Casual Algebra

This work seeks to clarify the relationships between concepts and to elucidate the positive or negative effects on each concept while clarifying knowledge of the relationships. Furthermore, an FCM structure allows systematic causal propagation, and arrows sequentially contribute to the convenient identification of the causes, effects, and affected factors [7, 16]. Figure 7 has seven variables that describe the impact of some conditions on bilateral economic relationships and causal variables. For example, (C1→C2, C1) are said to impact C4. This is apparent because C1 is the causal variable, whereas C4 is the effect variable. Suppose that the causal values are given by p {none ≤ some ≤ much ≤ a lot}. Causal relationship between concepts and the effect of these relations were presented by Alshayji et al. [9]. The FCM appears below in figure 4.

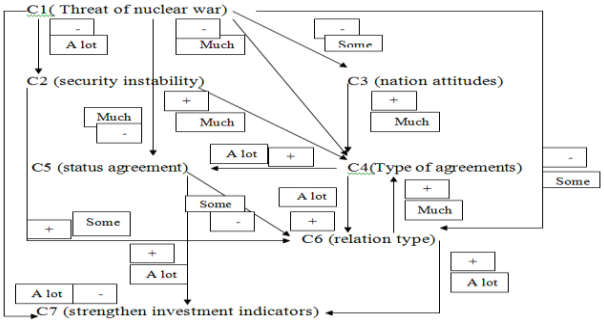

Figure 4: A fuzzy cognitive map on the impact of strengthening economic bilateral relationship

5 Inference system in the political domain

Incorporating the concept of specific domain, this step applies a method that can deal with dismantling each variable to several parameters. Decision-makers would be aided by a system that would allow them to formulate constructive rule conclusions by dealing with several parameters (membership)

for each variable. Alshayji et. al previously described the advantage of GUI tools in MATLAP [9] and the capability of building a productive graphical fuzzy inference system (FIS). There are five primary GUI tools for building a fuzzy inference systems: 1) the FIS editor; 2) the membership function editor (MFE), which allows users to define and shape the membership function associated with the input and output variables of the FIS; 3) the rule editor, for editing the list of rules that define the behavior of the system (IF-THEN); 4) the rule viewer, for diagnosing the behavior of specific rules and viewing the details (it is a technical computing environment); and 5) the surface viewer, which generates a 3D surface from two input variables and displays their dependencies. Further figures were presented by Alshayji et al. [9].

5.1 Data and modeling scenario

As mentioned in section 2.2 we need to collect all input/output data in a form that can be used by inference. Alshayji et al. [9] also presented the five primary GUI tools for building, editing, and monitoring FISs. Therefore, a need emerges for giving different interpretations according to the context. Table 1 presents the proposed "InvestmentIndicatorName" class with linguistic and semantic properties.

Country name	Investment Indicator
A	Encourage strongly
B	Encourage
C	Encourage weakly
D	Prevent
E	Caution
F	Redirect

Table 1. Fuzzy logic assigned to "CountryName" and "InvestmentIndicator"

For example, input 1 is "Bilateral Meetings result." In this step, we need to add the parameters for the "Bilateral Meetings" input, so we need to define all inputs and their values. The second step uses the membership function editor. In the third step, which involves the rule editor, we need to construct the rules; for example, we construct the first two rules as follows:

if (Bilateral Meetings result is strong negative), then (investment is redirect) (1).

if (Bilateral Meetings is strong positive), then (investment is encourage strongly)

These rules are verbose. The result is an extremely compressed version of the rules in a matrix where the number of rows is the number of rules and the number of columns is the number of variables, as follows:

1 1 0 0 0 0 0 0 0 0 0 0 0 3, 1 (1): 1

2 2 2 0 0 0 0 0 0 0 0 0 0 3, 3 (1): 1

Using such functions in the political domain provides the opportunity to choose a membership value with infinite accuracy. Reading across the first row, a literal interpretation of rule 1 is "input 1 is MF1" (the first value for the membership function associated with input 1). This means that from the first input (bilateral meeting result) we select {strong negative}, the value for the membership function associated with input 1. Continuing across, MF1 from input 2 was selected, and so on. Obviously, the functionality of this system does not depend on how well the operator named the variables and membership functions and does not even bother with variable names. The next step is to use the rule viewer to display the whole fuzzy inference process. The construction of the rules editor is presented in Figure 5.

Figure 5. the rules in the Rule Editor, in the verbose form

The decision will depend on the input values for the system. The defuzzified output (value) and the Fuzzy inference diagram containing calculation was displayed previously by Alshayji et.al [9]. The fourth step is using rule viewer was presented by Alshayji et.al [9]. Some information about inputs, memberships, and output (variables in the system) is presented in the following system:

ows:Name="Investment3,"Type="mamdani,"Version=2.0, NumInputs=13,NumOutputs=1,NumRules=8,AndMethod="min, "OrMethod="max,"ImpMethod="min,"AggMethod="max,"Def uzzMethod="centroid,"(Input1),Name="bilateral meeting,"Range=(01),NumMFs=3,MF1="weaknegative": "trimf"(-0.5 0 0.5),MF2="positive":"trimf"(0 0.5 1), MF3="strongpositive":"trimf"(0.511.5),(Input2),Name="Politic alStability."

The fifth step is using a surface viewer that generates a 3D surface from two input variables and displays their dependencies.

6 Conclusion and Future Work

This paper focuses on developing a fuzzy inference system in the political domain to handle imprecise data by controlling information uncertainty. We have built a fuzzy

inference system that has stronger abilities for expressing uncertain linguistic variables. Our further research lies in the automatic generation of fuzzy ontology from more fuzzy systems. In addition, more research needs to be done about "question marks", "exclamation marks" and "silent thought", In further research, we need to improve the application and development of technical political centers. We will present the intended functions of such political centers and the challenges that hinder their work.

7 References

[1] Abulaish, M. and Dey, L. "Interoperability among distributed overlapping ontologies: A fuzzy ontology framework". Proceedings of the 2006 IEEE/IWC/ACM International Conference on Web Intelligence, 2006.

[2] Al Asswad, M. M., Al-Debei, M. M., de Cesare, S. and Lycett, M. "Conceptual modeling and the quality of ontologies: A comparison between object-role modeling and the object paradigm". Proc. 18th European Conf. Information Systems, Pretoria, 2010.

[3] Al-Ibrahim, H. "In Qatar, do think tanks matter?". Brookings Doha Center, Doha, Qatar, 2011.

[4] Alshayji, S., El Kadhi, N. and Wang, Z. "Building Fuzzy-Logic for Political decision-maker". D 20, E 814, Naun.org/International journal on Semantic Web, Romania, 2011a.

[5] Alshayji, S., El Kadhi, N. and Wang, Z. "Building ontology for political domain". 2011 International. Conference on Semantic Web and Web Services. 'SWWS'11'. Inspec/IET/The Institute for Engineering & Technology; DBLP/CS Bibliography; CNRS, INIST databases, Las Vegas, USA, 2011b.

[6] Alshayji, S., ElKadhi, N. and Wang Z. "Fuzzy-based ontology intelligent DSS to strengthen government bilateral economic relations". Kcess'11 (Second Kuwait Conference on e-System and e-Services), April 9, ACM 978-1-4503-0793-2/11/04, 2011c.

[7] Alshayji, S., ElKadhi, N. and Wang, Z. "Fuzzy Cognitive Map Theory for the political Domain". Federated Conference on Computer Science and Information System, The Fed CSIS'2011 September 19-21, Szczecin, Poland, IEEE Digital library CEP1185N-ART, 2011d.

[8] Alshayji, S., El Kadhi, N. and Wang Z. "On fuzzy-logic-based ontology decision support system for government sector". 12th WSEAS International Conference on Fuzzy Systems, Brasov, 34, 2011e.

[9] Alshayji, S., Al-Sabah, N. and Al-Sabah A. "Building Fuzzy Inference System in the Political Domain." 12th International Conference on Scientific Computing (CSC'14), Las Vegas, USA, 2014.

[10] Alshayji, S., Al-Sabah, N. and Al-Sabah A. "Designing bilateralism and developing Fuzzy inference System in the political domain." 13th International Conference on Scientific Computing (CSC'15), Las Vegas, USA, 2015.

[11] Basha, R, and Ameen, J, "Consumer Behaviour Fuzziness in the New Market Environments." 12th WSEAS International Conference on Fuzzy Systems. April 2011, Transilvania University of Brasov, Romania. April 2011,pp.24-29

[12] Beck, H. and Pinto, H. S. "Overview of approach, methodologies, standards, and tools for ontologies". Agricultural Ontology Service (UN FAO), 2003.

[13] Fernandez-Lopez, M. "Overview of methodologies for building ontologies". Journal Data & Knowledge Engineering, 46, 2003.

[14] Inyaem, U., Meesad, P. and Haruechaiyasak C. "Dat Tran: Construction of fuzzy ontology-based terrorism event extraction". Third International Conference on Knowledge Discovery and Data Mining, IEEE. DOI 10.1109/WKDD.113, 2010.

[15] Islam N., Abbasi A. Z. and Zubair A. "Semantic Web: Choosing the right methodologies: Tools and Standards". IEEE, 2010.

[16] Jun, Z., Yan, C., Qinglian W., Miao, Lv. "Fuzzy Ontology Models Using Intuitionist Fuzzy Set for Knowledge Sharing on the Semantic Web." 978-1-4244-1651-6 IEEE,Dalian, pp China, 2008.

[17] Kosko, B. "Fuzzy cognitive maps". London: Academic Press Inc., 65-75, 1986.

[18] Muhammad, A., bulaish, L. D., 2006. Interoperability among Distributed Overlapping Ontologies-A Fuzzy Ontology Framework, Proceedings of the 2006 IEEE/WIC/ACM International Conference on Web Intelligence (WI 2006 Main Conference Proceedings)(WI'06) 0-7695-2747-7/06.

[19] Noy, N. and McGuinness, D. "Ontology development 101: A guide to creating your first ontology", 2001.

[20] Sharif, A.M. and Irani Z. "Knowledge dependencies in fuzzy information systems evaluation", 2005.

ISBN: 1-60132-430-8, CSREA Press ©

SESSION

COMPUTATIONAL SCIENCE: GRAPH BASED ALGORITHMS + OPTIMIZATION METHODS AND FUZZY LOGIC

Chair(s)

TBA

ISBN: 1-60132-430-8, CSREA Press ©

ISBN: 1-60132-430-8, CSREA Press ©

On Numerical Methods for Plasma 3-T Radiation Diffusion in Two and Three Dimensions

William W. Dai and Anthony J. Scannapieco
Los Alamos National Laboratory
Los Alamos, New Mexico, USA

Abstract— *Operator-splitting approaches are often used for plasma 3-T radiation diffusion equations, since many linear solvers could not effectively solve the coupled linear system resulted from plasma 3-T radiation diffusion equations. An approach of operator-splitting is proposed for numerically solving plasma 3-T radiation diffusion equations. To resolve sub-cell structure in mixed cells, interface reconstruction is implemented within any mixed cell. Therefore, the system of 3-T radiation diffusion equations is solved on two- and three-dimensional polyhedral meshes. The focus of this paper is on the coupling between radiation and material, the treatment of nonlinearity in the equations, and the discontinuity across cell interfaces in material properties. The discontinuity of material properties between different materials is correctly treated based on the governing physics principle for general polyhedral meshes. The treatment is exact for arbitrarily strong discontinuity. The features of the resulting scheme are demonstrated through comparing with more accurate methods and some existing operator-splitting methods for numerical examples. It is demonstrated that the proposed approach is much better than the existing splitting approaches and close to unsplit method.*

Keywords: diffusion, radiation, 3-T, coupling, interface, implicit

1. Introduction

Solving plasma 3-T radiation diffusion equations is often a critical step in numerical simulations of multi-physics. Many of these simulations involve mixed cells. Within a mixed cell there are more than one material. The existence of mixed cells is due to either initial distribution of material or other physics packages, such as hydrodynamics and advection.

For plasma 3-T diffusion equations to resolve the sub-cell structure within mixed cells are important for many problems. The importance is due to three facts. First, materials within a mixed cell are not necessarily in equilibrium with each other. The use of a single value for temperature within a mixed cell is inappropriate. Second, for real physics and engineering problems, tables for equation of state (EOS) are needed for diffusion coefficients, but EOS tables are unavailable for a mixture of materials. An averaging procedure of EOS tables cannot describe the mixture well. Third, an operator-splitting technique is used in many multi-physics codes, in which the result of one physics package is used as an input of a subsequent physics package. A subsequent physics could be temperature-sensitive, i.e., the result of subsequent physics sensitively depends on temperature of each material obtained from radiation diffusion solvers. If temperatures and material properties within a mixed cell are homogenized through some weighted average, after the homogenized temperature is updated through plasma 3-T radiation diffusion equations there is no physics principle available to separate the temperatures of different materials.

To resolve the sub-cell structure, a mixed cell is often decomposed to a set of sub-cells through interface reconstruction. The sub-cells generated through the reconstruction are general polygons in two dimensions and general polyhedrons in three dimensions. Therefore, the operator-splitting approach to be proposed here is for general polyhedral meshes.

For problems with multi-materials of dramatically different properties, a correct treatment for the discontinuity of material properties is important. One approach for the calculation of flux near material interfaces on unstructured meshes is to use mathematical approximations, for example, some weighted average of two adjacent materials. This approach would introduce numerical errors when thermal properties of two materials are very different. In this paper, we will give a general formulation to calculate the effective diffusion coefficients of radiation, electrons, and ions at an interface between two different materials within the framework of polyhedral meshes. Another important aspect in 3-T radiation diffusion equations is the treatment of the nonlinearity in the equations.

There are many investigations on numerical methods for diffusion equations. Some are for single diffusion equation, some for coupled systems, some for structured meshes, and some for single material. Very few papers discuss operator-splitting approaches. In practice, it is often to take some straightforward approach for the 3-T diffusion equations, but some of them are obviously wrong for some problems even for very small time steps. One of typical operator-splitting methods is to separate the diffusion process from the interaction between radiation and material, and another is to separate each diffusion process from each other with an inappropriate treatment of the nonlinearity in the interaction between radiation and electrons. Both approaches result in serious errors in simulation results for some problems.

ISBN: 1-60132-430-8, CSREA Press ©

In this paper, we will propose an operator-splitting approach for 3-T radiation diffusion equations. The focus of the development is on the coupling between radiation and material, the treatment of nonlinearity in the equations, and the discontinuity across cell interfaces in material properties. The discontinuity of material properties between different materials is correctly treated based on the governing physics principle for general polyhedral meshes. The plan of the paper is as follows. The second section is for 3-T radiation diffusion equations to be solved. In the third section, we will briefly describe a numerical scheme for 3-T radiation diffusion equations on general polyhedral meshes that is unsplit and fully nonlinear for the nonlinearity in the 3-T diffusion equations. After that we will present our operator-splitting algorithm for the 3-T equations. Numerical examples are given in Section 4 to demonstrate the features of the algorithm developed in this paper. In this section, we will also present comparison in simulation results among the proposed operator-split algorithm and the fully nonlinear and unpslit algorithm, and the two existing operator-splitting algorithms. Following numerical examples is the conclusion of this paper.

2. Plasma 3-T Radiation Diffusion Equations

In a system of plasma with radiation, when the time scale for equilibration of photons, electrons, and ions is much shorter than the time scale of the interaction between them, photons, electrons, and ions are each in a state of local thermodynamic equilibrium (LTE). Photons' energy is given by a Planck distribution, and those for electrons and ions are Maxwellian. Their associated temperatures, T_r, T_e, and T_p, are not necessarily in equilibrium.

Photons are described by an angle- and frequency-dependent equation of radiation transfer for radiation intensity. Expanding the intensity function in spherical harmonics, retaining the first two terms, and using Ficks's law, we get the frequency-dependent diffusion equation for photons. Further integrating the equation over frequency gives the diffusion equation of the energy of photons. Together with the electron and ion energy transport equations, the set of 3-T radiation diffusion equations is

$$a\frac{\partial \phi}{\partial t} = - \bigtriangledown \cdot \mathbf{F}_r + S_r. \tag{1}$$

$$C_{ve}\frac{\partial T_e}{\partial t} = - \bigtriangledown \cdot \mathbf{F}_e - S_r + S_e. \tag{2}$$

$$C_{vp}\frac{\partial T_p}{\partial t} = - \bigtriangledown \cdot \mathbf{F}_p - S_e. \tag{3}$$

Here $\phi \equiv T_r^4$, a is the radiation constant, C_{ve} and C_{vp} are heat capacities of electrons and ions, and they are related with material mass density ρ and specific heat capacities c_{ve} and c_{vp} through $C_{ve} \equiv \rho c_{ve}$ and $C_{vp} \equiv \rho c_{vp}$. $\mathbf{F}_r$, $\mathbf{F}_e$, and $\mathbf{F}_p$ are energy fluxes of radiation, electrons, and ions respectively, and they are defined as

$$\mathbf{F}_r \equiv -\sigma_r \bigtriangledown \phi, \tag{4}$$

$$\mathbf{F}_e \equiv -\sigma_e \bigtriangledown T_e, \tag{5}$$

$$\mathbf{F}_p \equiv -\sigma_p \bigtriangledown T_p. \tag{6}$$

Here σ_r, σ_e, and σ_p are diffusion coefficients of radiation energy and temperatures of electrons and ions. σ_r is inversely proportional to Rosseland opacity that includes atomic processes such as Bremsstrahlung, photo-ionization, line-absorption, and Thompson scattering. The source terms in Eqs.(1-3) are defined as

$$S_r \equiv ac\rho\kappa_p(T_e^4 - T_r^4), \tag{7}$$

$$S_e \equiv C_{ve}\kappa_{pe}(T_p - T_e). \tag{8}$$

In Eqs.(7,8), c is the light speed, κ_p Planck mean opacity, and κ_{pe} the coefficient for interaction between electrons and ions. The term, S_r, in Eqs.(1,2) allows for the exchange of energy between radiation and electrons.

3. Numerical Schemes

In this section, we will first briefly describe a recently developed algorithm [2] for plasma 3-T radiation diffusion equations, and then propose an operator-splitting algorithm. Since the resulting meshes through reconstruction of interfaces between materials are unstructured, the numerical schemes to be presented in this section are for Eqs.(1-3) on a general polyhedral mesh in two and three dimensions. We will particularly focus on the effective diffusion coefficient with discontinuity of material properties, nonlinearity of the equations, and the coupling between radiation and material.

Referring to a cell in an unstructured mesh, the red cell as shown in Fig.1, we denote N_i as a set of cells shown through the green cells in the figure, each of which neighbors the cell *i* with a non-vanishing interface. We will use $\triangle t$ for the size of time step, $\triangle V_i$ for the volume of cell *i*, A_{ik} for the area of the interface between cell *i* and cell k as shown in the figure. We will use T_{ei}, T_{pi}, and T_{ri} for the temperatures of electrons, ions, and radiation at $t = 0$, T_{ei}^n, T_{pi}^n, and $T_{ri}i^n$ for the temperatures at $t = \triangle t$, C_{vei} and C_{vpi} for heat capacities of electrons and ions in cell *i*, κ_{pei} for the value of κ_{pe} at cell *i*, and κ_{pi} for the value of Plank mean opacity κ_p at cell *i*. We will focus on Euler backward method in which the temperatures used in the calculation of fluxes $\mathbf{F}_r$, $\mathbf{F}_e$ and $\mathbf{F}_p$ are their values at $t = \triangle t$.

3.1 Fully Nonlinear Difference Equations

Considering a cell in an unstructured mesh, the red cell in Fig.1, we integrate Eq.(1-3) over the cell and one time step $0 < t < \triangle t$ with $\triangle t$ the size of time step. After converting the volume integral into a surface integral over the enclosed surface of the cell for the fluxes and evaluate

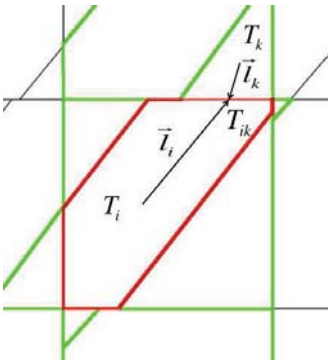

Fig. 1: Illustration of the procedure to calculate energy flux across the interface between cells *i* and *k*. $\mathbf{l_i}$ or $\mathbf{l_k}$ is the vector from the center of cell *i* or *k* to the center of the interface. T_i and T_k are the temperatures at the centers of cells *i* and *k* respectively. T_{ik} is the temperature at the center of the interface.

the fluxes through the temperatures at $t = \triangle t$, we could get the following set of nonlinear difference equations [2],

$$[a\gamma_i^n + \frac{\triangle t}{\triangle V_i}\sum_{k\in N_i}(\sigma_{rik}^n A_{ik}) + \tau_i^n]T_{ri}^n - \tau_i^n T_{ei}^n = a\gamma_i^n T_{ri} + \frac{\triangle t}{\triangle V_i}\sum_{k\in N_i}(\sigma_{rik}^n A_{ik} T_{rk}^n), \quad (9)$$

$$-\tau_i^n T_{ri}^n + [C_{vei} + \frac{\triangle t}{\triangle V_i}\sum_{k\in N_i}(\sigma_{eik}A_{ik}) + \tau_i^n + C_{vei}\kappa_{pei}\triangle t]T_{ei}^n - C_{vei}\kappa_{pei}\triangle t T_{pi}^n = C_{vei}T_{ei} + \frac{\triangle t}{\triangle V_i}\sum_{k\in N_i}(\sigma_{eik}A_{ik}T_{ek}^n), \quad (10)$$

$$-C_{vei}\kappa_{pei}\triangle t T_{ei}^n + [C_{vpi} + \frac{\triangle t}{\triangle V_i}\sum_{k\in N_i}(\sigma_{pik}A_{ik}) + C_{vei}\kappa_{pei}\triangle t]T_{pi}^n = C_{vpi}T_{pi} + \frac{\triangle t}{\triangle V_i}\sum_{k\in N_i}(\sigma_{pik}A_{ik}T_{pk}^n). \quad (11)$$

In Eqs.(9,10), γ_i^n and τ_i^n are defined as

$$\gamma_i^n \equiv [(T_{ri}^2)^n + T_{ri}^2](T_{ri}^n + T_{ri}), \quad (12)$$

$$\tau_i^n \equiv \kappa_{rei}[(T_{ei}^2)^n + (T_{ri}^2)^n](T_{ei}^n + T_{ri}^n)\triangle t, \quad (13)$$

The coefficients σ_{eik}, σ_{pik} and σ_{rik} in Eqs.(9-11) are

$$\sigma_{eik} \equiv \frac{\alpha_i\alpha_k\sigma_{ei}\sigma_{ek}}{l_k\alpha_i\sigma_{ei} + l_i\alpha_k\sigma_{ek}}, \quad (14)$$

$$\sigma_{pik} \equiv \frac{\alpha_i\alpha_k\sigma_{pi}\sigma_{pk}}{l_k\alpha_i\sigma_{pi} + l_i\alpha_k\sigma_{pk}}, \quad (15)$$

$$\sigma_{rik} \equiv \frac{\alpha_i\alpha_k\sigma_{ri}\sigma_{rk}}{l_k\alpha_i\sigma_{ri} + l_i\alpha_k\tilde{\sigma}_{rk}}(T_{rk}^2 + T_{ri}^2)(T_{rk} + T_{ri}). \quad (16)$$

σ_{rik}^n is the value σ_{rik} evaluated at T_{ri}^n and T_{ri}^n. The system of Eqs.(9-11) is nonlinear because σ_{rik}^n, γ_i^n, abd τ_i^n depend on T_{ei}^n, T_{pi} and T_{ri}^n.

The set of nonlinear difference equations, Eqs.(9-11), could be linearized, to get the following set of equations,

$$[a\gamma_i + \frac{\triangle t}{\triangle V_i}\sum_{k\in N_i}(\tilde{\sigma}_{rik}A_{ik}) + \tau_i]T_{ri}^n - \tau_i T_{ei}^n = a\gamma_i T_{ri} + \frac{\triangle t}{\triangle V_i}\sum_{k\in N_i}(\sigma_{rik}A_{ik}T_{rk}^n), \quad (17)$$

$$-\tau_i T_{ri}^n + [C_{vei} + \frac{\triangle t}{\triangle V_i}\sum_{k\in N_i}(\sigma_{eik}A_{ik}) + \tau_i + C_{vei}\kappa_{pei}\triangle t]T_{ei}^n - C_{vei}\kappa_{pei}\triangle t T_{pi}^n = C_{vei}T_{ei} + \frac{\triangle t}{\triangle V_i}\sum_{k\in N_i}(\sigma_{eik}A_{ik}T_{ek}^n), \quad (18)$$

$$-C_{vei}\kappa_{pei}\triangle t T_{ei}^n + [C_{vpi}T_{pi}^n + \frac{\triangle t}{\triangle V_i}\sum_{k\in N_i}(\sigma_{pik}A_{ik}) + C_{vei}\kappa_{pei}\triangle t]T_{pi}^n = C_{vpi}T_{pi} + \frac{\triangle t}{\triangle V_i}\sum_{k\in N_i}(\sigma_{pik}A_{ik}T_{pk}^n). \quad (19)$$

Here σ_{rik}, γ_i, abd τ_i are σ_{rik}^n, γ_i^n, abd τ_i^n but evaluated at the temperatures at $t = 0$, T_{ei}, T_{pi} and T_{ri}.

3.2 Operator Split Approaches for Plasma 3-T Diffusion Equations

One could try to iteratively solve the nonlinear system, Eqs.(9-11), but most existing solvers only could deal with linear systems. Although existing linear solvers seem working for coupled linear systems, for example, the system of Eqs.(17-19), it is hard to find an iterative solver working for the coupled linear system, since many iterative solvers decouple a coupled system into three uncoupled systems at some preliminary step, for example, within coarse grids of multigrid methods, and then solve the coupled system at the fine grid. For strongly coupled systems, such as Eqs.(17-19), these iterative solvers often fail to converge.

In this subsection, we will propose an operator-split approach to approximately solve Eqs.(1-3). Only a single variable, T_r, or T_e, or T_p is solved in each step of the operator-split approach. We first write the system of Eqs.(1-3) into three sets, which will be successively solved,

$$\begin{cases} a\frac{\partial\phi}{\partial t} = -\bigtriangledown\cdot\mathbf{F}_r + S_r \\ C_{ve}\frac{\partial T_e}{\partial t} = -S_r + fS_e \\ C_{vp}\frac{\partial T_p}{\partial t} = -fS_e \end{cases} \quad (20)$$

$$\begin{cases} C_{ve}\frac{\partial T_e}{\partial t} = -\bigtriangledown\cdot\mathbf{F}_e + fS_e \\ \\ C_{vp}\frac{\partial T_p}{\partial t} = -fS_e \end{cases} \tag{21}$$

$$\begin{cases} C_{ve}\frac{\partial T_e}{\partial t} = fS_e \\ \\ C_{vp}\frac{\partial T_p}{\partial t} = -\bigtriangledown\cdot\mathbf{F}_p \end{cases} \tag{22}$$

Here $f \equiv \frac{1}{3}$.

Therefore, to solve the original system, Eqs.(1-3), for one time step, we solve the system Eq.(20) first for the time step, which we called step 1, then we solve the system of Eqs.(21) called step 2 using the results obtained from step 1 as an initial condition, after that using the results of step 2, we finally solve Eqs.(22) called step 3. After these three steps, we will have updated the solution of Eqs.(1-3) one time step.

To solve Eq.(20) for one time step, considering a cell in an unstructured mesh, the red cell as shown in Fig.1, we integrate Eq.(20) over the cell and one time step $0 < t < \triangle t$ with $\triangle t$ the size of time step. After converting the volume integral into a surface integral over the enclosed surface of the cell for the fluxes and approximately evaluating the fluxes at cell interfaces through the temperatures at $t = \triangle t$, we get the following equation,

$$a\phi_i^n = a\phi_i - \frac{\triangle t}{\triangle V_i}\sum_{k\in N_i}\overline{F}_{rik}A_{ik} + \overline{S}_{ri}\triangle t, \tag{23}$$

$$C_{vei}T_{ei}^n = C_{vei}T_{ei} - \overline{S}_{ri}\triangle t + \overline{S}_{ei}\triangle t, \tag{24}$$

$$C_{vpi}T_{pi}^n = C_{vpi}T_{pei} - \overline{S}_{ei}\triangle t. \tag{25}$$

Here $\overline{S}_{ri}$ (or $\overline{S}_{ei}$) is the source terms defined as

$$\overline{S}_{ri} \equiv \frac{1}{\triangle t\triangle V_i}\int_0^{\triangle t}\int_{\triangle V_i} S_r(t,\mathbf{r})dVdt.$$

The superscript *n* in Eq.(23) stands for the *new* time $\triangle t$. ϕ_i^n, T_{ei}^n, and T_{pi}^n are the cell averages of ϕ, T_e, and T_p at $t = \triangle t$,

$$\phi_i^n \equiv \frac{1}{\triangle V_i}\int_{\triangle V_i}\phi(\triangle t,\mathbf{r})dV,$$

$$T_{ei}^n \equiv \frac{1}{\triangle V_i}\int_{\triangle V_i} T_e(\triangle t,\mathbf{r})dV,$$

$$T_{pi}^n \equiv \frac{1}{\triangle V_i}\int_{\triangle V_i} T_p(\triangle t,\mathbf{r})dV.$$

ϕ_i, T_{ei}, and T_{pi} are similarly defined at *t = 0*. $\overline{F}_{rik}$ in Eq.(23) is the time-averaged flux across the interface A_{ik} and is defined as

$$\overline{F}_{rik} \equiv \frac{1}{A_{ik}\triangle t}\int_0^{\triangle t}\int_{A_{ik}}\mathbf{F}_r\cdot d\mathbf{A}dt. \tag{26}$$

The summation in Eq.(23) is over the set N_i.

To approximately calculate the flux in Eq.(23), we evaluate the flux and the source term at the temperature at $\triangle t$. Thus we have

$$a\phi_i^n = a\phi_i - \frac{\triangle t}{\triangle V_i}\sum_{k\in N_i}F_{rik}^nA_{ik} + S_{ri}^n\triangle t. \tag{27}$$

$$C_{vei}T_{ei}^n = C_{vei}T_{ei} - S_{ri}^n\triangle t + S_{ei}^n\triangle t, \tag{28}$$

$$C_{vpi}T_{pi}^n = C_{vpi}T_{pei} - S_{ei}^n\triangle t. \tag{29}$$

Here the superscript *n* stands for the evaluation at $t = \triangle t$, F_{rik}^n is the flux evaluated at $t = \triangle t$, defined as

$$F_{rik}^n \equiv \frac{1}{A_{ik}}\int_{A_{ik}}\mathbf{F}_r(\triangle t,\mathbf{r})\cdot d\mathbf{A}. \tag{30}$$

In Eqs.(27-29), we have also evaluated the interaction between radiation and material and the interaction between electrons and ions at $t = \triangle t$.

$$S_{ri}^n \equiv \frac{1}{\triangle V_i}\int_{\triangle V_i} S_r(\triangle t,\mathbf{r})dV. \tag{31}$$

Now we move to the calculation of the fluxes from temperature needed in Eq.(27). As we stated before, there are discontinuities in diffusion coefficients across interfaces between cells, and thus spatial derivatives of temperature is discontinuous across the interfaces. Therefore, we could not use Taylor expansion across an interface to approximately evaluate flux if there is a strong discontinuity. Considering the interface between cell *i* and cell *k* in Fig.1, we use $\mathbf{l}_i$ to stand for the distance vector from the center of cell *i* to the center of the interface. l_i is the magnitude of $\mathbf{l}_i$, and we use $\mathbf{l}_k$ to denote the distance vector from the center of cell *k* to the center of the interface, l_k is its magnitude, $\mathbf{n}_k$ is the unit vector along $\mathbf{l}_k$. We use $\mathbf{n}_{ik}$ to denote the normal direction of the interface. We define α_i and α_k are the projections of the directions $\mathbf{l}_i$ and $\mathbf{l}_k$ along the normal direction.

$$\alpha_i \equiv \mathbf{n}_{ik}\cdot(\mathbf{l}_i/l_i), \quad \alpha_k \equiv -\mathbf{n}_{ik}\cdot(\mathbf{l}_k/l_k).$$

The radiation energy flux across the interface [1,2]

$$F_{rik} = -\sigma_{rik}(\phi_k - \phi_i), \tag{32}$$

with definition

$$\sigma_{rik} \equiv \frac{\alpha_i\alpha_k\sigma_{ri}\sigma_{rk}}{l_k\alpha_i\sigma_{ri} + l_i\alpha_k\sigma_{rk}}. \tag{33}$$

Here σ_{ri} and σ_{rk} are σ_r evaluated at cell *i* and cell *k* respectively.

We would like to point out that Eq.(16) are similar, but different. Equation (16) is the expression of the flux in term of the difference in T_r, but Eq.(33) is the one in term of the difference in ϕ.

To eliminate T_{pi}^n, From Eq.(29), and get

$$T_{pi}^n = \frac{T_{pi} + f(c_{vei}/c_{vpi})\kappa_{pei}\triangle tT_{ei}^n}{1 + f(c_{vei}/c_{vpi})\kappa_{pei}\triangle t}. \tag{34}$$

Also, from Eq.(28) we have

$$T_{ei}^n - T_{ei} = -\frac{ac\kappa_{pi}\triangle t}{c_{vei}}[(T_{ei}^n)^4 - (T_{ri}^n)^4) + f\kappa_{pei}\triangle t(T_{pi}^n - T_{ei}^n). \quad (35)$$

For the nonlinear term, $[(T_{ei}^n)^4 - (T_{ri}^n)^4)]$, we take the following approximation,

$$(T_{ei}^n)^4 - (T_{ri}^n)^4) \approx (T_{ei}^2 + T_{ri}^2)(T_{ei} + T_{ri})(T_{ei}^n - T_{ri}^n). \quad (36)$$

Through this approximation and Eqs.(34,35), we get

$$T_{ei}^n = \frac{1}{P}[T_{ei} + f\eta_i T_{pi} + \frac{ac\kappa_{pi}\triangle t}{c_{vei}}(T_{ei}^2 + T_{ri}^2)(T_{ei} + T_{ri})T_{ri}^n]. \quad (37)$$

Here P and η_i are defined as

$$P \equiv 1 + \frac{ac\kappa_{pi}\triangle t}{c_{vei}}(T_{ei}^2 + T_{ri}^2)(T_{ei} + T_{ri}),$$

$$\eta_i \equiv \frac{\kappa_{pei}\triangle t}{1 + f(c_{vei}/c_{vpi})\kappa_{pei}\triangle t}.$$

Substituting Eq.(37) for T_{ei}^n into Eq.(36), and putting the result into the souce term of Eq.(27), we have

$$S_{ri}^n\triangle t = \frac{1}{P}ac\rho_i\kappa_{pi}\triangle t(T_{ei}^2 + T_{ri}^2)(T_{ei} + T_{ri}) [T_{ei} + f\eta_i T_{pi} - (1 + f\eta_i)T_{ri}^n]. \quad (38)$$

To solve for T_{ri}^n in Eq.(27) with Eq.(37), we approximately T_r^n in Eq.(38) as

$$T_{ri}^n \approx \frac{3}{4}T_{ri} + \frac{1}{4T_{ri}^3}\phi^n. \quad (39)$$

Thus, we rewrite Eq.(38) as

$$S_{ri}^n\triangle t = a(\chi_i - \xi_i\phi^n). \quad (40)$$

Here

$$\chi_i \equiv \frac{1}{P_i}c\rho_i\kappa_{pi}\triangle t(T_{ei}^2 + T_{ri}^2)(T_{ei} + T_{ri}) [T_{ei} + f\eta_i T_{pi} - \frac{3}{4}(1 + f\eta_i)T_{ri}],$$

$$\xi_i \equiv \frac{c\rho_i\kappa_{pi}\triangle t}{4P_i T_{ri}^3}(T_{ei}^2 + T_{ri}^2)(T_{ei} + T_{ri})(1 + f\eta_i).$$

With this approximation, we get the linear system for ϕ_i^n,

$$[a(1 + \xi_i) + \frac{\triangle t}{\triangle V_i}(\sum_{k\in N_i}\sigma_{rik}^h A_{ik})]\phi_i^n = a(\phi_i + \chi_i) + \frac{\triangle t}{\triangle V_i}\sum_{k\in N_i}(\sigma_{rik}A_{ik}\phi_k^n), \quad (41)$$

The linear system, Eq.(41), could be iteratively solved for ϕ_i^n with $i = 1, 2, ...N$. For a given set of initial values of ϕ_i, T_{ei} and T_{pi}, we initial guess ϕ_i^n as ϕ_i. Then for each *i*, using most recent values of ϕ_k^n on all the neighboring cells *k*, we evaluate the right sides of Eq.(41) to update ϕ_i^n. After repeating this for each cell *i*, we will have finished one iteration. Of course, we could use any existing linear solver to iteratively solve the system.

Thus, we have solved one step of the three in the operator-splitting approach. The solution of this step is considered the initial condition of the second step, Eq.(21). We apply the same approach with Eq.(20) to Eq.(21), we get

$$C_{vei}T_{ei}^n = C_{vei}T_{ei} - \frac{\triangle t}{\triangle V_i}\sum_{k\in N_i}F_{eik}^n A_{ik} + fC_{vei}\kappa_{pei}\triangle t(T_{pi}^n - T_{ei}^n). \quad (42)$$

Here F_{eik}^n is the flux evaluated at the interface between cells *i* and *k* and at the time $t = \triangle t$. For the flux to work for the discontinuity in diffusion coefficient, we have the following form of the flux,

$$F_{eik}^n = -\sigma_{eik}(T_{ek}^n - T_{ei}^n). \quad (43)$$

Here σ_{eik} is defined in Eq.(14). To eliminate T_{pi}^n in Eq.(42), we integrate the second equation of Eq.(21) over one time step and cell *i* and get

$$T_{pi}^n = \frac{T_{pi} + f(c_{vei}/c_{vpi})\kappa_{pei}\triangle t T_{ei}^n}{1 + f(c_{vei}/c_{vpi})\kappa_{pei}\triangle t.} \quad (44)$$

Putting Eqs.(44) into Eq.(42), we have the following linear system for T_{ei}^n,

$$C_{vei}(1 + f\eta_i)T_{ei}^n + \frac{\triangle t}{\triangle V_i}(\sum_{k\in N_i}\sigma_{eik}A_{ik})T_{ei}^n = C_{vei}(T_{ei} + \eta_i T_{pi}) + \frac{\triangle t}{\triangle V_i}\sum_{k\in N_i}(\sigma_{eik}A_{ik}T_{ek}^n). \quad (45)$$

Again, the set of Eq.(45) forms a linear system for T_{ei}^n, *i = 1, 2, ..., N*. This linear system could be iteratively solved. This concludes the second step of the operator-splitting approach.

The third and last step of our operator-splitting approach is similar to the second step described above. From Eq.(22) and through integration over one time step and cell *i*, we have

$$T_{ei}^n = \frac{1}{1 + \kappa_{pei}\triangle t}(T_{ei} + \kappa_{pei}\triangle t T_{pi}^n), \quad (46)$$

$$C_{vpi}T_{pi}^n = C_{vpi}T_{pei} - \frac{\triangle t}{\triangle V_i}\sum_{k\in N_i}F_{pik}^n A_{ik} - S_{ei}^n\triangle t. \quad (47)$$

Here F_{pik}^n is the evaluation of the flux at the cell interface between cells *i* and *k* and at $t = \triangle t$, which has the form,

$$F_{pik}^n = -\sigma_{pik}(T_{pk}^n - T_{pi}^n), \quad (48)$$

and σ_{pik} is defined in Eq.(15). Substituting Eqs.(46,48) into

Eq.(47) we have the following difference equation for T_{pi}^n,

$$C_{vpi}(1+\frac{c_{vei}}{c_{vpi}}a\xi_i)T_{pi}^n+\frac{\triangle t}{\triangle V_i}(\sum_{k\in N_i}\sigma_{pik}A_{ik})T_{pi}^n=$$
$$C_{vpi}(T_{pi}+\frac{c_{vei}}{c_{vpi}}a\xi_i T_{ei})+\frac{c_{vei}}{c_{vpi}}a\xi_i T_{ei}+$$
$$\frac{\triangle t}{\triangle V_i}\sum_{k\in N_i}(\sigma_{pik}A_{ik}T_{pk}^n). \quad (49)$$

Again, this equation forms a linear system for unknowns $T_{pi}^n, i=1,2,...,N$.

Therefore, in this approximation, the solution of the coupled plasma 3-T diffusion equations for one time step is decomposed into three independent linear systems, Eqs.(41,45,49), which are successively solved with the solution of a previous step as the initial condition of the subsequent step. This operator-splitting approach turns out to be useful and practical since many existing solvers don't work for coupled linear or nonlinear systems.

At the end of this section, we would like to point out that some common operator-splitting approaches don't work well for some problems. Here are two examples. The first one is to separate diffusion and the iteration between material and radiation. Only three independent diffusions are involvedin the first step of this approach, and only interactions are involved in the second step. In both step of this approach, tepmeratures are fully implicitly solved. . Another inappropriate operator-splitting approach that is currently used is very similar to what we proposed in this paper, but the following approximation is used to linearize the resulting difference eqations,

$$(T_r)^n)^4-(T_e^4)^4\approx T_r^4-T_e^4+4(T_e^3T_e^n-T_r^3T_r^n). \quad (50)$$

We will show the problems of these two approaches through numerical examples in the next section.

4. Numerical Examples

In this section we will provide numerical examples to show the features of the schemes described in Sections 3. The first example involves only diffusion of radiation temperature. There are no interaction between radiation and electron, and between electrons and ions. Initially, there are two materials separated by the circle as shown in the middle image of Fig.2. There is a thin layer between two materials. Within the thin layer cells are mixed, and interfaces between materials are linearly reconstructed. Radiation temperatures are 1.0 in the inner and 4.0 outer regions respectively. The middle image of the figure displays the diffusion coefficient. In the image at the right of Fig.2, we show the radiation temperature after one time step. In Fig.3 we show the results after 10 time steps. In the figure, we also show the result from the numerical scheme of completely nonlinear and fully coupled system, Eqs.(9-11).

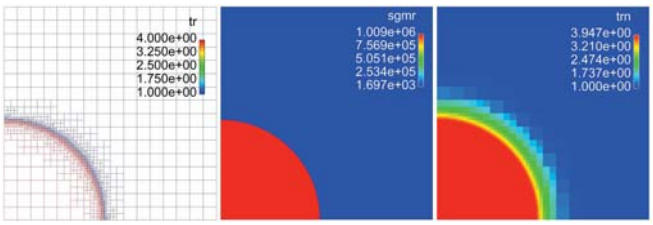

Fig. 2: The mesh, diffusion coefficient, and radiation temperature after one time step. The problem involve only radiation diffusion.

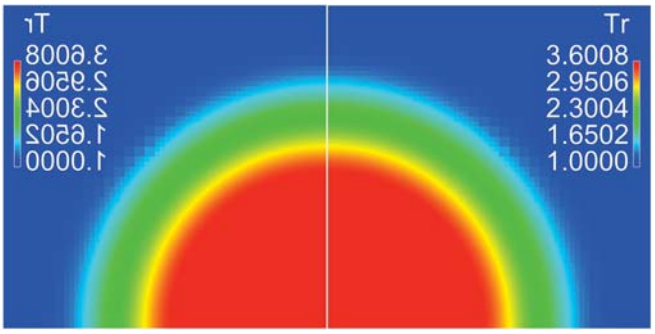

Fig. 3: The radiation temperature after 10 time steps. The image at the right is from the scheme presented in this paper, and the image at the left is from scheme Eq.(9-11), which is completely nonlinear and fully coupled.

The second example is a 3-T problem with the same geometry as the one in the last example. The feature of this problem includes large radiation diffusion coefficient, small diffusion coefficients of electrons and ions, large heat capacity, and strong coupling between radiation and electrons and between electrons and ions. Initially, the temperatures of radiation, electron, and ion are the same in the either inner or outer region, and they are 1.0 and 4.0. In Fig.4, we show the solutions after one time step. The temperatures at the bottom are from the scheme in this paper, and the temperatures at the top are obtained from the completely nonlinear and fully coupled scheme, Eqs.(9-11).

We would like to point out that some operator-splitting schemes don't work for this problem. For example, the operator-spliting scheme that completely separate diffusion and interaction results in the solution shown n Fig.5 after the time step. As the result, temperatures of electrons and ions almost don't change. This is obviously incorrect. For this problem, another operator-splitting scheme, which uses the linearization, Eq.(50), to remove the nonlinearity, produces the solution shown in Fig.6, in which temperature of electrons is much overheated. We would like to point out that even with much smaller time step, the operator-splitting approach that uses the approximation, Eq.(50), will produce this large overheat.

The last example is the same problem as the previous

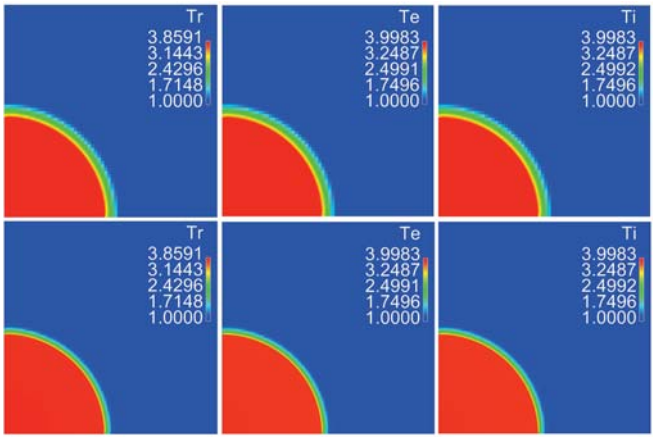

Fig. 4: The numerical solutions after one time step for a 3-T problem. The temperatures at the bottom are from the scheme described in this paper, and the ones at the top are obtained through the completely nonlinear and fully coupled scheme, Eqs.(9-11).

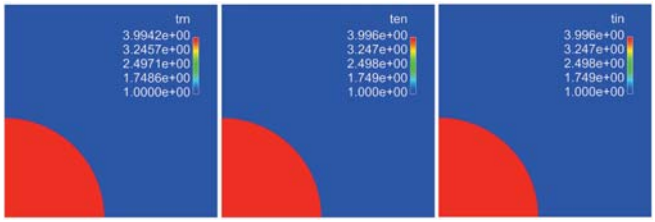

Fig. 5: The numerical solutions after the one time step obtained from an inappropriately splitting scheme, which separates diffusion and interaction completely. The solution is obviously incorrect.

one, but in three dimensions. Figure 7 displays the solutions after 10 time steps from two numerical schemes, one is the scheme described in this paper Eqs.(41,45,49)(the images at the bottom) and the other is the linear but fully coupled scheme Eqs.(17-19) (the images at the top).

5. Conclusions

Mixed cells are often encountered in numerical simulations. To resolve sub-cell structure of thermally non-equilibrium state within a mixed cell, we have implemented an approach to divide each mixed cell into a set of unstructured cells through linear interface reconstruction in two- and three-dimensions, and then to solve 3-T radiation diffusion equations on the reconstructed meshes. The reconstructed meshes include arbitrarily polygons in two dimensions and arbitrarily polyhedrons in three dimensions.

Typically, numerical schemes for 3-T radiation diffusion equations on the resulting polyhedral meshes are coupled systems of three temperatures, T_r, T_e and T_i. Unfortunately, for many problems, most linear solvers failed to work for the coupled system defrived from plasma 3-T equations, and some operator-splitting schemes don't work either. In this paper, we have developed an operator-splitting scheme for plasma 3-T diffusion equations, which will give reasonable solutions for many problems some other operator-splitting scheme failed. The calculation of energy fluxes in the scheme is based on the conservation of energy across interfaces between cells. Therefore the scheme is accurate for the discontinuity of material properties across a cell interface. We have demonstrated the properties of the scheme through numerical examples.

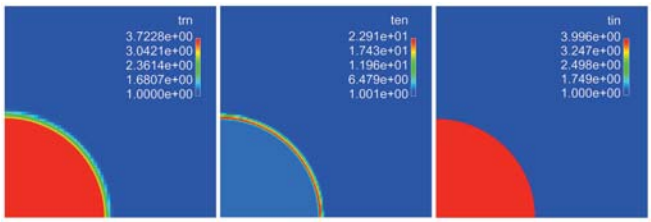

Fig. 6: The numerical solutions after the one time step obtained from an inappropriately splitting scheme, which uses the linearization Eq.(50). The solution is obviously incorrect, because the temperatures of electrons and ions are much overheated.

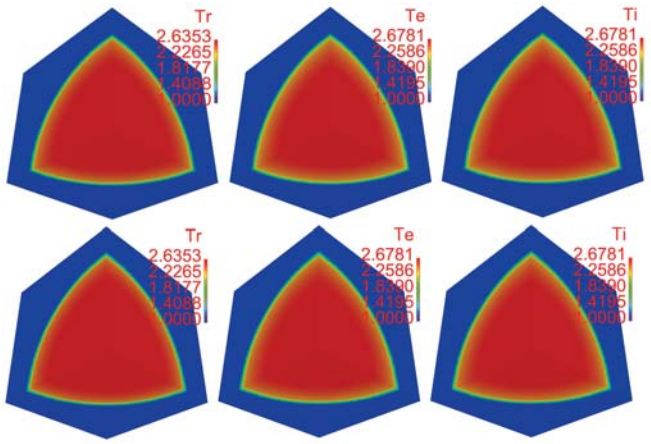

Fig. 7: The numerical solutions after ten time steps for a 3-T problem. The temperatures at the bottom are from the scheme described in this paper, and the ones at the top are obtained through the linear but fully coupled scheme (18-20).

References

[1] W. Dai and A. J. Scannapieco. "Second-order accurate interface- and discontinuity-aware diffusion solvers in two and three dimensions," *J. Comput. Phys.*, vol. 281, pp. 982-1002, 2015.

[2] W. Dai and A. J. Scannapieco. "Interface-and discontinuity-aware numerical schemes for plasma 3-T radiation diffusion in two and three dimensions," *J. Comput. Phys.*, vol. 300, pp. 643-664, 2015.

Chaotic Motion of Single-Walled Carbon Nanotube Due to Damping Effects

Tai-Ping Chang[1] **and Quey-Jen Yeh**[2]
[1] *Department of Construction Engineering, National Kaohsiung First University of Science and Technology, Kaohsiung, Taiwan*
[2] *Department of Business Administration, National Cheng-Kung University, Tainan, Taiwan*

Abstract - *This paper investigates the effects on chaotic motion of single-walled carbon nanotube (SWCNT) subject to the linear and nonlinear damping. By using the Hamilton's principle, the nonlinear governing equation of the single-walled carbon nanotube embedded in a matrix is formulated. The Galerkin's method is utilized to simplify the integro-partial differential equation into a nonlinear dimensionless governing equation for the SWCNT, which turns out to be a forced Duffing equation. The variations of the Lyapunov exponents of the SWCNT with damping and harmonic forcing amplitudes are studied. Based on the calculations of the top Lyapunov exponent, it is concluded that the chaotic motion of the SWCNT occurs when the amplitude of the periodic excitation exceeds certain value, besides, the chaotic motion of the SWCNT occurs with small linear damping and tiny nonlinear damping.*

Keywords: Chaotic motion, Damping, Lyapunov exponents, Single-walled carbon nanotube.

1 Introduction

Carbon nanotubes (CNTs) has drawn worldwide attention because of their potential applications in the fields of chemistry, physics, nano-engineering, electrical engineering, materials science, reinforced composite structures and construction engineering [1-3] . However, the study about the chaotic motion of nonlinear system of single-walled carbon nanotubes is very limited. The chaotic motion is mainly attributed due to the nonlinear effects in the physical system. For a single-walled carbon nanotube (SWCNT) system, the nonlinear effects may be due to the elastic elements, nonlinear damping, system with fluids, nonlinear boundary conditions, etc. In the present study, the chaotic motion of nonlinear vibration of the single-walled carbon nanotube (SWCNT) subjected to linear and nonlinear damping is investigated by considering the effects of the geometric nonlinearity. The small scale effects on the nonlinear vibration of the SWCNT are considered by using the theory of nonlocal elasticity. Based on the Hamilton's principle, the nonlinear governing equations of the single-walled carbon nanotube subjected to linear and nonlinear damping are formulated. The Galerkin's method is utilized to discretize the integro-partial differential equation leading to a nonlinear dimensionless governing equation for the SWCNT, which turns out to be a forced Duffing equation with the linear and nonlinear damping. In the past, many researches have been reported on the chaotic motion of forced Duffing equations [4-7]. The main purpose of the present study is to investigate the chaotic behavior of the nonlinear dimensionless governing equation under linear and nonlinear damping by computing the Lyapunov exponents, which have been reported in several researches [8-9].

2. Governing equation of nonlinear vibration

The single-walled carbon nanotube (SWCNT) embedded in a matrix with the linear and nonlinear damping is modeled as a single-tube pipe which has the radius R . The thickness of the tube is h , the length is L , the Young's modulus of elasticity is E and the mass density of SWCNT is ρ . The linear damping coefficient of the matrix is c_1 and the nonlinear damping coefficient of the matrix is c_3 . In addition, the boundary conditions of the SWCNT are considered as simply-supported at both ends.

Based on the Hamilton's principle and nonlocal elasticity theory, the nonlocal governing equations of the SWCNT in terms of the displacements can be obtained as follows:

$$EI\frac{\partial^4 w}{\partial x^4}+\left[\frac{\mathrm{EA}}{2L}\int_0^L\left(\frac{\partial w}{\partial x}\right)^2 dx\right]\frac{\partial^2}{\partial x^2}\left[(e_0a)^2\frac{\partial^2 w}{\partial x^2}-w\right]=\rho\mathrm{A}\frac{\partial^2}{\partial \bar{t}^2}\left[(e_0a)^2\frac{\partial^2 w}{\partial x^2}-w\right]$$
$$+c_1\frac{\partial}{\partial \bar{t}}\left[(e_0a)^2\frac{\partial^2 w}{\partial x^2}-w\right]+c_3\frac{\partial}{\partial \bar{t}}\left[(e_0a)^2\frac{\partial^2 w}{\partial x^2}-w\right]^3+q(x,\bar{t})-(e_0a)^2\frac{\partial^2 q(x,\bar{t})}{\partial x^2} \quad (1)$$

where $\bar{t}$ denotes the time, $q(x,\bar{t})$ is distributed transverse load, e_0 is a constant appropriate to each material, a is an

internal characteristic length (e.g., length of C–C bond, lattice parameter, and granular distance). Beside, c_1 and c_3 are the linear and nonlinear damping coefficients respectively. In this study, we consider the nonlinear viscous damping since it is shown more effective in suppressing the resonant peak of a nonlinear system than linear damping.

Now we utilize one term approximation to obtain the displacement for the nonlinear system based on Galerkin's approach, then the displacement function can be written as follows:

$$w(x,\bar{t}) = \bar{W}(\bar{t})\sin\frac{\pi x}{L} \tag{2}$$

where $\bar{W}(\bar{t})$ is the function of time $\bar{t}$.

Substituting Eq. (2) into Eq. (1), multiplying $\sin(\pi x/L)$ and integrating along the nanotube length, we can come up with the following nonlinear differential equation:

$$\frac{d^2\bar{W}}{d\bar{t}^2} + \omega_0^2\bar{W} + C_1\frac{d\bar{W}}{d\bar{t}} + K_N\bar{W}^3 + C_3\frac{d\bar{W}^3}{d\bar{t}} = \bar{Q}_0 + \bar{Q}_1(\bar{t}) \tag{3}$$

where

$$\omega_0 = \sqrt{\frac{1}{\rho A}\left[\frac{EI(\pi/L)^4}{1+(e_0a)^2(\pi/L)^2}\right]}, C_1 = \frac{c_1}{\rho A}, K_N = \frac{E\pi^4}{4\rho L^4}, C_3 = \frac{3c_3}{4\rho A}. \tag{4}$$

In addition, $\bar{Q}_0$ denotes the time-independent loading and $\bar{Q}_1(\bar{t})$ denotes the time-dependent loading individually.

For convenience, the following parameters are introduced to deal with the tiny values in nano systems:

$$W = \frac{\bar{W}}{L}, t = \frac{\bar{t}}{T}, T = \sqrt{\rho A\left[\frac{1+(e_0a)^2(\pi/L)^2}{EI(\pi/L)^4}\right]} \tag{5}$$

Substituting Eq. (5) into Eq. (3), the following dimensionless equations are obtained:

$$\frac{d^2W}{dt^2} + W + \mu_1\frac{dW}{dt} + \gamma W^3 + \mu_3\frac{dW^3}{dt^3} = Q_0 + Q_1\cos(\Omega t) \tag{6}$$

where

$$\mu_1 = C_1T, \gamma = K_NT^2L^2, \mu_3 = C_3\frac{L^2}{T}, \quad Q_0 = \bar{Q}_0\frac{T^2}{L}, Q_1\cos(\Omega t) = \bar{Q}_1(\bar{t})\frac{T^2}{L}. \tag{7}$$

where the time-dependent loading is assumed as a periodic excitation, and Ω is the driving frequency of the periodic loading. Eq. (6) is a forced Duffing equation with the linear and nonlinear damping.

3. Chaotic motion of nonlinear system

The main purpose of the present study is to investigate the chaotic motion of the nonlinear differential equation shown in Eq. (6) by evaluating Lyapunov exponents. The chaotic phenomena occurs when Lyapunov exponents changes from negative to positive. In order to compute Lyapunov exponents, it is necessary to study the growth of vectors tangent to the surface defined by the equations of motion in the phase space of the physical system. In the present study, the approach to evaluate Lyapunov exponents is based on Wolf's algorithm [8] so that the system as defined in Eq. (6) can be written into the following simultaneous equations, with

$W = W_1, \dot{W} = W_2, t = W_3$:

$$\dot{W}_1 = W_2 \tag{8}$$

$$\dot{W}_2 = -W_1 - \gamma W_1^3 - \mu_1W_2 - \mu_3W_2^3 + Q_0 + Q_1\cos(\Omega t) \tag{9}$$

$$\dot{W}_3 = 1.0 \tag{10}$$

where "$\bullet$" denotes $\frac{d}{dt}$.

Based on Wolf's basic idea, is it necessary to evaluate the long-term evolution of an infinitesimal n-sphere, here n=3, of initial conditions. Lyapunov exponents are denoted as follows:

$$\lambda_i = \lim_{t\to\infty}\frac{1}{t}\log_2\frac{d_i(t)}{d_i(0)} \quad i = 1,2,3 \tag{11}$$

where λ_i are ordered from largest to smallest and $d_i(t)$ are the lengths of the ellipsoidal principal axes of the sphere. In order to be consistent with the definition of Lyapunov exponents, the separations of the initial conditions must be as small as the computer limitations tolerance. The nonlinear differential equations are integrated with these different initial conditions. However, in a chaotic system, the conditions of small separations can't be guaranteed, which is required for the convergence of Lyapunov exponents spectrums. In order to cope with this problem, a "reference" trajectory is set up by the action of the nonlinear equations on some initial conditions. Then the trajectories of points on the surface of the sphere are computed by integrating the linearized equations of motion utilizing initial conditions infinitesimally separated from the reference trajectory. The principal axes are denoted by the evolution from the linearized equations of an initially orthonormal vector frame fixed to the reference trajectory. For a system shown in Eq. (6), dimension n=3 and nine linearized equations can be established. In Eq. (8-10), there are several parameters which can influence the chaotic

motion of the system, such as γ, μ_1, μ_3, Q_0, Q_1, Ω and the initial conditions. First of all, we deal with the system without the nonlinear damping parameter μ_3 and fix all the parameters except Q_1, we vary the amplitude of the periodic excitation from $Q_1 = 0$ to a certain value when the top Lyapunov exponents change from negative to positive, that is when the chaotic motion occurs. After that we increase the value of Q_1 gradually, then at certain value of Q_1, the top Lyapunov exponents will change from positive to negative which implies that the motion of the system will change from chaotic motion to periodic motion until we hit the next critical value when the top Lyapunov exponents will change from negative to positive. The main purpose of the present study is to investigate the chaotic motion of the system shown in Eq. (6) with linear damping and nonlinear damping based on the computation of the top Lyapunov exponents, Therefore, after the first critical value of Q_1 is found, we fix the value of Q_1 slightly bigger than the critical one and all the parameters except the linear damping parameter μ_1. Then we can study the effect of linear damping parameter on the chaotic motion of the system based on the computation of the top Lyapunov exponents. As we increase the value of linear damping parameter gradually, the top Lyapunov exponents will change from positive to negative at a certain value of μ_1 so that the system will change from chaotic to periodic motion. Finally we fix all the parameters except the nonlinear damping parameter to study the effect of nonlinear damping parameter on the chaotic motion of the system, it can be detected that with a small value of nonlinear damping parameter, the top Lyapunov exponents of the system would change from positive to negative so that the chaotic motion of the system would switch back to periodic motion.

4. Numerical results and discussions

In the numerical computations, the simply supported boundary conditions are considered for the SWCNT. The dimensionless governing equation for SWCNT is written as in Eq (6), the main purpose of the present study is to investigate the chaotic motion for the nonlinear system in Eq. (6) with linear and nonlinear damping; therefore, the investigations are divided into two sections below.

A. The nonlinear system with linear damping only, $\mu_3 = 0$.

First of all, the numerical values of the parameters in Eq. (6) are fixed as follows:

$$\mu_1 = 0.1, \gamma = 1.0, \mu_3 = 0.0, Q_0 = 3.0, \Omega = 1.0. \quad (12)$$

In addition, the initial conditions in Eqs. (8-10) are as follows:

$$W_1(0) = 1.0, W_2(0) = 0.0, W_3(0) = 0.0 \quad (13)$$

Now we gradually vary the amplitude of the periodic excitation Q_1 from $Q_1 = 0$ to $Q_1 = 30.0$. As we can see from Figs. 1a-1c, Lyapunov exponents of the system are computed for different values of Q_1. In Figs. 1a-1b, the top Lyapunov exponent is computed as $\lambda_1 = -0.00022$ when $Q_1 = 14.31$ as shown in Fig 1a; while $\lambda_1 = +0.00178$ when $Q_1 = 14.32$ as shown in Fig. 1b. Therefore, the system is originally stable under $Q_1 = 14.31$ because the top Lyapunov exponent is negative, then appears to be losing its stability when $Q_1 = 14.32$ because the top Lyapunov exponent changes from negative into positive, which implies the chaotic motion occurs when Q_1 is slightly larger than 14.32. Therefore, we conclude that the first critical value to produce the chaotic motion for the system is $Q_1 = 14.32$. Now we fix the value of Q_1 as $Q_1 = 16.0$, which is slightly bigger than the first critical value 14.32, all the other parameters remain the same as those in Eqs. (12-13). In Figs. 2a-2c, we plot the time history, phase portrait and Poincare map of SWCNT. As we can detect from Fig. 2c, the chaotic motion of the system is quite obvious. For simplicity, from now on we only present the top Lyapunov exponent for the nonlinear system. It is well known that the displacement of the system gets smaller as the linear damping parameter increases. In Figs. 3a-3c, we evaluate the top Lyapunov exponents by increasing the linear damping parameter from $\mu_1 = 0.1$ to $\mu_1 = 0.3$ individually. As we can detect from Figs. 3a-3b, the top Lyapunov exponents are still positive up to $\mu_1 = 0.28$, however, when $\mu_1 = 0.29$ the top Lyapunov exponent becomes negative as shown in Fig. 3c. In Figs. 4, we present the corresponding Poincare maps for linear damping parameter $\mu_1 = 0.3$, it is quite understood to notice that the Poincare map show periodic motion for the nonlinear system. Based on the above numerical computations, the chaotic motion will occur with small linear damping until the linear damping parameter exceeds the critical linear damping value, in the present case, $\mu_1 = 0.29$.

B. The nonlinear system with linear damping and nonlinear damping

Now we are ready to study the chaotic motion of the nonlinear system with both the linear and nonlinear damping. Here we adopt the same data as those in Eqs. (12-13) except the nonlinear damping parameter is added. Besides, we fix the amplitude of the periodic excitation as $Q_1 = 16.0$ because it is slightly over the first critical value to create the chaotic motion for the nonlinear system. We gradually increase the value of nonlinear damping from $\mu_3 = 0.001$ to $\mu_3 = 0.1$ for the system, it can be seen from Fig. 5a that the top Lyapunov exponent is $\lambda_1 = +0.004$ when $\mu_3 = 0.0055$; while the top Lyapunov exponent is $\lambda_1 = -0.004$ when $\mu_3 = 0.0060$ as shown in Fig. 5b. Therefore, we can conclude that the chaotic motion of the system still happens with tiny nonlinear damping until $\mu_3 = 0.0060$, when the nonlinear damping parameter is larger than 0.006, the periodic motion of the system is expected to appear. The corresponding Poincare maps are presented in Figs. 6a-6c, as it can be detected from Fig 6a, the nonlinear system still presents chaotic phenomena with tiny nonlinear damping parameter, however, the nonlinear system regains its stability, namely, periodic motion, with nonlinear damping parameter bigger than 0.006 as seen from Figs. 6b-6c. Based on the above numerical computations, the chaotic motion will occur with tiny nonlinear damping until the nonlinear damping parameter exceeds the critical damping value, in the present case, $\mu_3 = 0.0060$.

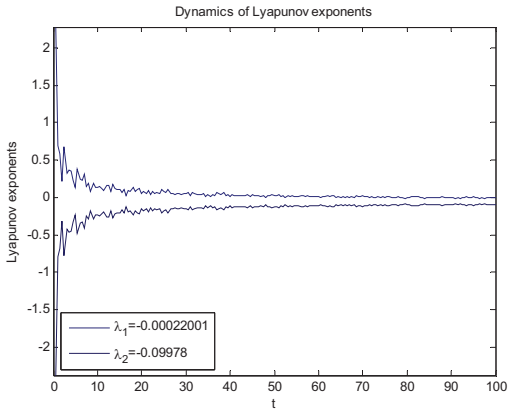

Fig. 1a. Lyapunov exponents versus time for $Q_1 = 14.31$.

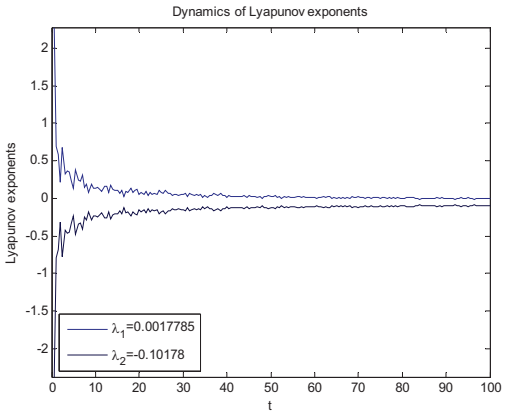

Fig. 1b. Lyapunov exponents versus time for $Q_1 = 14.32$.

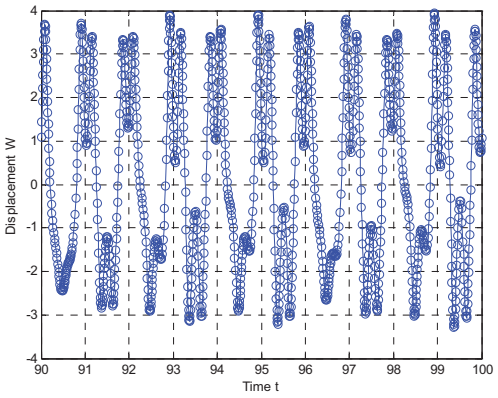

Fig. 2a. Time history of SWCNT.
$(\mu_1 = 0.1, \gamma = 1.0, \mu_3 = 0.0, Q_0 = 3.0, \Omega = 1.0, Q_1 = 16.0)$

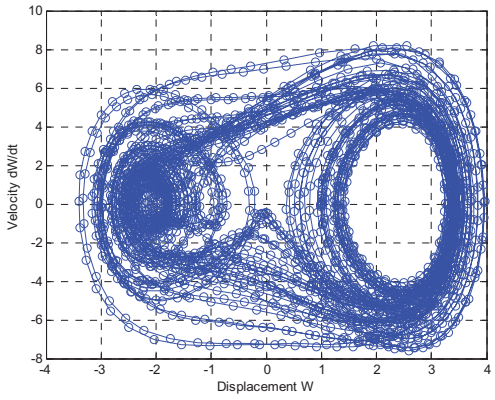

Fig. 2b. Phase portrait of SWCNT.
$(\mu_1 = 0.1, \gamma = 1.0, \mu_3 = 0.0, Q_0 = 3.0, \Omega = 1.0, Q_1 = 16.0)$

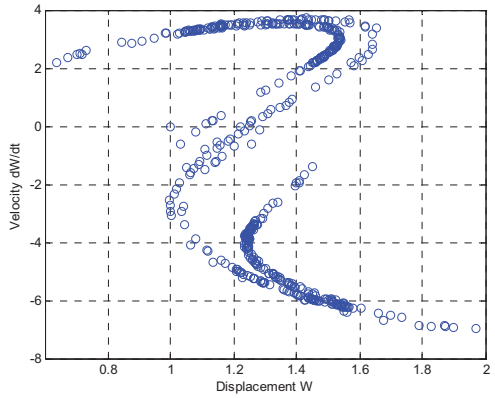

Fig. 2c. Poincare map of SWCNT.
($\mu_1 = 0.1, \gamma = 1.0, \mu_3 = 0.0, Q_0 = 3.0, \Omega = 1.0, Q_1 = 16.0$)

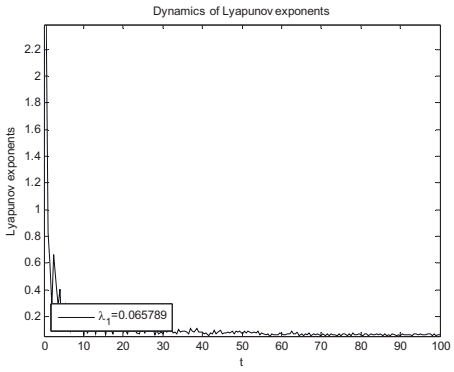

Fig. 3a. Top Lyapunov exponents versus time for
$\mu_1 = 0.1$.

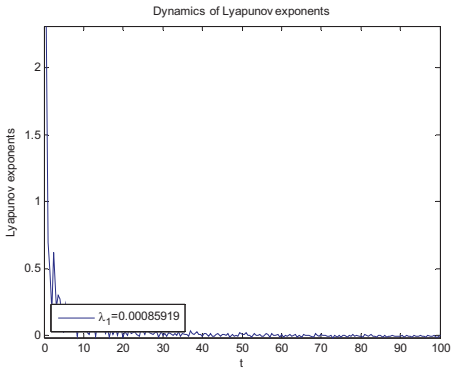

Fig. 3b. Top Lyapunov exponents versus time for
$\mu_1 = 0.28$.

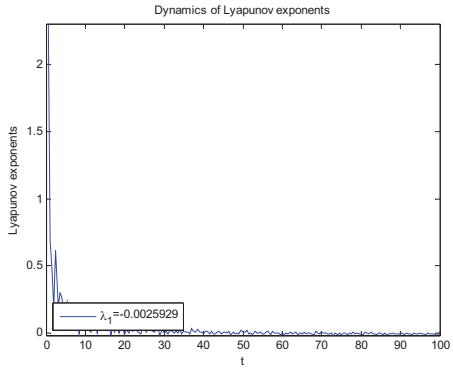

Fig. 3c. Top Lyapunov exponents versus time for
$\mu_1 = 0.29$.

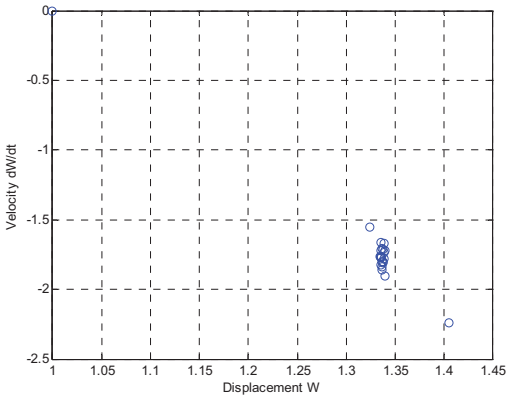

Fig. 4. Poincare map of SWCNT.
($\mu_1 = 0.3, \gamma = 1.0, \mu_3 = 0.0, Q_0 = 3.0, \Omega = 1.0, Q_1 = 16.0$)

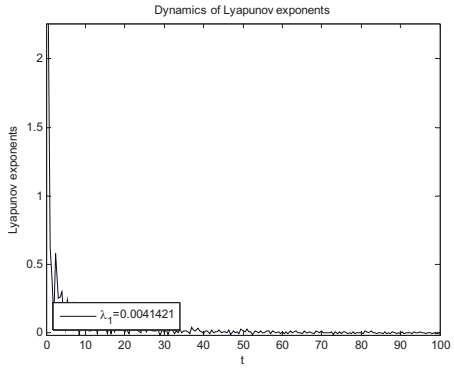

Fig. 5a. Top Lyapunov exponents versus time for
$\mu_1 = 0.1, \mu_3 = 0.0055$.

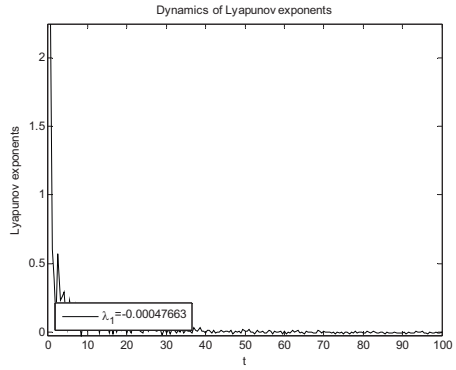

Fig. 5b. Top Lyapunov exponents versus time for $\mu_1 = 0.1, \mu_3 = 0.006$.

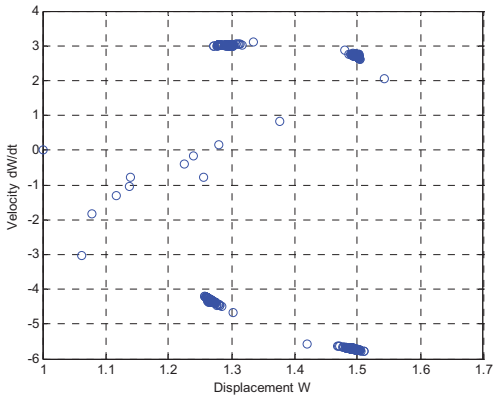

Fig. 6a. Poincare map of SWCNT.
$(\mu_1 = 0.1, \gamma = 1.0, \mu_3 = 0.001, Q_0 = 3.0, \Omega = 1.0, Q_1 = 16.0)$

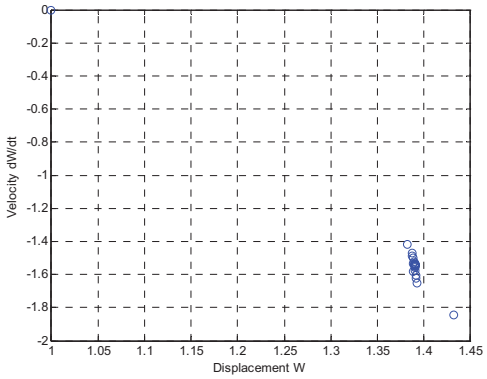

Fig. 6b. Poincare map of SWCNT.
$(\mu_1 = 0.1, \gamma = 1.0, \mu_3 = 0.01, Q_0 = 3.0, \Omega = 1.0, Q_1 = 16.0)$

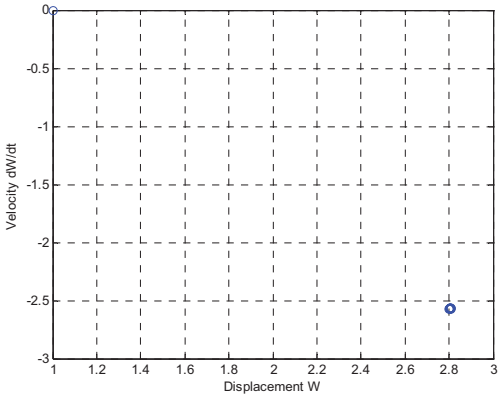

Fig. 6c. Poincare map of SWCNT.
$(\mu_1 = 0.1, \gamma = 1.0, \mu_3 = 0.1, Q_0 = 3.0, \Omega = 1.0, Q_1 = 16.0)$

5. Conclusions

In the present study, we study the effects on chaotic behaviors of single-walled carbon nanotube (SWCNT) due to the linear and nonlinear damping. By using the Hamilton's principle, the nonlinear governing equation of the single-walled carbon nanotube embedded in a matrix is derived. We utilize the Galerkin's method to discretize the integro-partial differential equation leading to a nonlinear dimensionless governing equation for the SWCNT, which turns out to be a forced Duffing equation with the linear and nonlinear damping. The chaotic phenomena occurs when the top Lyapunov exponent of the forced Duffing equation changes from negative to positive. Based on the computations of the top Lyapunov exponent, we can conclude that the chaotic motion of the nonlinear system occurs when the amplitude of the periodic excitation exceeds certain value by fixing all the other parameters. When the nonlinear system is without the nonlinear damping, the chaotic motion occurs with small linear damping until the linear damping parameter exceeds the critical linear damping value. Furthermore, if the system is with both the linear and nonlinear damping, the chaotic motion occurs with tiny nonlinear damping until the nonlinear damping parameter exceeds the critical damping value.

Acknowledgments This research was partially supported by the National Science Council in Taiwan through Grant No. MOST-103-2221-E-327-011. The authors are grateful for this support.

References

[1] S. Iijima, Helical microtubules of graphitic carbon, Nature 354 (1991) 56–58.
[2] K.T. Lau, C. Gu, D. Hui, A critical review on nanotube and nanotube/nanoclay related polymer composite materials, Compos. Part B 7 (2006) 425–436.
[3] Z. Spitalsky, D. Tasis, K. Papagelis, C. Galiotis, Carbon nanotube-polymer composites: chemistry, processing, mechanical and electrical properties, Prog. Polym. Sci. 35 (2010) 357–401.
[4] R.V. Dooren, H. Janssen, A continuation algorithm for discovering new chaotic motions in forced Duffing systems, J Comput Appl Math 66 (1996) 527-541.
[5] X. Han, Q. Bi, Bursting oscillations in Duffing's equation with slowly changing external forcing, Commu Nonlinear Sci Numer Simulat 16 (2011) 4146-4152.
[6] M.U. Akhmet, M.O. Fen, Chaotic period-doubling and OGY control for the forced Duffing equation, Commu Nonlinear Sci Numer Simulat 17 (2012) 1929-1946.
[7] A. Sharma, V. Patidar, G. Purohit, K.K. Sud, Effects on the bifurcation and chaos in forced Duffing oscillator due to nonlinear damping, 17 (2012) 2254-2269.
[8] A.Wolf, J.B. Swift, H.L. Swinney, J.A. Vastano, Determining Lyapunov exponents from a time series, Physica D 16 (1985) 285-317.
[9] A.R. Zeni, J.A.C. Gallas, Lyapunov exponents for a Duffing oscillator, Physica D 89 (1995) 71-82.

Statistical Characteristics of Multiple Scattered Electromagnetic Waves in the Collision Magnetized Turbulent Plasma

G. Jandieri[1] , J. Diasamidze[2], N. Mchedlishvili[3], and I. Nemsadze[2]
[1]Special Department, Georgian Technical University, Tbilisi, Georgia
[2]Physics Department, Batumi Shota Rustaveli State University, Batumi, Georgia
[3]Control System Department, Georgian Technical University, Tbilisi, Georgia

Abstract *- The features of the spatial power spectrum of multiple scattered electromagnetic waves in the collision magnetized turbulent plasma with strongly prolated anisotropic electron density irregularities are investigated analytically using the modify smooth perturbation method taking into account diffraction effects. Correlation functions and variances of the phase fluctuations are obtained for arbitrary correlation function of electron density fluctuations. Statistical moments of scattered ordinary and extraordinary waves and the „Double-humped Effect" are investigated analytically and numerically using the anisotropic Gaussian spectral function of electron density irregularities for the polar ionospheric F-region applying the experimental data.*

Keywords: plasma, ionosphere, irregularities, intensity, electromagnetic waves.

1 Introduction

Investigation of effects caused by the anisotropy of the *F* layer irregularities is of great interest in the ionospheric physics. It is well known that the irregularities are elongated in the direction of the geomagnetic field of lines, especially at high latitudes. The anisotropy is usually investigated by correlation analysis of radio signals from satellites, observed by space receiver on the ground. Ionospheric electron density irregularities cause fluctuations in the amplitude and phase of radio waves propagating through the ionosphere. Strong scattering anisotropy is observed at multiple scattering of electromagnetic (EM) waves on large-scale elongated inhomogeneities.

"Double-humped Effect", the features of the spatial power spectrum (SPS), spectral width and the displacement of its maximum of multiple scattered electromagnetic (EM) waves in the turbulent collisionless magnetized plasma was analyzed in [1,2]. The influence of the collision frequency between plasma particles on the statistical characteristics of scattered EM waves in the turbulent magnetized plasma with both electron density and external magnetic field fluctuations was investigated in [3,4] in the complex ray (-optics) approximation.

Within the scope of this paper we investigate evolution of the SPS of multiple-scattered radiation in the turbulent collision magnetized plasma with anisotropic electron density irregularities. Analytical expressions of the correlation function of phase fluctuations of both scattered ordinary and extraordinary waves are obtained for the arbitrary correlation functions of electron density fluctuation using modify smooth perturbation method taking into account the diffraction effects. The "Double-humped Effect" in the collision magnetized plasma with prolate electron density irregularities is considered for the first time. Formation of a gap in the SPS of scattered radiation for the anisotropic Gaussian spatial spectrum of electron density fluctuations at different angles of inclination of prolate irregularities with respect to the external magnetic field and anisotropy factor is analyzed numerically for the polar ionospheric *F*-region using the experimental data. Finally, paper concludes the obtain results and significance.

2 Statistical characteristics of the phase fluctuations in the collision magnetized plasma

Electric field in the turbulent collision magnetized plasma satisfies the wave equation:

$$\left(\frac{\partial^2}{\partial x_i \, \partial x_j} - \Delta \delta_{ij} - k_0^2 \, \varepsilon_{ij}(\mathbf{r}) \right) \mathbf{E_j}(\mathbf{r}) = 0 \qquad (1)$$

components of the dielectric permittivity are [5]:

$$\varepsilon_{xx} = 1 - \frac{\mathrm{v}\, g}{g^2 - u}, \quad \varepsilon_{xy} = -\varepsilon_{yx} = i \, \frac{\mathrm{v}\sqrt{u}\cos\alpha}{g^2 - u},$$

$$\varepsilon_{xz} = -\varepsilon_{zx} = -i \frac{\mathrm{v}\sqrt{u}\,\sin\alpha}{g^2 - u}, \quad \varepsilon_{yy} = 1 - \frac{\mathrm{v}(g^2 - u\sin^2\alpha)}{g\,(g^2 - u)},$$

$$\varepsilon_{yz}=\varepsilon_{zy}=\frac{u\,\mathrm{v}\sin\alpha\cos\alpha}{g\,(g^2-u)},\quad \varepsilon_{zz}=1-\frac{\mathrm{v}(g^2-u\,\cos^2\alpha)}{g\,(g^2-u)} \quad (2)$$

where: $g=1-i\,s$, $s=\nu_{eff}/\omega$, $\nu_{eff}=\nu_{ei}+\nu_{en}$ is the effective collision frequency of electrons with other plasma particles, α is the angle between the *Z*-axis (the direction of the wave propagation) and the static external magnetic field $\mathbf{H_0}$ in the *YZ* principle plane; $\omega_p(\mathbf{r})=[4\pi N(\mathbf{r})e^2/m]^{1/2}$ is the plasma frequency, $N(\mathbf{r})$ is the electron concentration, $u(\mathbf{r})=(e\,H_0(\mathbf{r})/m\,c\,\omega)^2$ and $\mathrm{v}(\mathbf{r})=\omega_p^2(\mathbf{r})/\omega^2$ are the magneto-ionic parameters.

Wave field we introduce as [1,2] $E_j(\mathbf{r})=E_{0j}\cdot$ $\cdot\exp(\varphi_1+\varphi_2+i\,k_\perp\,y+i\,k_0\,z)$ $(k_\perp<<k_0)$. Electron density fluctuations are random function of the spatial coordinates $\mathrm{v}(\mathbf{r})=\mathrm{v}_0\,[1+n_1(\mathbf{r})]$; $\varepsilon_{ij}(\mathbf{r})=\varepsilon_{ij}^{(0)}+\varepsilon_{ij}^{(1)}(\mathbf{r})$, $|\,\varepsilon_{ij}^{(1)}(\mathbf{r})\,|<<1$. First component represents zero-order approximation; fluctuations of complex phase are of the order $\varphi_1\sim\varepsilon_{ij}^{(1)}$, $\varphi_2\sim\varepsilon_{ij}^{(1)\,2}$. Polarization coefficients are [4,5]

$$\frac{<E_y>_{1,2}}{<E_x>_{1,2}}=-\,i\,\mathrm{P}''_j-s\,\mathrm{P}'_j\,,$$

$$\frac{<E_z>_{1,2}}{<E_x>_{1,2}}=i\,(m_1-s^2\,m_3)+s\,m_2\equiv i\,\Gamma''_j+s\,\Gamma'_j\,, \quad (3)$$

where: $\mathrm{P}''_j=2\sqrt{u_L}\,\left[\,(1-\mathrm{v})\mp s^2\,\alpha_0\,\right]\left(u_T\mp\sqrt{a_0}\right)^{-1}$,

$\mathrm{P}'_j=2\sqrt{u_L}\,\left[1\pm\alpha_0(1-\mathrm{v})\right]\left(u_T\mp\sqrt{a_0}\right)^{-1}$, upper sign (index 1) corresponds to the ordinary wave; the lower sign (index 2) to the extraordinary wave; $u_T=u\,\sin^2\alpha$, $u_L=u\,\cos^2\alpha$,

$$\alpha_0=\frac{b_0}{2\sqrt{a_0}}\,\frac{1}{u_T\mp\sqrt{a_0}},\ a_0=u_T^2+4\,u_L\left[(1-\mathrm{v})^2-s^2\right],$$

$$b_0=8\,(1-\mathrm{v})\,u_L,\ \ m_1=\frac{\sqrt{u_T}}{t_0}(\mathrm{v}+\sqrt{u_L}\,\mathrm{P}''_j),$$

$$m_2=\frac{\sqrt{u_T}}{t_0^2}\left[\mathrm{v}\,(t_0+t_3)+\sqrt{u_L}\,(t_3\,\mathrm{P}''_j+t_0\,\mathrm{P}'_j)\right],$$

$$m_3=\frac{\sqrt{u_T}}{t_0^2}\left[\mathrm{v}\,t_3+\sqrt{u_L}\ \mathrm{P}''_j(3-\mathrm{v})+\sqrt{u_T}\ t_3\,\mathrm{P}'_j)\right],$$

$t_0=1-u-\mathrm{v}+\mathrm{v}\,u_L$, $t_3=3+u-2\,\mathrm{v}$.

Taking into account the conditions characterizing the smooth perturbation method [6]

$$\left|\frac{\partial\varphi_1}{\partial z}\right|<<k_0\,|\,\varphi_1\,|\ ,\quad \left|\frac{\partial\varphi_2}{\partial z}\right|<<k_0\,|\,\varphi_2\,|\,,\ \left|\frac{\partial^2\varphi_1}{\partial z^2}\right|<<k_0\left|\frac{\partial\varphi_1}{\partial z}\right|,$$

in the first approximation we obtain:

$$\left[\frac{\partial^2\varphi_1}{\partial x_i\,\partial x_j}+\frac{\partial\varphi_0}{\partial x_i}\,\frac{\partial\varphi_1}{\partial x_j}+\frac{\partial\varphi_1}{\partial x_i}\,\frac{\partial\varphi_0}{\partial x_j}-\delta_{ij}\left(\Delta_\perp+2\,i\,k_\perp\,\frac{\partial\varphi_1}{\partial y}+\right.\right.$$

$$\left.\left.+\,2\,i\,k_0\,\frac{\partial\varphi_1}{\partial z}\right)-k_0^2\,\varepsilon_{ij}^{(0)}\right]E_{0j}=0\ , \quad (4)$$

where $\Delta_\perp=(\partial^2\varphi_1/\partial x^2)+(\partial^2\varphi_1/\partial y^2)$ is the transversal Laplasian.

2D Fourier transformation of the phase fluctuation in the principle plane (*YZ*)

$$\varphi_1(x,y,z)=\int_{-\infty}^{\infty}d\,k_x\int_{-\infty}^{\infty}d\,k_y\ \psi(k_x,k_y,z)\exp(i\,k_x x+i\,k_y y)\,,$$

gives the stochastic differential equation:

$$\frac{\partial\psi}{\partial z}+\frac{i\,\tilde d_1-\tilde d_2}{\Gamma''k_x+i\,(2k_0-s\,\Gamma'\,k_x)}\,\psi(k_x,k_y,z)=$$

$$-\frac{k_0^2}{\Gamma''\,k_x+i\,(2k_0-s\,\Gamma'\,k_x)}\left[\,Q_1(k_x,k_y,z)+i\,s\,Q_2(k_x,k_y,z)\,\right] \quad (5)$$

where: $\tilde d_1=-\,\mathrm{P}''\,k_x(k_y+k_\perp)+\Gamma''\,k_0\,k_x$, $\tilde d_2=k_y(k_y+2\,k_\perp)$

$+\,s\left[\,\mathrm{P}'\,k_x(k_y+k_\perp)-\Gamma'\,k_0\,k_x\right]$.

The solution of equation (5) satisfying the boundary condition $\psi(k_x,\,k_y,z=0)=0$ for *X* spectral component is:

$$\psi(k_x,k_y,L)=i\ \frac{k_0}{2}\,(Z'+i\,s\,Z'')\int_{-\infty}^{\infty}dz'\ n_1(k_x,k_y,z')$$

$$\exp\left(\frac{1}{4\,k_0^2}\left\{\left[\tilde d_2\,\Gamma''k_x-\tilde d_1(2\,k_0-s\,\Gamma'k_x)\right]-\right.\right.$$

$$\left.\left.-\,i\left[\tilde d_1\,\Gamma''k_x+\tilde d_2(2\,k_0-s\,\Gamma'k_x)\right]\right\}(L-z')\ \right), \quad (6)$$

here: $Z'=Z_{xx}+Z_{xy}+Z_{xz}$, $Z''=\tilde Z_{xx}+\tilde Z_{xy}+\tilde Z_{xz}$, $Z_{xx}=\varepsilon_{xx}^{(1)}$,

$Z_{xy}=\varepsilon_{xy}^{(1)}\,\mathrm{P}''+s^2\,\tilde\varepsilon_{xy}^{(1)}\,\mathrm{P}'$, $Z_{xz}=\varepsilon_{xz}^{(1)}\,\Gamma''+s^2\,\tilde\varepsilon_{xz}^{(1)}\,\Gamma'$,

$\tilde Z_{xx}=-\,\tilde\varepsilon_{xx}^{(1)}$, $Z_{xy}=-\,\varepsilon_{xy}^{(1)}\,\mathrm{P}'+\tilde\varepsilon_{xy}^{(1)}\,\mathrm{P}''$, $Z_{xz}=-\,\varepsilon_{xz}^{(1)}\,\Gamma'+\tilde\varepsilon_{xz}^{(1)}\,\Gamma''$.

Components of the permittivity tensor can be easily restored from the equation (2).

Second order statistical moments of scattered EM waves in randomly inhomogeneous collision magnetized plasma can be calculated using equation (6). The variance and the correlation function of the phase fluctuations have the following forms:

$$<\varphi_1^2(\mathbf{r})>=\frac{\pi\,k_0^2}{2}(Z'+i\,s\,Z'')^2\int_{-\infty}^{\infty}dk_x\int_{-\infty}^{\infty}dk_y\ \frac{\tilde G_1+i\,\tilde G_2}{\tilde G_1^2+\tilde G_2^2}\cdot$$

$$\cdot\left\{1-\exp\left[(\tilde G_1-i\,\tilde G_2)L\right]\right\}\ V_n(k_x,k_y,i\,\tilde G_3-\tilde G_4)\,, \quad (7)$$

$$W_\varphi(\rho_x,\rho_y,L)\equiv<\varphi_1(\mathbf{r})\varphi_1^*(\mathbf{r}+\boldsymbol{\rho})>=\frac{\pi k_0^2 L}{2}(Z'^2+s\,Z''^2)\cdot$$

$$\int_{-\infty}^{\infty}dk_x\int_{-\infty}^{\infty}dk_y\;V_n\left[k_x,k_y,-\frac{\tilde d_1\Gamma''k_x+\tilde d_2(2k_0+\Gamma' k_x)}{4k_0^2}\right]\cdot$$

$$\cdot\exp(-i\,k_x\,\rho_x-i\,k_y\,\rho_y),\qquad(8)$$

where:

$$\tilde G_1=k_0\left[(\Gamma''\mu+\mathrm{P}'')\,y\,x+\frac{s}{2}(\Gamma''\mathrm{P}'-\mathrm{P}''\Gamma')\,\mu\,x^2\right],$$

$$\tilde G_2=\frac{k_0}{2}\left\{\left[\Gamma''(-\mathrm{P}''\mu+\Gamma'')-s^2\,\Gamma'\mathrm{P}'\mu+s^2\,\Gamma'^2\right]x^2+\right.$$

$$\left.+2\,s(\mathrm{P}'-\Gamma'\mu)\,y\,x+2\,y^2\right.,$$

$$\tilde G_3=\frac{k_0}{4}\left[(2\Gamma''-2\mathrm{P}''\mu-\Gamma''\,y^2)\,x-s(\Gamma''\mathrm{P}'-\mathrm{P}''\Gamma')\,y\,x^2\right],$$

$$\tilde G_4=\frac{k_0}{4}\left[-(\Gamma''\mathrm{P}''+s^2\,\Gamma'\mathrm{P}')\,y\,x^2+s(2\mathrm{P}'\mu-2\Gamma'-\Gamma'\,y^2)\,x\right.$$

$$\left.+4\,\mu\,y\right],\quad\tilde d_1=k_0^2\,x\left[\Gamma''-\mathrm{P}''(y+\mu)\right],$$

$$\tilde d_2=k_0^2\left\{y(y+2\mu)+x\left[\Gamma' k_0+\mathrm{P}'(y+\mu)\right]\right\};$$

$y=k_y/k_0$, $x=k_x/k_0$, $V_n(\mathbf{k})$ is the 3D spectral function of electron density fluctuations, L is a propagation distance in the turbulent plasma, parameter $\mu=k_\perp/k_0$ describes the diffraction effects, ρ_y and ρ_x are distances between observation points spaced apart in the principle and perpendicular planes, respectively. From equation (8) follows that in non-magnetized isotropic plasma $H_0=0$, $\chi=1$, neglecting diffraction effects $(\mu=0)$, the power spectra of the phase fluctuations of scattered radiation $W_\varphi(k_x,k_y,L)$ and the function $V_n(\mathbf{k})$ are related by the well-known formula [7]: $W_\varphi(k_x,k_y,L)=2\pi(r_e\lambda)^2L\cdot$

$\cdot V_n(k_x,k_y,k_z=0)$, where r_e is the classical electron radius.

Second order approximation of the phase fluctuations yields the following stochastic differential equation for the *X* - component:

$$\frac{\partial^2\varphi_2}{\partial x\,\partial y}(-s\,\mathrm{P}'-i\,\mathrm{P}'')+\frac{\partial^2\varphi_2}{\partial x\,\partial y}(s\,\Gamma'+i\,\Gamma'')+\frac{\partial\varphi_2}{\partial x}\left[i\,k_\perp(-s\,\mathrm{P}'-i\,\mathrm{P}'')\right.$$

$$\left.+i\,k_0(s\,\Gamma'+i\,\Gamma'')\right]-\frac{\partial^2\varphi_2}{\partial y^2}-2i\,k_\perp\frac{\partial\varphi_2}{\partial y}-2i\,k_0\frac{\partial\varphi_2}{\partial z}=$$

$$=-\frac{\partial\varphi_1}{\partial x}\frac{\partial\varphi_1}{\partial y}(-s\,\mathrm{P}'-i\,\mathrm{P}'')+\left(\frac{\partial\varphi_1}{\partial y}\right)^2.\qquad(9)$$

The solution of the equation (9) is:

$$\mathrm{Re}<\varphi_2(k_x,k_y,L)>=\frac{\pi}{4}k_0\int_{-\infty}^{\infty}dk_x\int_{-\infty}^{\infty}dk_y\;\frac{1}{\tilde G_1^2+\tilde G_2^2}$$

$$\left\{A\left[L\,\tilde A_1+\frac{\tilde A_1\tilde G_1-\tilde B_1\tilde G_2}{\tilde G_1^2+\tilde G_2^2}-\frac{\tilde A_2}{\tilde G_1^2+\tilde G_2^2}\exp(\tilde G_1 L)\right]-\right.$$

$$\left.-B\left[L\,\tilde B_1+\frac{\tilde B_1\tilde G_1+\tilde A_1\tilde G_2}{\tilde G_1^2+\tilde G_2^2}-\frac{\tilde B_2}{\tilde G_1^2+\tilde G_2^2}\exp(\tilde G_1 L)\right]\cdot\right.$$

$$V_n(k_x,k_y,i\,\tilde G_3-\tilde G_4)\;,\qquad(10)$$

where: $A=Z'^2-s^2Z''^2$, $B=2\,s\,Z'\,Z''$. Transverse correlation function of a scattered field $W_{EE^*}(\boldsymbol{\rho})=<E(\mathbf{r})\,E^*(\mathbf{r}+\boldsymbol{\rho})>$ is expressed via correlation function and the variances of the phase fluctuations [8]:

$$W_{EE^*}(\boldsymbol{\rho},k_\perp)=E_0^2\exp\left[\frac{1}{2}\,\mathrm{Re}\left(<\varphi_1^2(\mathbf{r})>+<\varphi_1^{2*}(\mathbf{r}+\boldsymbol{\rho})>\right)+\right.$$

$$\left.+2\,\mathrm{Re}<\varphi_2>+<\varphi_1(\mathbf{r})\,\varphi_1^*(\mathbf{r}+\boldsymbol{\rho})>\right]\cdot\exp(-i\,\rho_y\,k_\perp),\qquad(11)$$

here: E_0^2 is the intensity of an incident radiation. If a distance L traveling by the wave in a turbulent collisional magnetized plasma is substantially big, $L>>(l/\lambda)$, diffraction effects become essential. SPS of a scattered field in the case of an incident plane wave can be easily calculated by the Fourier transform of the transversal correlation function of a scattered field. If the SPS of an incident wave has a finite width and its maximum is directed along the *Z*-axis, SPS of a scattered radiation is given by [1,2]:

$$I(k)=\int_{-\infty}^{\infty}dk_\perp\int_{-\infty}^{\infty}d\rho_y\;W_{EE^*}(\rho_y,k_\perp)\exp(i\,k\,\rho_y-k_\perp^2\,\beta^2),\qquad(12)$$

where β characterizes the disorder of an incident radiation.

Let Δ_+ and Δ_- designate the displacements of the SPS maximum of scattered ordinary and extraordinary waves in the turbulent collision magnetized plasma, respectively in the principle *YZ* plane; $\Sigma_\pm$ is the width of the SPS spectrum of scattered waves. These expressions are obtained by differentiation of the correlation function of the phase fluctuations [1-4]

$$\Delta_\pm=\frac{2}{i}\left.\frac{\partial W_\varphi}{\partial\eta_y}\right|_{\eta_x=\eta_y=0},\quad\Sigma_\pm=-\left.\frac{\partial^2W_\varphi}{\partial\eta_y^2}\right|_{\eta_x=\eta_y=0}.\qquad(13)$$

3 Numerical calculations

Two types of field-aligned irregularities have been differentiated: the first type irregularities due to the two-stream instability [9] and the second type irregularities due to the gradient drift instability [10]. In the *F*-region, field-aligned irregularities were observed continuously up to the

upper *F*-region by the HF radar systems [11]. As the irregularities are observed in the *F*-region near the reflection level, their size is comparable or larger than the Fresnel zone, defined as $(2\lambda h)^{1/2}$ if λ is the radar wavelength and h is the reflection altitude. This size is in the range 7 km (for 3 MHz at 250 km) and 3 km (for 9 MHz at 150 km).

Analytical and numerical calculations are carried out for the anisotropic 3D Gaussian spectral function [1-4]

$$V_N(\mathbf{k}) = \sigma_N^2 \frac{l_\perp^2 l_\parallel}{8\pi^{3/2}} \exp\left(-\frac{k_x^2 l_\perp^2}{4} - p_1 \frac{k_y^2 l_\parallel^2}{4} - p_2 \frac{k_z^2 l_\parallel^2}{4} - \right.$$

$$\left. - p_3 k_y k_z l_\parallel^2 \right), \qquad (14)$$

where: $p_1 = (\sin^2\gamma_0 + \chi^2 \cos^2\gamma_0)^{-1}\left[1 + (1-\chi^2)^2 \sin^2\gamma_0 \cdot \right.$

$\left. \cos^2\gamma_0 / \chi^2 \right]$, $p_2 = (\sin^2\gamma_0 + \chi^2 \cos^2\gamma_0)/\chi^2$,

$p_3 = (1-\chi^2)\sin\gamma_0 \cos\gamma_0 / 2\chi^2$, σ_n^2 is the variance of electron density fluctuations. This function contains parameter $\chi = l_\parallel / l_\perp$ (the ratio of longitudinal and transverse linear scales of plasma irregularities) that measures the anisotropy of the irregularities and the inclination angle γ_0 of prolate irregularities with respect to the external magnetic field. Anisotropy of the shape of irregularities is connected with the difference of diffusion coefficients in the field align and field perpendicular directions.

Substituting (14) into (8) for the polar ionosphere $(\alpha = 0^0)$ we obtain

$$W_\varphi(\eta_x, \eta_y, L) = \sigma_n^2 \frac{\xi^3 k_0 L}{16\sqrt{\pi}\,\chi^2} (Z'^2 + s^2 Z''^2) \int_{-\infty}^{\infty} dx \int_{-\infty}^{\infty} dy$$

$$\left(-\frac{\xi^2}{4} \left\{ \frac{p_2}{16} C_1^2 x^4 + \frac{p_2}{8} C_1 C_2 x^3 + \left[\frac{1}{\chi^2} + \frac{p_2}{16} (C_2^2 + 2C_1 C_3) \right.\right.\right.$$

$$\left. - p_3 y C_1 \right] x^2 + \left(\frac{p_2}{8} C_2 C_3 - p_3 y C_2 \right) x + \left(p_1 y^2 + \frac{p_2}{4} C_3^2 - \right.$$

$$\left.\left. - p_3 y C_3 \right) \right\} \Big) \cdot \exp(-i\eta_x \rho_x - i\eta_y \rho_y), \qquad (15)$$

$$2\,\mathrm{Re} < \varphi_2 > = -\sigma_n^2 \frac{\xi^2}{8} \frac{k_0 L}{\chi} (1-\varphi_1)^{-1/2} \int_{-\infty}^{\infty} dy$$

$$\left\{ A \left[1 - \frac{\sin(k_0 L y^2)}{k_0 L y^2} \right] - \frac{2B}{k_0 L y^2} \sin^2\left(\frac{1}{2} k_0 L y^2 \right) \right\} \cdot$$

$$\cdot \exp\left[-\frac{\xi^2}{4} (p_1 + p_2 \mu^2 - 4 p_3 \mu) y^2 \right], \qquad (16)$$

where: $C_1 = \Gamma''\left[\Gamma'' - \mathrm{P}''(y+\mu)\right] + \Gamma'\left[\Gamma' + \mathrm{P}'(y+\mu)\right]$,

$C_2 = 2\left[\Gamma' + \mathrm{P}'(y+\mu)\right] + \Gamma' y (y+2\mu)$, $C_3 = 2y(y+2\mu)$,

$\eta_x = k_0 \rho_x$, $\eta_y = k_0 \rho_y$, $\xi = k_0 l_\parallel$,

$$\varphi_1 = \frac{p_2}{4} \mu^2 \chi^2 \left[1 + s^2 \frac{3}{(1-\mathrm{v})^2} \right].$$

Numerical calculations are carry out for an incident EM wave with the frequency 3 MHz (plasma parameters are $u = 0.22$, $\mathrm{v} = 0.28$; $k_0 = 6.28 \cdot 10^{-2}$ m^{-1}).

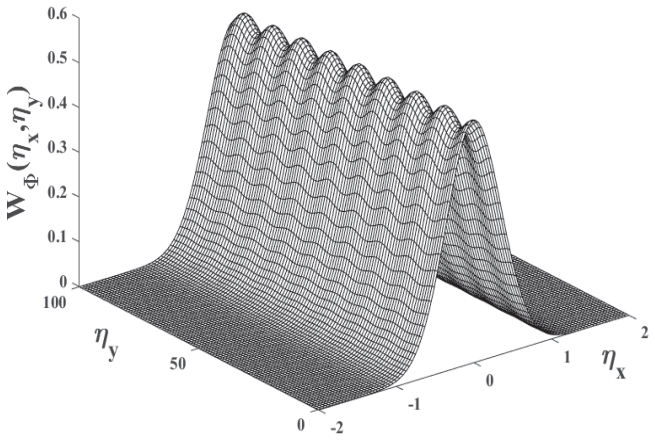

Fig. 1. 3D picture of the phase correlation function versus distances between observation points in the principle and perpendicular planes.

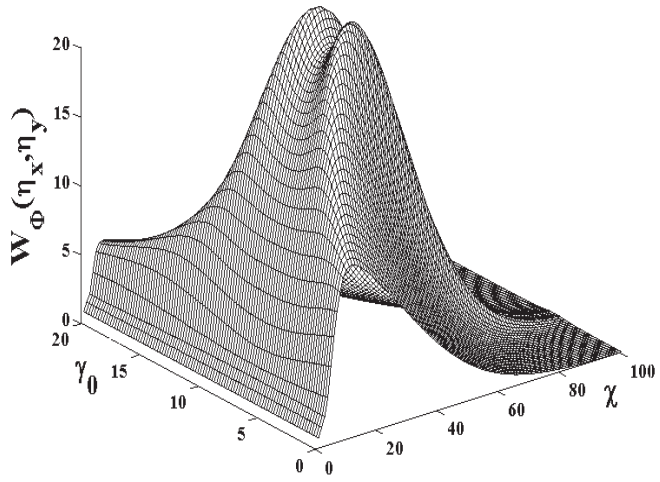

Fig. 2. Dependence of the phase correlation function versus parameter of anisotropy and inclination angle.

Three dimension surface of the function $W_\varphi(\eta_x, \eta_y)$ is plotted in Fig. 1 at: $\sigma_n^2 = 10^{-5}$, $\chi = 20$, $\gamma_0 = 10$, $\mu = 0.06$, $s = 0.1$, $l_\parallel = 160$ m, $L = 80$ km. Increasing characteristic spatial scale of irregularities oscillations disappears. Growing the anisotropy factor χ oscillations of a surface are increased.

Fig.2 depicts 3D double-humped shape phase correlation function for small scale plasma irregularities $l_\parallel = 600$ m

varying parameters in the interval: $\chi = 1-100$, $\gamma_0 = 0^0 - 20^0$. Fig. 3 shows the dependence of the phase correlation function of scattered radiation in the magnetized turbulent plasma in the principle plane. Prolate plasma irregularities are stretched along the external magnetic field ($\alpha = 0^0$) having characteristic spatial scale $l_{||} = 80$ km. The gap in the SPS arises propagating by ordinary EM wave distance $L \approx 920$ km in the magnetized plasma. Varying collision frequency of electrons with other plasma particles, the curves smoothly deformed and a gap arises.

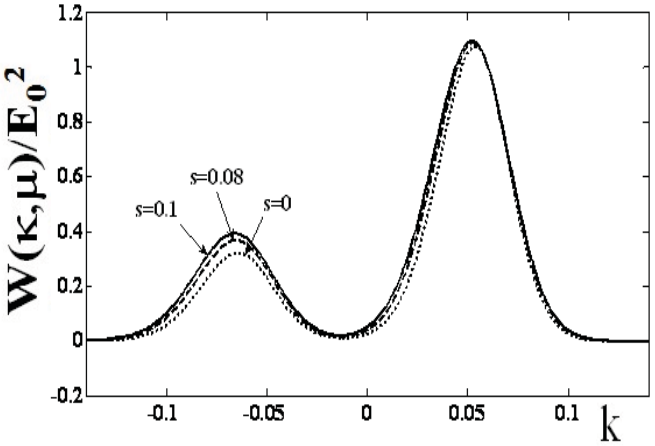

Fig. 3: Dotted line corresponds to the collisionless magnetized plasma ($s = 0$), dashed line is devoted to the collision frequency $s = 0.08$, solid line to the $s = 0.1$.

The "Double-humped Effect" of the ordinary wave in the turbulent collision magnetized plasma with prolate electron density irregularities versus non-dimensional wavy parameter k for fixed collision frequencies: $s = 0$ (dotted line), $s = 0.2$ (dashed line) and $s = 0.3$ (solid line); characteristic spatial scale of irregularities with $l_{||} \approx 64$ km strongly stretching along the external magnetic field is shown in Fig. 4. Analyses show that the SPS broadens, maximum symmetrically displaces and its depth increases in proportion to the collision frequency. For collisionless $(s = 0)$ magnetized plasma minimum and maximum of the SPS are at $k = 0.02$ and $k = \pm 0.3$, respectively. In the collision magnetized plasma at $s = 0.2$ minimum and maximum of the SPS are at $k = 0.01$ and $k = \pm 0.5$ respectively. In the collision magnetized plasma broadening of the SPS two times exceeds the width in the collisionless plasma.

Figures 5 and 6 depict the evaluation of a double-humped shape of SPS in the collision magnetized plasma varying angle γ_0 and parameter s at: $l_{||} = 64$ km, $\chi = 200$, $\beta = 10$, $\eta_x = 0$, $L = 1600$ km. In the collisionless plasma $(s = 0)$ (Fig. 5) if the directions of prolate large-scale irregularities coincide with the magnetic lines of force, intensities of both ordinary and extraordinary waves have a double-humped shape with symmetrically oriented maximums with respect to $k = 0$ with the gap in the same direction. Increasing angle in the interval $\gamma_0 = 2.5^0 - 3^0$ SPS broadens, then narrows and internal slopes oscillates. The "Double-humped" effect in the collision plasma has other feature (Fig.

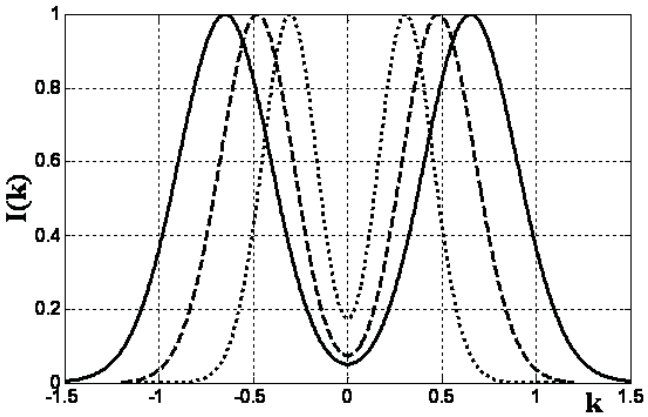

Fig. 4: Depicts SPS of scattered ordinary wave versus k for: $l_{||} = 64$ km, $\chi = 200$, $\gamma_0 = 0^0$, $\mu = 0.06$, $\alpha = 0^0$, $\beta = 10$, $L = 1600$ km.

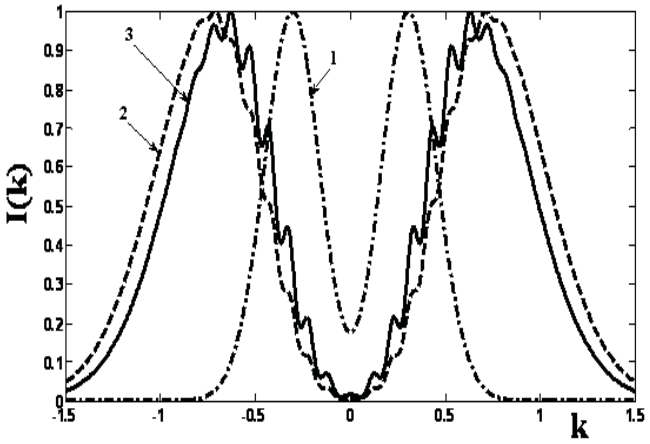

Fig. 5. The dependence of the intensity of scattered ordinary wave in the collisional magnetized plasma versus nondimensional wave parameter at different angle of inclination of prolate irregularities with respect to the external magnetic field $\gamma_0 = 0^0, 2.5^0, 3^0$.

6): at $\gamma_0 = 0^0$ and $s = 0.1$ the spectrum of scattered radiation has symmetrical double-humped shape with a gap at $k = 0$ (curve 1). Fixing angle $\gamma_0 = 3^0$ increasing collision frequency SPS broadens: if $s = 0$, $s = 0.05$ and $s = 0.1$ maximums of this spectrum are at: $k = 0.635$; $k = 0.731$ and $k = 0.825$, respectively. Maximums of the curves symmetrically displace and the depth of a gap

increases. Particularly, at $s = 0.01$ (the curve 2) oscillations of an internal slope of a double-humped spectrum arise; at $s = 0.1$ oscillations become smooth (curve 3). Formation of a gap at $\gamma_0 = 3^0$, $s = 0.1$, $l_{\|} = 64$ km, $\beta = 10$, $\eta_x = 0$, $L = 1600$ km is shown in Fig. 7. A gap appears at big anisotropy factors when the diffusion processes along the magnetic lines of force exceeds diffusion processes in a transverse direction.

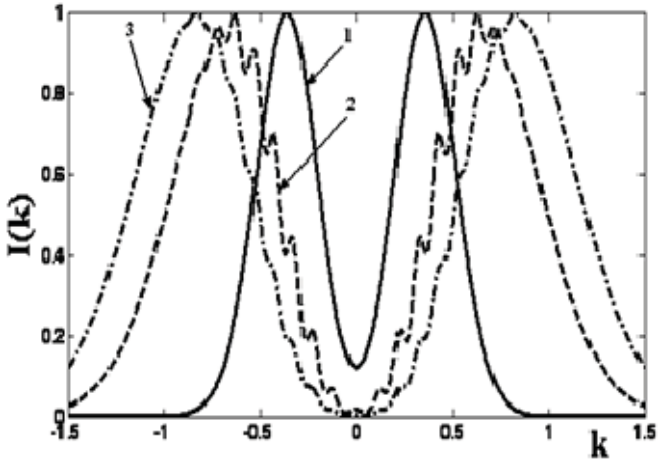

Fig. 6. Evaluation of the double-humped shape of the intensity of scattered radiation in the collisional magnetized turbulent plasma varying angle γ_0 and the collision parameter $s = 0.01;\ 0.1$

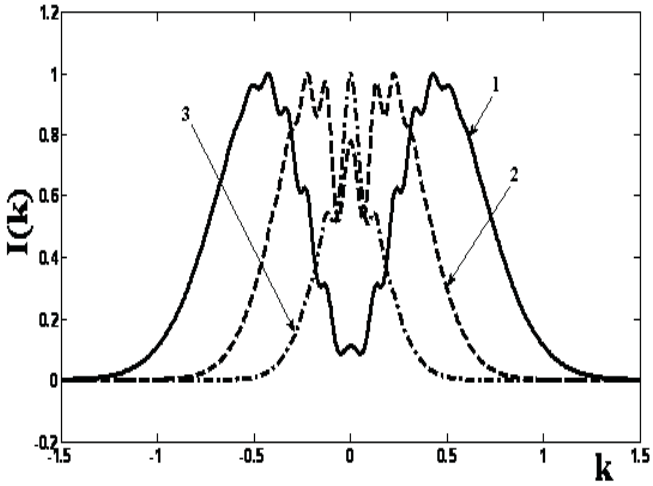

Fig. 7. Formation of a gap at fixed angle of inclination $\gamma_0 = 3^0$ increasing anisotropy factor from $\chi = 100$ up to $\chi = 150$.

4 Broadening of the SPS and shift of its maximum

Second order statistical characteristics: shift of maximum and the broadening of the SPS of both ordinary and extraordinary waves scattered in the turbulent collision magnetized plasma are calculated for the following parameters: $l_{\|} = 3$ km, $L = 100$ m, $\mu = 0.06$, $s = 10^{-3}$. Shift of maximum in the principle plane decreases for both waves inversely proportion to the inclination angle (Fig. 8). Varying angle $\gamma_0 = 10^0 - 20^0$ shift of maximum of the ordinary wave seven times exceeds shift of maximum of the extraordinary wave, $\Delta_+ / \Delta_- = 7$. Particularly, shift of maximum for both waves and $\gamma_0 = 10^0$ is located at $\chi = 30$.

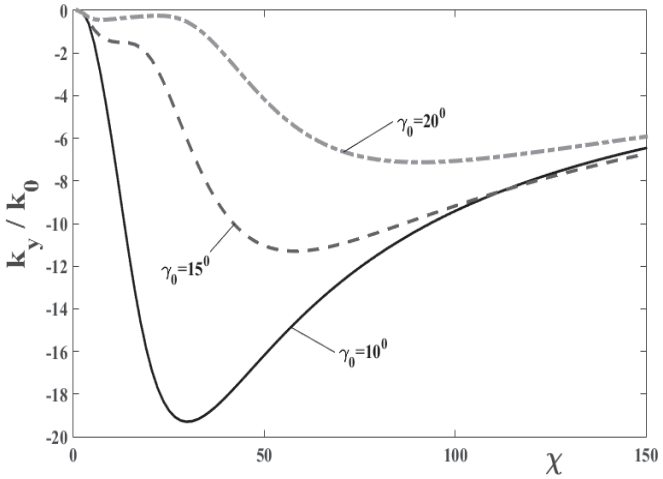

Fig. 8. Plots of the maximum displacement Δ_- of the SPS of the ordinary wave as a function of χ, at fixed inclination angle γ_0 in the principle plane.

Fig. 9 shows the dependence of the SPS broadening Σ_+ for the ordinary wave as a function of the anisotropy parameter χ at fixed inclination angle γ_0. If $\gamma_0 = 5^0$ maximum of the function Σ_+ is at $\chi = 16$, if $\gamma_0 = 12^0$ maximum is at $\chi = 42$.

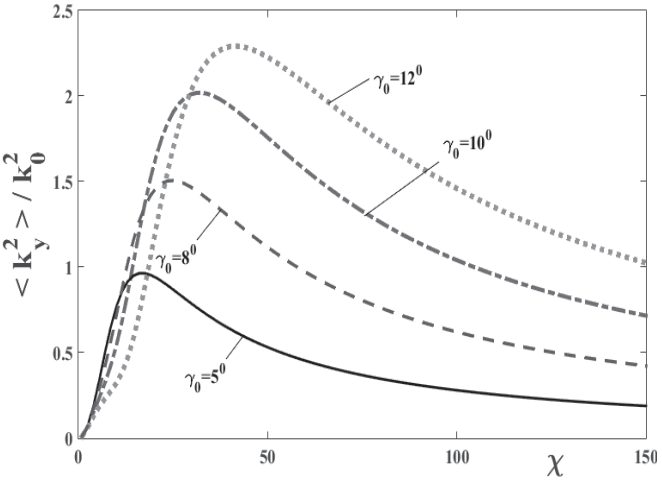

Fig. 9. Plots of the SPS broadening of scattered ordinary wave versus parameter of anisotropy χ at different angle of inclination γ_0.

In the interval $\gamma_0 = 5^0 - 12^0$ amplitude of the function Σ_+ increases in 2,4 times and the spectrum broadens in two times. The ratio of the widths of the ordinary and extraordinary waves not depends of the inclination angle γ_0: $\Sigma_+(\gamma_0 = 5^0 - 12^0) / \Sigma_-(\gamma_0 = 5^0 - 12^0) = 7$. The width of the SPS Σ_+ for the ordinary wave as a function of the angle γ_0 in the principle plane has a gap if prolate plasma irregularities are strongly stretched along the geomagnetic lines of force at $\gamma_0 = 3^0$. Increasing parameter of anisotropy in the interval $\chi = 15 - 30$ the location of a gap not varies but maximums of the function Σ_+ having double-humped shape are increased. Particularly, for $\chi = 15$ two maximums are at $\gamma_0 = -1.5^0$ and $\gamma_0 = 8^0$; for $\chi = 30$ maximums are at $\gamma_0 = -4.5^0$ and $\gamma_0 = 11^0$ angles. This means that the scattered ordinary wave broadens asymmetrically with respect to the static external magnetic field. The curve Σ_+ has a symmetrical double-humped shape not taking into account diffraction effects $(\mu = 0)$.

5 Conclusion

Second order statistical moments of scattered ordinary and extraordinary EM waves in the polar ionospheric plasma: correlation function of the phase fluctuation and the SPS are investigated analytically for arbitrary correlation function of electron density fluctuations in the first and second order approximations using modify smooth perturbation method taking into account diffraction effects. Polarization coefficients, anisotropy factor and the angle of inclination of prolate irregularities with respect to the external magnetic field are taking into account. Numerical calculations were carried out for the anisotropic Gaussian correlation function, the incident wave with 3MHz frequency. New peculiarities of the "Double-humped Effect" in the SPS of multiple scattered EM waves have been revealed for the first time.

In the collision magnetized plasma spectrum broadens at fixed collision frequency *s* increasing inclination angle γ_0; decreasing parameter *s* and at fixed γ_0 internal slopes of a double-humped SPS oscillate. Increasing collision frequency and the distance travelling by EM waves in the ionospheric plasma the SPS has a double-humped shape, it broadens and the depth of a gap increases, the location of its maximum weakly displaces varying collision frequency of electrons with other plasma particles. Anisotropy factor and the angle of inclination of prolate irregularities have a substantial influence on a gap of the SPS. The obtained results could find practical application in propagation of short-wavelength radio waves in the Earth's ionosphere, where random plasma irregularities are aligned with the geomagnetic field [8]; also in communication.

Acknowledgments

This work has been supported by the International Science and Technology Center (ISTC) under Grant # G-2126 and Shota Rustaveli National Science Foundation under Grant # FR/3/9-190/14.

6 References

[1] G.V. Jandieri, A. Ishimaru, N.F. Mchedlishvili, I.G. Takidze. "Spatial spectrum of multiple scattered waves in ionospheric plasma with anisotropic electron density and external magnetic field fluctuations"; PIER M, Vol. 25, 87-100, 2012

[2] G.V. Jandieri, A. Ishimaru. "Some peculiarities of scattered electromagnetic waves in randomly inhomogeneous magnetized plasma with electron density and external magnetic field fluctuations", PIER B, Vol. 50, 77-95, 2013.

[3] G.V. Jandieri, A.G. Khantadze, Z.M. Diasamidze. „Model computations of angular power spectra for anisotropic absorptive turbulent magnetized plasma"; Progress In Electromagnetic Research, PIER, Vol. 70, 307-328, 2007.

[4] G.V. Jandieri, A. Ishimaru, B.S. Rawat, N.K. Tugushi. "Peculiarities of the spatial spectrum of scattered electromagnetic waves in the turbulent collision magnetized plasma", PIER, Vol. 152, 137-149, 2015.

[5] V.L. Ginzburg, Propagation of Electromagnetic Waves in Plasma, Gordon and Beach, New York. 1961.

[6] A. Ishimaru, Wave Propagation and Scattering in Random Media, Vol. 2, Multiple Scattering, Turbulence, Rough Surfaces and Remote Sensing, IEEE Press, Piscataway, New Jersey, USA, 1997.

[7] B.N. Gershman, L.M. Eruxhimov, Yu.Ya. Yashin, Wavy Phenomena in the Ionosphere and Cosmic Plasma, Moscow, Nauka, 1984 (in Russian).

[8] G.V. Jandieri, V.G. Gavrilenko, A.V. Sarokin, V.G. Jandieri. „Some properties of the angular power distribution of electromagnetic waves multiply scattered in a collisional magnetized turbulent plasma"; Plasma Physics Report, Vol. 31, 604–615, 2005.

[9] D.T. Farley. „A plasma instability resulting in field-aligned irregularities in the ionosphere"; Journal of Geophysical Research, Vol. 68, 6083-6097, 1963.

[10] G.C. Reid. „The formation of small-scale irregularities in the ionosphere"; Journal of Geophysical Research, Vol. 73, 1627, 1968.

[11] E. Blanc, B. Mercandalli, E. Houngninou. „Kilometric irregularities in the E and F regions of the daytime equatorial ionosphere observed by a high-resolution HF radar"; Geophysical Research Letter, Vol. 23, 645-648, 1996.

Re-think the network as a sensor and security tool

Fabrizio Ippoliti [1], **Marco Maccari**[1], **Alberto Polzonetti**[1]
[1]School of Science Universiti of Camerino Italy

Abstract - *Nowadays, networks are more important than ever in order to achieve corporate objectives. In fact, on both cable and wireless networks more data that are sensitive are being circulated. Such a huge quantity of precious data that are transferred within companies has been attracting an increasing number of hackers and malware applications. However, the related intrinsic intelligence and distributed nature of networks (that is what makes them so attractive to IT criminals) may also transform them into proactive safety tools. Thanks to traffic's visibility and segmentation, corporate networks may also work as sensors and safety instruments.*

Keywords: *Security Policies, Mobility Management, Network Security Management*

1 Introduction

The increase in the number of mobile devices has enabled users to be ubiquitously connected through wireless and mobile communications technologies. However, unlike conventional mobile ad hoc networks, persistent connectivity is not a necessity in every type of network. This has led to a very progressive kind of social network called mobile social networks (MSNs). MSNs can be viewed as modern kinds of delay-tolerant networks (DTNs) in which mobile users interact with each other to share user-centric data objects among interested observers [1].

Together with the spreading of the 'third platform', as defined by IDC (International Data Corporation), a new technology and application paradigm is also emerging, one that is based on cloud, mobility, big data, and social business. Networks have acquired a strategic function that facilitates innovation. One of the reasons for such a change may be the fact that, through the third platform, critical applications have become accessible 24/7. Within such a context, cooperation is facilitated, space and time barriers have been disappearing and innovation has been gaining speed. In order to cope with the stunning increase of new devices and applications within companies, highly sensitive data are now circulating throughout networks. Therefore, more safety is needed, at both core and EDGE network levels. In reality, 80% of companies is doomed to suffer from at least one safety attack. Moreover, even if serious violations are excluded, a company still loses 1.3 million dollars a year, on average, because of safety threats and attacks.

Safety can be described as the condition of being protected against different types of failure, damage, error, accidents, harm, or any other no desirable event. In early works, like [2], the term security was used to convey this meaning, but later, with the emergence of various networks and safety issues, security has been specified to a more technical concept. What we mean by safety in this paper is to be in control of recognized hazards and to achieve an acceptable level of trust, security, and privacy. This can take the form of protection from an event or exposure to something that causes damage. It includes the protection of users or their possessions (information, identity, location, etc.).

In fact, corporate networks have never been so complex. All the nodes, certificates, clouds, devices, users and apps that access the network may potentially be infected or compromised. If they do not get immediately spotted, and if no corrective actions are immediately taken, malware and other vectors that enter the environment can spread quite quickly throughout networks. Nevertheless, the interconnected nature of the resources that are exposed to attacks may also become a fundamental resource. In other words, the intelligence available on the networks may also be used in a proactive manner to detect and correct a whole range of attacks and breaches. Thanks to intelligence advances, networks may be used as sensors to gather immediate information about possible threats. They may also be used to check the 'regular working' status of many items and to quickly identify anomalous activities. That is how their role as safety resources is reinforced, since they are in turn transformed into safety tools for access and attack control.

2 SAFETY'S MOBILE TARGET

A method of protecting data items in an organizational computer network, including, defining multiple information profiles for classifying the data item, defining rules for protecting the data item belonging to a specific information profile, classifying the data item according to the defined information profiles, applying a protection method to the data item responsive to the classification and the defined rules, automatically updating the classification of the data item responsive to a change in the content or location of the data item; and automatically transforming the applied protection method, throughout the lifecycle of the data item, responsive to a change in classification or location of the data item, according to the defined rules. [3]

Within many companies, because of the BYOD (Bring Your Own Device) approach and corporate mobility, two trends that are quite common nowadays, a huge number of devices can access corporate networks. Clearly, there are several important advantages for employees and employers when employees bring their own devices to work. But there are also significant concerns about security privacy. Companies and individuals involved, or thinking about getting involved with BYOD should think carefully about the risks as well as the rewards. [4]

The BYOD approach makes network protection more difficult and increases the quantity of sensitive data circulating within networks. Moreover, if more devices are connected to corporate networks, there are more endpoints that need protection. At the same time, staff are pressing to use mobile devices for mission critical tasks and, therefore, this enhances the expansion of mobile cloud applications within the ecosystem. Such applications make the networks' traffic flow more complex, as the applications and associated data may be stored in-house or off-premises, on a public or private cloud, or on a host. Afterwards, data are sent to various locations within corporate networks, i.e. from headquarters to branches and even to remote staff connected through mobile devices. Apart from being, new items to attack that contain large quantities of potentially sensitive data; applications may also pave the way for network intrusions.

Social networking concepts have been applied to several communication network settings, which span from delay-tolerant to peer-to-peer networks. More recently, one can observe a flourish of proposals aimed at giving social-like capabilities to the objects in the Internet of Things. Such proposals address the design of conceptual (and software) platforms, which can be exploited to easily develop and implement complex applications that require direct interactions among objects. The major goal is to build techniques that allow the network to enhance the level of trust between objects that are "friends" with each other. Furthermore, a social paradigm could definitely guarantee network navigability even if the number of nodes becomes orders of magnitude higher than in the traditional Internet.[5]

The advent of the Internet of Things (IoT) within companies adds another level of complexity. The IoT is a 'network of networks' (or 'items') that are identifiable in a univocal manner and that are able to communicate without human interaction through IP connectivity, both at local and global level. According to IDC's forecast, by 2020 there will be almost 30 billion of IoT devices fully implemented. These endpoints, or sensors, significantly increase the surface available for attack within networks. At this initial phase of the IoT evolution, it may not be possible to set up safety interfaces in an intuitive manner, and it may be difficult to integrate them within the safety infrastructure. Uncertainties in the field of IoT safety raise some serious concerns. A great deal of the IoT value depends on the data that IoT devices/sensors are able to gather. The volume, range and depth of such data are simply staggering. IoT devices are already part of production environments and collect large quantities of precious, structured and unstructured data. Many of those data are highly sensitive as far as safety and privacy are concerned. In order to make the most of IoT usage, a close integration with networks' safety is required.

Given the constant evolution of corporate mobility, the increasing number of applications based on public clouds that are added to enhance productivity and the fast IoT implementation, IT teams need to review their approach about network safety, a requirement that network safety decision makers understand very well. In fact, a recent survey carried out by IDC that targeted safety experts has revealed that 52% of respondents are worried, since staff don't seem to fully understand the importance of complying with safety policies. Almost the same percentage (45%) stated to be worried about the increasing complexity of cyber-attacks. Moreover, a significant portion of respondents (38%) mentioned that available budgets might be inadequate to counteract the new challenges. [6]

The challenges in question are becoming more and more pressing (together with the problems related to obtaining enough funds and support to tackle network safety) and may represent some serious obstacles for IT teams that, therefore, would experience more difficulties in detecting violations and in adopting the necessary measures to prevent them. According to IDC's data, over a year may be needed to integrate the updates of the third platform's safety infrastructure, such as endpoint enhancement and user management. In the third platform age, it is especially important to implement a kind of network safety architecture that should be reactive, smart and scalable, as well as platform-based and fully integrated within the network's infrastructure. This safety model benefits from an intrinsic distributed intelligence, so that networks may become active defense elements against intrusions, instead of being just a vulnerable surface. However, hackers move quickly, therefore, ensuring network safety is a crucial issue and even the smallest advantages available should be used to deploy an adequate response.

Content distribution over the internet has increased dramatically in the recent years. A recent study published by Cisco System, Inc [7] revealed that the global internet video traffic has surpassed peer-to-peer traffic since 2010, becoming the largest internet traffic type. Cisco Systems also forecasts that internet video traffic will reach 62% of the consumer internet traffic by 2015. The vast majority of this traffic consists of big popular content transport, including high-quality videos. Nowadays, a large amount of data is stored "in the network". This allows users to ease data sharing and retrieval, anywhere in the world. In the cloud, customers and providers come with storage service guarantees, such as QoS metrics, drawn up in Service Level Agreement (SLA)

contracts. The provider is therefore responsible to ensure data durability and availability. To enforce SLAs, providers rely on content replication. Yet, they need to do this carefully; it can have a huge impact on storage and bandwidth consumptions, even more for big contents. As data popularity is highly non-uniform, it is important to avoid replicating unpopular data, that will never be accessed, and also to ensure enough number of replicas for a popular content which may be retrieved concurrently by hundreds of users.

In parallel with the standardization of network management, companies have acquired an unprecedented network visibility, from datacenters to EDGE networks and in various geographical areas too.

EDGE (Enhanced Data GSM Environment) is a faster version the Global System for Mobile (GSM) wireless service designed to deliver data at rates up to 384 Kbps and enable the delivery of multimedia and other broadband applications to mobile phone and computer users. The EDGE standard is built on the existing GSM standard, using the same time-division multiple access (TDMA) frame structure and existing cell arrangements.

Devices, users and applications share the same kind of visibility. Given the opportunity to gather such a large amount of data, in addition to the increasing ability to analyze them, (contrary to what used to happen in the past), nowadays networks can detect anomalous and suspicious activities. The unlawful use of networks through malware, anomalous traffic flows, unauthorized apps and other user policy breaches, in addition to unauthorized devices and wireless access points (AP), can now be identified, placed in quarantine and removed more easily through the network intelligence.

To exploit networks for safety purposes, they need to be considered and used as sensors and safety elements in every location, including datacenters, branches and campuses, as well as in all the endpoints and applications that get into contact with them. The use of network infrastructures as safety tools does not imply the replacement of traditional safety instruments, such as firewalls and Advanced Malware Protection, as it can actually enhance them. The following section is going to illustrate how Cisco's comprehensive solution can be used to achieve such a goal.

3 USE CASE: A SMALL UNIVERSITY

The solutions implemented are based on the concept that safety should be integrated everywhere within the network. By using NetFlow (that enables the network to work as a sensor) and thanks to the integration with the Identity Services Engine (ISE) (for a granular control of policies), and with TrustSec (for the implementation of network segmentation), network safety is applied in a fluid manner, from the infrastructure to the end users. The tools discussed in this section support an end-to-end implementation in order to use the network for safety purposes.

3.1 NetFlow

Cisco's NetFlow [8] and the recent standardization effort IPFIX [11] have made flow export technologies widely popular for network monitoring. They owe this success to their applicability to high-speed networks and widespread integration into network devices. The pervasiveness of these technologies has resulted in a variety of new application areas that go far beyond simple network monitoring, such as flow-based intrusion detection [9] and traffic engineering [10]. Regardless of the application, flow data is expected to reflect the network traffic faithfully. Flow export is a complex process that includes both real-time aggregation of packets into flows and periodic export of flow information to collectors. This aggregation naturally results in a coarser view on the network traffic. Several works have already compared the precision of flow-based applications to their packet-based counterparts [9,10]. The scalability gain of using flow data normally excuses the loss of precision. Any flow-based application will, however, be impaired by flow data of poor quality, which can be caused by implementation decisions. For example, the imprecision in flow timestamps has already been discussed in [11,12]. Similarly, artifacts found in flow data from Juniper devices are extensively analyzed in [13]. However, these works do not investigate how widespread these artifacts are in flow data from different flow export devices

NetFlow is central to the 'network as a sensor' approach. It is a tool that can create continuous records of all the conversations going through routers, switches and a series of wireless devices. All the communication sessions taking place on a NetFlow-enabled device provide visibility and in-depth analyses, including six areas that are often quite important: network scanning, botnet detection, denial of service, attacks on segmentation, host reputation amendments and worm propagation.

As data may be saved for future use, NetFlow becomes an essential tool to identify safety violations. Detailed communication logs for forensic and end-to-end analyses provide comprehensive information on suspicious activities taking place within the network, allowing for a more effective detection and improved corrective actions. NetFlow and Lancope StealthWatch together ensure better network visibility and send real-time alerts to identify safety threats. The integration of Lancope StealthWatch with ISE further improves the correlation between the context of a device (who, what, where, when and how) and the network traffic. This enables to isolate from the network any infected devices quickly.

3.2 Identity Services Engine

One of the significant objective of most university information security measures is to ensure providing robust identity and access management (IAM) to its users. This encompasses systems straddling across the globe allowing the access of sensitive as well as confidential data of the enterprise at any point in time. With rapid mounting proliferation of mobile devices but with limited resources, cloud computing has emerged as an obvious predilection for performing resource intensive tasks over the cloud. To address the security issues, cloud service providers (CSPs) are coming up with new services such as Security as a Service (SecaaS). From our analysis of security threats and its measures, we feel that additional controls are required for Identity and Access Management for mobile cloud users. We have made some security recommendations along with best practices for consumers and service providers to consider ensuring robust information security including IAM for growing mobile users in cloud.

Conventionally privacy of data relates to obligation as well as trust compliance related to any information pointing to an identified or identifiable individual i.e. data subject. The objects that accumulate the personalized information of their client or any individual for delivering business services are known as data controllers. The objects that collect the personalized information from the data controllers for the purpose of processing data are known as data processors. Privacy of data is not restricted to certain permanent uniqueness attributes for identity like SSN or social security number, account number of bank, PIN (Personal Identification Number), non-encrypted password or even personalized information related to health such as prolonged illness or treatment cycle. Privacy of data also comprise varied information [14] like utterance or speech uttered (desires to conceal an utterance from some individual or a group of individuals), demographic identity data (user location, date of birth, photograph, name etc.), actions (what did I do last night), identification of resource, facts or transactional records or logs related to access (account number of bank, non-encrypted password, wealth possessed etc., and acquaintances (address book, identity information of the people in known contacts and the people who contacted me). In mobile based cloud infrastructure, privacy of data is a major area of concern. Both mobile, cloud and associated intercommunication amid the mobile devices (Tablet, Smartphone etc.) to backend cloud servers are intrinsically vulnerable to data privacy threats.

Identity Services Engine (ISE) is the platform used to manage safety policies. It ensures that a continuous control of access safety within cabled and wireless networks and VPN connections can be carried out in a rational manner. Access protection through ISE starts with user authentication and device classification. ISE integrates such details with contextual information to improve decisional processes, so that an adequate level of access control can be constantly assigned. By using more granular information, such as role, location and time, ISE can decide to assign a restricted access to the network that is extremely safe in terms of depth and scope. Based on policy criteria, ISE can grant a series of accesses to be selected according to users and devices. An integrated policy within the network improves operating performance, since it avoids the need to manage and apply separate and individual policies by integrating the visibility of policy application.

3.3 TrustSec software-defined segmentation

"TrustSec" is a set of computer programs and message communications protocols providing access control and other security features developed by Cisco Systems, Inc., San Jose, Calif., with the goal of providing self-defending networks. TrustSec introduced the concept of peer authentication and authorization between network devices. TrustSec is designed to determine, based on policies and roles assigned to users and devices in the network, whether access to a secure and trusted network can be granted or restricted. A Cisco TrustSec (CTS) network comprises network devices and end-hosts. In a CTS network, each network device authenticates its neighbor to an authentication, authorization and accounting (AAA) server. During the authentication process, the device sends an authentication request to the AAA server and retrieves from the AAA server authorization policies pertaining to the neighbor. The authentication and authorization may occur within the same protocol exchange or within a separate protocol exchange. A neighbor can be either another network device or an end-host. A secure link between network devices or a network device and an end-host has associated security properties, such as encryption and authorization schemes. By performing peer authentication and authorization, and by establishing trust relationships with other entities in a trusted network, a neighbor becomes a part of a trusted domain or "cloud." Messages exchanged during the AAA process comprise various characteristics specific to the secure and trusted relationships that are established in the trusted cloud.

TrustSec is a technology embedded in Cisco's switches, routers, and wireless and safety devices. It enables companies to implement software-defined network segmentation. TrustSec applies access controls based on roles (created in ISE) to ensure a safe access to all the network resources, which are highly sensitive in terms of identity and role. TrustSec's function is to simplify the processes of setting up and managing those policies that specify who can speak with whom (or with what) on the network, who can access the resources and how the systems involved can communicate with other systems. The implementation of TrustSec starts in the datacenter and reaches both the access EDGE and the remote VPNs.

4 BENEFITS OF USING NETWORKS AS SAFETY TOOLS

In an age when corporate capital and operating costs undergo painstaking analyses, it is essential for IT teams to justify their investment decisions and to find ways to draw more value from their networks. By using the network infrastructure as a sensor and safety tool, it is possible to benefit from in-house solutions to protect the network from attacks that may damage the company and cause profit losses. An integrated, end-to-end, safety network infrastructure, as the one implemented, exploits precious metadata to speed up traffic analysis. By using TrustSec and ISE together, it is possible to carry out a granular check of network accesses based on policies, with a software-defined segmentation that helps to control threats and to avoid their moving around inside the network. Moreover, this kind of safety paradigm is extremely scalable, since NetFlow, ISE and TrustSec can be activated within the network to protect the resources it connects to.

4.1 A. Challenges and opportunities

Re-thinking the power that corporate network safety holds require a significant change of paradigm, since protection is generally seen as something that should come from external resources, instead than from inside the network itself. Just as it happens when re-thinking the IT infrastructure in a radically different way, in this case too it is necessary to make an effort in order to explain the new paradigm and the cultural change involved to those who are in charge of the company's decision-making processes. Moreover, as regards companies that are equipped with complex safety infrastructures, the stakeholders may hesitate to re-think the systems that are being used (especially if they seem to be working well). IT teams often have to find the right balance between the need to optimize existing investments and the need to ensure that the infrastructure being used can cope with future challenges. In addition, this is one of those cases. However, as it happens with any challenges, difficult situations may also offer great opportunities. As already mentioned, the implementation of a network architecture that includes highly integrated safety components may be a more effective investment, since it would eliminate the redundancies caused by the implementation of fragmented safety solutions. Operating efficiency and ROI optimization, thanks to a network that works as a sensor and safety tool, seem to be the best arguments to prove that such a solution is a great opportunity that should not be missed.

5 Conclusions

In the third-platform age, corporate networks play a new role in the business, in involving customers and staff, in differentiating competitors and in terms of innovation. However, given the huge quantity of sensitive data circulating throughout corporate networks, a variegated generation of hackers and cyber criminals has been actively trying to use corporate networks to access such data. Therefore, they may cause serious damages, as well as unpleasant inconveniences to customers and staff, in addition to spoiling the company's reputation. However, the good news is that now safety tools can be integrated within networks, in an in-depth and end-to-end manner, to offer unprecedented defense ability against attacks. In the current IT era, it is of paramount importance to take into consideration a network infrastructure featuring safety functions that are closely integrated. The solutions discussed here may reveal to be the most suitable ones for many companies.

6 References

[1] N. Vastardis and K. Yang, "Mobile social networks: Architectures, social properties and key research challenges," IEEE Commun. Surveys Tuts., vol. 15, no. 3, pp. 1355–1371, 3rd Qtr., 2013

[2] L. Lilien, Z. Kamal, V. Bhuse, and A. Gupta, "The concept of opportunistic networks and their research challenges in privacy and security," in Mobile and Wireless Network Security and Privacy, S. K. Makki, P. Reiher, K. Makki, N. Pissinou, and S. Makki, Eds. New York, NY, USA: Springer-Verlag, 2007, pp. 85–117

[3] Eldar, Y., & Oz, R. (2016). U.S. Patent No. 20,160,028,772. Washington, DC: U.S. Patent and Trademark Office.

[4] Miller, K. W., Voas, J., & Hurlburt, G. F. (2012). BYOD: Security and privacy considerations. It Professional, (5), 53-55.

[5] Atzori, L., Iera, A., & Morabito, G. (2014). From" smart objects" to" social objects": The next evolutionary step of the internet of things. Communications Magazine, IEEE, 52(1), 97-105.

[6] Najaflou, Y., Jedari, B., Xia, F., Yang, L. T., & Obaidat, M. S. (2015). Safety challenges and solutions in mobile social networks. Systems Journal, IEEE,9(3), 834-854.

[7] Cisco visual networking index: Forecast and methodology, 2010-2015. http://www.cisco.com, June 2011.

[8] Claise, B.: Cisco Systems NetFlow Services Export Version 9. RFC 3954 (Informational) (2004)

[9] Sperotto, A., Schaffrath, G., Sadre, R., Morariu, C., Pras, A., Stiller, B.: An Overview of IP Flow-Based Intrusion Detection. IEEE Communications Surveys & Tutorials 12(3), 343–356 (2010)

[10] de Oliveira Schmidt, R., Sperotto, A., Sadre, R., Pras, A.: Towards Bandwidth Estimation Using Flow-Level Measurements. In: Proceedings of the 6th International Conference on Autonomous Infrastructure, Management, and

Security (AIMS 2012). pp. 127–138 (2012)
[11]K¨ogel, J.: One-way Delay Measurement based on Flow Data: Quantification and Compensation of Errors by Exporter Profiling. In: Proceedings of the 25th International Conference on Information Networking (ICOIN 2011). pp. 25–30 (2011)
[12]Trammell, B., Tellenbach, B., Schatzmann, D., Burkhart, M.: Peeling Away Timing Error in NetFlow Data. In: Proceedings of the 12th International Conference on Passive and Active Network Measurement (PAM 2011). pp. 194–203 (2011)
[13]. Cunha, I., Silveira, F., Oliveira, R., Teixeira, R., Diot, C.: Uncovering Artifacts of Flow Measurement Tools. In: Proceedings of the 10th International Conference on Passive and Active Network Measurement (PAM 2009). pp. 187–196 (2009)
[14] Jeffrey MacKie-Mason, University of Michigan 2014, Can We Afford Privacy from Survillence, IEEE Security & Privacy magazine – IEEE Computer Society, September/October 2014, pages 86-89

Aspects of Cloud Computing

Jamal Birt, Krunal Patel, and Jin Wang
Department of Mathematics and Computer Science
Valdosta State University, Valdosta, GA 31698, USA

ABSTRACT

The goal of this paper is to provide a detail overview of how a cloud computing system is structured and how it operates. Along with this, the paper also describes the various types of deployment and service models, as well as discusses the underlying purpose and functions of each. It also provides information about the importance of scheduling and its process. The various needs and characteristics of job scheduling are also discussed in this paper with introduction to supporting algorithms such as FCFS, Round Robin, and SJF. Lastly, the paper evaluates different security issues within a cloud and introduces a few solutions.

Keywords: Cloud Computing; Scheduling Algorithm; Internet security

1. INTRODUCTION

Cloud computing is a form of technology that is becoming increasingly prevalent in numerous businesses and organizations throughout the world today. It can be defined as an internet based technology that utilizes remote servers and the internet in order to maintain and process data and several types of applications. Cloud computing is typically utilized for processing power and on-demand storage and permits the sharing of various computing resources and applications. With the help of innovative cloud computing technologies, businesses and organizations are able to achieve economies of scales where they can increase the volume of productivity. Cloud computing not only increase the productivity, but it also improve accessibility and flexibility by making data access easier and convenient for consumers. This particular form of computing also helps consumers and businesses to save a tremendous amount of money by reducing the overall cost by eliminating the need to purchase supporting software and hardware.

2. TYPES OF CLOUDS

Cloud computing can be divided into four deployment models which are also known as clouds. As shown in Figure 1 the deployment model consist of four categories, Public, Private, Community, and Hybrid.

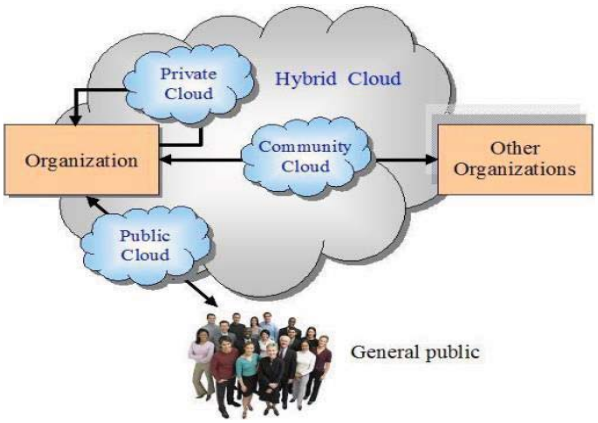

Figure 1. Structure of Cloud computing development models [7]

2.1 Public Cloud

A public cloud is a deployment model or cloud infrastructure that is made accessible to the general public or to a large business group on a commercial basis. It is maintained by organizations marketing cloud services. This particular cloud allows a user to develop and implement a service in the cloud environment with minimal financial implications [1]. However, this particular model does not allow the consumer to possess any control over the infrastructures location.

2.2 Private Cloud

A private cloud infrastructure is primarily for single organization for business purposes. This particular deployment model can be managed not only by the predominate business, but by a third party as well. The information technology of the private cloud is often attached to a virtualized infrastructure within the enterprise firewall and expended in what they call a per transaction basis or as a capital expenditure that is repaid over time [1]. In viewing the private cloud in comparison to the public cloud, there is no difference in the structural design, with the exception of the level of security offered for various services provided.

2.3 Community Cloud

A community cloud is a deployment model that is often shared by numerous businesses and organizations and is structured to serve a specific community with similar or shared interest including things such as their objective, different policies, and

various security needs and concerns. In relation to the private cloud, this deployment model also has the capability of being managed by the primary business or by a third party. Along with that, it can also be presented internally or externally meaning that it can exist on or off premises.

2.4 Hybrid Cloud

A hybrid cloud is a deployment model that often merge or combines two or more of the previously mentioned cloud or development model together. This model offers standardized access to applications and data as well as application manageability. In hybrid environment, the business and infrastructure processes reside within the enterprise and is partially consumed by a third party. The hybrid cloud structure also permits the user to increase the capability of aggregation or customization with different cloud models.

3. CLOUD ARCHITECTURE

The architecture of cloud computing can be broken down into to three subcategories or three layers of service models which consist of Infrastructure as a Service (IaaS), Platform as a Service (PaaS), and Software as a Service (SaaS). These three service models structures and various examples of each are displayed in Figure 1.

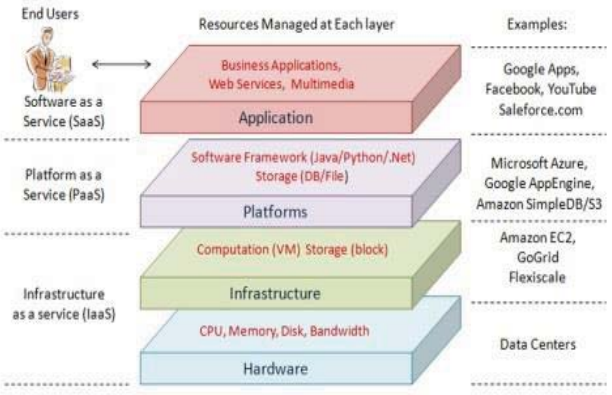

Figure 2.Structure of cloud computing service model [8]

3.1 IAAS

Within the cloud computing's structure or architecture, the IaaS tends to serve as the base or foundational building block of the cloud structure for the other service models. Out of all three service models, IaaS is considered to be the most flexible. One of the unique function of IaaS is that it is capable of facilitating fast utilization of applications and progresses the nimbleness or quickness of information technology services by incorporating storage, network capacity, and processing power. This particular service model also provides consumers the capability to utilize storage, networks, and several other fundamental resources where users are able to operate different applications and operating systems as on-demand services. There are numerous examples of IaaS which include GoGrid, a cloud computing service that is managed by a multi-server control panel and hosts Windows and Linux Virtual Machines, and Amazon's cloud drive, which allows users to upload and access their digital content.

3.2 PAAS

PaaS the second service model that makes up the structure of cloud computing. PaaS often aid a set of application program interface to cloud applications. This particular service model provides businesses the ability to design and cultivate usable applications in a timely and proficient manner while being operated in a cloud-based setting. The unique factor of PaaS is that it permits application developers to implement the created applications on a hosted infrastructure. The user or developer can also run their own software solutions on the platform without having to worry about the expense or intricacy of acquiring and managing the essential software and hardware layers. However, this particular model does not permit the user to control the essential cloud network, operating system, and its infrastructure.

3.3 SAAS

SaaS is a software model which is provided through an online service and aims to replace common applications regulated on a PC. This particular service model provides the ability for an individual cloud users to utilize commercially available applications or software programs via cloud infrastructure using web browsers from numerous devices. The SaaS doesn't permit the user to govern the core functions of the cloud infrastructure. This comprises various areas such as cloud storage and network. However, the service model does permit the user to utilize specific application configuration settings which consist of spreadsheet or word processing tools such as Google Docs. One major advantage of the SaaS service model is that it increases user adoption and the speed of deployment. It also reduce the cost of implementation. Another advantage of SaaS is that not only it eliminates the need to install software on users' PC, but it allows the users to save money through pay-per-use policy instead of purchasing the software at a higher price.

4. CLOUD SCHEDULING

There are several functions and background operations that facilitate the process of cloud computing. For instance, the scheduling of resources has served a significant role in cloud computing and affect many factors or aspects such as network performance and distributed computing. "Scheduling can be defined as a process of allocating tasks to available resources on the basis of tasks' qualities and need [3]". The main objective of scheduling is to increase the application of resources without affecting various services provided by the cloud infrastructure.

Numerous researchers have introduced various algorithms for the purpose of scheduling, allocating, and scaling resources proficiently in the cloud infrastructure. The scheduling process in a cloud environment can be divided into three phases, resource discovering and filtering, resource selection, and task allocation [2]. In resource discovering and filtering, an individual known as a datacenter broker or cloud broker basically discovers the available resources within the network system and gathers status information about the resources. The process of resource selection is the deciding platform where the target resource is chosen based on specific requirements of

resource and task. After the process of selection is over, the task is then allocated the chosen resource.

The process of scheduling consists of various needs. In scheduling, the system must be able to allocate various resources in a fair or rational manner. Along with this, scheduling algorithms must be able to provide maximum resource utilization and save or reduce the amount of energy being consumed. Developers also have to keep in mind that numerous jobs and resources must be scheduled in a way that permits the achievement of Quality of Services (QOS).

4.1 Job Scheduling

One of the type of scheduling that is used in cloud computing is known as job scheduling. Job scheduling serves as a mapping mechanism from the user's tasks to the appropriate selection of resources and its execution [3]. There are several needs and characteristics that make up job scheduling. One of the characteristics of job scheduling is that it can be considered to be globally centralized. It means that cloud computing provides the centralized resource to numerous distributed applications, making several processes of interoperate easier to be executed. Because of this, emulating services and virtualized technology permits scheduling of cloud computing to accomplish global centralized scheduling. Scalability is known as another characteristic of job scheduling. Within the cloud infrastructure, scheduling must meet the scalability requirements so that the amount of the scheduling isn't too low. Another characteristic of job scheduling is that each node in the cloud environment can be classified as being independent. Each node in the cloud's internal scheduling is considered to be autonomous, making the schedulers within the cloud environment incapable of interfering with the scheduling guidelines of the nodes. At last, job scheduling can also be described as being self-adaptive, meaning that depending on certain requirements, the resources and the applications can be shrunk or expanded when necessary.

As far as the needs for the process of job scheduling, one thing developers must think about is load balance. Load balance can be maintained through various task scheduling algorithms which are also accountable for optimal pairing of both resources and task. Another requirement that must be meet is obtaining the best possible run time. Depending on the consumer's needs, jobs can be distributed into numerous categories, where specific algorithms can be applied to them for the best running time, based on the goals for each task. The throughput of the system can also be considered a need for job scheduling. Within the cloud computing structure, an increase of throughput can be considered a benefit for both providers and consumers. One final need of job scheduling is the quality of service. The cloud's primary job is to supply users with necessary cloud storage and computing services, and when the management of scheduling reaches the job allocation stage, it must also guarantee the quality of service of various resources.

4.2 Round Robin

The Round Robin scheduling algorithm is one of the most widely used scheduling algorithm in today's computing world. It is fixated on the concept of fairness. Round Robin works by utilizing a ring as its queue to store jobs. Each queue has the same time allotted for execution and is executed in turn, meaning that once one job is done, the next will proceed. In an instance where a job or task is not completed in its allotted time, then it will be placed back on the queue, where it will then wait for the next available turn. If the job is completed prior to the end of the quantum, it then releases the CPU voluntarily. One of the advantage of Round Robin algorithm is that each process is executed at its fair turn and do not have to be waited for the previous process to be completed [2]. However, one disadvantage of Round Robin is that the largest job will have to take more time to complete due to fixed quantum time.

4.3 First Come First Serve

The First Come First Serve (FCFS) scheduling algorithm is a simple and easy algorithm to implement [3]. Here, the processes or jobs are distributed based on their arrival time in the ready queue. The disadvantage of the First Come First Serve algorithm is that it is non-preemptive. Due to that, the short jobs which are at the back of the ready queue will have to wait for the long jobs at the front to finish. Its turnaround and response is quite low. Below are the basic common steps for implementing the First Come First Serve algorithm [3].

Step 1: Initialize the tasks
Step 2: Assign the first task to the queue and add tasks up to n numbers.
Step 3: Add the task 'I' at the last position in the main queue

4.4 Shortest Job First

The Shortest Job first (SJF) algorithm operates by selecting the process with the shortest execution time. In this algorithm, the processes with the smallest execution time is selected first to execute putting processes with larger execution time at the end of the queue. Below is the pseudo code for Shortest Job First algorithm implementation [3].

SJF Algorithm:

```
for i = 0 to i < main queue-size
        if task i+1 length < task i length then
                add task i+1 in front of task i in the queue
        end if
        if main queue-size = 0 then
                task i last in the main queue
        end if
end for
```

4.5 Priority Scheduling

Priority scheduling algorithm prioritize processes based on their size. The processes which are larger in size are given higher rank, where the smaller processes are given lower rank [2]. According to the algorithm, the processes with higher rank get a chance to execute first and therefore processes with lower rank have to wait till higher rank processes finish executing. This situation creates "starvation", where processes with lower rank have to too long to execute. Priority scheduling algorithm can be implemented using various Virtual Machines such as Cloud Sim.

Algorithm
This particular algorithm shown below stores all suitable Virtual Machines in a VM List [2].

```
prev −99
push first vertex
while Stack 6= Empty do
        get unvisited vertex adjacent to stack top
        if no adjacent vertex then
                if prev 6= StackTop then
                        copy all stack contents to VM List
                end if
                pop
                if Stack 6= Empty then
                        prev = StackTop
                end if
                else
                        mark the node as visited
                        push adjacent vertex
                end if
end while
```

Step 1: Create VM to different Datacenter according to computational power of host/physical server in term of its cost processor, processing speed, memory and storage.
Step 2: Allocate cloudlet length according to computational power.
Step 3: VM Load Balancer maintain an index table of Vms, presently VM has zero allocation.
Step 4: Cloudlet bound according to the length and respective MIPS.
Step 5: Highest length of cloudlet get highest MIPS of virtual machine.
Step 6: Datacenter broker sends the request to the VM identified with id
Step 7: Update the available resource.

5. SECURITY ISSUES

When it comes to cloud computing one of the widely discussed problem is the security. With security being a reoccurring issue, many consumers stay away from the use of cloud services. User's privacy or confidentiality is one of the most impacted factor of security issues. Individuals store their confidential data or information in could environment believing that it should be only accessed by the authorized users only and no one else. However, it is hard to prevent a security breach due to most of the cloud computing infrastructures are business oriented making various resources sharable, which increases the risk of data compromise. One of the solution to enhance user's confidentiality is done by data encryption and a process known as tokenization. Tokenization is the process of replacing of sensitive information by a dummy token. In cloud storage environment, the data is stored on service provider's server which could be located any part of the world. Yet, the service providers have to obey the privacy and confidentiality laws of whichever country where the server is placed [4]. In today's advanced technological environment many users become victims of hacking and data theft. These malicious activities are performed using some commonly known hacking techniques such as phishing, injection, malwares, and other erroneous manipulations. One of the solution to prevent hacking or data theft is known as a Two-Factor authentication [5]. Two factors typically are 'something you know, like pin code or password' and 'something you have like hardware token, mobile phone, and fingerprint. It includes like One-Time password (OTP), a digital certificate and biometric verification [5].

Integrity also is an important factor in the realm of cloud computing. In cloud computing, integrity can only be achieved by approved parties. One solution that ensures integrity assurance is the utilization of storage systems that implements a program known as Rain-6. Rain-6 is capable of recovering network failure, hard disk failure or corruption, and power supply shortages [4]. The data integrity can also be improved by adding a digital signature to the data.

Issues dealing with security can also occur within a cloud's deployment model such as Infrastructure-as-a-Service and Platform-as-a-Service. There is a high possibility that data can be routed through an intruder's infrastructure, because in cloud environment data is transmitted through umpteen number of third party infrastructure devices [6]. Due to the fact that many cloud computing infrastructure utilize the same technology to transmit data, it can face the same kind of threats to security that are often seen throughout the internet. A cloud's security can also be threatened or effected through the use of Virtual Machines and can occur during the process of communication between both host and Virtual Machines. Also when Virtual Machines forward information between both host and Virtual Machine, the hackers take advantage of this feature to interchange data between cooperating malicious programs in VMs. Within the PaaS deployment model, various events can open up the door for network intrusion. However, cloud providers can use tools such as Virtual Private Network and Multi-Protocol Label Switching to ensure the prevention of network intrusion and that virtually secured networks are accessible.

6. CONCLUSION

Cloud computing has become a major part of our computing world now. With various types of clouds and infrastructures, it provide us the flexibility to choose appropriate environment for our use. Introduced cloud infrastructures in this paper are the backbone of cloud computing. Due to increased number of cloud computing users, there is more need of better and efficient scheduling algorithms to manage the jobs. As seen before, Round Robin is promising solution yet there are still many researchers who are working in effort to develop even more efficient algorithms. Meanwhile cloud computing world also facing many potential threats such hacking and data theft. Hacking is a major security issue for cloud computing and many efforts being made to stop these malicious activities as introduced solution earlier. In near future, the cloud computing world will change the face of our storage systems, data accessibility, and networking.

7. REFERENCES

[1] Asma, Anjum, Mousmi Ajay Chaurasia, and Hala Mokhtar. "Cloud Computing Security Issues." *International Journal of Application or Innovation in Engineering & Management* 1.2 (October 2012): 141-47.
[2] Agarwal, Dr. Amit, and Saloni Jain. "Efficient Optimal Algorithm of Task Scheduling in Cloud Computing

Environment." International Journal of Computer Trends and Technology IJCTT 9.7 (2014): 344-49.

[3] Kaur, Rajveer, and Supriya Kinger. "Analysis of Job Scheduling Algorithms in Cloud Computing." International Journal of Computer Trends and Technology IJCTT 9.7 (2014): 379-86.

[4] D. Zissis, D. Lekkas, "Addressing cloud computing security issues", Future Generation Computer Systems,elsvier, PP 583 592, 2010, doi:10.1016/j.future.2010.12.006.

[5] Dave Abraham, CEO, Signify, "Why 2FA in the cloud?", Network Security, Volume 2009, Issue 9, PP 4-5, September 2009.

[6] S. Subashini, V. Kavitha, "A survey on security issues in service delivery models of cloud computing", Journal of Network and Computer Applications 34 (2011), PP 1–11. doi:10.1016/j.jnca.2010.07.006

[7] "The cloud computing deployment models." Open-i. [2016]. *Openi.nlm.nih.gov*.

[8] Qi Zhang, Lu Cheng , Raouf Boutaba, " Cloud computing: state-of-the-art and research challenges", Springer, 20 April 2010

Intelligent Mental Health Diagnosis Architecture using Data Mining and Machine Learning

Ghassan Azar
Lawrence Technological University
Southfield, MI, USA
gazar@ltu.edu

Naser El-Bathy
North Carolina A&T State University
Greensboro, NC, USA
nielbath@ncat.edu

Su Yu
Shanghai University of Engineering and Science
Shanghai,China
suyu_sh@hotmail.com

Rajasree Himabindu Neela
Lawrence Technological University
Southfield, MI, USA
rneela@ltu.edu

Kholoud Alfarwati
North Carolina A&T State University
kwalfarw@aggies.ncat.edu

Abstract—**Inappropriate diagnosis of mental health illnesses leads to wrong treatment and causes irreversible deterioration in the client's mental health status including hospitalization and/or pre-mature death. About 12 million patients are misdiagnosed annually in US. In this paper, a novel study introduces an Intelligent Mental Health Diagnosis Architecture using Data Mining and Machine Learning that aids in preliminary diagnosis of the psychological disorder patient. This is accomplished based on matching description of a patient's mental health status with the mental illnesses illustrated in DSM-IV-TR, Fourth Edition Text Revision. The study constructs the semi-automated system based on an integration of the technology of genetic algorithm, classification data mining and machine learning. The goal is not to fully automate the classification process of mentally ill individuals, but to ensure that a classifier is aware of all possible mental health illnesses could match patient's symptoms. The classifier/psychological analyst will be able to make an informed, intelligent and appropriate assessment that will lead to an accurate prognosis. The analyst will be the ultimate selector of the diagnosis and treatment plan.**

I. INTRODUCTION

In societies, diagnosing mental disorders in individuals is often poor due to the lack of understanding of their behavior, symptoms and inadequate knowledge. The therapists and/or psychiatrists possess to weed through the many mental health illnesses identified in the Diagnostic Statistical Manual IV, Fourth Edition Text Revision (DSM-IV-TR) [1]. Many a times, improper diagnosis leads to wrong treatment which may cause irreversible deterioration in the client's mental health status including hospitalization and/or pre-mature death [2].

The objectives of this study include reducing biased and incomplete assessment while introducing a consistency in diagnosing mentally ill individuals and minimizing further deterioration in mentally ill individuals due to miss-diagnosis. Objectives also include enhancing prognosis by utilizing multiple expert's knowledge base and their cumulative years of training and practical experience in solving new cases.

The final objective is improving diagnosis results through intelligently using and implementing approved previous successfully-solved cases based on the historical data as well. This method can be used just rather than depending on textbook rules & only individual assessor's experience [3].

The rest of this paper is structured as follow: Section two identifies the study model and procedures. Section three presents the full text indexing, Section 4 introduces intelligent genetic algorithm, Section five present experimental results, and finally the conclusion is given.

ISBN: 1-60132-430-8, CSREA Press ©

II. Study Model and Procedures

Figure 2 illustrates the study model and procedures. The book 'Diagnosis and statistical manual of mental disorders' in text format has a softcopy. Its data (that is keywords) related to each disorder have been loaded into the database. Criteria for each disorder have been identified and formed into a question that needs to be asked to the user and loaded into the database.

An intelligent genetic algorithm has been developed to extract keywords from the user's symptoms. Finally, a graphical user interface has been developed such that the users can enter the description of their symptoms [4].

Based on description, match keyword to the keywords presented in the database to extract classification. The classification order must be from highest probability of disorder to lowest. Classification is shown in percentage basis [5]. The interface allows the user to ask questions relevant to highest classification. Based on users input, new classification is generated and reordered from highest to lowest. Based on the symptoms, 10 relevant disorders are classified along with the percentage of matching. Some disorders have specific criteria which are formed into questions.

Based on the questions answered, the percentage value will be changed. If all the questions are answered yes, then the percentage value increases. If all the questions are answered no, then the percentage value decreases. If few questions are answered yes and no, then according to number of yes and no, the percentage is calculated. The final result shows highest percentage disorder from the classification. If doctor does not accept the given the classified disorder, then doctor will be given a choice to determine his/her own perspective disorder for the patient.

III. Full Text Indexing

FULLTEXT search function matches a natural language query against a text collection (which is simply the set of columns covered by a FULLTEXT index). For every row in a table it returns relevance - a similarity measure between the text in that row (in the columns that are part of the collection) and the query.

The rows returned are automatically sorted and retrieved. Relevance is a non-negative floating-point number. Zero relevance means no similarity. Relevance is computed based on the number of words in the row, the number of unique words in that row, the total number of words in the collection, and the number of documents (rows) that contain a particular word. Any "word" that is present in the stopword list is ignored. Every correct word in the collection and in the query is weighted, according to its significance in the query or collection [5]. The weights of the words are then combined to compute the relevance of the row. For calculating relevance value, frequency Ft of each term will be analyzed, normal frequency of each term is calculated using formula 1:

$$T_f = F_t / \text{Max}(F_t) \quad (1)$$

Inverse Document Frequency measure is calculated as follow:

$$Id_f = \log (N / d_f) \quad (2)$$

$N \rightarrow$ Total Number of records
$d_f \rightarrow$ Number of records where the term appears

Weight of each term is calculated as follows:

$$W = T_f X Id_f \quad (3)$$

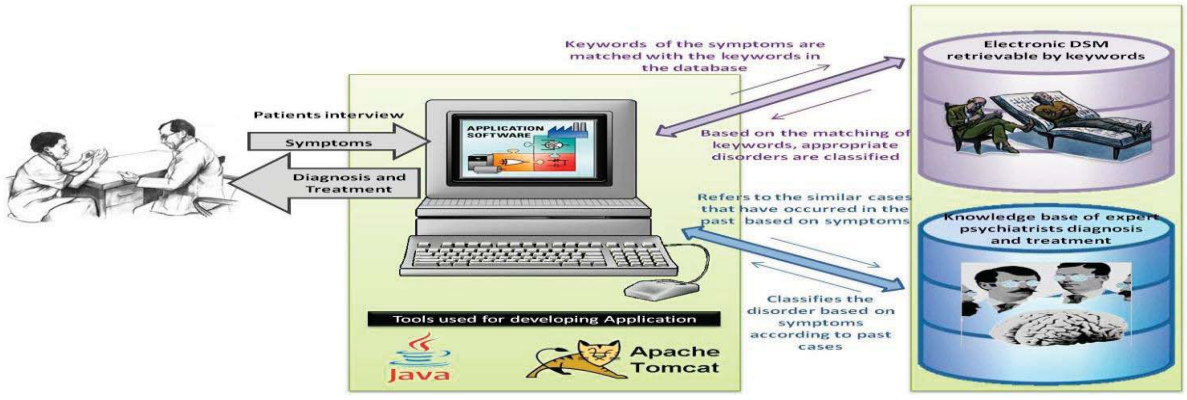

Fig. 1. The study model and procedures

Similarity of each record(relevance value) is calculated as follows:

$$Sim(Q,D) = \sum_{i=1}^{t} \frac{W_{qi} * W_{di}}{\sqrt{\sum (W_{qi})} * \sum (W_{di})} \quad (4)$$

The above formula which represents the similarity is the relevance value which will be in floating numbers. By using this, percentage is calculated as figure 2 shows.

The study system has been developed via two phases. in phase 1, a database of MySQL is created and content of the DSM IV text book is loaded into the database tables. These tables include Symptoms table. This table includes symptoms for each disorder. User query is compared against the contents of this table to retrieve the output. Questions table includes questions belonging to each disorder that has to be asked to the user. Answers table stores user symptoms, the user input to the questions and questions are inserted for further reference.

In phase 1, the graphical user interface is developed as well.

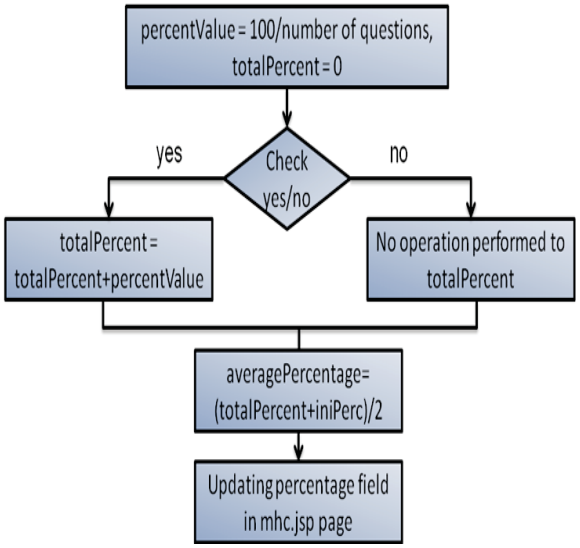

Fig. 2. Calculating Percentage

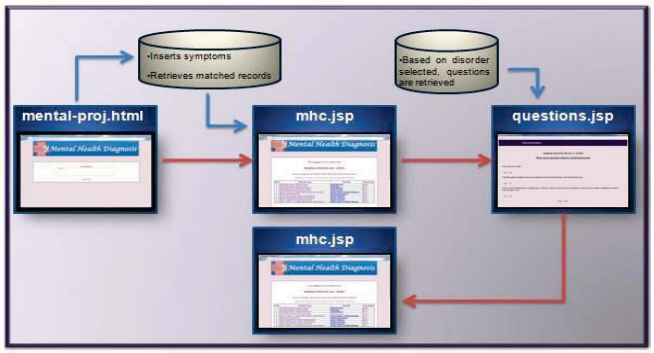

Fig. 3. Phase 1

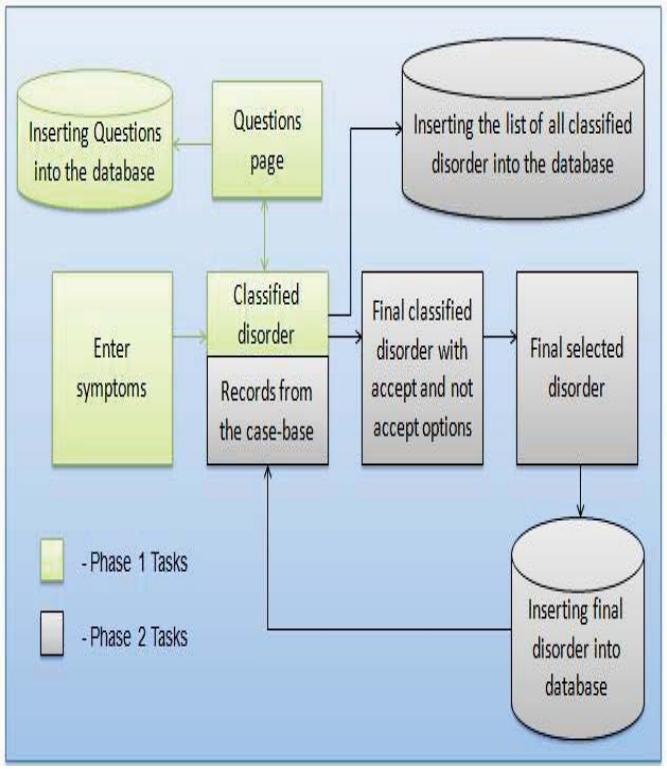

Fig. 4. System Functionality

In phase 2, the classification is done, user answers the questions, and final disorder selected by the application is displayed. (This considers the disorder having highest percentage)

IV. Intelligent Extended Genetic Algorithm

The intelligent extended genetic algorithm that has been implemented to extract keywords from the user's symptoms uses Business Process Execution Language (BPEL) to be an optimal solution for information retrieval. It improves the efficiency and performance for retrieving a proper information results that satisfy user's needs. The implemented algorithm uses several mutation operators simultaneously to produce next generation. This series of random mutation process depend on chromosome best fitness in the population and rely on high relevancy as well. The mutation operation will guarantee the success of algorithm for extracting keywords from the user's symptoms since it expands the search [6]. So the highly effective mutation operators the greater effects on the genetic process.

By implementing the algorithm, data can evolve into information in a way that produces robust flexibility [6]. While other algorithms have made numerous advancements, there is still a lack of the ability to evolve. Nowadays, various applications of genetic algorithms are in the early stages of being used to actively and efficiently extract data based on relevancy. Such applications aim to produce information that has adapted over time based on user requests.

The structure of genetic algorithm is extended to hold multiple populations in the population space. The Algorithm is designed using artificial intelligence methodologies, not geometric approaches, to the information retrieval problem [6].

Our method uses an extended genetic algorithm to find an ideal solution instead of a more mathematical methods such as the k-means algorithm. This key difference allows for more adaptive behavior within our algorithm. Also, web services can induce very large amounts of data.

As it is important to manipulate data accurately and efficiently, Business Process Execution Language approach has been proposed. It implements dynamic service capabilities with genetic algorithms to apply reasoning and flexible service workflows [7], [8], and [9].

This paper builds a utility-based intelligent agent that implements a faster genetic algorithm with greater efficiency than the original algorithm. The genetic algorithm supports a flexible service composition mechanism while having the ability to improve efficiency over time, all while reusing previously tested efficiency. While semi-system can be made bigger, modern paradigm breakthroughs are evolving to make semi-system smarter. The orchestrations of genetic algorithm provide flexible service workflows that can quickly adapt to changes. The orchestration of web services is supported by Business Process Execution Language [9]. BPEL composes, or orchestrates, the services into business flows.

Web service is a technology that enables programs to communicate through Hypertext Transfer Protocol (HTTP) on the Internet [8]. Service standards are effective platforms for publishing services. These standards are Web Services Description Language (WSDL), Extensible Markup Language (XML), and Simple Object Access Protocol (SOAP). WSDL provides a model for describing services. XML adds an intelligent level to distribute information on the Internet. SOAP exchanges structured information in the implementation of the service [7].

Chromosomes are encoded to represent a genetic algorithm and to be parsed into tree structures, which prevents syntax crossovers and allows for mutation stages. Once proper genetic algorithms are put in place, the desired service item from the web part can be requested. Upon this initial request, the first generation of information retrieval is randomly generated, which can lead to a slight decrease of efficiency. What makes up for this initial sacrifice in performance is that as the workflow processes information, the algorithm creates a new generation of logic and the results are assessed based on goodness of fit to results. As new logic workflows are developed, they can be selected and mutated to produce better results. As this process continues, eventually the service matchmaking with user requirements can be provided in such a way to enable increased efficiencies over time. Upon delivery of the user request, the generation cycle is terminated.

The fitness of an individual is computed based on the "distances" between the keywords appearing within the user's symptoms. The keywords are compared by their weights, meaning the ratio of their appearances to the total sum of words in the user's symptoms. These weights are then treated as if they were coordinated for the user's symptoms point on an n-dimensional grid, where n is the number of different keywords appearing within the set of the user's symptoms being retrieved by algorithm.

In the algorithm, an individual with a lower fitness value actually represents a solution of greater quality than one with a greater fitness value. This is because the quality of the retrieval solution is the closeness of the keywords being extracted. Only the most individual fit is passed on to the next generation. The fitness for a chromosome is found through repetition of the math used for finding the similarity of the keywords in the user's symptoms. For each chromosome in the generation, the fitness is computed by finding the average of the similarities for each keyword. By using this method, the fitness is also the average distance between any two keywords in any one user's symptoms in the solution.

Mutation is a way that changes the population to produce the best solution [10]. The process involves a series of mutations that will evolve over time taking only the mutations with a high relevancy, and mutating those further. The algorithm used one type of mutation. This type is known as a one-point mutation. Either a single keyword's position is moved through the chromosome, switching its place in the user's symptoms with another symptom, or the point at which a symptom is organized is moved.

To further increase the genetic diversity present in each generation of the algorithm, the algorithm includes a step where a new individual is added to the population. This individual is randomly generated with each generation iterated, to create additional diversity, even without the crossover step's inclusion in the algorithm.

This algorithm removed crossover step although it is a key part of numerous genetic algorithms. The reason is that crossover decreases the efficiency of our algorithm. It would build new chromosomes out of sections from two different chromosomes, creating new generations with greater diversity. The lesser number of generations required comes with a cost in the form of a drop in efficiency.

Currently, extended genetic algorithm stores each chromosome as a sequence of characters representing the user's symptoms. The order of the characters in our chromosomes is of great importance and no repeats are allowed. Traditional genetic algorithms use a series of bits which represent in turn a series of operations and values. Using crossovers in the source code of our genetic algorithm negatively affects the efficiency of the algorithm more than it would lower the amount of generations required. With just our current generation loop utilizing only varying degrees of mutations, we are likely creating the same chromosomes which would result from crossovers. The proposed genetic algorithm is simply a way to go through a vast number of possible solutions with greater speed and efficiency than other strategies. With or without crossovers, our genetic algorithm should arrive at the same value.

1. Create initial random population P of N individuals
2. i ← 0
3. If i is equal to the number of desired generations,
   return the best individual of the most recent generatic
4. P_{i+1} ← empty set
5. B ← the most fit individual of the previous generatic
6. Add B to P_{i+1}
7. Insert into P_{i+1} mutate(B)
8. Repeat 7 until P_{i+1} has N individuals
9. Evaluate the fitness for all individuals from P
10. i ← i + 1
11. Goto 3

Fig. 5. The Algorithm

V. Experimental Results

The algorithm is tested on set of sample data. The data is based on 50 generations/iterations of the IECGA or K-means respectively, using the same random sample set of 15 symptoms with 600 words each.

The results are listed in Table 1 were collected over 15 test runs of both clustering methods on the same data set. The table shows the statistics collected from our genetic algorithm and K-Means algorithm to demonstrate their relative performance capabilities. The values given are the fitness of the final solution generated by each run, which means that the lower fitness are from better solutions, while higher fitness values are worse solutions. As each method uses a random starting point, there is room for variation in solutions.

From this data, we can observe that on average, implementing IECGA algorithm excels k-means algorithm. The test runs did not find as good a solution with k-means as the best solution from the genetic algorithm, and even the worst solution from the genetic algorithm is of better fitness than the average solution from k-means.

While the data collected does not represent all possible input cases, and cannot claim to represent all of them, it shows a trend of the genetic algorithm exceeding the performance shown the clustering process we had used previously.

As a result, The classifier/psychological analyst is able to make an informed an accurate prognosis. The analyst will be the ultimate selector of the diagnosis and treatment plan. Figure 6 shows that doctor now has option of selection accepting or not accepting the final classified disorder. If not accepted, doctor can select another disorder.

Figure 7 presents the description of all disorders entered into the database.

TABLE 1
IECGA AND K-MEANS PERFORMANCE

	IECGA	*K-Means*
Maximum	1.66384	1.86476
Average	1.56938	1.67881
Minimum	1.35574	1.40269

Fig. 6. Semi-system Options

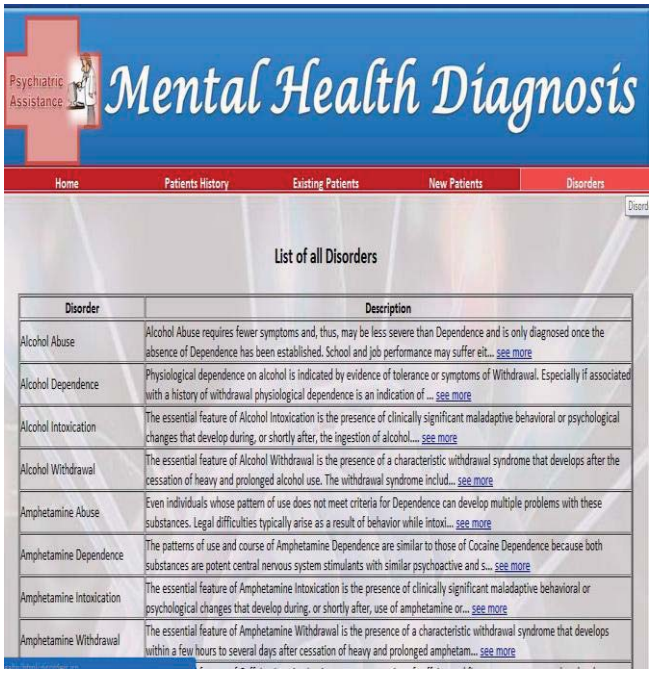

Fig. 7. Disorder Description

VI. CONCLUSION

The main objective of this paper is to ensure that classifier/psychological analyst is capable of making an informed, intelligent, appropriate assessment, and an accurate prognosis. This study proved the applicability of potential Extended Clustering Genetic Algorithm to solve the efficiency and limitation problems in data extraction. The algorithm solution has markedly increased the success of information retrieval and relevancy between keywords-matching and relevant user's symptoms as shown.

The intelligent data extraction is a challenging research problem that arises in many applications. This Genetic Algorithm can be used for many different applications requiring data mining, information retrieval, computational biology, text categorization and image annotation. It enhances an organization's ability to collect information faster at lower cost and to make accurate decisions. Implementing this algorithm provides acceptable benefits in terms of agility and integrity. The orchestrations of genetic algorithms by implementing Business Process Execution Language allow flexible service workflows to be immediately adjusted to modifications and make systems smarter.

Our future work will concentrate on the implementation of the algorithm to large data sets, generalization of the proposed approach to general graph structures, and investigation of the possibility of integrating multiple sources of data for improving the data extraction quality.

REFERENCES

[1] American Psychiatric Association. [DSM-IV-TR], (2000). Diagnostic and statistical manual of mental disorders (Revised 4th ed.). Washington, DC: Author

[2] S. Fernando, "Mental Health in a Multi-Ethnic Society," A Multi-Disciplinary Handbook, Routledge

[3] J. Shedler, "The illusion of Mental Health," American Psychologist, Vol 48 No 11 1117-1131, 1993.

[4] N. El-Bathy, G. Azar, M. El-Bathy, and G. Stein, "Intelligent Extended Clustering Genetic Algorithm," IEEE, Electro/Information Technology, Mankato, MN, United States, pp. 1-5, 2011.

[5] R. Akerkar and P. Lingras, Building an Intelligent Web – Theory and Practice. Sudbury, Massachusetts: Jones and Bartlett Publishers, 2008.

[6] B. Coppin, Artificial intelligence illuminated. Sudbury, Massachusetts: John and Bartlett Publishers, 2004.

[7] N. El-Bathy, P. Chang, G. Azar, and R. Abrahiem , "An Intelligent Search of Lifecycle Architecture for Modern Publishing and Newspaper Industries Using SOA," IEEE, Electro/Information Technology, Normal, IL, United States, pp. 1-7, 2010.

[8] N. El-Bathy and G. Azar, "Intelligent Information Retrieval and Web Mining Architecture Applying Service-Oriented Architecture," KG. Saarbrücken, Germany: LAP LAMBERT Academic Publishing AG & Co. 2010.

[9] N. El-Bathy, G. Azar, M. El-Bathy, and G. Stein, "Intelligent Information Retrieval Lifecycle Architecture Based Clustering Genetic Algorithm using SOA for Modern Medical Industries," IEEE, Electro/Information Technology, Mankato, MN, United States, pp. 1-7, 2011.

[10] H. P. Pfeifer, "An exhaustive Analysis of Recombination and Mutation variances for Genetic Algorithms," Protocol Labs, Munich, 2010.

Data Mining Programming in R Language

Coby Veal, Krunal Patel, and Jin Wang
Department of Mathematics and Computer Science
Valdosta State University, Valdosta, GA 31698, USA

ABSTRACT

Datamining has been used in Computer Science and Mathematical domains since as early as the 1960s. It has many wide reaching applications, and can be performed in many different ways. The R programming language is one such method, and will be the main method discussed in this paper.

Keywords: K-means Clustering; R Language; Linear Regression

I. What is Data Mining?

The term "data mining" is used to describe the computational process of discovering patterns in large data sets, often referred to as "big data". The goal of data mining is to take this "big data" and find the useful information in it, thus transforming it into a much more easily understood data set that can then be used in many different ways. However, the way in which the data is mined is what distinguishes data mining from a simple search method. The searching takes place in an automatic way, and to such an extent that this field is very closely tied with that of AI, or Artificial Intelligence.

Data mining itself is actually only a part of a larger process called Knowledge Discovery of Databases (KDD), which consists of five steps:

(1) Selection
(2) Pre-processing
(3) Transformation
(4) *Data Mining
(5) Interpretation/Evaluation

Many companies will tailor this strategy somewhat to fit their needs, but the basic idea doesn't change.

We won't analyze the other four steps in depth, but Data Mining can be broken down into six different types of "tasks":

(1) Anomaly Detection
(2) Association Rule learning
(3) *Clustering
(4) Classification
(5) *Regression
(6) Summarization
(7)

All of these tasks are useful, the application is what will determine which task needs to be used and when. Often times, more than one task will be used in a "mine". Now that the data mining and its applications have been covered, the question arises: How do we utilize the power of data mining?

II. The R Language

The R language is an open source standard programming language that is used heavily in statistical computing. Ross Ihaka and Robert Gentleman create the R language at the University of Auckland in New Zealand in the early to mid-1990s. Though R has many different functions and applications, we will focus on its data mining capabilities. Specifically, we will see how the R Language can be used to simulate k-means clustering, as well as how to implement basic linear regressions in R.

III. K-means Clustering in R

Clustering describes taking a set of data and grouping it based on some predetermined specifications. K-means keeps true to this idea, with the stipulation that there should be *k* number of groups.

To perform this in R, we first need an initial data set to work with. The [2]data I have chosen is one containing detailed information on

different species of the Iris plant, totaling one hundred and fifty elements. The first step is to read in the information and get it into a workable state.

```
> iris <- read.csv("~/Desktop/iris.csv")
>   View(iris)
> iris.features <- iris
> iris.features$X <- NULL
> view(iris.features)
Error: could not find function "view"
> View(iris.featrues)
Error in View : object 'iris.featrues' not found
> View(iris.features)
> results <- kmeans(iris.features, 3)
```

Typos aside, you can see that it was a matter of specifying the path, and using the assignment character '<-' to place that into the value "iris". In the initial data set, there was a column labeled "X" that listed all of the species names corresponding to each entry, which was unnecessary. This led to the creation of "iris.features", which had all of the same information, minus the 'x' column. Once that was done, the actual k-means algorithm could be run in one line, with the dataset in question on the left, followed by the number of clusters on the right. I knew how many different clusters there would be because of access to the dataset and knowledge that there were three different species. I assigned this value to "results".

```
> results
K-means clustering with 3 clusters of sizes 38, 62, 50

Cluster means:
  sepal.length sepal.width petal.length petal.width
1     6.850000    3.073684     5.742105    2.071053
2     5.901613    2.748387     4.393548    1.433871
3     5.006000    3.418000     1.464000    0.244000

Clustering vector:
  [1] 3 3 3 3 3 3 3 3 3 3 3 3 3 3 3 3 3 3 3 3 3 3 3 3 3
 [25] 3 3 3 3 3 3 3 3 3 3 3 3 3 3 3 3 3 3 3 3 3 3 3 3 3
 [49] 3 3 2 2 1 2 2 2 2 2 2 2 2 2 2 2 2 2 2 2 2 2 2 2 2
 [73] 2 2 2 2 2 1 2 2 2 2 2 2 2 2 2 2 2 2 2 2 2 2 2 2 2
 [97] 2 2 2 2 2 1 2 1 1 1 1 2 1 1 1 1 1 1 2 2 1 1 1 1 2
[121] 1 2 1 2 1 1 2 2 1 1 1 1 1 2 1 1 1 1 2 1 1 1 2 1
[145] 1 1 2 1 1 2

Within cluster sum of squares by cluster:
[1] 23.87947 39.82097 15.24040
 (between_SS / total_SS =  88.4 %)

Available components:

[1] "cluster"      "centers"      "totss"
[4] "withinss"     "tot.withinss" "betweenss"
[7] "size"         "iter"         "ifault"
```

Running the k-means gave me my results of three clusters of sizes thirty-eight, sixty-two, and fifty. It also shows which cluster each element was mapped to under the "clustering vector:" line.

This information does not give us an idea of how accurate our clusters are, so we need to find a way to compare it to our original data set and figure out how close we are.

```
> table(iris$X, results$cluster)

                 1  2  3
  Iris-setosa    0  0 50
  Iris-versicolor  2 48  0
  Iris-virginica  36 14  0
```

The best way to do this is to make a table of the information, using the species for the rows and the clusters as the columns. As seen above, it appears that the clusters were fairly accurate, with the "Iris-setosa" species getting cluster three all to itself. There is some overlapping, but that is all right. Now that we've analyzed the "results" in comparison to the original data set, perhaps it would be useful to get a look at the graph of the k-means to get a better idea of their distribution. For this demonstration, the plot will use the petal.length for the x-axis and the petal.width for the y-axis.

```
> plot(iris[c("petal.length", "petal.width")], col = results$cluster)
```

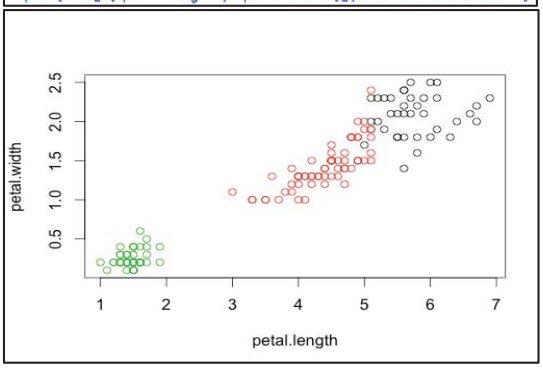

It would appear that cluster 3 is the green cluster corresponding to "setosa" species. It seems to have a short petal length and petal width. The red cluster corresponds to cluster 2, would appear to be mostly "versicolor", having a medium length and width petal between the three. The black cluster corresponds with cluster 3 above, and is made up of mostly "virginica", though there are quite a few "versicolor" as well.

We can compare this graph to the graph of the orginal data set sorted by species to see how close our clusters were, in a similar way to the comparison of the table above.

```
> plot(iris[c("petal.length", "petal.width")], col = iris$X)
```

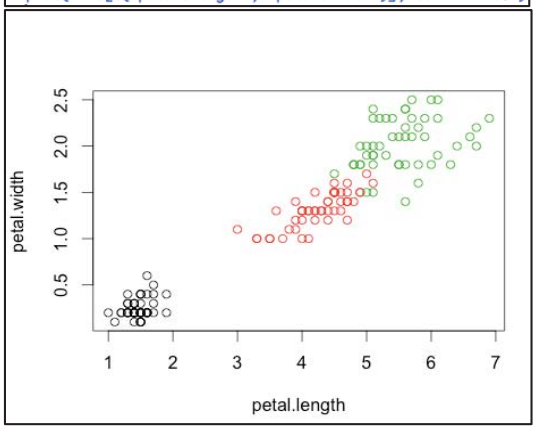

Comparing the two, it would appear that the clusters were very accurate, though there were a few outliers that were unable to be mapped correctly. Considering the nature of the data set, plantlife, it is impossible to eliminate them completely due to the variance in which plants can grow. However, our clusters give us a very good idea of the relationship between each species and the length and width of their petals.

IV. Linear Regression in R

A good understanding of how to implement basic K-means clustering in R, and how to analyze your data should have been acquired from the previous section. However, a clustering analysis is not always the ideal technique to use when attempting to compare and analyze data. Another very popular and powerful technique is linear regression, which R has built in functionality for.

As with any data analysis problem, we must first read in the data we will be using.

```
> iris = read.csv("C:/Users/colby/Desktop/iris.csv")
> View(iris)
> summary(iris)
  sepal.length    sepal.width     petal.length    petal.width          X
 Min.   :4.300   Min.   :2.000   Min.   :1.000   Min.   :0.100   Iris-setosa    :50
 1st Qu.:5.100   1st Qu.:2.800   1st Qu.:1.600   1st Qu.:0.300   Iris-versicolor:50
 Median :5.800   Median :3.000   Median :4.350   Median :1.300   Iris-virginica :50
 Mean   :5.843   Mean   :3.054   Mean   :3.759   Mean   :1.199
 3rd Qu.:6.400   3rd Qu.:3.300   3rd Qu.:5.100   3rd Qu.:1.800
 Max.   :7.900   Max.   :4.400   Max.   :6.900   Max.   :2.500
```

The previous data set seemed to work well and have a strong correlation, so that is the data that will be used for this as well. Since the contents of the data set has already been discussed, it will not be covered again here. A summary of the important information from the data set has been included in the figure above.

```
> lm(petal.width ~ petal.length, data=iris)$coefficients
 (Intercept) petal.length
  -0.3665140    0.4164191
>
> plot(iris$petal.length, iris$petal.width, pch=21, bg=c("red","green","blue")[unclass(iris$X)],
 xlab="petal length", ylab="petal width")
```

Now that the data is in a usable state, the first thing that must be done is to make a linear model out of the data. This is done with the "lm" command. Within that command, we must specify what elements of that data exactly should be used to make the model. In keeping with the previous test on k-means, we will analyze the petal width in conjunction with petal height, using the "~" symbol to denote the nature of the relationship. Once the relationship is established, we can easily plot the data.

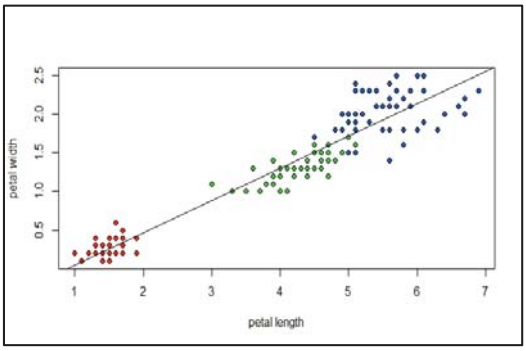

Ignoring the black line for a moment, we can see that we get a generally similar graph as the one we got before, which a byproduct of the linear model function.

```
> abline(lm(petal.width ~ petal.length, data=iris)$coefficients, col="black")
```

With the "abline" function, a regression line can easily be added that corresponds to the trend found in the data in relation to petal width and petal length.

```
> summary(lm(petal.width ~ petal.length, data=iris))

Call:
lm(formula = petal.width ~ petal.length, data = iris)

Residuals:
     Min       1Q   Median
-0.56543 -0.12409 -0.01647
      3Q      Max
 0.13251  0.64278

Coefficients:
             Estimate Std. Error
(Intercept)  -0.366514   0.039889
petal.length  0.416419   0.009613
             t value Pr(>|t|)
(Intercept)   -9.188 3.35e-16 ***
petal.length  43.320  < 2e-16 ***
---
Signif. codes:
  0 '***' 0.001 '**' 0.01 '*'
  0.05 '.' 0.1 ' ' 1

Residual standard error: 0.207 on 148 degrees of freedom
Multiple R-squared:  0.9269,    Adjusted R-squared:  0.9264
F-statistic:  1877 on 1 and 148 DF,  p-value: < 2.2e-16
```

Using the summary function again, a lot of useful data from the regression can be obtained. Each piece of data is useful in certain situations, but for the purpose of checking how well our regression line matches the linear model can be seen in the p-value. Generally, a good p-value is less than 0.5, which would tell you that your data is useful. As you can see, ours is displayed as p-value: < 2.2e-16. This is actually the smallest value that R can produce, which means that we have a very good relationship between petal length and petal width.

V. Summary and Conclusion

Datamining is a very broad topic, with research ongoing in a lot of different areas. What has been presented here is nothing more than a snapshot of a few different methods that "big data" can be analyzed, and how to perform these analytics in the R language.

R is a great tool for performing research on datasets of all sizes, and gives a plethora of useful functions that make the analytics very easy to perform. In most cases this can be done in a few lines! However, R is just that; a tool. Datamining does still rely on the user to know how to reach their desired result. What it excels at is simplifying the process of coding and offering many different tools and methods to obtain the desired result.

References

1. Kiri Wagstaff, Clair Cardie, Seth Rogers, Stefan Schroedl (2001) *Constrained K-means Clustering with Backround Knowledge (*18th Internation Conference on Machine Language p.577-584)
2. Lichman, M. (2013). UCI Machine Learning Repository [http://archive.ics.uci.edu/ml]. Irvine, CA: University of California, School of Information and Computer Science.
3. Leemis, Lawrence , *Learning Base R*. The College of William and Mary1 ed , Vol . 1.2015.
4. Yau, C , "Simple Linear Regression in R". RetrievedDecember , 2015 Available: http://www.r-tutor.com/elementary-statistics/simple-linear-regression
5. Kabacoff, R , "Cluster Analysis". RetrievedDecember , 2015 Available: http://www.statmethods.net/advstats/cluster.html

Pilot Assignment of Massive MIMO Systems for Pilot Decontamination Based on Inter-cell Cross Gain

Fang Yong*(IEEE Senior Member)*[1], **Mei Sulin**[1], **Wang Du**[1]
[1]Key Laboratory of Specialty Fiber Optics and Optical Access Networks, School of Communication and Information Engineering, Shanghai University, Shanghai, 200444, China

Abstract – *It is essential to achieve accurate channel state information (CSI) for fully utilizing the potential benefits of massive MIMO systems. Many researchers have stressed the influence of pilot contamination (PC) on channel estimation. Under the condition of hundreds of antennas at the base station (BS), the irrelevant noise and fast fading will vanish. However, the inter-cell influence will never disappear even if the number of antennas at the BS is infinite. In this paper, we analyze the influence of PC on the channel estimation. Simulation results show that the impact of PC mainly depends on the value of inter-cell cross gain. Then, a novel pilot assignment based on inter-cell cross gain is proposed to mitigate PC for massive MIMO systems. The numerical results validate the effectiveness of the proposed scheme.*

Keywords: Massive MIMO, Pilot contamination, Channel estimation, Inter-cell cross gain

1 Introduction

Multiple Input Multiple Output (MIMO) has been considered as a promising approach for exploiting the spectral efficiency of wireless systems [1]. However, the traditional MIMO technology can not satisfy the increasing demands of higher data rate. The massive MIMO system as a new system has been considered for future wireless communication networks.

The massive MIMO system is a novel multi-user MIMO (MU-MIMO) architecture, which equips a large number of antennas at the base station (BS), serving a multiplicity of single-antenna terminals. This system has coherent benefits, such as, higher channel capacity and spectrum efficiency. In traditional communication system, the system capacity can be improved by scaling down the cells. But in massive MIMO system, with the increase of the number of antennas at the BS, the capacity will be improved as well. From the perspective of information theory, when the number of antennas at the BS approaches infinite, the channel capacity should be infinite in terms of theory. However, this is impossible in practice. The main factor that affects the capacity is the pilot contamination (PC)[2]. In massive MIMO system, users in different cells share the same orthogonal pilots, thus channel estimation will be contaminated by the pilots from the neighbor cells [3]. As is well known, accurate channel state information (CSI) is very important in achieving the benefits of systems. Therefore, it is necessary to take the effect of PC on channel estimation into account in massive MIMO system.

Several methods have been proposed to mitigate the impact of PC on channel estimation in massive MIMO system. The solution presented in [4] suppressed PC without the need for coordination among cells. At each transmission slot, the pilot sequence hops, which make the PC randomize. By using a modified Kalman filter, the PC can be significantly suppressed. In [5], in contrast to the conventional schemes which assign the pilot sequences to the users randomly, the proposed method assigns the pilot sequences with the smallest inter-cell interference to the user having the worst channel quality in a sequential way to improve its performance. Pilot contamination pre-coding scheme is also an effective method to mitigate PC [6-7]. It is possible to eliminate PC entirely when the number of antennas at the BS gets infinite. The work in [8-10] is based on channel estimation algorithm to eliminate the effect of PC. In [8], analytical expressions show that minimum mean square error (MMSE) is more resistant to PC compared to least square (LS). A simple channel estimator is proposed in [9] for a multi-cell massive MIMO with pilot contamination, the performance of proposed estimator is closed to the ideal MMSE estimator. Although these methods can mitigate the influence of PC to some degrees, few of them take inter-cell cross gain into account, which plays an important role in PC.

In this paper, we analyze the impact of PC on the performance of LS and MMSE channel estimation algorithms in massive MIMO system. Analytical expressions show that when the number of antennas at the base station (BS) becomes infinite, the impact of PC mainly depends on the value of inter-cell cross gain. Then, a pilot assignment scheme is proposed according to the inter-cell cross gain to mitigate PC for massive MIMO.

Notations: We use bold italic font variables to denote matrices and vectors. $(\cdot)^T$, $(\cdot)^*$ and $(\cdot)^H$ denote transpose, conjugate and Hermitian transpose, respectively. $(\cdot)^{-1}$ and $(\cdot)^+$ denote the inverse and pseudo inverse operations, respectively. $CN(\boldsymbol{\Gamma}, \Upsilon)$ denotes complex Gaussian distribution with mean $\boldsymbol{\Gamma}$ and covariance metric Υ. $\|\cdot\|_F$

denotes the Frobenius norm operation. $\mathbb{E}\{\cdot\}$ stands for expectation operations. $C^{M\times K}$ represents the spaces of $M\times K$ matrices with complex entries.

2 System model

Let us consider a multi-cell MU-MIMO system with L cells, as shown in Fig. 1. Each cell equips one BS with M antennas and K single-antenna mobile stations (MSs). For massive MIMO system, it satisfies that $M \gg K$. The time division duplex (TDD) protocol is considered in this system, since the channel reciprocity property can be exploited to estimate the downlink channel by using the uplink channel estimation.

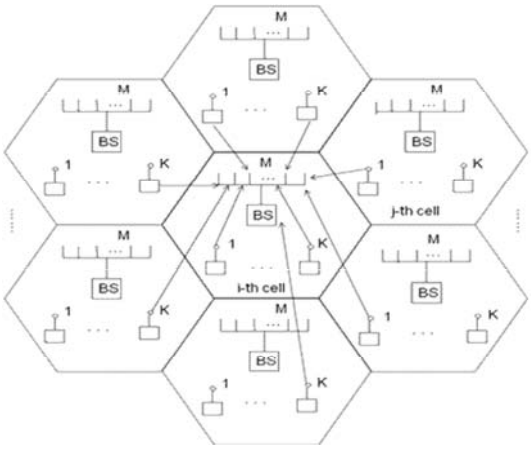

Fig. 1 Multi-cell MU-MIMO system

During the pilot transmission, the BS in the l th cell will receive the following signal

$$\mathbf{Y}_l = \sum_{j=1}^{L} \mathbf{H}_{jl}\mathbf{S}^T + \mathbf{N}_l \tag{1}$$

where $\mathbf{S} = \left[\mathbf{s}_1, \mathbf{s}_2, \cdots, \mathbf{s}_K\right]_{K\times K}$ is the orthogonal pilot sequences used in all cells with $\mathbf{s}_k^H \cdot \mathbf{s}_k = 1, \forall k$. $\mathbf{H}_{jl} = \mathbf{G}_{jl} \cdot \mathbf{D}_{jl}^{\frac{1}{2}}$ is the channel matrix between the j th MS in the l th cell and the BS. $\mathbf{D}_{jl} = diag\left\{\left[\beta_{jl1}, \beta_{jl2}, \cdots, \beta_{jlK}\right]\right\}$ is the distant dependent path loss and $\mathbf{G}_{jl} = \left[\mathbf{g}_{jl1}, \mathbf{g}_{jl2}, \cdots, \mathbf{g}_{jlK}\right]$ is the fast fading part, and $\mathbf{g}_{jlk} = \left[g_{jlk1}, g_{jlk2}, \cdots, g_{jlkM}\right]^T$. It is assumed that g_{jlkm} is independently and identically distributed (i.i.d) random variable with $g_{jlkm} \sim CN(0,1)$, $\forall j,l,k,m$. $\mathbf{N}_l$ is also i.i.d $CN(0,\sigma_n^2\mathbf{I}_M)$ noise vector. Furthermore, the path loss in this paper is designed as follows

$$\beta_{jlk} = \begin{cases} 1, & j = l \\ a, & j \neq l \end{cases} \tag{2}$$

where a is the inter-cell cross gain and $0 < a < 1$.

3 Impact of PC on LS and MMSE

In this section, the PC impact on traditional LS and MMSE channel estimation algorithms is investigated in massive MIMO system.

3.1 LS channel estimation

Firstly, we separate the local channel $\mathbf{H}_{ll}$ and the interference channels $\mathbf{H}_{jl}(j \neq l)$, the received signal can be expressed as

$$\mathbf{Y}_l = \mathbf{H}_{ll}\mathbf{S}^T + \sum_{j\neq l}^{L-1} \mathbf{H}_{jl}\mathbf{S}^T + \mathbf{N}_l \tag{3}$$

According to the LS channel estimator $\mathbf{\Delta}_{ll}^{LS} = \mathbf{S}^*(\mathbf{S}^T\mathbf{S}^*)^{-1}$, the channel estimate of LS in the presence of PC is given by

$$\begin{aligned} \hat{\mathbf{H}}_{LS,PC} &= \mathbf{Y}_l \cdot \mathbf{\Delta}_{ll}^{LS} \\ &= \mathbf{H}_{ll} + \sum_{j\neq l}^{L-1} \mathbf{H}_{jl} + \mathbf{N}_l \cdot \mathbf{S}^*(\mathbf{S}^T\mathbf{S}^*)^{-1} \end{aligned} \tag{4}$$

The mean square error (MSE) between estimate channel with PC and without PC is defined as ε_{LS} .

$$\begin{aligned} \varepsilon_{LS} &= \mathbb{E}\left\{\left\|\hat{\mathbf{H}}_{LS,PC} - \hat{\mathbf{H}}_{LS}\right\|_F^2\right\} = \mathbb{E}\left\{\left\|\sum_{j\neq l}^{L} \mathbf{H}_{jl}\right\|_F^2\right\} \\ &= \mathbb{E}\left\{\left\|\sum_{j\neq l}^{L} \mathbf{G}_{jl} \cdot \mathbf{D}_{jl}^{\frac{1}{2}}\right\|_F^2\right\} \\ &= a\mathbb{E}\left\{\left\|\sum_{j\neq l}^{L} \mathbf{G}_{jl}\right\|_F^2\right\} \end{aligned} \tag{5}$$

If we ignore the influence of noise on channel estimation, the result of LS algorithm will be the superposition of local channel and interference channels. The latter one is caused by the PC. When there is no PC and the number of antennas at the BS becomes infinite, the error of channel estimate can be negligible, so $\mathbf{H} \approx \mathbf{H}_{LS}$, the MSE of LS algorithm is $MSE_{LS} \approx \varepsilon_{LS}$.

3.2 MMSE channel estimation

According to the principle of MMSE, its estimator can be expressed as

$$\mathbf{\Delta}_{ll}^{MMSE} = \arg\min_{\mathbf{H}} \mathbb{E}\left\{\left\|\mathbf{H}_{ll} - \hat{\mathbf{H}}_{ll}\right\|_F^2\right\} \tag{6}$$

The MSE of the MMSE is given by

$$\begin{aligned} MSE &= \mathbb{E}\left\{\left\|\mathbf{H}_{ll} - \hat{\mathbf{H}}_{ll}\right\|_F^2\right\} \\ &= \mathbb{E}\left\{tr\left\{\left(\mathbf{H}_{ll}^H - \mathbf{\Delta}^H \mathbf{Y}_l^H\right)\left(\mathbf{H}_{ll} - \mathbf{Y}_l\mathbf{\Delta}\right)\right\}\right\} \end{aligned} \tag{7}$$

Then, the estimator of MMSE is given by $\frac{\partial MSE}{\partial \mathbf{\Delta}^*} = 0$.

$$\mathbf{\Delta}_{ll}^{MMSE} = \left(\mathbf{S}^*\left(\mathbf{R}_{ll} + \sum_{j\neq l}^{L-1}\mathbf{R}_{jl}\right)\mathbf{S}^T + M\sigma_n^2\mathbf{I}\right)^{-1}\mathbf{S}^*\mathbf{R}_{ll} \tag{8}$$

where $\mathbf{R}_{jl} = \mathbb{E}\left\{\mathbf{H}_{jl}^H\mathbf{H}_{jl}\right\}$ is the autocorrelation matrix of $\mathbf{H}_{jl}$. The channel estimate of MMSE can be expressed as

$$\hat{\mathbf{H}}_{MMSE,PC} = \mathbf{Y}_l \cdot \mathbf{\Delta}_{ll}^{MMSE} \tag{9}$$

The number of antennas at the BS M is very large in massive MIMO system, thus, based on the properties of Gaussian random variables, we can get

$$\begin{aligned} \mathbf{R}_{jl} &= \mathbb{E}\left\{\mathbf{H}_{jl}^H\mathbf{H}_{jl}\right\} \\ &= \mathbb{E}\left\{\left(\mathbf{G}_{jl}\cdot\mathbf{D}_{jl}^{\frac{1}{2}}\right)^H\mathbf{G}_{jl}\cdot\mathbf{D}_{jl}^{\frac{1}{2}}\right\} \\ &\approx \begin{cases} Ma\mathbf{I}_K & j\neq l \\ M\mathbf{I}_K & j = l \end{cases} \end{aligned} \tag{10}$$

So the (9) can be equivalently formulated as

$$\hat{\mathbf{H}}_{MMSE,PC} = \rho\cdot\left(\mathbf{G}_{ll} + \sqrt{a}\sum_{j\neq l}^{L-1}\mathbf{G}_{jl} + \mathbf{N}_l\mathbf{S}^*\right) \tag{11}$$

where $\rho = \left(\left(1+\left(L-1\right)a\right)+\sigma_n^2\right)^{-1}$. From (5) and (11), we can see that the accuracy of LS and MMSE channel estimation is affected by the MS in other cells. The number of cells L and inter-cell cross gain a are the main factors to the interference error.

4 Proposed pilot assignment

As is well known, the inter-cell cross gain a is determined by the distance between the two cells, and the value of a is inversely proportional to the distance. In this section, we propose a new scheme of pilot assignment to mitigate PC. Two sets of orthogonal pilot sequences are designed for transmission. During pilot training, the transmission signal is

$$\mathbf{S} \in \left\{\mathbf{S}_1, \mathbf{S}_2\right\} \tag{12}$$

where $\mathbf{S}_i = \left[\mathbf{s}_{i1}, \mathbf{s}_{i2}, \cdots, \mathbf{s}_{iK}\right]_{K\times K}$, $\mathbf{s}_{ik}^H\cdot\mathbf{s}_{ik} = 1$ $\forall k,\quad i = 1,2$ and $\mathbf{S}_1^H\cdot\mathbf{S}_2 = \mathbf{I}_K$.

We assume that the target cell chooses $\mathbf{S}_1$ as the pilot sequence. If the distance between two cells is larger than d_0 (threshold preset), namely, $a > a_0$ (threshold preset), they will share the same orthogonal pilot sequences. Otherwise, $\mathbf{S}_2$ will be chosen as the transmission signal. The received signal can be expressed as

$$\mathbf{Y}_l = \sum_j^{L_1}\mathbf{H}_{jl}\mathbf{S}_1^T + \sum_p^{L_2}\mathbf{H}_{pl}\mathbf{S}_2^T + \mathbf{N}_l \tag{13}$$

where L_1 and L_2 denote the number of cells satisfied $a > a_0$ and $a < a_0$ respectively, and $L = L_1 + L_2$. Then, the channel estimation could be rewritten as

$$\hat{\mathbf{H}}_{LS,PC} = \mathbf{H}_{ll} + \sum_{j\neq l}^{L_1-1}\mathbf{H}_{jl} + \mathbf{N}_l\cdot\mathbf{S}^*(\mathbf{S}^T\mathbf{S}^*)^{-1} \tag{14}$$

$$\hat{\mathbf{H}}_{MMSE,PC} = \rho_1\cdot\left(\mathbf{G}_{ll} + \sqrt{a}\sum_{j\neq l}^{L_1-1}\mathbf{G}_{jl} + \mathbf{N}_l\mathbf{S}_1^*\right) \tag{15}$$

where $\rho_1 = \left(\left(1+\left(L_1-1\right)a\right)+\sigma_n^2\right)^{-1}$. Observe in (14) and (15) that the PC is partly mitigated.

5 Experimental results

In this section, we provide simulation results. For this simulation, we considered a multi-cell multi-user MIMO system, $L = 3$ cells, and $K = 10$ users in each cell. The orthogonal pilot sequences are used in each cell.

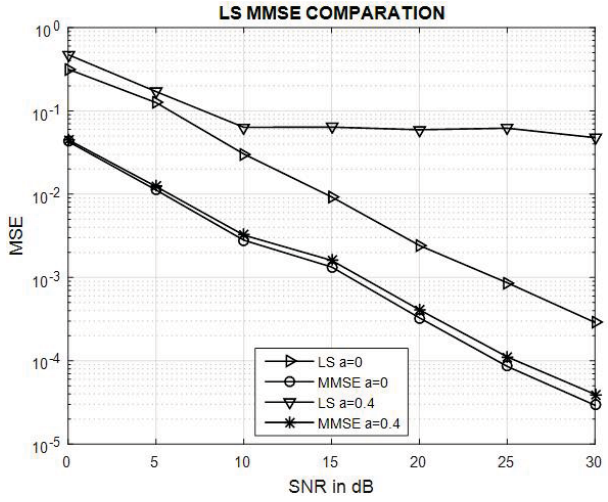

Fig. 2 MSE versus SNR with different a at $L=3$, $M=50$

The MSE performance of LS and MMSE algorithms as a function of SNR with different a at $L=3$, $M=50$ is depicted in Fig. 2. As we can see from the picture, MMSE is more resistant to PC compared to LS. This is because more prior information is used in MMSE algorithm. The MSE of LS tends to stable in the present of PC with the increase of SNR.

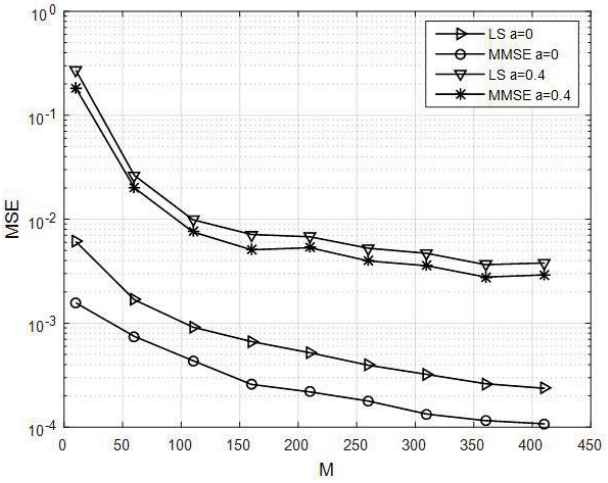

Fig. 3 MSE versus M with different a at $L=3$, SNR=15dB

Fig. 3 shows the MSE performance of LS and MMSE algorithms as a function of M with different a at $L=3$, SNR=15dB. The performance of both algorithms improves significantly with M increasing no matter the value of a is. The MSE decrease sharply when the number of antennas at the BS increases from 10 to 150, however, it turns to be stable when M continues to increase. This is because the impact of PC still exists no matter how many M is.

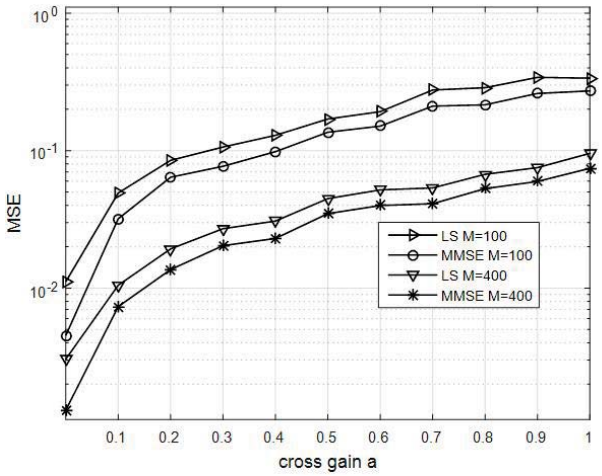

Fig. 4 MSE versus a with different M at $L=3$, SNR=15dB

Fig. 4 shows the MSE performance of LS and MMSE algorithms with different M at SNR=15dB as a function of the inter-cell cross gain a. The MSE of both algorithms has an obvious increase with the inter-cell cross gain a increasing. Meanwhile, the performance will be improved as $a<0.5$ and tend to be stable as $a>0.5$.

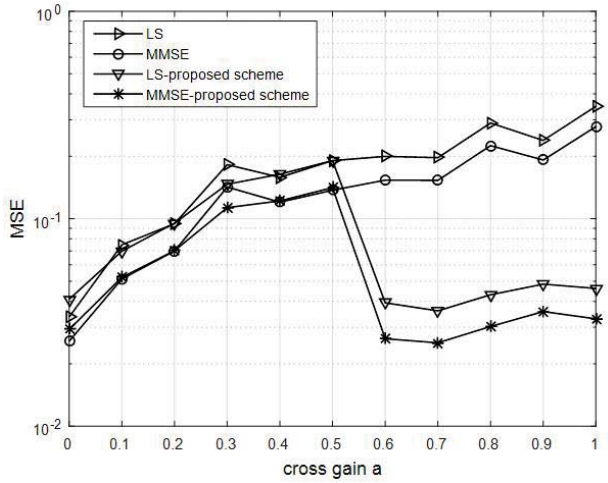

Fig. 5 Comparison of the proposed scheme and the exiting scheme for $L=3, M=100$ SNR=15dB

In this simulation, we consider a massive MIMO system with 3 cells, one target cell and two neighbor cells. We assume that one of the neighbor cells is next to the target cell, so the inter-cell cross gain between them is a constant a_c, and the cross gain of the other is a variable a_v. The preset threshold is 0.5. Fig. 5 shows the proposed and the existing scheme for different cross gain with $L=3$, $M=100$ SNR=15dB. As can be seen in the picture, if a_v is larger than the preset threshold, the proposed scheme can effectively mitigate the impact of PC.

6 Conclusions

In this paper, the impact of PC on the conventional LS and MMSE channel estimation has been investigated in massive MIMO system. Analytical and simulation results show that MMSE is more resistant to PC compared to LS. With the increase of antennas at the BS, the impact of PC mainly depends on the value of inter-cell cross gain. The MSE of both algorithms improves significantly with M increasing no matter the value of a is. Then, we design a novel pilot assignment based on inter-cell cross gain a. It can be seen that the proposed scheme can improve the performance of channel estimation effectively.

Acknowledgement

The work is supported by NSF of China (61271213) and the Ph.D. Programs Foundation of Ministry of Education of China (20133108110014).

7 References

[1] F. Boccardi, R. Heath, A. Lozano, T. Marzetta, and P. Popovski. "Five disruptive technology directions for 5G"; IEEE Commun. Mag., Vol. 52, No. 2, Feb 2014.

[2] F. Rusek, D. Persson, B. K. Lau, E. Larsson, T. Marzetta, O. Edfors, and F. Tufvesson. "Scaling up MIMO: Opportunities and challenges with very large arrays"; Signal Processing Magazine, IEEE, Vol. 30, pp. 40-60, Jan 2013.

[3] T. L. Marzetta. "Noncooperative cellular wireless with unlimited numbers of base station antennas"; IEEE Trans. Wirel. Commun., Vol. 9, No. 11, pp. 3590-3600, Nov 2010.

[4] J. Sorensen and E. de Carvalho. "Pilot Decontamination Through Pilot Sequence Hopping in Massive MIMO Systems"; in IEEE GLOBECOM, pp. 3285–3290, 2014.

[5] X. Zhu, Z. Wang, L. Dai, and C. Qian. "Smart Pilot Assignment for Massive MIMO"; IEEE Commun. Lett., Vol. 19, No. 9, pp. 1644-1647, Sept 2015.

[6] A. Ashikhmin and T. Marzetta. "Pilot contamination precoding in multicell large scale antenna systems"; in IEEE International Symposium on Information Theory (ISIT), 2012.

[7] A. Adhikary, A. Ashikhmin, and T. L. Marzetta. "Uplink interference reduction in large scale antenna systems"; in Proc. IEEE Int. Symp. On Inf. Theory (ISIT), Honolulu, HI, pp. 2529–2533, June 2014.

[8] Peng Xu, Jinkuan Wang, Jiangzhou Wang. "Effect of pilot contamination on channel estimation in massive MIMO systems"; in Wireless Communications & Signal Processing (WCSP), 2013 International Conference on , Vol., No., pp.1-6, 24-26 Oct. 2013.

[9] Amin Khansefid, and Hlaing Minn. "On Channel Estimation for Massive MIMO With Pilot Contamination"; IEEE Communication Letters, Vol. 19, No. 9, September 2015.

[10] Bogale, T.E., Long Bao Le. "Pilot optimization and channel estimation for multiuser massive MIMO systems"; in Information Sciences and Systems (CISS), 2014 48th Annual Conference on , Vol., No., pp.1-6, 19-21 March 2014.

Museums Security System Using Electromagnetic Identification algorithm of Antiquities

Haythem H Abdullah, Tamer G. Aboelnaga, Hala Elsadek and Hesham Eldeeb.

Electronics Research Institute, Eltahrir St., Dokki, Giza, Egypt, 12622

hhelsadek92@gmail.com

Abstract — The time domain scattered field response of a targeted object has been observed to be composed of an early-time forced period followed immediately by a late-time period during which the target reflected/scattered signal oscillates freely. One of the main merits of the conducting objects is that the natural modes of the target do not depend on the scattering angle. On contradictory to the dielectric objects it depends mainly on the incident and scattered angles. The late-time portion can be decomposed into a finite sum of damped sinusoids that are oscillating at frequencies determined purely by target properties which is called object natural E-pulse print. This is useful in identifying original historical antiquates in museums. The E-pulse technique is effectively used in such cases. In this paper, convoluted E-pulse technique is utilized to identify metallic as well as non metallic original antiquities. Numerical algorithm is designated and coded while experimental tests reveal promising identification results for several objects.

Index Terms — Security systems, priceless objects, late time response, E-Pulse, convoluted E-pulse print technique, Method of Moments, target identification.

I. INTRODUCTION

Time domain response in resonance based radar target discrimination schemes has generated a considerable interest in the past [1-4].Targets can be identified by their natural frequencies, which are extracted from the late time scattered responses when irradiated with transient electromagnetic signals. One of the most popular methods used in recent time for resonance based target discrimination is the Extinction pulse (E-pulse) discrimination technique. Two algorithms has been used, the first algorithm is based on the knowledge of the natural modes of the target, while the second is based directly on the measured response from the target. The time domain scattered field response of a target has been observed to be composed of an early-time forced period, when the excitation field is interacting with the scatterer (object), followed immediately by a late-time period during which the target oscillates freely. The late-time portion can be decomposed into a finite sum of damped sinusoids (excited by an incident field waveform of finite usable bandwidth), oscillating at frequencies determined purely by target properties: geometry, size and material properties. The natural resonance behavior of the late-time portion of the scattered field response can be utilized to provide an aspect-independent means for radar target discrimination. An extinction (E-pulse) is defined as a finite duration waveform which, upon interaction with a particular target, eliminates a preselected portion of the target's natural mode spectrum. By basing E-pulse synthesis at the target natural frequencies, the E-pulse waveform is made aspect-independent. Discrimination is accomplished by convoluting an E-pulse waveform with the measured late-time scattered field response of a target. If the scattered field comes from the anticipated target, the convoluted response will be composed of an easily interpreted portion of the expected natural mode spectrum. If the target is different, a portion of its dissimilar natural mode spectrum will be extracted, resulting in an unexpected convoluted response. It is important to note that the E-pulse waveform need not be transmitted to employ this concept. It is assumed that an excitation waveform with finite usable bandwidth will be used to illuminate the target, resulting in a measured scattered field with the desired (finite) modal content. The E-pulse can then be convoluted numerically with the measured target response, yielding results analogous to E-pulse transmission that can be called object E-pulse print. If the maximum modal content of the target scattered field can be estimated from the frequency content of the excitation pulse, then the E-pulse waveform can be constructed to yield a null late-time convoluted response, [5,6]. In some cases, it is difficult to extract the natural modes of the target, so the need for a technique that have the ability to synthesis the E-pulse directly from its measured response becomes of main interest. There are several attempts in this topic, [7-9]. In fact, all of them give very similar algorithms but each one reaches it from his point of view. In this paper, a simplified analysis is introduced that gives a simple detailed algorithm for designing an E-pulse from the measured or calculated response of the required target. Target scattered response for several objects with different geometrical models and material properties are measured experimentally using simple similar transmit and receive antennas. The designated time domain E-pulse extinction algorithm is applied on these objects' scattered signals. The convoluted E-pulse print of these objects are extracted which verifying the idea of object discrimination/identification using this technique. Many

applications can be utilized from the convoluted E-pulse print technique as in security systems in museums, the main application in this research, where the unique identifying of antiquities resembles great importance for protecting priceless ornaments and historical statues..

II. Convoluted E-pulse Technique

An extinction-pulse (E-pulse) $e(t)$ is defined as a waveform of finite duration Te which extinguishes the backscattered signal $E^s(t)$ in its late time portion. That is the convolution of $e(t)$ and $E^s(t)$ that yields the null result.

$$c(t) = e(t) * E^s(t) = \int_0^{T_e} e(\acute{t})\, E^s(t-\acute{t})d\acute{t} = 0 \qquad t < T_L + T_e \qquad (1)$$

Where T_L describes the beginning of the late time period, and T_e is the duration of the E-pulse signal.

Now, it is worth to mention that this technique is capable of designing an E-pulse signal for each target directly without the need to know the natural modes of the target. In addition, as a check, one can also calculate the natural modes of the target from the designed E-pulse coefficients.

Design of the E-pulse Signal

An E-pulse waveform can be represented as an expansion over a set of basis functions

$$e(t) = \sum_{k=1}^{K} \alpha_k f_k(t) \qquad (2)$$

where α_k are the basis function amplitudes. $K = 2N$, and N is the number of the target natural frequencies. Choosing K = 2N results in a homogeneous equation which has solutions only at discrete values of $T = T_L + T_e$, so it is recommended to take K=2N+1 that results in a definite system of linear equations which can be solved easily. One can choose sub sectional basis functions in the E-pulse expansion as follows

$$f_k(t) = \begin{cases} S(t-[k-1]\Delta), & (k-1)\Delta \le t \le k\Delta \\ 0 & \text{elsewhere} \end{cases} \qquad (3)$$

Applying (3) in (2), equation (3) can be rewritten as

$$\sum_{k=1}^{K} \alpha_k \int_0^{T_e} f_k(\acute{t}) E^s(t-\acute{t})d\acute{t} = 0 \qquad (4)$$

By choosing a set of testing functions $w_m(t)$ and applying a moment method testing procedure to equation (4) yields

$$\langle w_m(t), \sum_{k=1}^{K} \alpha_k \int_0^{T_e} f_k(\acute{t}) E^s(t-\acute{t})d\acute{t}\rangle = 0, \qquad m = 1, 2, 3, \ldots\ldots, K \qquad (5)$$

where the brackets $\langle . \rangle$ indicate the inner product

$$\langle f(t), S(t)\rangle = \int f(t)\, S(t)dt \qquad (6)$$

The number N reflects the number of modes believed to be in $E^s(t)$.

To solve for the coefficients α_k, one can rearrange equation (5) to be easily implemented. First, one can assume the testing function is the same as the basis function. The test function is defined only in the interval $(m-1)\Delta \le t \le m\Delta$ so, one can assume a unity value in this interval. Equation (5) can be averaging the outer integral by the value of the integrand at the beginning of the assumed interval multiplied by the interval width Δ , i.e. at $(m-1)\Delta$, in other words, equation (5) can be rewritten as follows after the removal of the interval width Δ

$$\sum_{k=1}^{K} \alpha_k \int_0^{T_e} f_k(\acute{t}) E^s\big((m-1)\Delta - \acute{t}\big)d\acute{t} = 0 \qquad (7)$$

The interval T_e can be divided into 2N+1 subinterval of width $\Delta = T_e/(2N+1)$.

Equation (7) can be approximated to be

$$\sum_{k=1}^{K} \alpha_k M_{mk} = -F_m \qquad (8)$$

where

$$M_{mk} = \int_{k\Delta}^{(k+1)\Delta} S(\acute{t}-[k-1]\Delta) E^s\big((m-1)\Delta - \acute{t}\big)d\acute{t} \qquad (9)$$

and $$F_m = \int_0^{\Delta} S(\acute{t}-[k-1]\Delta) E^s\big((m-1)\Delta - \acute{t}\big)d\acute{t} \qquad (10)$$

The algorithm can be summarized in the following matrix equation

$$[M_{mk}]_{2N\,X\,2N}[\alpha_k]_{2N} = [-F_m]_{2N} \qquad (11)$$

Equation (11) can be solved for the unknown E-pulse coefficients α_k.

III. Results and Discussions

The experiment is performed using the commercial Digital Sampling Converter GZ10. The converter has two channels, a transmitter and a receiver. Each port is connected to a wide band horn antenna operating from 2 to 18 GHz. The statue/object under test is positioned in front of the two antennas. The two antennas are similar and in line with each other. Figure (1) depicts the back scattered signal from a cat statue constructed from unknown dielectric material. The synthesized E-pulse signal is shown in Fig.2. The convolution of the E-pulse waveform with the back scattered signal is shown in Figure (3) where it is noticed that after the duration of the whole E-pulse is elapsed 9late time of targeted object), the convolution results in a null wave form which indicates right target identification. Completely different convoluted E-pulse signal is reached to each object that verifies the object identification print. These signals can be recorded in a museum database and appeals objects' discrimination when needed. Fig. 4 verifies this idea by convoluting the Cat statue E-pulse signal with other metal statue object scattered signal. The comparison between figures 3 and 4 shows that the convoluted signals are decaying after late time of 1.5ms in figure 3 while this isn't happened in figure 4 hence the convoluted signal decays/tends to null after 2ms. Also the convoluted signal shape is completely different which verifies the object

identification/discrimination from its E-pulse convolution technique.

Another example is the impinging of waves on a metallic statue. The back scattered signal is shown in Fig. 5. The synthesized E-pule is shown in Fig. 6. As in the previous example, the convolution of the E-pulse shown in Fig. 6 with the back scattered signal of the metal statue is illustrated in Fig. 7. Fig. 7 illustrates null results after the late time duration of the whole E-pulse is elapsed and tends to null at 1.5ms which indicates right target identification. The two experimentally used objects are comparable in size which resembles the similarity in their late time response value, however the two signals in figures 3 and 7 are different.

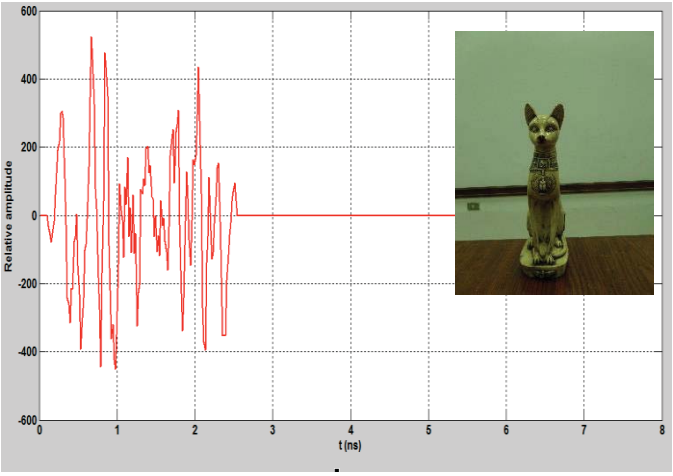

Fig.1 the Back scattered signal from a dielectric cat statue

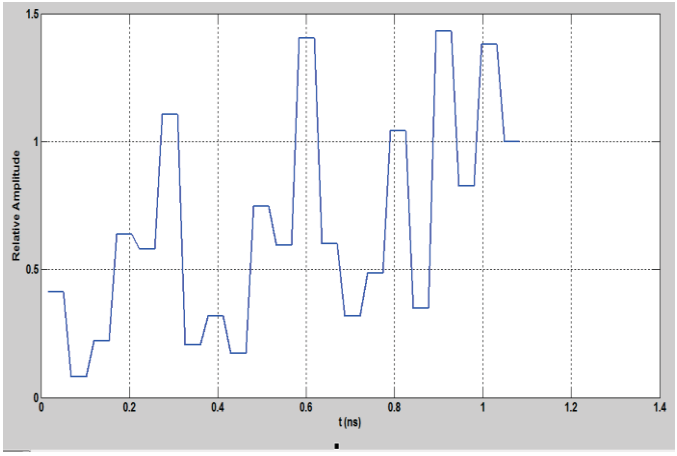

Fig.2 the Synthesized E-pulse waveform for the cat statue

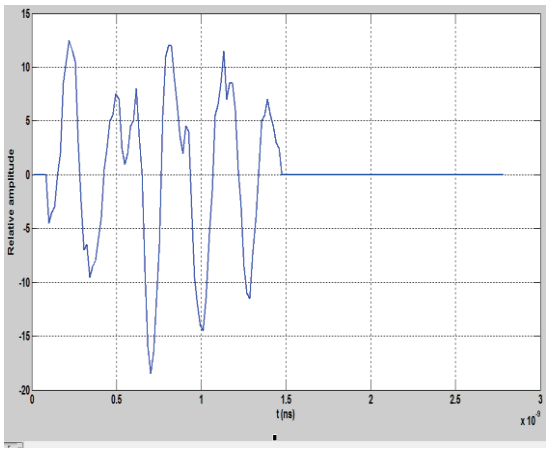

Fig.3 The convolution of the E-Pulse designed for the cat statue with the back scattered signal from the cat statue

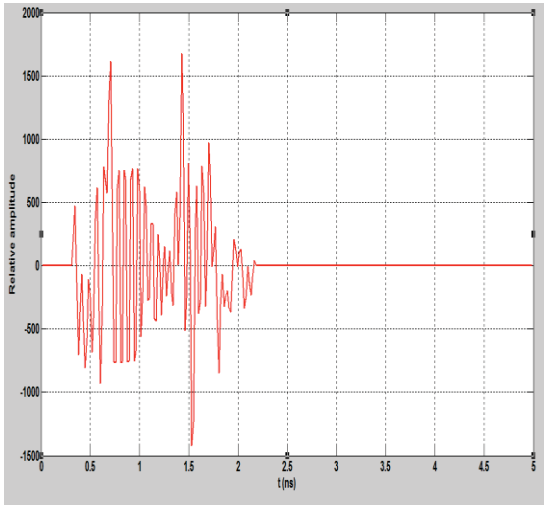

Fig.4 The convolution of the E-Pulse designed for the cat statue with the back scattered signal from metallic statue

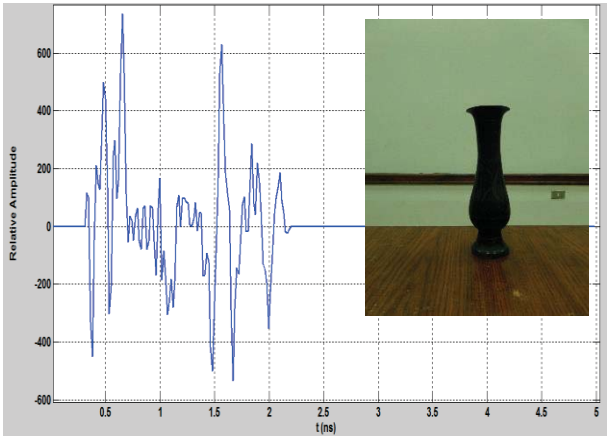

Fig.5 the Back scattered signal from a metallic object statue

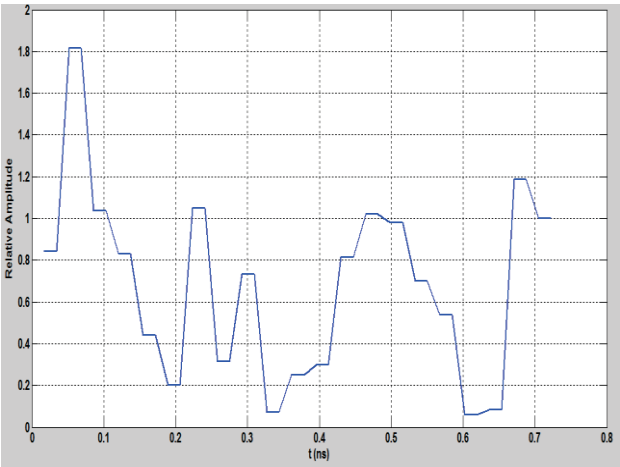

Fig.6 the Synthesized E-pulse waveform for the metallic statue

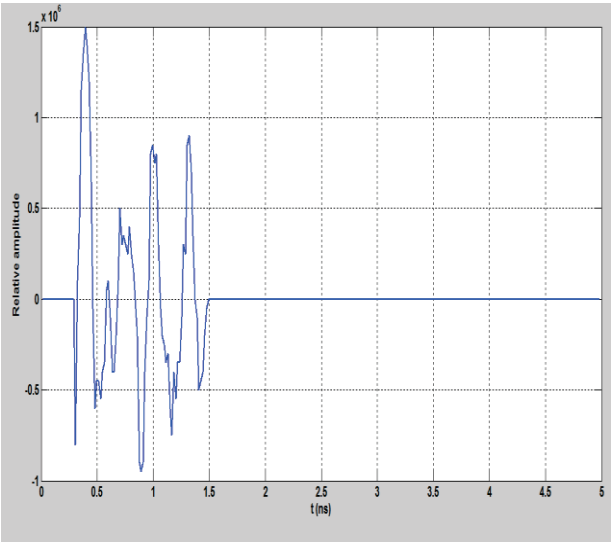

Fig.7 The convolution of the E-Pulse designed for the metallic statue with the back scattered signal from it

IV. Conclusion

The E-pulse technique is re-investigated over dielectric with fixed positions as in the case of ancient antiquates. The investigation reveals good results as in the case of the conducting objects except in the capability of moving which is not required in applications of museums security systems.

V. Acknowledgment

This research is being done under the fund from Science and Technology Development Fund, Egypt, contract number: 2477.

VI. References

[1] Baum, C. E., \The singularity expansion method," Transient Electromagnetic Field, L. B. Felsen(ed.), 129-179, Springer-Verlag, New York, 1976.

[2] 2. Baum, C. E., \Radiation of impulse-like transient ¯elds," Sensor and Simulation Note#321, Nov. 25, 1989.

[3] 4. Ilavarasan, P., J. E. Ross, E. J. Rothwell, K. Chen, and D. P. Nyquist, "Performance of an automated radar target discrimination scheme using E pulses and S pulses," IEEE Transactions on Antennas and Propagation, Vol. 41, 582-588, May 1993.

[4] 5. Carrion, M. C., A. Gallego, J. Porti, and D. P. Ruiz, "Sub sectional-polynomial E-pulse synthesis and application to radar target discrimination," IEEE Transactions on Antennas and Propagation, Vol. 41, No. 9, 1204-1211, Sep. 1993.

[5] A. A. Ksienskl, Y. T. Lin and L. J. White, Low-Frequency Approach to Target Identification,11 PROC. IEEE, Dec. 1975.

[6] K. M. Chen, D. P. Nyquist, E. J. Rothwell, L. L. Webb, and B. Drachman," Radar target discrimination by convolution of radar return with extinction-pulses and single-mode extraction signals," IEEE Trans. Antennas Propagation., vol. AP-35, pp. 715-720, June 1987.

[7] E. Rothwell, D. P. Nyquist, K. M. Chen, and B. Drachman, "Radar target discrimination using the extinction-pulse technique," IEEE Trans. Antennas Propagat., vol. AP-33, pp. 929-937, Sept. 1985.

[8] E. Rothwell, K. M. Chen, and D. P. Nyquist, "Frequency domain E-pulse synthesis and target discrimination," IEEE Trans. Antennas Propagat., vol. AP-35, pp. 426-434, April 1987.

[9] P. Ilavarasan, J. E. Ross, E. J. Rothwell, K. M. Chen, and D. P. Nyquist, "Performance of an automated radar target pulse discrimination scheme using E pulses and S pulses," IEEE Trans. Antennas Propagation., vol. 41, no. 5, pp. 582–588, May 1993.

Second Order Statistical Moments of the Phase Fluctuations of Scattered Radiation in the Collision Magnetized Plasma

G. Jandieri[1], M. Diasamidze[2], I. Takidze[2], and N. Tugushi[3]
[1]Special Department, Georgian Technical University, Tbilisi, Georgia
[2]Department of Exact and Natural Sciences, Batumi State Maritime Academy, Batumi, Georgia
[3]Energetics Department, Georgian Technical University, Tbilisi, Georgia

Abstract – *Statistical characteristics of multiply scattered electromagnetic waves in the turbulent magnetized collision plasma with electron density fluctuations are considered. Analytical expression for the phase correlation function is derived for arbitrary correlation function of fluctuating plasma parameters using modify smooth perturbation method taking into account the diffraction effects. Evolutions of the second order statistical moments are analyzed analytically and numerically for the anisotropic Gaussian correlation function of electron density fluctuations in the polar ionospheric F-region using the experimental data.*

Keywords: Plasma, ionosphere, statistical moments, turbulence.

1 Introduction

Investigation of the statistical characteristics of scattered radiation in randomly inhomogeneous anisotropic media is of great interest. The elongated large-scale plasma irregularities are observed in the polar ionosphere. It was shown [1] that at fixed collision frequency between plasma particles, the degree to which the absorption influences the spatial power spectrum (SPS) of the scattered waves depends strongly on the propagation direction of the original incident wave with respect to the plasma boundary and also on the strength of an external magnetic field using the complex geometrical optics approximation. The width of the SPS of the received radiation for sufficiently strong absorption in the plasma is greater than in the collisionless plasma; the spectral maximum is substantially displaced with respect to the direction of the source. Broadening of the SPS of scattered electromagnetic waves in turbulent collision magnetized plasma for both power-law and anisotropic Gaussian correlation function of electron density fluctuations was analyzed in [2,3] in the complex ray (-optics) approximation.

In this paper we will consider second order statistical moments of scattered radiation: phase correlation function of both the ordinary and extraordinary waves, broadening of the SPS and displacement of its maximum in the collision magnetized plasma.

2 Statistical characteristics of the phase fluctuations

Electric field of electromagnetic wave in the magnetized collision plasma with electron density fluctuations satisfies the wave equation:

$$\left(\frac{\partial^2}{\partial x_i \, \partial x_j} - \Delta \delta_{ij} - k_0^2 \, \varepsilon_{ij}(\mathbf{r}) \right) \mathbf{E_j}(\mathbf{r}) = 0 \,. \qquad (1)$$

Electric field we introduce as $E_j(\mathbf{r}) = E_{0j} \exp\{\Phi(\mathbf{r})\}$ where $\Phi(\mathbf{r}) = \varphi_0 + \varphi_1 + \varphi_2 + \ldots$ is the complex phase, $\varphi_0 = i k_0 x + i k_\perp y$ $(k_\perp << k_0)$ is the unperturbed phase. Complex phase fluctuations are of the order $\varphi_1 \sim \varepsilon_{ij}^{(1)}$, $\varphi_2 \sim \varepsilon_{ij}^{(1)\,2}$. Dielectric permittivity of turbulent magnetized plasma is a random function of the spatial coordinates $\varepsilon_{ij}(\mathbf{r}) = \varepsilon_{ij}^{(0)} + \varepsilon_{ij}^{(1)}(\mathbf{r})$, $|\varepsilon_{ij}^{(1)}(\mathbf{r})| << 1$. The first term is the regular (unperturbed) component of the dielectric permittivity connecting with the ionization distribution in the ionospheric layers at different altitudes; the second term is the fluctuating term describing electron density fluctuations in the ionosphere. If EM wave propagates along the Z axis and the unit vector $\boldsymbol{\tau}$ of an external magnetic field lies in the YOZ plane ($\mathbf{k} \parallel z$, $< \mathbf{H_0} > \in YOZ$ is the principle plane), the components of the second-rank tensor ε_{ij} of collision magnetized plasma have the following form [4]:

$$\varepsilon_{xx} = 1 - \frac{\mathrm{v}\, g}{g^2 - u}, \quad \varepsilon_{xy} = -\varepsilon_{yx} = i \, \frac{\mathrm{v}\sqrt{u}\cos\alpha}{g^2 - u},$$

$$\varepsilon_{xz} = -\varepsilon_{zx} = -i \frac{\mathrm{v}\sqrt{u}\,\sin\alpha}{g^2 - u}, \quad \varepsilon_{yy} = 1 - \frac{\mathrm{v}(g^2 - u\,\sin^2\alpha)}{g(g^2 - u)},$$

$$\varepsilon_{yz} = \varepsilon_{zy} = \frac{u\,\mathrm{v}\sin\alpha\cos\alpha}{g(g^2 - u)}, \quad \varepsilon_{zz} = 1 - \frac{\mathrm{v}(g^2 - u\,\cos^2\alpha)}{g(g^2 - u)}, \quad (2)$$

where: $g = 1 - i\,s$, $s = \nu_{eff}/\omega$, $\nu_{eff} = \nu_{ei} + \nu_{en}$ is the effective collision frequency of electrons with other plasma particles, α is the angle between the *Z*-axis and a static external magnetic field. Plasma frequency $\omega_p(\mathbf{r}) = [4\pi N(\mathbf{r}) e^2/m]^{1/2}$ and the gyro frequency $u(\mathbf{r}) = (e H_0(\mathbf{r})/m\,c\,\omega)^2$ are random functions of the spatial coordinates; $N(\mathbf{r})$ is the electron density, $\mathrm{v}(\mathbf{r}) = \omega_p^2(\mathbf{r})/\omega^2$ is the magneto-ionic parameter. If the wavelength λ is small in comparison with the characteristic linear scale of electron density fluctuations l, the scattered waves are concentrated in a narrow solid angle. If a distance L travelling by wave in the magnetized turbulent plasma is substantially big, diffraction effects become essential. In this case, multiple scattering is effectively described by the smooth perturbation method (narrow-angle scattering) taking into account diffraction effects [5,6]. Zero-order approximation of the wave equation contains the set of three algebraic equations for the regular field components E_{0j} $(j = x,\ y,\ z)$.

2D Fourier transformation of the phase fluctuation

$$\varphi_1(x,y,z) = \int_{-\infty}^{\infty} d\,k_x \int_{-\infty}^{\infty} d\,k_y\ \psi(k_x,k_y,z)\exp(i\,k_x x + i\,k_y y),$$

satisfying the boundary condition $\psi(k_x,\,k_y,\,z=0) = 0$ is:

$$\psi(k_x,k_y,L) = i\,\frac{k_0}{2}\,(Z' + i\,s\,Z'')\int_{-\infty}^{\infty} dz'\ n_1(k_x,k_y,z')$$

$$\exp\left(\frac{1}{4\,k_0^2}\left\{\left[\tilde{d}_2\,\Gamma''\,k_x - \tilde{d}_1(2\,k_0 - s\,\Gamma'\,k_x)\right] - \right.\right.$$

$$\left.\left. - i\left[\tilde{d}_1\,\Gamma''\,k_x + \tilde{d}_2(2\,k_0 - s\,\Gamma'\,k_x)\right]\right\}(L - z')\right), \qquad (3)$$

where: $Z' = Z_{xx} + Z_{xy} + Z_{xz}$, $Z'' = \tilde{Z}_{xx} + \tilde{Z}_{xy} + \tilde{Z}_{xz}$,

$Z_{xx} = \varepsilon_{xx}^{(1)}$, $Z_{xy} = \varepsilon_{xy}^{(1)}\,\mathrm{P}'' + s^2\,\tilde{\varepsilon}_{xy}^{(1)}\,\mathrm{P}'$, $Z_{xz} = \varepsilon_{xz}^{(1)}\,\Gamma'' + s^2\,\tilde{\varepsilon}_{xz}^{(1)}\,\Gamma'$,

$\tilde{Z}_{xx} = -\,\tilde{\varepsilon}_{xx}^{(1)}$, $Z_{xy} = -\,\varepsilon_{xy}^{(1)}\,\mathrm{P}' + \tilde{\varepsilon}_{xy}^{(1)}\,\mathrm{P}''$, $Z_{xz} = -\,\varepsilon_{xz}^{(1)}\,\Gamma' + \tilde{\varepsilon}_{xz}^{(1)}\,\Gamma''$.

Polarization coefficients have the following form [3,4]

$$\frac{< E_y >_{1,2}}{< E_x >_{1,2}} = -\,i\,\mathrm{P}''_j - s\,\mathrm{P}'_j, \quad \frac{< E_z >_{1,2}}{< E_x >_{1,2}} = i\,\Gamma''_j + s\,\Gamma'_j, \qquad (4)$$

here: $\mathrm{P}''_j = 2\sqrt{u_L}\ \left[\ (1-\mathrm{v}) \mp s^2\,\alpha_0\right]\left(u_T \mp \sqrt{a_0}\right)^{-1}$,

$\mathrm{P}'_j = 2\sqrt{u_L}\ \left[1 \pm \alpha_0(1-\mathrm{v})\right]\left(u_T \mp \sqrt{a_0}\right)^{-1}$, upper sign (index 1) corresponds to the ordinary wave; the lower sign (index 2) to the extraordinary wave; $u_T = u\,\sin^2\alpha$, $u_L = u\,\cos^2\alpha$,

$$\alpha_0 = \frac{b_0}{2\sqrt{a_0}}\,\frac{1}{u_T \mp \sqrt{a_0}},\ a_0 = u_T^2 + 4\,u_L\left[(1-\mathrm{v})^2 - s^2\right],$$

$b_0 = 8\,(1-\mathrm{v})\,u_L$.

Correlation function of the phase fluctuations of both ordinary and extraordinary waves in the turbulent collision magnetized plasma has the following form

$$< \varphi_1(\mathbf{r})\,\varphi_1^*(\mathbf{r}+\boldsymbol{\rho}) > = \frac{\pi\,k_0^2\,L}{2}\,(Z'^2 + s\,Z''^2)\cdot$$

$$\int_{-\infty}^{\infty} dk_x \int_{-\infty}^{\infty} dk_y\ V_n\left[k_x, k_y, -\frac{\tilde{d}_1\,\Gamma''k_x + \tilde{d}_2(2\,k_0 + \Gamma'\,k_x)}{4\,k_0^2}\right]\cdot$$

$$\cdot\ \exp(-i\,k_x\,\eta_x - i\,k_y\,\eta_y), \qquad (5)$$

where: $\tilde{d}_1 = k_x\left[\ \Gamma'' - \mathrm{P}''(k_y + k_\perp)\ \right]$, $\tilde{d}_2 = k_y\,(k_y + 2\,k_\perp) +$

$+\ k_x\left[\ \Gamma'\,k_0 + \mathrm{P}'(k_y + k_\perp)\ \right]$; $V_n(\mathbf{k})$ is the arbitrary 3D spectral function of electron density fluctuations, parameter $\mu = k_\perp/k_0$ describes diffraction effects, η_y and η_x are the distances between observation points spaced apart in the principle and perpendicular planes, respectively. From equation (5) follows that in non-magnetized plasma $H_0 = 0$ at $\chi = 1$ (isotropic case), neglecting diffraction effects $(\mu = 0)$, correlation function of the phase fluctuations $W_\varphi(k_x,k_y,L)$ and $V_n(\mathbf{k})$ are related by the well-known formula [7]: $W_\varphi(k_x,k_y,L) = 2\pi\,(r_e\,\lambda)^2\,L\,V_n(k_x,k_y,k_z=0)$, where r_e is the classical electron radius.

Let Δ_+ and Δ_- designate the displacements of the SPS maximum of scattered ordinary and extraordinary waves in the turbulent collision magnetized plasma, respectively in the principle *YZ* plane; $\Sigma_\pm$ is the width of the SPS spectrum of scattered waves. These expressions are obtained by differentiation of the correlation function of the phase fluctuations [1]

$$\Delta_\pm = \frac{2}{i}\,\frac{\partial W_\varphi}{\partial \eta_y}\bigg|_{\eta_x=\eta_y=0}, \quad \Sigma_\pm = -\frac{\partial^2 W_\varphi}{\partial \eta_y^2}\bigg|_{\eta_x=\eta_y=0}. \qquad (6)$$

3 Numerical calculations

Analytical and numerical calculations are carried out for the anisotropic Gaussian correlation function of electron density fluctuation [2,8]:

$$\tilde{V}_n(k_x,k_y,k_z) = \sigma_n^2\,\frac{l_\perp^2\,l_\parallel}{8\,\pi^{3/2}}\ \exp\left(-\frac{k_x^2\,l_\perp^2}{4} - p_1\,\frac{k_y^2\,l_\parallel^2}{4} - p_2\,\frac{k_z^2\,l_\parallel^2}{4} - \right.$$

$$\left. - p_3\,k_y\,k_z\,l_\parallel^2\right). \qquad (7)$$

This function contains both anisotropy factor of irregularities $\chi = l_{\|} / l_{\perp}$ (ratio of longitudinal and transverse characteristic linear scales of plasma irregularities with respect to the external magnetic field) and inclination angle γ_0 of prolate irregularities with respect to the external magnetic field,

$$p_1 = 1 + (1-\chi^2)^2 \sin^2\gamma_0 \cos^2\gamma_0 / \chi^2,\ p_2 = (\sin^2\gamma_0 + \chi^2 \cos^2\gamma_0)/\chi^2,\ p_3 = (1-\chi^2)\sin\gamma_0 \cos\gamma_0 / 2\chi^2.$$

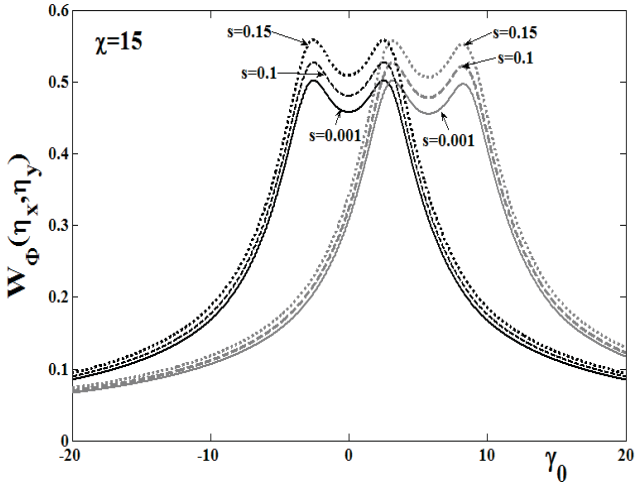

Fig. 1. Dependence of the correlation function of the phase fluctuations versus angle of inclination γ_0 at fixed anisotropy factor $\chi = 15$ varying collision frequency in the interval $s = 10^{-3} - 10^{-1}$.

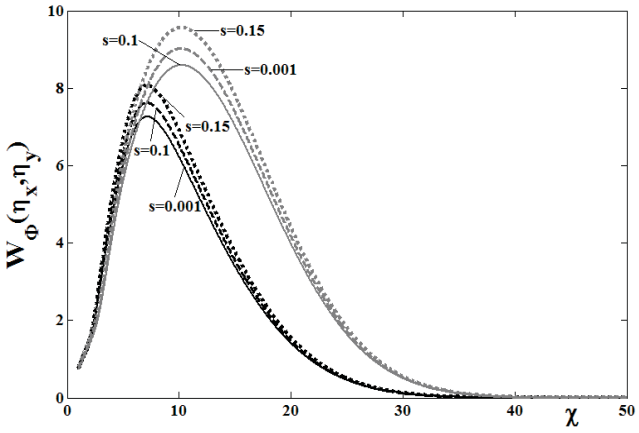

Fig. 2. Correlation function of the phase fluctuations versus parameter of anisotropy for different collision frequency s.

Anisotropy of the irregularities is connected with the difference of the diffusion coefficients in the field align and field perpendicular directions. Figure 1 shows the dependence of the phase correlation function of the ordinary wave in the collision magnetized plasma versus angle of inclination γ_0 of prolate plasma irregularities ($l_{\|} = 200$ m) with respect to the external magnetic field at fixed anisotropy factor $\chi = 15$ in the polar ionospheric F-region. Thickness of a plasma slab is of the order 32 km, distance between observation points is the same $\eta_x = \eta_y = 1$. Correlation function has a double-humped shape with symmetrically locating maximums in the absence of diffraction effects ($\mu = 0$) at $s = 10^{-3}$ and $\gamma_0 = 2.5^0$. Increasing collision frequency up to $s = 0.15$ location of maximums not varies but depth of a gap increases by 13%. If the diffraction effects are taken into account ($\mu = 0.1$) double-humped correlation function becomes asymmetrical. At $s = 10^{-3}$ location of the left and right maximums are at $\gamma_0 = 3.2^0$ and $\gamma_0 = 8.3^0$, respectively. Increasing parameter up to $s = 0.15$ phase correlation function $W_\varphi(\eta_x,\eta_y)$ has the same shape: location of maximums and depth of a curve not vary. Increasing parameter of anisotropy up to $\chi = 20$ the depth of a gap decreases to 11%. Hence correlation function of the phase fluctuations becomes asymmetric for large scale plasma irregularities taking into account diffraction effects. Increasing collision frequency from $s = 10^{-3}$ up to $s = 0.15$ the depth of a curve increases not varying location of the maximums. Increasing anisotropy parameter χ the depth of a double-humped shape decreases.

Figure 2 presents the dependence of the phase correlation function versus parameter of anisotropy χ for small scale irregularities with characteristic linear scale $l_{\|} \approx 200$ m taking into account diffraction effects and collision between plasma particles at $\eta_x = \eta_y = 1$. In both cases the curve has the asymmetric form. If $\mu = 0.15$, increasing collision parameter s correlation function broadens in 15% and its amplitude increases in comparison with a case without diffraction effects. 3D surface of the

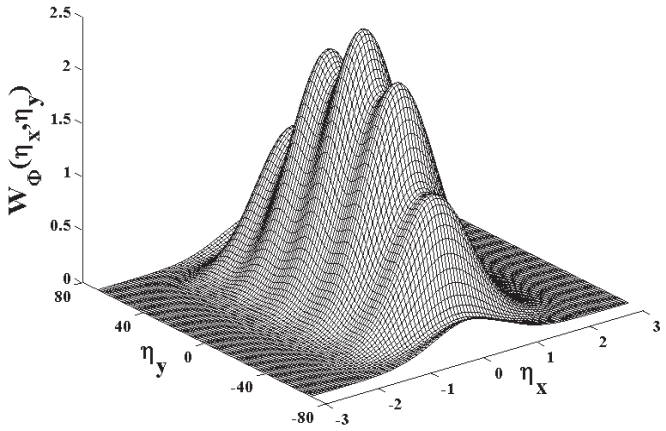

Fig. 3. Figure depicts 3D picture of the phase correlation function versus distances between observation points in the principle and perpendicular planes.

$W_\varphi(\eta_x,\eta_y)$ function is presented on Figure 3 at: $\chi=15$, $\gamma_0=10$, $\mu=0.1$, $s=10^{-3}$, $l_{\|}=200$ m, $l_{\|}=200$ m, $L=32$ km. Increasing characteristic spatial scale of irregularities oscillations disappears. Growing the anisotropy factor χ oscillations of a surface are increased.

Numerical calculations of both the maximum displacement and the broadening of the SPS are carried out for the following parameters: $l_{\|}=3$ km, $L=100$ m, $\mu=0.06$, $s=10^{-3}$. Analysis show that the maximum displacement of the SPS in the principle plane decreases for both waves

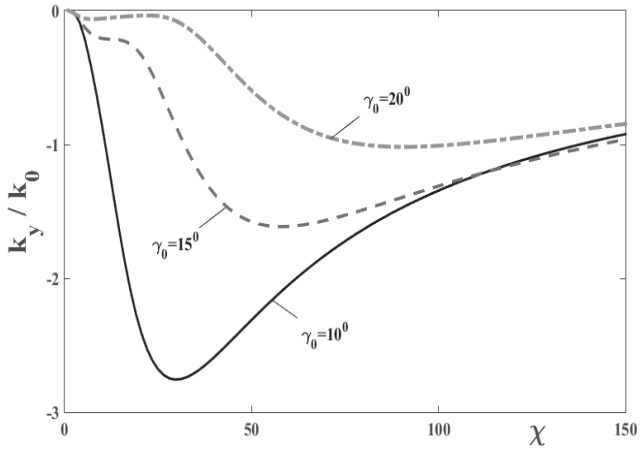

Fig. 4. Plots of the maximum displacement Δ_- of the SPS of the extraordinary wave as a function of χ, at fixed inclination angle γ_0 in the *YZ* plane.

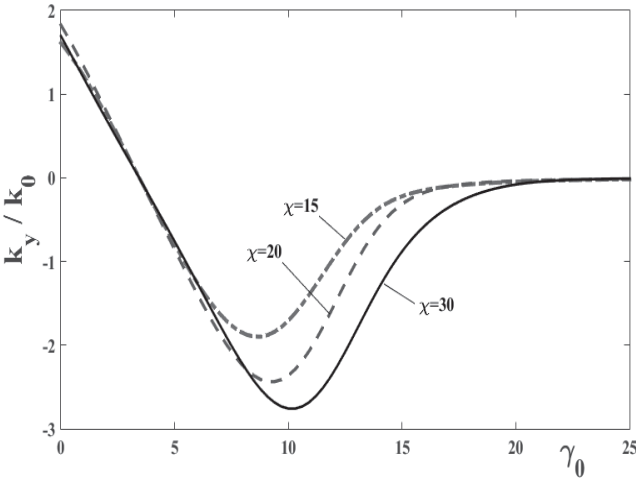

Fig. 5. Plots of the maximum displacement Δ_- of the SPS of the extraordinary wave as a function of γ_0 at fixed anisotropy parameter χ in the *YZ* plane.

increasing inclination angle (Fig. 4). Varying angle in the interval from $\gamma_0=10^0$ up to $\gamma_0=20^0$ the ratio is equal to $\Delta_\pm(\gamma_0=10^0)/\Delta_\pm(\gamma_0=20^0)\approx 3$. The displacement of the SPS maximum for the ordinary wave always exceed the maximum displacement for the extraordinary wave, $\Delta_+>\Delta_-$. Particularly, maximum of the displacement for both waves in the principle *YZ* plane at $\gamma_0=10^0$ is at $\chi=30$ and $\Delta_+/\Delta_-=7$. In the interval $\gamma_0=10^0-20^0$ the maximum displacement of the SPS for the ordinary wave by seven times exceeds maximum displacement for the extraordinary wave.

Figure 5 shows the dependence of the maximum displacement of the SPS versus angle of inclination of prolate ionospheric irregularities with respect to the external magnetic lines of force at different parameter of anisotropy χ.

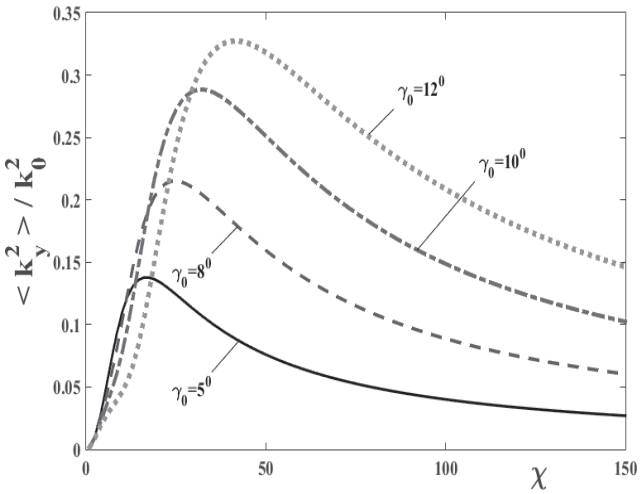

Fig. 6. Plots of the SPS broadening of scattered extraordinary wave versus parameter of anisotropy χ at different angle of inclination γ_0.

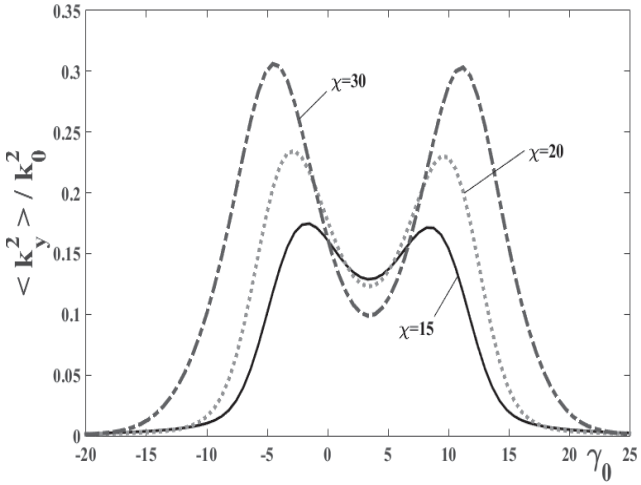

Fig. 7. Plots of the SPS broadening of scattered extraordinary wave versus angle γ_0 at different parameter of anisotropy χ.

Maximum for both waves in the *YZ* plane increases in proportion to the parameter χ. It has maximum at $\gamma_0=10^0$

and tends to the saturation at $\gamma_0 = 20^0$; $\Delta_{\pm}(\chi = 30)/\Delta_{\pm}(\chi = 15) \approx 1.45$, $\Delta_{+}(\chi = 30)/\Delta_{-}(\chi = 30) = 7$.

Figure 6 shows the dependence of the SPS broadening Σ_{-} for the extraordinary wave as a function of the parameter of anisotropy χ varying inclination angle γ_0. If $\gamma_0 = 5^0$ maximum of the function Σ_{-} is at $\chi = 16$, if $\gamma_0 = 12^0$ maximum is at $\chi = 42$. In the interval $\gamma_0 = 5^0 - 12^0$ amplitude of the function Σ_{-} increases in 2,4 times and the spectrum broadens in two times. The ratio of the widths of both ordinary and extraordinary waves not depends of the inclination angle γ_0: $\Sigma_{+}(\gamma_0 = 12^0)/\Sigma_{-}(\gamma_0 = 12^0) = 7$, $\Sigma_{+}(\gamma_0 = 5^0)/\Sigma_{-}(\gamma_0 = 5^0) = 7$. The broadening of the SPS Σ_{-} for the extraordinary wave as a function of the angle γ_0 in the principle plane has a gap if prolate plasma irregularities are strongly stretched along the geomagnetic lines of force, at the angle of inclination $\gamma_0 = 3^0$. Increasing parameter of anisotropy in the interval $\chi = 15 - 30$ the location of a gap not varies but maximums of the function Σ_{-} having double-humped shape are increased. Particularly, for $\chi = 15$ maximums are at the angles $\gamma_0 = -1.5^0$ and $\gamma_0 = 8^0$; for $\chi = 30$ maximums are displaced at the angles $\gamma_0 = -4.5^0$ and $\gamma_0 = 11^0$. This means that the scattered extraordinary wave broadens asymmetrical with respect to the external magnetic field. The curve Σ_{-} has a symmetrical double-humped shape not taking into account diffraction effects $(\mu = 0)$; increasing parameter $k_0 L$ maximums of the broadening function Σ_{-} proportionally are increased.

4 Conclusions

Correlation function of the phase fluctuations for the ordinary and extraordinary waves in the collision magnetized plasma is obtained for the arbitrary correlation function of electron density fluctuations in the polar ionospheric *F*-region taking into account diffraction effects. Numerical calculations were carried out for the anisotropic Gaussian correlation function of electron density fluctuations taking into account both anisotropy factor χ and the angle of inclination γ_0 of prolate irregularities with respect to the external magnetic field varying collision frequency in the band $s = 10^{-3} - 10^{-1}$. Depending on the angle γ_0 correlation function and the width of the SPS has a double-humped shape. Increasing parameter of anisotropy from $\chi = 15$ up to $\chi = 20$ the depth of a gap decreases to 11%. If the diffraction parameter is equal to $\mu = 0.15$, increasing parameter $s = 10^{-3} - 0.15$ correlation function broadens in 15% and its amplitude increases in comparison with a case without diffraction effects. Surface of the 3D correlation function of the phase fluctuations oscillates for small-scale irregularities $l_{\parallel} = 200$ m, at $\gamma_0 = 10$, $s = 10^{-3}$, $L = 32$ km. Growing the anisotropy factor χ oscillations become intensive. Oscillations are disappeared increasing characteristic spatial scale of plasma irregularities.

In the principle *YZ* plane displacement of the SPS maximum Δ_{-} decreases if the angle γ_0 is increased. The scattered extraordinary wave broadens asymmetrical with respect to the external magnetic field. This curve Σ_{-} has a symmetrical double-humped shape (Fig. 7) not taking into account diffraction effects $(\mu = 0)$; increasing parameter $k_0 L$ maximums of the function Σ_{-} proportionally are increased.

Acknowledgments

This work has been supported by the International Science and Technology Center (ISTC) under Grant # G-2126 and Shota Rustaveli National Science Foundation under Grant # FR/3/9-190/14.

5 References

[1] Jandieri G. V., V. G. Gavrilenko, and A. A. Semerikov, "On the effect of absorption on multiple wave-scattering in a magnetized turbulent plasma," Waves Random Media, Vol. 9, 427-440, 1999.

[2] Jandieri G.V., A. Ishimaru, V. G. Jandieri, A. G. Khantadze, and Z. M. Diasamidze, "Model computations of angular power spectra for anisotropic absorptive turbulent magnetized plasma," Progress In Electromagnetic Research, PIER 70, 307-328, 2007.

[3] Jandieri G.V., A. Ishimaru, B.S Rawat and N.K. Tugushi, "Peculiarities of the spatial spectrum of scattered electromagnetic waves in the turbulent collision magnetized plasma,"PIER Vol. 152, pp. 137-149, 2015.

[4] Ginzburg V. L., Propagation of Electromagnetic Waves in Plasma. New York: Gordon and Beach, USA, 1961.

[5] Ishimaru, A. Wave Propagation and Scattering in Random Media, Vol. 2, Multiple Scattering, Turbulence, Rough Surfaces and Remote Sensing, IEEE Press, Piscataway, New Jersey, USA, 1997.

[6] Tatarskii, V. I. Wave Propagation in a Turbulent Medium, New York, McGraw-Hill, USA, 1961.

[7] Gershman, B. N., L. M. Eruxhimov, and Yu. Ya. Iashin, Wavy Phenomena in the Ionosphere and Cosmic Plasma, Nauka, Moscow, Russia, 1984 (in Russian).

[8] Jandieri G. V., A. Ishimaru A, V. G. Jandieri, and T. N. Bzhalava, "A radio scintillation in the turbulent collision magnetized plasma," Proceedings of the WORLDCOMP'07, "CSC 2007", 189-195, Las Vegas, Nevada, USA, 2007.

Gamma-jet measurement using Different designs of Forward EM Calorimeter

Baba V.K.S. Potukuchi[*1] , Sakshi Gupta[1]
[1]Department of Physics&Electronics, University of Jammu,
JAMMU–TAWI, J&Kstate, INDIA. 180006.

Abstract - For studying Quark Gluon Plasma (QGP) state, a highly energetic quark regarded as a probe. We can not produce an external isolated quark source due to confinement. So "photon + jet" production has been hailed as the "golden channel" to investigate energy loss of partons in the medium . We can estimate the jet energy loss by measuring the isolated-photon, which was produced back to back with hadron jet in pp collisions. Forward Calorimeter (FoCAL) geometry has been implemented , using GEANT code in AliRoot Frame work [1]. As designed FoCAL contains 4 super modules and each containing 30 unit modules . We have measured energy of Isolated-Photons using 3 different geometrical designs of FoCAL detector. Among the three , one of the geometry designs found showing around 40% increase in Energy deposition (Edep). in the FoCAL , three different geometry designs are implemented , tested and one of the designs found best suited for doing such type of analysis of "photon + jet" measurement.

Keywords: Gamma , Calorimeter, AliRoot , Jet , FoCAL, QGP.

1 Introduction

The discoveries at RHIC were accomplished primarily via direct measurement of particle multiplicities and spectra. On the other hand, there is an indirect method to study a state of matter. One can shoot a high momentum particle and probe the modification of it after passing through the medium. We may use a highly energetic quark as a probe to examine the QGP. But we can not produce an external isolated quark source due to confinement. This obstacle can be resolved by creating the probe internally at the initial state of nuclei collision. From the nucleon-nucleon interactions it is known that when two partons undergo a scattering with large momentum transfer Q2 in the early stages of collision, the hard-scattered partons fragment into jets of hadrons with high transverse momentum (P_T > 2GeV/c). These jets are emitted in opposite directions in the centre-of-mass frame in order to conserve momentum. When the hard scattered partons will traverse the hot and dense nuclear matter created in a high energy nucleus-nucleus collision, they lose energy through gluon bremsstrahlung with the energy lost depending on the density of color charges in the matter through they pass.

This effect is called Jet Quenching and the most directly measurable consequence is the suppression of high transverse momentum hadrons in the final state (See FIGURE 1). Therefore any modification in the high pT spectrum is probing the high density medium created in the collision.

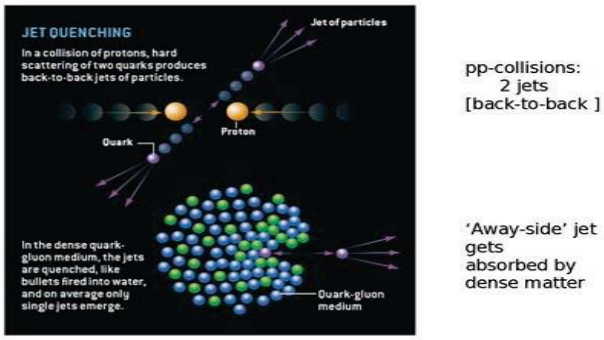

FIGURE 1 : DIAGRAM SHOWING "JET QUENCHING"

In order to disentangle the initial from final state effects, we have to measure the energy of Direct photons or prompt photons. Photons are produced back-to-back with an associated parton (jet) having close to the same transverse momentum. Furthermore, these photons do not strongly interact with the medium. Therefore, photon + jet production has been hailed as the "golden channel" to investigate energy loss of partons in the medium [2, 3]. Direct photons produced in collisions can be divided into prompt photons produced in hard processes in the initial collision, and non-prompt photons produced by jet fragmentation, in-medium gluon conversion and medium-induced bremsstrahlung. Prompt processes such as $q+g \rightarrow q+\gamma$, $q^{-}+g \rightarrow \gamma+q$, $q+^{-}q \rightarrow g+\gamma$ and $g+g \rightarrow \gamma+g$ lead to final states with a high p_T parton (gluon or quark) balanced by a prompt photon with roughly comparable p_T [4] as shown in Figure 2. Thus, they provide a calibrated parton inside of the medium, allowing a direct, quantitative measurement of the energy loss of partons in the medium and of the medium response. Experimentally, events with enriched production of

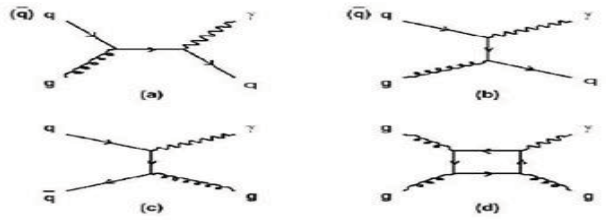

Figure 1: Feynmann Diagrams Contributing to Photon Production.

prompt photons are selected using an isolation requirement. Background photons from the decays of neutral mesons, such as π^0, η and ω, are suppressed by taking γ/π^0 discrimination ratio, as they are predominantly produced via jet fragmentation. Feynmann Diagrams (See Figure:2) Contributing to Photon Production .

2 FORWARD CALORIMETER (FOCAL)

Forward Calorimeter (FoCAL) is sampling EMCAL. It is one of the upgrade plans for the ALICE. FoCAL intends to locate at z ~ 360cm from IP and cover the positive rapidity (A-side of ALICE) of $2.5 < \eta < 4$ in maximum as shown in Figure 3. FoCAL will make it possible to perform the electromagnetic measurements such as π0 and photons, jet measurements and their correlations with respect to the central rapidity region. The FoCAL design consists of the following parts :

• 40 layers of Super Modules . And each Super Module consists of 30 Unit Modules in 2 different types of arrangements. A-Type Super module (SM) consists (6 Col X 5 Row) Unit Modules and B-Type Super module (SM) consists (5 Col X 6 Row) Unit Modules . Each Layer consists of 2 A-type and 2 B-type Super modules as shown in the Figure -3.

The FoCAL is a sampling type calorimeter in which Tungsten(W) follows Polystyrene(PS) scintillator for all the 40 layers. The tungsten is used as the converter material between two Polystyrene scintillators. The Polystyrene scintillator gives the better position resolution. Geometry1 of FoCAL in which Absorber width (Awid) is 0.3cm & Scintillator width (Swid) is 0.3cm. Each layer consists of two types of super modules A − type and B − type. Each type of super module has unit modules distributed in a matrix of specific rows and columns. A−type super module has 30 unit modules distributed in 6 Col × 5 Rows, while B − type super module also has 30 unit module distributed in 5 Col × 6 Rows. One unit module is 12 cm × 12 cm giving a total of 144 cells. Thus one unit cell is a square cell of 1 cm × 1 cm dimensions.

The pair of each A − type and B − type super module are adjusted in such a manner that the center of each layer remains unallocated by any cell. The region is reserved for beam pipe when the interaction takes place at a distance z = 360 cm from the first layer of detector plane .

• In Geometry2 of FoCAL we only changed the width of Scintillator (i.e). Awid = 0.3cm & Swid=0.4cm.

• In Geometry3 of FoCAL we changed widths of both Absorber and Scintillator (i.e.) Awid = 0.4cm & Swid = 0.4cm.

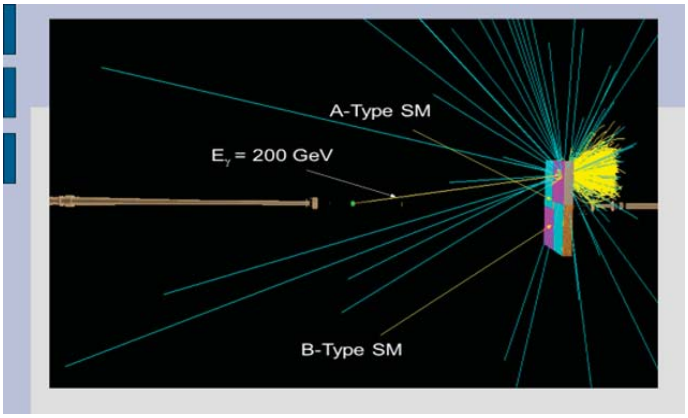

Figure 2: FoCAL With A & B type modules.

3. Energy Response

FoCAL is mainly used to measure the energy of γ, e^-, e^+ particles impinged on it. A particle deposits energy in calorimeter in eV to KeVs and the total energy deposited inside the calorimeter by the particle is called "Total Deposited Energy" by that particle. The total deposited energy of the particle is always proportional to the incident particle energy i.e., $E_{dep} = \alpha E_\gamma$, where α is constant and its value is different for different particles. The relative energy response of FoCAL is the ratio E_{dep}/E_γ. The FoCAL response increases linearly as a function of the incident particle energy. Such a calorimeter, like FoCAL, is said to be linear for detection of that particle. Linearity of a calorimeter response is an important property of the device.

In Figure 4 , one can see that the energy " E_{dep} " has been plotted with various Incident Photon energies. One can see a very Linear response of FoCAL Detector. The Increase " E_{dep} " has been seen very Linear for 1.0 to 200 GeV of Incident Photon Energies . In that Figure a comparison of " E_{dep} " for all three geometries are given. From that Figure one can conclude that Photon energies from 1.0 to 200 GeV can be measured with large accuracy in all three Geometries , which is very important requirement for our "Gamma-Jet" analysis.

The width of the Absorber and Scintillator is a very important factor for the shower containment, and thus for the physics also. In the present work we measure energy of

Photons from "γ − jet events" produced by PYTHIA using 3 different detector Geometries of FoCAL, which are defined above.

4. Comparison of Total Energy Deposition(Tot. Edep.) of all Geometries.

From [Figure 4] One can see that large increase in Tot.Edep. of Geometry2 & Geometry 3 , than the Geometry1, this is due to an increase in Swid=0.1cm than Geometry1 Swid width. If we compare Tot. Edep. of Gemetry2 (Awid=0.3cm, Swid=0.4cm) with the Tot. Edep. of Geometry3(Awid=0.4cm, Swid=0.4cm) as shown in [Figure 4] one can see that slight but definite increase in Tot.Edep. of Geometry2(Awid=0.3cm, Swid=0.4cm) than the Geometry3(Awid=0.4cm, Swid=0.4cm). From here we conclude that Geometry2(Awid=0.3cm, Swid=0.4cm) can be better suited for γ-jet analysis. Further discussions on Edep from various Geometries is there in the following sections .

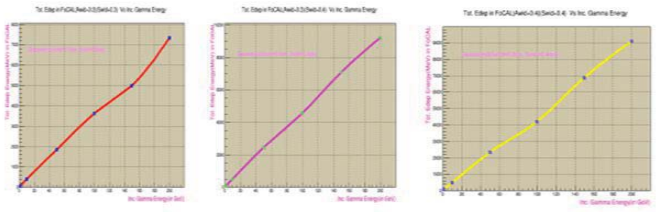

Figure 3: "Edep" Vs Incident Photon Energy for Geometry 1, Geometry2, and Geometry3.

5. Physics Simulation Results

In present work we measure Gamma energies from γ-jet using Geometry1 , Geometry2 and Geometry3. In Figure 5, we plotted Total Energy Deposition(Tot. Edep.) Vs Incident Gamma Energy for Geometry1, Geometry2 and Geometry3. If we compare Tot.Edep. for Geometry2 and Geometry3 with Geometry1. One can find definite increase in Gamma Energy response of Geometry2 and Geometry3 than Geometry1 but if we compare Tot.Edep. of Geometry2 and Geometry3, we find Geometry2 has a slight more Tot.Edep. than Geometry3 as clearly seen from Figure 5. Let us try to understand the reason for Tot.Edep. of Geometry3 be lesser than Tot.Edep. of Geometry2. In high-density materials (tungsten, Z=74), the signal from an electron or photon absorbed in the FoCAL is the ionization or excitation of the active layers (i.e. Scintillator) by all shower electrons and positrons that traverse these layers [5,6,7,8]. However a significant amount of energy is carried by low energy photons (Eγ < 1MeV) that have a short range in the sampling layers, thus suppressing the energy response. This effect is called the transition effect [9]. The soft γ_s responsible for the suppression of the EM calorimeter response in high-Z sampling calorimeters interact overwhelmingly in the absorber layers. The γ_s produced in these interactions only contribute to the calorimeter signal if the interaction occurs in a thin region, with an effective thickness (δ), near the boundary between the active and passive layers. To increase the fraction of shower γs that interact in the δ region, the sampling frequency can be increased. By making the absorber layers thinner, the transition effects can be overcome [9].Thus, Geometry2(Awid=0.3cm, Swid=0.4cm) in which we increase the width of Scintillator only is better described for γ-jet analysis , as in this Geometry low-energy photons also contribute to the energy response. Hence, Gamma Energy from γ-jet events produced in PYTHIA generator can be measured more accurately with the Geometry2 (i.e.), by increasing the width of the Scintillator only.

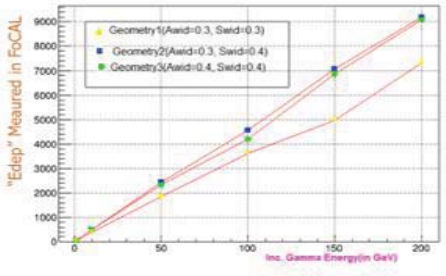

Figure 4: Comaring EDEPs of all Geometries.

6. Analysis & Conclusions :

In Figure 6 we plotted Energy deposition for Geometry2/Geometry1 and Geometry3/Geometry1 in terms of their excess percentages . From Figure 6 the energy deposition for Geometry3/ Geometry1 roughly increases by 20% to 30% than the Geometry1.

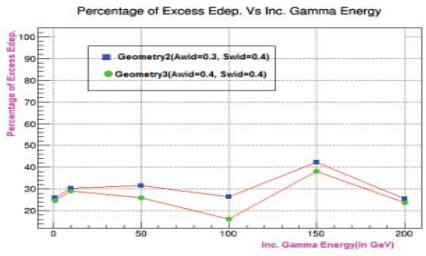

FIGURE 6: PERCENTAGE OF EDEP EXCESS IN GEOMETRY 2 &3 OVER GEOMETRY 1.

Similarly for Geometry2/Geometry1, if we see the Figure 6 where we find the increase in Energy deposition(Edep.) is roughly from 30% to 40 % than

Geometry1. For Geometry2, one can see that there is 30% increase in Tot.Edep. than the Geometry1 from 10 GeV to 200 GeV of γ-energies except for 150 GeV where it comes to be 40%.

It may be due to statistical fluctuations but otherwise we expect the excess should be definitely more than 30%. Similarly for Geometry3 Tot.Edep. excess is less than or around 30% for all the Incident γ-energies which can be clearly seen from Figure 6. We can conclude that for γ-jet analysis our FoCAL Geometry2 will be much suitable. We also expect to get better results by increasing the statistics to the level of 1,00,000 events in each Geometry case. So we conclude that Geometry2 of FoCAL is best suited for doing γ-jet analysis , as evident from the results discussed above.

7. References

[1] http://aliweb.cern.ch/Offline/AliRoot .

[2] X.-N. Wang, Z. Huang, I. Sarcevic, Phys. Rev. Lett. 77 231, arXiv:9701227 , http://dx.doi.org/10.1103/PhysRevLett.77.231 (1996).

[3] X. -N. Wang, Z. Huang, Phys. Rev. C 55 3047, arXiv:9605213, http://dx.doi.org/10.1103/PhysRevC.55.3047 (1997).

[4] S. Chatrchyan, et al., Phys. Lett. B 710 256, http://dx.doi.org/10.1016/j.physletb.2012.02.077 (2012).

[5] A. Anderson et al. Nucl. Instr. Meth., A290:95 (1990)

[6] T. Akesson et al. Nucl. Instr. Meth., A262:243 (1987)

[7] E. Bernardi et al. Nucl. Instr. Meth., A262:229 (1987)

[8] K. Pinkau, Phys. Rev., 139B:1548 (1965)

[9] R. Wigmans, Nucl. Instr. Meth., A259:389 (1987)

Apply Web Services with SOA and Web 2.0 Applications

Ming-Chang Huang
Department of Business Information Systems / Operation Management
University of North Carolina at Charlotte
mhuang5@uncc.edu

Abstract - It is important how wireless hosts find other hosts efficiently for load and web service purposes because hosts in an ad-hoc network move dynamically. In this paper, I propose a three-tier architecture which includes content networks, social networks and service networks. It is a new web and load services structure for ad-hoc computer networks using SOA (Service Oriented Architecture) and Web 2.0 concepts to implement functions for web and load service purposes. This structure applies web service functions to implement services seeking and load distributions. Furthermore this project discusses the construction of a knowledge sharing and learning platform based on the three-tier architecture. Different communities may provide their services to each other using that new knowledge platform, and this forms a "virtual community." This also leads to the desired accomplishments of "Service Reusability" and "Service Innovation." In addition, it can also propose frameworks of new SOA, and evolve in other applications in web 2.0 style. It furthermore provides a platform and more resources to enhance the interactions among different fields.

Keywords: Web Services, Web 2.0, Service Oriented Architecture (SOA), Load service and distribution

1. Introduction

Computer networks provide parallel computation and services. It is important that hosts find services form other hosts, and send loads to other hosts for some certain function implementations through network transfers. With the increasing popularity of mobile communication and computing, the demands for web and load services grow fast. When a computer is overloaded or it needs special services from others, it may send requests to other computers for web and load services it needs. For example, a computer may need some jobs to be executed with higher quality of services or it needs some jobs to be done within a short period of time, while its processor is too slow to perform those jobs. Therefore, it sends part those jobs to other computers which have higher execution speeds. Since wireless networks have been wildly used, how a host finds services it needs or how it transfers loads to others has become a very important issue because not all hosts have the abilities to manipulate their loads. For instance, a host with low battery power cannot finish all its jobs on time and should ask other nodes to provide services to finish the jobs on time, or it should transfer some of them to other nodes.

Before a host transfers its loads to other hosts or asks for load services from other hosts, it must find available hosts using resource allocation algorithms. There are several resource allocation protocols been developed for this purpose, for example, IEFT Service Location Protocol (SLP) [8] and Jini [25] software package from Microsystems. However, these protocols only address how to find the resources in wired networks, not in wireless networks. Maab [15] develops a location information server for location-aware applications based on the X.500 directory service and the lightweight directory access protocol LDAP [26]; while it does not cover some important issues about the movements of mobile hosts, for example, how to generate a new directory service and how a host gets the new services, when a directory agent moves away its original region. In an Ad-Hoc network, its system structure is dynamic and hosts can join or leave the network any time. How to provide load services and how to find available hosts providing load services become important issues. The goal of this paper is that users can easily find and share resources based on the concepts of "service reusability" and "service innovation"

Due to the great population of Web Services techniques, this new architecture is structured for web services using SOA model with Web 2.0 [8, 11]. By using Web 2.0 with SOA, hosts which need services can easily find network resources. SOA service systems can be used in any computer system platform [1, 2, 3] with XML. This is a very important characteristic for hosts to share or request services from different platforms or network systems. With the help of Web 2.0, hosts can find the required services easily from the Internet [4].

Figure 1 shows the basic SOA structure [5, 6, 7], which is built by three major components – the Directory, Service consumer, and Service provider. SQA is operated by the following: The Directory provides a platform for information that a service provider can register in the Directory for providing services; a service consumer can find its desired service it needs in the Directory. Once the Directory finds services that a service consumer needs, it sends a query response back to the service consumer to notify it the result. At this moment, the service consumer has the information about the hosts which can provide services; the consumer contacts the service provider directory by sending requests. The service provider now will send responses back to the consumer for the services the consumer needs. This is also called the "invoke" process.

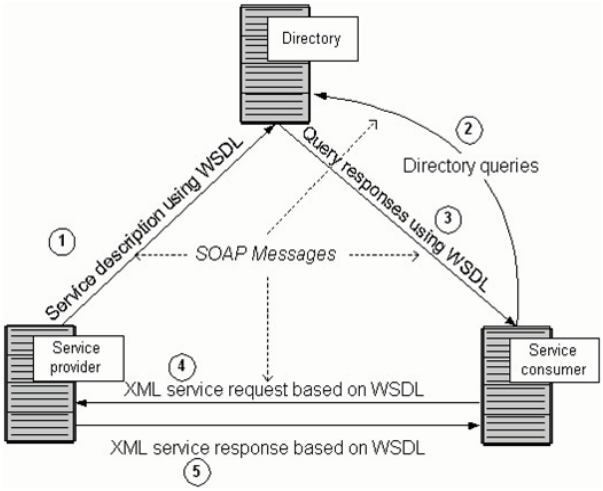

Figure 1: SOA structure

2. System structure

The system structure for the SOA model is illustrated in Figure 2. There are two layers in this structure – the Service Network layer, and the Service Logic layer.

The Service Network layer is the main network that connects to the internet using the regular network protocols. It receives requests from internet and forwards requests to the Service Logic layer in Web Service (WS) object forms. Each WS object is based on the SOA model which can communicate each other in social network way. The Service Logic layer is the main layer that uses WS objects to communicate each other in the sub-network under the Service Network layer. Different WS object has different objectives, for example, some WS objects are used for social network communication, while other WS objects are used for accessing contents in Content Networks. Since they are in SOA form, it is easy for them to find the resources they need for different purposes. Inside the Service Logic layer, there are sub-networks for different purposes and functions. For example, nodes can form social networks; storage devices can also form a content network for data accessing. All these operations are managed by the WS objects under the SOA model. For the service reusability purpose, most WS objects are generated by the Service Network layer for data and object consistency.

In Figure 2, all the services and requests are in the forms of Web Service objects which are defined and implemented by XML. For users who need services, requests are sent by those users to the Service Network Layer. The Service Network is the gateway for accepting requests and sending back requesting results to the requesters.

All the requests are processed by the Service Logic Layer, which finds the required information and applications for requests. The Content Network is a network which communicates with databases. The Social Network contains relations for social communities. The following procedure illustrates how it works.

1) Users send requests to a Service Network.
2) The Service Network forwards requests to Service Logic Layer via Web service functions.

   In this step, requests are transferred to objects that can communicate with the Service Logic layer.
3) When users send requests, Service Network has the ability to generate the desired WS objects according to the requests forwarded by the Service Network.

4) Service Logic Layer performs the required functions for these requests. It accesses data and information from Content Network according to Web service functions. A User can also contact other users using WS objects under the Service Logic Layer.

5) After the Service Logic Layer has the results for the requests, it sends the results back to the Service Network using Web service functions.

6) Service Network then sends the results back to the users who sent initial requests.

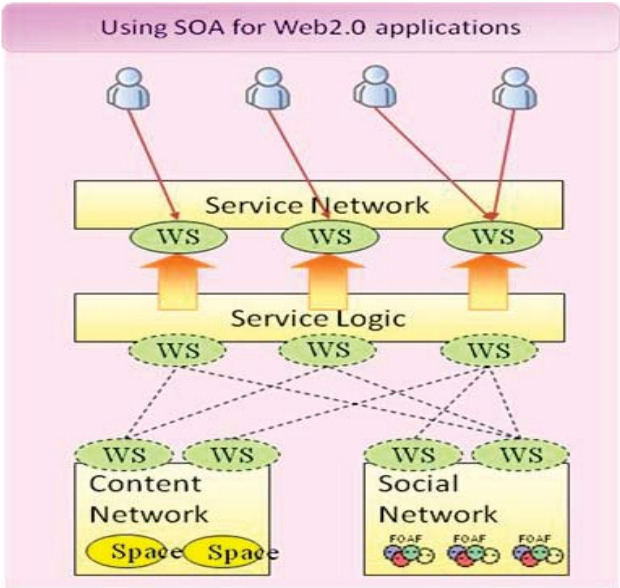

Figure 2: Using SOA for Web2.0 applications

There are several advantages with this design structure.

1) With the system structure, users can join the desired networks anywhere once they connect to the Internet.

2) With the characteristics of Web 2.0 with SOA model, users can join the desired networks they need to share or find resources easily they need.

3) Using WS objects for the communication makes it easy for service reusability and service innovation. Users do not need to construct special system or programs for data accessing and analysis.

4) Different Service Networks communicate with each other to find and share available resources.

3. Implementation and Simulation

Based on the structure of SOA model with Web 2.0 application, the system can be built in a three-tier structure. The lowest level is the sub-networks including Content Network, Social Network, which provides resources for data sharing. The middle level is the Service Logic layer, which provides WS objects. The top level is the Service Network layer that accepts requests or sends request results back to the users.

Ajax and other tools are used to construct the system at first. I am also going to construct a virtual community, and work on a simulation for data generation and analysis. Ten thousand nodes with 1000 Web services will be used in the simulation. The simulation will compare the performance for data sharing and load transferring to the system without using SOA structure.

4. Conclusion

Usually it is hard to find the required network resources in the Internet for load balance and load service purposes. Because of this, I propose a new structure for hosts in computer networks to easily find web service resources, especially when a host needs services which are not commonly provided in the Internet. With the help of Web 2.0 and SOA, hosts can find what they need because of the "long tail" property of Web 2.0 and the platform free property of SOA. Hosts can find and use the services easily since all the requests and services are constructed in the same service structures. This can also improve network system performances. With this new system, hosts can join and share resources in their service communities.

This system performance will be evaluated by using a simulation. Usually it is very hard to evaluate the performance for Web 2.0. This project should have great helps in finding performances for network systems with the usage of Web 2.0 and SOA.

References

[1] Ross J. Anderson, "The eternity service," *Pragocrypt* 1996, 1996.

[2] Stephanos Androutsellis-Theotokis and Diomidis Spinellis, "A survey of peer-to-peer content distribution technologies," *ACM Computing Surveys*, 36(4):335–371, December 2004. doi:10.1145/1041680.1041681.

[3] Yvonne Balzer, "Improve your SOA project plans," *IBM*, 16 July 2004

[4] Biddle, Peter, Paul England, Marcus Peinado, and Bryan Willman, "The Darknet and the Future of Content Distribution," *2002 ACM Workshop on Digital Rights Management*, 18 November 2002.

[5] Jason Bloomberg, "Mashups and SOBAs: Which is the Tail and Which is the Dog?," *Zapthink*

[6] Channabasavaiah, Holley and Tuggle, "Migrating to a service-oriented architecture," *IBM DeveloperWorks*, 16 Dec 2003

[7] Thomas Erl, "About the Principles," *Serviceorientation.org*, 2005-2006

[8] E. Guttman, C. Perkins, J. Veizades and M. Day, "Service Location Protocol," Version 2, IEFT, RFC 2165, November 1998.

[9] Dion Hinchcliffe, "Is Web 2.0 The Global SOA?," *SOA Web Services Journal*, 28 October 2005

[10] Huang, M., S. H. Hosseini, and K. Vairavan, *Load Balancing in Computer Networks*, Proceedings of ISCA 15th International Conference on Parallel and Distributed Computing Systems (PDCS-2002), Special session in Network Communication and Protocols. Held in the GALT HOUSE Hotel, Louisville, Kentucky, Sep. 19 - 21.

[11] Kim, A.J. (2000), "Community Building on the Web: Secret Strategies for Successful Online Communities," *London: Addison Wesley (ISBN 0-201-87484-9).*

[12] Christopher Koch, "A New Blueprint For The Enterprise," *CIO Magazine*, Mar 1 2005

[13] Peter Kollock (1999), "The Economies of Online Cooperation: Gifts and Public Goods in Cyberspace," *Communities in Cyberspace*, Marc Smith and Peter Kollock (editors). London: Routledge.

[14] Paul Krill, "Make way for SOA 2.0," *InfoWorld* , May 17, 2006

[15] H. Maab, "Location-Aware Mobile Application Based on Directory Services," MOBICOM 97, pp23-33.

[16] Joe McKendrick, "Anti-SOA 2.0 petition nears 400," *ZDNet.com*, June 29, 2006

[17] Yefim Natis & Roy Schulte, "Advanced SOA for Advanced Enterprise Projects," *Gartner*, July 13, 2006

[18] Andy Oram et al., "Peer-to-Peer:Harnessing the Power of Disruptive Technologies," Oreilly 2001

[19] Howard Rheingold (2000), "The Virtual Community: Homesteading on the Electronic Frontier," *London: MIT Press. (ISBN 0-262-68121-8)*.

[20] Ross, T. J., Fuzzy Logic with Engineering Applications, McGraw Hill, 1995.

[21] Antony Rowstron and Peter Druschel, "Pastry: Scalable, Decentralized Object Location, and Routing for Large-Scale Peer-to-Peer Systems," *Proceedings Middleware 2001 : IFIP/ACM International Conference on Distributed Systems Platforms*, Heidelberg, Germany, November 12-16, 2001. Lecture Notes in Computer Science, Volume 2218, Jan 2001, Page 329.

[22] Ralf Steinmetz, Klaus Wehrle (Eds), "Peer-to-Peer Systems and Applications," *ISBN: 3-540-29192-X,* Lecture Notes in Computer Science, Volume 3485, Sep 2005

[23] Smith, M. "Voices from the WELL: The Logic of the Virtual Commons," *UCLA Department of Sociology*.

[24] I. Stoica, R. Morris, D. Karger, M. F. Kaashoek, and H. Balakrishnan, "Chord: A scalable peer-to-peer lookup service for internet applications," *Proceedings of SIGCOMM 2001*, August 2001.

[25] J. Waldo, "The Jini Architecture for network-centric computing," Communication of the ACM, pp 76-82, July 1999.

[26] W. Yeong, T. Howes, and S. Kille, "Lightweight Directory Access Protocol," RFC 1777, March 1995.

[27]http://opengroup.org/projects/soa/doc.tpl?gdid=10632

Recognition of Mexican Sign Language through the Leap Motion Controller

Luis Obed Romero Nájera, Máximo López Sánchez, Juan Gabriel González Serna, Rodrigo Pineda Tapia, Julia Yazmín Arana Llanes
Department of Computer Science
National Center for Research and Technological Development, CENIDET
Interior Internado Palmira S/N, Col. Palmira
Cuernavaca, Morelos 62490, México
{obedrn; maximo; gabriel; rodrigo; juliaarana}@cenidet.edu.mx

ABSTRACT - *The Mexican Sign Language (MSL) is the language used by the Deaf community in the urban regions of Mexico. The National Institute of Statistics and Geography (INEGI in Spanish) showed in the results of the National poll of Income and Household Expenditure 2012 that 6.6% of the population of this country has a disability to achieve at least one of the activities such as walking, seeing, hearing, speaking or communicate, learn, and be able to make personal and mental care. Also reports that 8.6% of the national population presents disability to speak and 16.5% to hear* [1]. *This paper aims to show the use of Leap Motion Controller (LMC) to identify the elements of the Mexican Sign Language, as well as finding an opportunity area to help people who have this disability, and can communicate with people who do not suffer it; and learn the MSL.*

Keywords – *HCI, Mexican Sign Language, Leap Motion Controller, Deafness.*

1 Introduction

Hearing impairment is the restriction on the perception of sound, people who leads with this impairment from this disability have to use different forms of communication to relate with others. *INEGI* (in spanish, *Instituto Nacional de Estadística y Geografía*) in the study of Persons with disabilities in Mexico, "A vision to 2010", reports that for every 100 people with disabilities, 12 of them have difficulty hearing. This same study reports that the causes of hearing impairment are 13.4% in births, 25% through illness, 9% by an accident, 44.5% due to advanced age and 6.5% corresponds to some other cause [2]. In Mexico the natural language of people with this condition is known as the Mexican Sign Language [3].

The General Law for the Inclusion of Persons with Disabilities (Current text published in the Official Journal of the Federation on May 30, 2011) says: *"The language of a deaf community, which consists of a series of gestural signs articulated with the hands and accompanied by facial expressions, deliberate look and body movement, endowed with linguistic function is part of the linguistic heritage of the community and the grammar and vocabulary is so rich and complex as any oral language"* [4].

1.1 Mexican Sign Language - MSL

The Mexican Sign Language or MSL is the natural language of the Deaf community. Usually these languages have emerged between the deaf communities and are part of their culture and a reflection of his worldview; Also this language is in a constant production process, as happens with any other natural language [5].

The Mexican Sign Language (MSL) contains special rules, for example, point to a person is not considered as disrespectful or impolite.

Similar, if a person wants to be an interpreter of the MSL must wear colors that contrast with his skin, avoid wearing rings with movements, necklaces, long earrings, bracelets and scarves, should not be used painted nails and avoid chewing gum during interpretation, because sometimes the mouth movements correspond to words that are being made with the signs.In the case of men, if they wear a tie, it is recommended to use vest as it is can interfere with hand movements [6].

The Mexican Sign Language can be represented in two ways: *dactylology* and *ideograms*. The *dactylology* is the representation of the spelling of the spoken language and is represented by the alphabet, each word of the alphabet can be represented by making a hand sign. While the *ideogram* way is the representation of a word with one or more signs. [6].

2 Related works

During the investigation we found some related works, the following being the most representative:

2.1 Design and implementation of a translator hands sign language to a language text system using artificial vision in a controlled environment [7]

This system interprets the Ecuadorian signs language alphabet made with hands and then converts into text and voice; also, has a coach that shows how to do the signs for the user without hearing disabilities, so the user can communicate with other people that have this disability, and vice versa. It was developed in different stages, to name a few, the acquisition stage, digital image processing, Labview Vision Asistant, etc.

The system was developed in a controlled environment, it use a commercial computer camera with USB peripheral input, a fluorescent bulb for lighting and black colored fomix, this because the color black does not generate much shine when is illuminated with focus.

They performed 6 samples per letter because there is a small difference between the two hands. With the help of and Vision Assistant and the classification methods: nearest neighbor, nearest neighbor and minimum distance, they were generated 9 databases with 24 letters of the alphabet having a 82.15% success rate in tests.

2.2 Image recognition of Mexican Sign Language. [8]

The system developed in this work can recognize 25 words of the Mexican Sign Language alphabet using the Kinect device. The system has two main modules which are: learning and recognition. These modules are supported by three processes: standardization, strengthening and forgetfulness, which recognize the signs by using patterns that are stored in evolutionary matrices.

The recognition module starts when the Kinect takes capture of the image of the performed sign and this is compared to those found in the database, while the learning module appears when it detects a new pattern, ie there is at least 90% similarity between the image stored in the database and taken by Kinect.

The process of strengthening gathers information patterns, which have a value equal or above the threshold. During the process of forgetting eliminate pattern areas with few occurrences and and they are insignificant. The end result was the recognition of 25 letters of the MSL alphabet with a similarity percentage of 90% and above.

2.3 Transforming Indian Sign Language into text using Leap Motion [9]

The system implements algorithms such as *Dynamic Time Warping* (DTW), *Intelligence Sense* (IS), using Leap Motion Controller device converts the signs of Indian language text in an appropriate Signs.

The sign recognized by a viewer and a optimal match between two time series is calculated from capture of the text and the DTW algorithm. In these time, the data are deformed into nonlinearly form, causing similar region alineation thereby obtaining a minimum distance between them, adding them to a knowledge base that contain the metric calculation of each signal.

The Leap Motion Controller assigns a unique ID when it detects a hand, finger or tool. The ID remains the same, as long as that entity remains visible within the field of view of the device. If tracking is lost and recovered, the Leap Motion can assign a new ID, just as the system discards an inappropriate signal that does not match the knowledge base.

2.4 Arabic Sign Language recognition using the Leap Motion Controller. [10]

This paper proposes an approach to the recognition of sign language Arabic, it was developed with the Java programming language in conjunction with the NetBeans IDE using the device Leap Motion Controller (LMC) for detection of the hands and fingers; thus the LMC will provide data and information of the movements.

In the acquisition of data, the system includes a pre-processing state, a state of extraction and a classification state. To develop the system were required to implement classifiers such as: Multiplayer Perceptron Neural Networks (MLP) and Nave Bayes Classifier (NBC).

They were taken 10 samples of each letter and each sample has 10 data frames, which implies a total of 100 samples per letter; taking into account the 28 letters of alphabet system would 2800 data tables. All this information was collected and imported into MATLAB for analysis and processing. The results obtained in this study were: With 98.3% of the NBC classifier and 99.1% of MLP classifier.

2.5 Towards the development of a mexican speech-to-sign-language translator for the deaf community [11]

This Paper present an application in which the development of a mexican speech-to-sign-language translator can assist to normal people to interact with deaf people. The ASR (Mexican Automatic Speech Recognizer)

is the main module and likewise has the Text Interpreter and MSL (Mexican Sign Language) Database.

To have a good performance the ASR was necessary the use of a corpus Mexican Spanish Corpus DIMEx100. This corpus aims to make it possible the construction of acoustic models and pronunciation of dictionaries. With the tool TranscribeMex it is possible to obtain the definition of the phonemes Mexican Spanish language.

One requirement is that the samples must be labelled at the orthographic and phonetic levels to perform supervised training of the acoustic models of the ASR system. The Orthographic labelling was performed manually with the software Wavesurfer. The algorithm used was the HMM (Hidden Markov Models).

In the module of Text Interpreter and MSL Database; where the word is found, the interpreter proceeds to display the sequence of MSL movements associated to that word, otherwise, if the word is not found in the database, the word is "spelled" and described the dactylology way of MSL.

The vocabulary consists of 25 words, 23 letters of the alphabet, obtaining accuracy at 97.2% and a set of 400 words used in total.

3 Implementation of Leap Motion in identifying signs

3.1 Leap Motion Controller

The Leap Motion Controller (LMC) is a USB peripheral device that detects and reads movements within a 3-D interaction space to precisely translate and control software on a computing device [12]. As is illustrated in Figure 1, the controller consists of three Infrared Light emitters and two Infrared Light cameras [13].

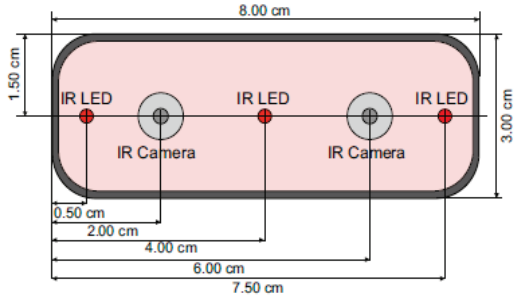

Figure 1 Schematic View of LMC [13]

The effective range of the Leap Motion Controller extends from approximately 25 to 600 millimeters above the device (1 inch to 2 feet). In Figure 2 the origin is centered at the top of the Leap Motion Controller.

The x- and z-axes lie in the horizontal plane, with the x-axis running parallel to the long edge of the device. The y-axis is vertical, with positive values increasing upwards while the z-axis has positive values increasing toward the user [12].

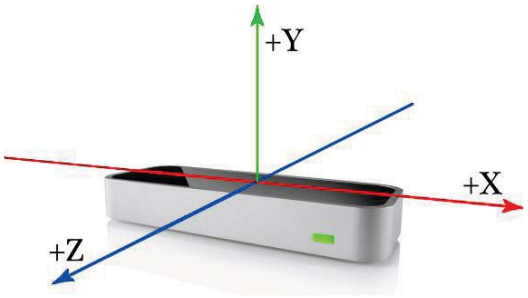

Figure 2 Coordinate system [12]

In the paper of Potter, Araullo & Carter (2013) The Leap Motion controller: A view on sign language they give an approach suitability of use of Leap Motion Controller for recognition of Australian sign language, showing its strengths and weaknesses of the mentioned device.

The strengths that stand out is the accuracy level with which the LMC account if you include the Leap Motion API. The LMC can consistently recognize individual digits in a hand, being able to identify, measure digit, address and fingertip location, likewise the LMC is also capable of tracking very small movements.

The weaknesses in the LMC are the precision and fidelity of detection when the hands do not have linear of sight with the controller. Another weakness mentioned is when the fingertips of one hand touching the fingertips of the other hand or when there is a close approximated between the fingertips, the LMC is unable to recognize the gesture and therefore cannot be displayed.

3.2 Identification of the Mexican Sign Language

The signs are made with hands, facial gestures and body movements.

The book *"Manos a Voz"* [6] which has a collection of 1,113 words divided into 15 topics: alphabet, food, animals, antonyms, house, calendar, colors, school, family, fruits and vegetables, numbers and related words, body parts, pronouns - adjectives - prepositions - articles, and other words. Some of the signs presented in the book *"Manos a voz"*, will be used to perform the research of the recognition of the Mexican Sign Language using the Leap Motion Controller; only some signs of this book because of the limitations that the LMC has be recognized, as illustrated in Figure 3 the LMC only recognizes our hands and arm, before that limit the number of signs to be recognized is restricted.

Figure 3 Word blow in LSM *[6]*

Signs like the one illustrated in Figure 4 which is the word blow comes with a facial gesture; these signs are accompanied by facial gestures they will not be detected by the LMC.

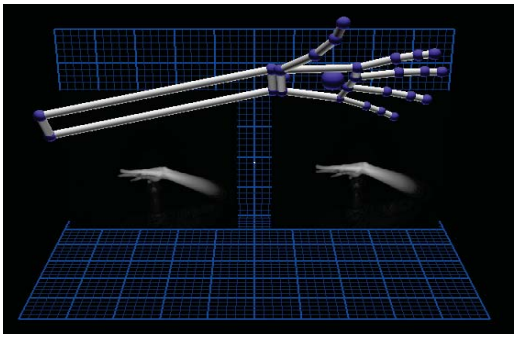

Figure 4 Display LMC.

4 Future work

Order to overcome the limitations that the Leap Motion Controller might implement algorithms for pattern recognition, to sign on which must unite hand or fingertips are recognized. Among the algorithms that could be used they are:

▪*Hidden Markov Model* – HMM: Composed of a finite set of states in which each of them is associated with a probability distribution. The major feature is its double stochastic process, hidden or not observable either observable [14].

▪*Support Vector Machine* – SVM: This is a supervised classification method aimed at determining the optimal boundary between two groups [15]. Applications that can be developed with the use of this algorithm are: image classification, character recognition, protein detection, pattern classification, identification of functions, etc. [16].

▪*Multilayer Perceptron* – MLP: This is a supervised neural network consists of several layers, usually they are three: the input layer, the hidden layer and output layer. The integration of several layers allows you to solve problems that are not linearly separable [17].

▪*Dynamic Time Warping* – DTW: Algorithm used to find the optimal alignment between two temporal sequences. This algorithm is used primarily in applications for speech recognition [18].

5 Conclusions

Based on the study of related research and study of Leap Motion Controller made by [19] we can conclude that it will be necessary to implement an algorithm of those mentioned before for the wide range of signs that contains the Mexican Sign Language, it can be recognized.

Likewise catalog signs which are candidates to be recognized and discard those that may not be recognized even with the support of an algorithm.

Furthermore, seek the support of a specialist in the area of sign language, to make the sign correctly and check if there is any sign that represents the same as those signs that have not been recognized.

6 References

[1] INEGI, "Estadistícas a propósito del dia internacional de las personas con discapacidad", México, D.F.: Instituto Nacional de Estadísticas y Geografía., 2012.

[2] INEGI, "Las personas con discapacidad en México : una visión al 2010," Instituto Nacional de Estadística y Geografía., México, 2010.

[3] CONADIS, "Glosario de términos sobre discapacidad", México, D.F.: CONADIS, 2012.

[4] Secretaría de Gobernación, "DOF - Diario Oficial de la Federación," 28 Septiembre 2015. [En línea]. Available: http://dof.gob.mx/nota_detalle.php?codigo=5191516&fecha=30/05/2011.

[5] DIELSEME, "Estudio introductorio al léxico de la LSM," Dirección de Educación Especial., México, D.F., 2004.

[6] M. E. Serafín de Fleischmann y R. González Pérez, "Manos con Voz - Diccionario de Lengua de Señas Mexicana", Mexico, D.F., 2011.

[7] E. . F. Chiguano Rodríguez y N. V. Moreno Díaz , "Diseño e implementacion de un sistema traductor de lenguaje de manos a un lenguaje de texto mediante vision artificial en un ambiente contralado.", Quito, 2011.

[8] F. P. Priego Pérez, "Reconocimiento de imágenes del Lenguaje de Señas Mexicano", México, D.F.: Instituto Politécnico Nacional, 2012.

[9] P. Karthick, N. Prathiba, V. Rekha y S. Thanalaxmi, "Transforming Indian Sign Language into Text Using Leap Motion," International Journal of Innovative Research in Science, Engineering and Technology, vol. 3, nº 4, 2014.

[10] M. Mohandes, S. Aliyu y M. Deriche, "Arabic Sign Language Recognition using the Leap Motion Controller," Institute of Electrical and Electronics Engineers, 2014.

[11] F. Trujillo Romero y S. . O. Caballero Morales, "Towards the Development of a Mexican Speech-to-Sign-Language Translator for the Deaf Community", Red de Revistas Científicas de América Latina, el Caribe, España y Portugal, pp. Vol 22, pp. 83-89, 2012.

[12] Leap Motion, "Leap Motion Developer Portal", 07 Octubre 2015. [En línea]. Available: https://developer.leapmotion.com/Leap_Motion_App_Store_Distribution_Agreement_100914.pdf.

[13] F. Weichert, D. Bachmann, B. Rudak y D. Fisseler, "Analysis of the accuracy and robustness of the Leap Motion Controller. Sensors", Switzerland, 2013.

[14] D. X. Macas Macas y W. A. Padilla Pineda, Estudio de los modelos ocultos de markov y desarrollo de un prototipo para el reconocimiento automatico del habla, Cuenca, Ecuador, 2012.

[15] J. Vargas, B. Conde, V. Paccapelo y L. Zingaretti, "Máquinas de soporte vectorial: Metodología y aplicación en r," 2012.

[16] J. A. Resendiz Trejo , "Las maquinas de vectores de soporte para identificación en línea", México, D.F, 2006.

[17] S. E. Nope R., H. Loaiza C. y E. Caicedo B., "Estudio comparativo de técnicas para el reconocimiento", Revista Avances en Sistemas e Informática, pp. pp. 127-134, 2008.

[18] A. Gonzáles de Dios, "Desarrollo y evaluación de un sistema de teleoperación de robots basado en reconocimiento de gestos usando el sensor kinect", Madrid. España, 2014.

[19] L. E. Potter, J. Araullo y L. Carter, "The Leap Motion controller: A view on sign language", Association for Computing Machinery, 2013.

Updated DSP Filter Calculation for a Digital Doppler Velocity Flow Meter

Daniel L. Garcia
Kennesaw State University
1100 S. Marietta Parkway
Marietta, GA 30060-2896, USA
678-925-9672
dgarcia3@spsu.edu

Daren R. Wilcox
Kennesaw State University
1100 South Marietta Parkway
Marietta, Georgia 30060-2896, USA
678-915-7269
dwilcox@spsu.edu

Introduction

The goal of this article is to provide updated results for the proof of concept that digital signal processing has progressed to the point of equivalence to traditional analog Doppler flow meter designs. This article will show the non-linear formula and a new correction filter coefficients for low end carrier frequency noise previously uncorrected.

Categories and Subject Descriptor

Proof of Concept for a Digital Ultrasonic Doppler Liquid Velocity Flow Meter Updated

General Terms

Digital Ultrasonic Doppler Liquid Velocity Flow Meter

Keywords

Doppler Liquid Flow Meter, Doppler Effect, Liquid Doppler Effect Formula

Background

The ability to read the speed of liquids flowing through a pipe without breaking the pipe wall is extremely coveted. Using the Doppler Effect, a close approximation (typically within 2%) can be calculated given prerequisites (which can be found in the original article) [1].

This article is a follow up to the previous article CSC3521 published in July 2014. The goal of this article is to provide updated results for the proof of concept that digital signal processing has progressed to the point of equivalence to traditional analog Doppler flow meter designs. This article will show the non-linear formula and a new correction filter values for low end carrier frequency noise previously uncorrected.

Originally, the thought was that the Doppler Effect formula was something like $\frac{frequency}{72-\frac{frequency}{150}} = fps$ (this was outside the scope of the first article so an empirically formula was determined. Since then the calculations for the frequency to velocity formula has been formulated.

Another issue previously unresolved was the low frequency carrier noise (detected by abnormally high amplitude values near the 0 Hz region). In the original testing, a high pass filter was added to eliminate the low end noise, but this did not compensate for the carrier added noise. A new filter was used to attempt to minimize and semi-compensate for the carrier noise.

Original Results

Plots and Graphs

Here are the original test 2 results using the ≈70.4Hz to 1 fps conversation value. "The following will be screen shots of the collected frequency-domain results from test 2:

- For approximately 0.950 fps an approximate 68 Hz was the peak.

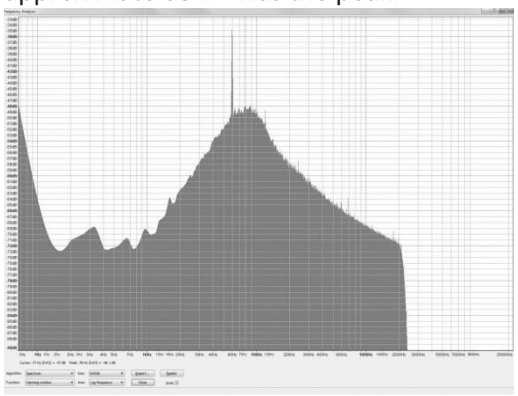

A 60Hz power peak is also present. A notch filter at 60Hz needs to be applied.

- For approximately 1.950 fps an approximate 137 Hz was the peak.

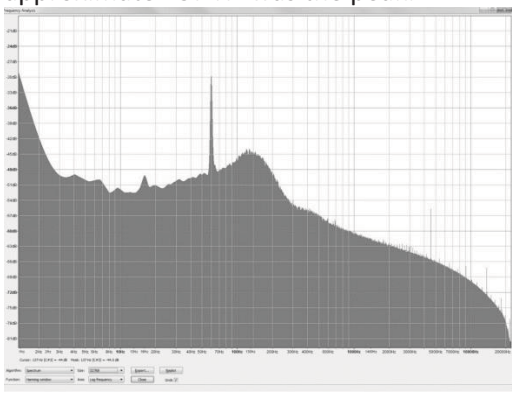

Again, a notch filter at 60 Hz needs to be applied to eliminate the power peak.

- For approximately 3.400 fps an approx. 237 Hz was the peak.

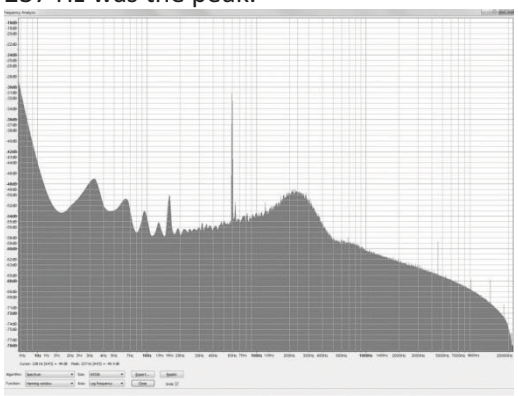

Again, a notch filter at 60 Hz should be applied to eliminate the power noise peak.

- For approximately 4.400 fps an approximate 301 Hz was the peak.

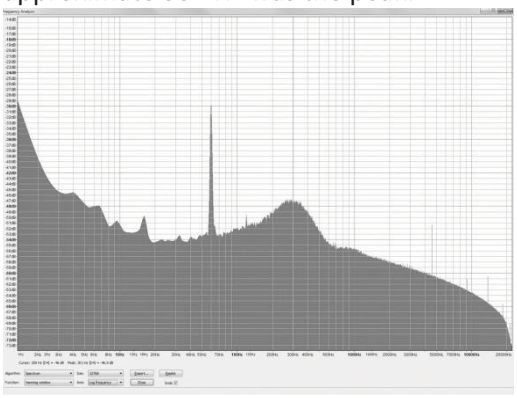

Again, a notch filter at 60 Hz needs to be applied to eliminate the power peak.

- For approximately 6.700 fps an approximate 446 Hz was the peak.

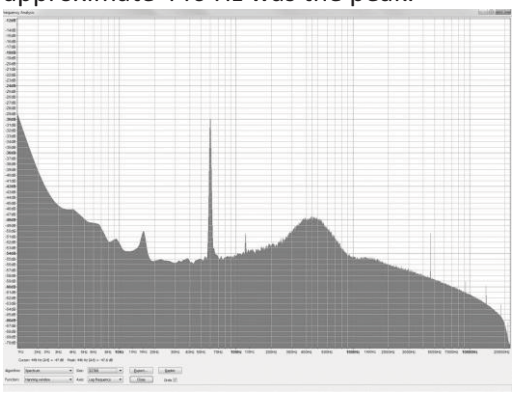

Again, a notch filter at 60 Hz needs to be applied to eliminate the power peak.

- For approximately 8.900 fps an approximate 530 Hz was the peak.

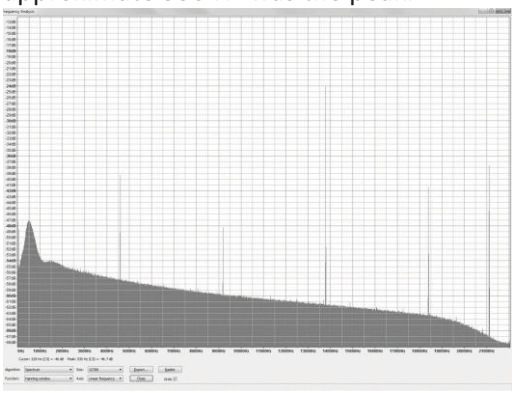

Again, a notch filter at 60 Hz needs to be applied to eliminate the power peak.

The complete non-corrected results for Test 2 are as followed:

Test 2

Reference		Results		
gpm	fps	Hz	Calculation	Error
2.6	0.965	78	1.091	13.057%
5.25	1.949	133	1.927	-1.129%
9.25	3.434	235	3.366	-1.980%
11.95	4.436	301	4.300	-3.066%
18	6.682	446	6.461	-3.307%
20.85	7.74	530	7.741	0.013%

[1]"

As you can see, originally there is an approximate 2-3% error present. This is acceptable due to the generic conversion value used, but a more accurate conversion formula is possible.

Updated Results

Doppler Effect Formula

The original thinking was as followed: "After testing, it appears to be almost linear around 70.4Hz. On the lower speeds, it was about 67.96Hz at a velocity of 0.947 feet per second (fps) which is about 71.75 Hz per fps. At the maximum speed available with the testing flow loop, it was approximately 524.1Hz at a velocity of 7.684fps which is 68.2Hz per fps. A mid-flow test was also done which yielded a return frequency of 318.1Hz for a liquid speed of 4.566fps which is 69.666Hz per fps. A nonlinear pattern appears to be present in the lower velocities. More testing is required to grasp the full formula, but at first glance it appears to be something like:

$$\frac{frequency}{72-\frac{frequency}{150}} = fps$$ [1]."

Since the initial results were published, the following was formulated. "The change in frequency of a wave emitted by a moving source is calculated from the component of its velocity moving towards (or away) from the sensor. The general Doppler Effect ratio of emitted and detected frequencies shift is given by the following formula:

$$\frac{c + v_r}{(c + v_s)} = \%$$

where:

- c is the wave velocity within the liquid medium in meters per second (mps).
- v_s is the velocity in mps of variation of density moving within the pipe.
- v_r is the velocity of the sensor moving." [2]

Due to the sound speed of water varying depending on its temperature, the liquid sound speed should be taken into account when testing the design. Also the angle of which the crystal is penetrating the pipe will affect the return frequency shift. The transducer should not be moving therefore v_r should be zero. The final formula is:

$$\%\ of\ Change = \frac{Mediam\ SS_{mps} + 0}{\cos \emptyset° * V_{mps} + Mediam\ SS_{mps}}$$

After applying some algebraic principles and including the transmission frequency, the formula for the Doppler shift to velocity is:

$$V_{mps} = \frac{Medium\ SS_{mps} * (Trans\ Freq_{Hz} - Return\ Freq_{Hz})}{Return\ Freq_{Hz} * \cos \emptyset°}$$

After a few test velocities, the frequency to mps is discovered to be nonlinear. Rather, it is more like the linear region of a parabola. Therefore a flat 70.4Hz per fps calculation will not reap the most accurate result spanning the spectrum as previously assumed. Preliminarily using the following formula shows a greater accuracy result:

$$V_{mps} = \frac{medium\ SS_{mps} * \Delta f}{(f_0 - \Delta f) * \cos \emptyset°}$$

where:

- Medium SS=sound speed of the liquid in mps
- Δf=the delta frequency shift in Hz
- f_0=the transmission frequency in Hz
- Ø°=the angle of the crystals.

Results Using New Formula

Reference		Results		
gpm	fps	Hz	Calculation	Error
2.60	0.965	68*	1.006	4.249%
5.25	1.949	134	1.983	1.744%
9.25	3.434	235	3.478	1.281%
11.95	4.436	301	4.455	0.428%
18.00	6.682	446	6.603	-1.182%
20.85	7.740	530	7.848	1.395%

*Typo Corrected from Original Table

Carrier Frequency Noise Reduction

According to Dr. Theodore Grosch, Dr. Wojciech Klimkiewicz, Dr. Peter Moosbrugger, and Dr. Lynn Carpenter who wrote an article called "Automotive Radar Design for Collision Warming" (1993, December) [3], the carrier frequency noise can be compensated using a simple high pass filter starting at the max frequency. In this paper, they commented on a method to eliminate naturally occurring low frequency carrier noise by adding a high pass filter starting at the highest frequency expected. The filter formula is:

$$\frac{1}{(\max \text{Frequency})^3}$$ [3].

According to their paper, this will approximate the naturally occurring noise and thereby flatten out the increasing amplitude noise created by the carrier signal near the low end frequencies.

Current High Pass Digital Filter Coefficients

A simple first order high pass filter is required. The current high pass filter coefficients used in the z-domain calculated are: 0.995 -0.995 for the numerator, and 1.0000 -0.9949 for the denominator. More research needs to be done to determine if these are the optimal coefficients.

Updated Graphs with High Pass Filter Coefficients

The following are screen shots of the original Test 2 data collected with the new high pass filter added in the frequency-domain (calculations for the velocity were calculated using the Doppler Shift to velocity formula):

- For approximately 1.006fps an approximate 68 Hz was the peak.

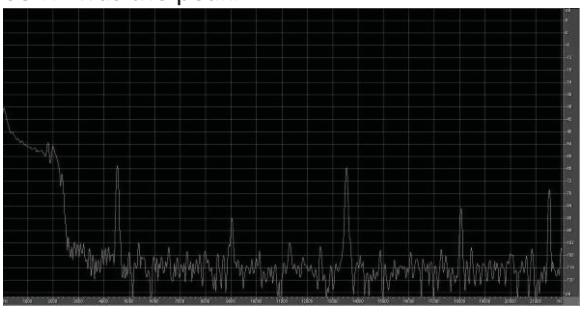

- For approximately 1.983fps an approximate 134 Hz was the peak.

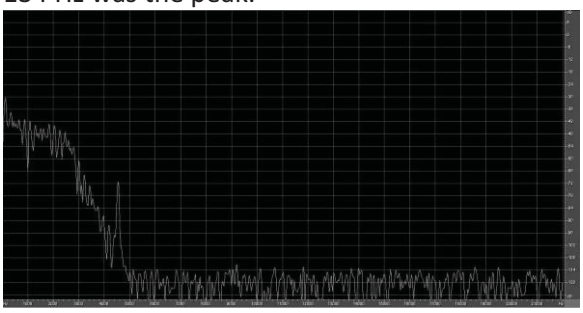

- For approximately 3.478fps an approximate 235 Hz was the peak.

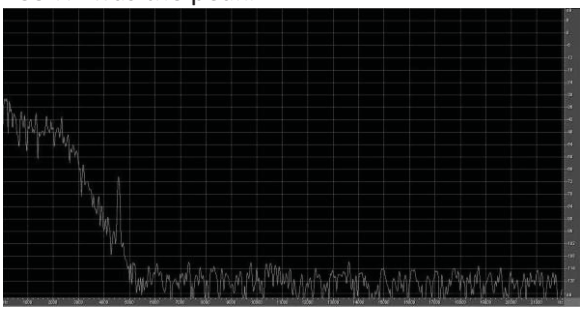

- For approximately 4.455fps an approximate 301 Hz was the peak.

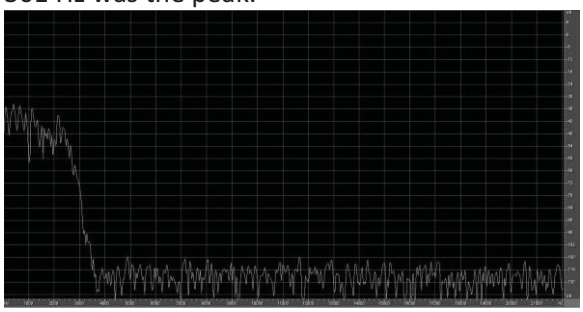

- For approximately 6.603fps an approximate 446 Hz was the peak.

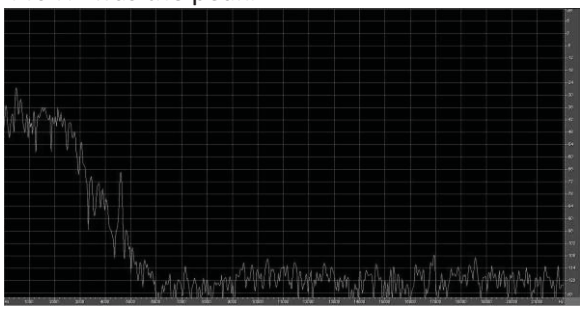

- For approximately 7.848fps an approximate 530 Hz was the peak.

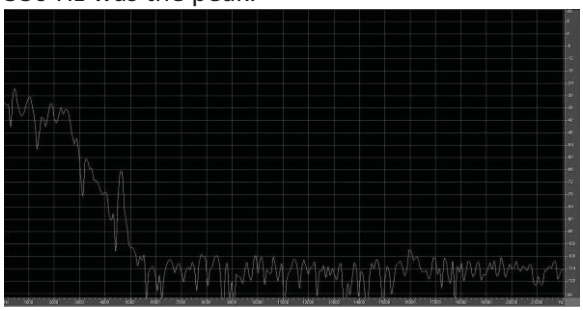

Conclusion

By using: $v_{mps} = \frac{medium\ SS_{mps} * \Delta f}{(f_0 - \Delta f) * \cos \emptyset^\circ}$ as the formula to convert the Δf to velocity instead of the approximation of 70.4Hz per fps originally used gives increased accuracy, and adding a simple additional:

$$\frac{1}{(\max \text{Frequency})^3}$$

high pass filter sudo-flattens the noise created by the carrier frequency. As a result, the ability to locate the maximum amplitude is significantly simplified. All that is required is to determine the max() amplitude of the given sample group down to yet an undetermined frequency.

These two simple additions simplify and increase the accuracy of the process to convert the Doppler Effect frequency shift to the liquid velocity speed.

MATLab Code Sample [4]

```
NameOfFile=['APPROX 2FPS.WAV'];
[y,fs,nBits]=wavread(NameOfFile);

Lfft=2048;

Nth=10;
Hpth=1;
wl=2500/fs;

%create Butterworth low pass filter
[numl,denl]=butter(Nth,wl,'low');
[irl, time]=impz(numl,denl,Lfft);

%create 1/max^3 high pass filter
[numh,denh]= butter(HPth,wl^3,'high');
[irh, time]=impz(numh,denh,Lfft);

%convoluting filter w/ signal in
%frequency-domain
Y=abs(fft(y,Lfft));
IRl=fft(irl,Lfft);
IRh=fft(irh,Lfft);

YC=Y.*IRh;
YC=IRl.*YC;
```

References and Citations

[1] Garcia, Daniel L. and Wilcox, Daren R. (2014, July) DSP Filter Calculation for a Digital Doppler Velocity Flow Meter. (CSC3521). *Las Vegas Nevada, USA: CSREA Press*, 21 July, 2014, ISBN: 1-60132-266-6.

[2] Rosen, Joe, and Lisa Quinn Gothard. (2010). Encyclopedia of Physical Science. *New York: Facts on File, eBook Collection (EBSCOhost)*, [Retrieved on 1 February, 2015] ISBN:0-8160-70113. Pg. 155.

[3] Theodore Grosch, Wojciech Klimkiewicz, Peter Moosbrugger, and Lynn Carpenter, "A 24 GHz FM/CW automotive radar designed for collision warning," *SPIE International Symposium on Photonic Sensors and Controls for Commercial Applications*, 13 October- 4 November 1994, Boston MA.

[4] MATLab, 2015, http://www.mathworks.com, Copyright © 1994-2015 The MathWorks, Inc. Reprinted with Permission.

Simulation study of annihilation $A + B \rightarrow \emptyset$ of diffusing particles created at a planar wall

D. di Caprio[1], J. Stafiej[2], and J. Stępień[3]
[1]ENSCP Chimie, Paristech, Paris, France
[2]Faculty of Mathematics and Natural Sciences. School of Exact Sciences,
Cardinal Stefan Wyszynski University, Warsaw, Poland.
[3]Institute of Physical Chemistry, Polish Academy of Sciences, Warsaw, Poland.

Abstract— *We present a computer simulation study of binary annihilation reaction $A + B \rightarrow \emptyset$ where A and B are generated at a planar interface. The simulations are based on discrete lattice cellular automata type model where diffusion is represented by a random walk. The results are presented as stationary particle profiles with an attempt to determine the exponent in the power law for the decaying profile. In some cases it is different from the classical mean field result.*

Keywords: Cellular automata, random walk, chemical kinetics, annihilation

1. Introduction

The binary annihilation reaction $A + B \rightarrow \emptyset$ has been of a recurrent interest over the past 40 years [1], [2]. The annihilation reaction appears in astrophysical and cosmological problems [1] down to a rather microscopic length scales [3]. The electron - hole recombination in semi conductors, acid - base neutralization in solution chemistry are the examples. In the mesoscopic description the relaxation of a single component nonuniformities can be tackled with this annihilation model as positive excess can be represented by A particles and negative by B particles bringing about uniformity by annihilation when the both species meet.

In the batch volume system in the absence of perfect mixing the kinetics of this reaction displays a slow down compared to the classical ideal mixing case [4]. The slow down results from segregation *i. e.* formation of A and B filled regions with the annihilation possible mainly at their boundaries. If we start from a random distribution of such particles there is a first period of faster kinetics. It corresponds to annihilation of the well mixed part of the batch. Then however the segregated regions of A and B remain because of random excesses of one of the species in these regions. A further annihilation can proceed only through the boundaries. It marks a crossover from the classical regime to the slower so called Zeldovitch regime [4]. Our own interest in this reaction comes from our previous work on mechanisms of corrosion where we observe a coupling between segregation and autocatalytic mechanism of corrosion [5]. We have not found any work so far on the annihilation reaction in an inhomogeneous system. Here we take a simpler case than our corrosion model. The annihilating species A and B are produced at a planar wall. When the production of A and B is balanced *i. e.* at the vsame rate for each species then a stationary decay profile of their density exists. How the anomalous kinetics can influence this decay? How far can A and B carry the information about the distribution of their sources away from the interface? The rest of the paper is organized as follows. In the next section we provide the classical, ideal mixing results. Then we briefly present our numerical simulation approach. Next we present and discuss several simulation results in the form of stationary profiles. We conclude the paper with a perspective on our future studies particularly in the domain of corrosion.

2. Reagent decay profile

Reagent decay profile can be readily obtained from classical chemical kinetics:

$$\left\{ \frac{dc_{A,B}}{dt} \right\}_{annihilation} = -K_{AB} c_A c_B \tag{1}$$

combined with mass conservation in transport processes:

$$\left\{ \frac{\partial c_{A,B}}{\partial t} \right\}_{transport} + \nabla \vec{j}_{A,B} = 0 \tag{2}$$

and Fick's law:

$$\vec{j}_{A,B} = -D_{A,B} \nabla c_{A,B}. \tag{3}$$

where c_A, c_B, $\vec{j}_A$, $\vec{j}_B$ denote concentrations and fluxes of particles A and B respectively. K_{AB} denotes the rate constant of annihilation, $D_A = D_B = D$ is the diffusion coefficient of A and B particle assumed equal in this paper. Using arguements of symmetry $c_A = c_B$ and $j_{z,A} = j_{z,B} = j_z$ is the flux component perpendicular to the surface and those parallel vanish. Then it is straightforward to obtain the solution.

$$c(z) = \frac{3D}{8K_{AB}} \frac{1}{(z - z_0)^2} \tag{4}$$

where $z_0^2 = \frac{3}{8} \frac{D}{K_{AB} c_0}$ if we set the wall where A and B are created at $z = 0$ with boundary condition $c(z = 0) = c_0$.

We can obtain somewhat more general result following the field theoretical approach of Toussaint and Wilczek [4] in the limit of fast annihilation irrespective of the form of the kinetic law for this annihilation provided that the reaction is fast.

2.1 Toussaint-Wilczek approach

If annihilation is fast enough soon we find the system in a state described by:

$$f(\vec{r},t) = c_A(\vec{r},t) - c_B(\vec{r},t) \tag{5}$$

where for $c_A > 0$ we have $c_B = 0$ or vice -versa for $c_B > 0$ we have $c_A = 0$. Hence we have:

$$c_A(\vec{r},t) + c_B(\vec{r},t) = |f(\vec{r},t)| \tag{6}$$

Taking into account the planar symmetry the partial Fourier transform of $f(\vec{r},t)$ can be written as:

$$\tilde{f}(\omega,K,z) = \int f(\vec{r},t)\exp(-i\omega t - i\vec{K}\cdot\vec{R})dtd^s\vec{R} \tag{7}$$

where ω is the angular frequency and $\vec{K}$ is the wave vector in the space inverse to the $\vec{R}$ space and $K = |\vec{K}|$ is its modulus. In the usual three dimensional space $s = 2$ is the plane dimensionality. Generally $s = d - 1$ in d dimensions.

$$\left[i\omega - DK^2 + D\frac{\partial^2}{\partial z^2}\right]\tilde{f}(\omega,K,z) = 0 \tag{8}$$

In the stationary condition $\omega \to 0$ we can solve this equation requiring that $\tilde{f}(\omega = 0,K,z) \to 0$ far away from the plane.The solutions have the form:

$$\tilde{f}_0(K,z) = \tilde{f}_0(K,0)\exp(-Kz) \tag{9}$$

Let us postulate the following form for the probability of $\tilde{f}_0(\vec{K},0)$:

$$\mathcal{P}[\tilde{f}_0(K,0)] = \frac{1}{Z}\exp\left(-\frac{1}{2}\int|\tilde{f}_0(K,0)|^2 h(K)d\vec{K}\right) \tag{10}$$

as it follows from $\vec{R}$ invariance that the effective hamiltonian linear operator for the Gaussian model must be diagonal in $\vec{K}$ space and only $K = |\vec{K}|$ dependent. Anticipating that $K \to 0$ determines the long distance behavior of the profile we postulate $h(K)$ in the form:

$$h(K) = \frac{1}{K^\mu}(h_0 + h_2K^2 + ...) \tag{11}$$

where we have isolated the eventual singular term $K^{-\mu}$ from the regular part. Let us limit the expansion just to this term.

It can be verified that the moments of $f_0(\vec{R} = 0,z)$ can be obtained from the following Gaussian functional integral:

$$Z(\lambda) = \int \mathcal{D}\tilde{f}_0(K,0)\, e^{\left(-\int\left(\frac{1}{2}|\tilde{f}_0(K,0)|^2 h_0K^{-\mu} - \lambda\tilde{f}_0(K,0)e^{-Kz}\right)\frac{d\vec{K}^s}{(2\pi)^s}\right)} \tag{12}$$

from the derivatives $\frac{-d^n\ln Z(\lambda)}{d\lambda^n}$ for $\lambda = 0$ and in particular $Z_0 = Z(\lambda = 0)$ is the partition function for the Gaussian model. The Gaussian integral can be done analytically by standard methods [4]:

$$Z(\lambda) = Z_0\exp\left(\frac{\lambda^2 * I_s}{2}\right) \text{ where } I_s = \int\frac{K^\mu e^{-Kz}}{h_0(2\pi)^s}d\vec{K}^s \tag{13}$$

Following [4] we immediately have that:

$$c(z) = \frac{1}{2} < |f(\vec{R},z)| >= \sqrt{\frac{I_s}{2\pi}} \propto z^{-\frac{\mu+s}{2}} \tag{14}$$

Let us note that $\mu = 0$ corresponds to even distribution in $\vec{K}$-space. It leads to the profile decay law $c(z) \propto z^{-1}$. In contrast, to obtain the classical decay law $c(z) \propto z^{-2}$ we have to assume $\mu = 2$.

3. Cellular automata model and its parallel implementation

We use a discrete, cellular automata type approach to the annihilation reaction. We assume in this paper that the two annihilating species execute randome walk over the lattice sites by swapping with empty, randomly selected nearest neighbor lattice sites S.

$$A_{nn1} + S_{nn2} \to S_{nn1} + A_{nn2} \tag{15}$$
$$B_{nn1} + S_{nn2} \to S_{nn1} + B_{nn2} \tag{16}$$

We assume symmtry between A and B. Both species occupy just one site. Their random walks conform to simple exclusion, in which at most one species A or B can occupy a site.

$$A_{nn1} + A_{nn2} \to A_{nn1} + A_{nn2} \tag{17}$$
$$B_{nn1} + B_{nn2} \to B_{nn1} + B_{nn2} \tag{18}$$

It follows that if the pair of random neighbours $A - A$ or $B-B$ is selected for swapping nothing really happens. When A and B meet *i. e.* A wants to step on B or *vice versa* we select two outcomes fot this event. One is annihilation:

$$A_{nn1} + B_{nn2} \to S_{nn1} + S_{nn2} \tag{19}$$
$$B_{nn1} + A_{nn2} \to S_{nn1} + S_{nn2} \tag{20}$$

The other one is: nothing happens:

$$A_{nn1} + B_{nn2} \to A_{nn1} + B_{nn2} \tag{21}$$
$$B_{nn1} + A_{nn2} \to A_{nn1} + B_{nn2} \tag{22}$$

The probability to choose annihilation P_{ann} is one of the model parameters. Note that reactions 16, 18 and 22 conserve the numbers N_A and N_B while reactions 20 do not. They conserve however $N_A - N_B$ i. e. the charge if we think about A and B as oppositely charged species in an electrolyte that may mutually discharge and become a part of an irrelevant environment. Reaction 20 is the only way A and B are removed from the system and it is in pairs. They

are created independent of one another on the surface of the wall.

$$M_{nn1} + S_{nn2} \rightarrow M_{nn1} + A_{nn2} \quad (23)$$
$$M_{nn1} + S_{nn2} \rightarrow M_{nn1} + B_{nn2} \quad (24)$$

Ideally they should be created in pairs. However this poses several problems and we choose another solution.The particles A and B are created independently of each other initially with probability $P_{crea} = 0.5$ for A nad for B. We imagine that the creation of particles is associated with charging of a capacitor and requires energy $\phi_C dQ$ where $dQ = 1$ for A creation and $dQ = -1$ for B creation. The potential $\phi_C = Q/C$ where $Q = N_A - N_B$ is created because of the the charge imbalance. If the capacity is huge then A and B are created practically independently with $P_{crea} = 0.5$ and a possible drifting of the charge imbalance. The drift may radically change the kinetic behavior as the decay profile of one species in the excess of the other species is exponential. Therefore we have to use the capacity small enough to suppress the drifting and maintain charge neutrality. If the capacity is too small the system overreacts the charge imbalance leading to oscillations. However there is an intermediate range of capacity values where the charge fluctuates only slightly and the average profiles are independent of this capacity value. We use sequential programming for simulations in 1D and 2D. It becomes inexpedient in 3D and we use a parallel algorithm suitable for CUDA environment as described in our paper [6] and ref. [7]. The 1D system is 1024 sites long, A and B are randomely generated at the first site. The simulations in 2 D are performed on a rectangular grid of sizes 256×1024 sites. the simulations in 3D are done in a $384 \times 384 \times 192$. It takes from 200 000 to 500 000 time steps to reach a steady state of which we can take the data for subsequent averaging to reduce the statistical noise. Periodic boundary conditions are applied along axes x and y in 3D and x axis in 2D. For z axis impenetrable wall conditions are imposed at the boundaries.

4. Results and discussion

In Figures 1 and 2 we present stationary profile for 1D system in the usual and log-log representation. A nonlinear fit to the data has been performed based on the following dependence:

$$c_{AB}(z) = \frac{A}{(z - z_0)^\gamma} \quad (25)$$

We use implementation of the nonlinear least-squares Marquardt-Levenberg algorithm as embedded in gnuplot plotting package [8].The results of the fit are:

$$\begin{aligned} A &= 0.440984 \pm 0.001349(0.3058\%) \\ z_0 &= -0.697827 \pm 0.002913(0.4174\%) \\ \gamma &= 0.879757 \pm 0.001251(0.1422\%) \end{aligned} \quad (26)$$

where the values and standard deviations are taken "as is" from the gnuplot software. They are pretty sensitve to the initial guess of the parameters and the assumed data ranges so that the range of plausible obtaned values for γ is 0.88-0.92. From the Toussaints-Wilczek approach we expect $\gamma = frac\mu + s2$. Here $s = 0$ and here we have to assume $\mu = 2$ to obtain the nearest integer value of $\gamma = 1$. We will see that this assumption seems to work in higher dimensions even if it is hard now to give a meaning to K^2 in 0 dimension. Let us see the results for $s = 1$ in 2D system in Figure 3. The set of fitted parameters is:

$$\begin{aligned} A &= 0.898733 \pm 0.002726(0.3033\%) \\ z_0 &= -1.31978 \pm 0.00235(0.1781\%) \\ \gamma &= 1.50609 \pm 0.001485(0.09863\%) \end{aligned} \quad (27)$$

Now for $\gamma = \frac{\mu+s}{2} = \frac{3}{2}$ if $\mu = 2$ well matches result of the fit. The range of plausible values based on initial fit parameter values and changing the range of data is $\gamma = 1.48 - 1.51$. It follows that the exponent can be slightly lower but generally the tendency to have Coulomb like K^{-2} correlation at the initial plane dominates. Finally let us inspect 3D simulation, where we should find $\gamma = 2$. The data are presented in Figure 4. The fitted parameters are

$$\begin{aligned} A &= 179706 \pm 364.2(0.2026\%) \\ z_0 &= -1.60451 \pm 0.002067(0.1288\%) \\ \gamma &= 1.98246 \pm 0.000725(0.03657\%) \end{aligned} \quad (28)$$

Again this is slightly lower but rather close to the expected value $\gamma = 2$ for $\mu = s = 2$ in three dimension. Manipulating data ranges has much less influence than in the previous cases and we estimate the variation of $\gamma = 1.98 - 1.99$.

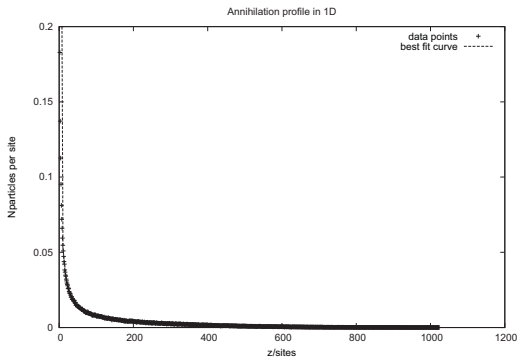

Fig. 1

4.1 Conclusion

We have presented simulation data on the profile of mutually annihilating particles produced at random at a wall and decaying with a power law away from the wall. The decay is much slower, $\gamma \approx 1$ and $\gamma \approx 1.5$ in 1 and 2 D sytems than predicted by classical kinetics $\gamma = 2$ and found

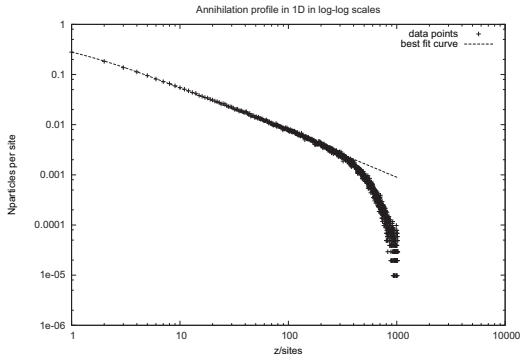

Fig. 2

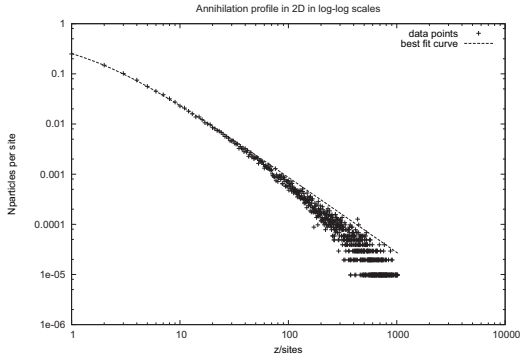

Fig. 3

in simulations for 3D system $\gamma = 2 \approx 1.98$. This is in line with the Toussaint and Wilczek based approach here applied to stationary profile in spacial coordinate rather than time. It seems that stationary regime is dominateded by a critical K^2 type concentration fluctuation of the species at their production plane. Surprisingly this is also true in 0 dimension. These systems are likely to display segregation already observed in anomalous fluctuation governed kinetics in 1 and 2 dimension for initially spatially homogeneous sytems [9]. The search for this kind of phenomena motivates our present and future work on inhomogeneous stationary systems of annihilating A and B species.

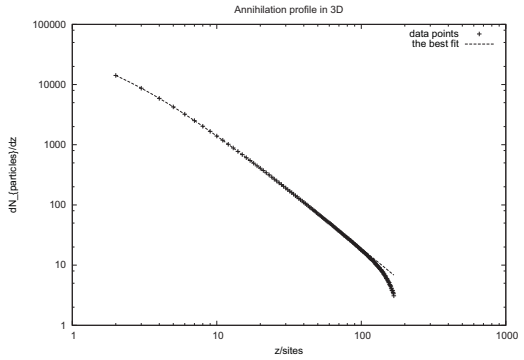

Fig. 4

References

[1] Ya.B. Zeldovich and M.Yu. Khlopov,“ On the concentration of relic magnetic monopoles in the universe”, Physics Letters B, vol. 79, issue 3, pp. 239-241 Nov. 1978.

[2] D.A. Benson, D. Bolster and A. Paster, “A full solution of the annihilation reaction A + B based on timesubordination”,The Journal of Chemical Physics, vol. 138,issue 7, pp.131101:1-4, Apr. 1983.

[3] A.A. Ovchinnikov and Ya.B. Zeldovich, “Role of density fluctuations in bimolecular reaction kinetics”, Chemical Physics vol. 28, issues 1âĂŞ2, Feb. 1978.

[4] D. Toussaint and F. Wilczek,“ParticleâĂŞantiparticle annihilation in diffusive motion”, The Journal of Chemical Physics, vol. 78, issue 5, pp. 2642-2647, Mar. 1983.

[5] C. Vautrin-Ul, A. Chausseé, J. Stafiej and J.P. Badiali, “Simulation of Corrosion Processes with spontaneous separation of cathodic and anodic reaction zones”, Polish Journal of Chemistry, vol. 78, issue 9, pp. 1795-1810., Sep. 2004.

[6] Ł. Bartosik, J. Stafiej and D. di Caprio,“3D simulations of ordered nanopore growth in alumina”, Electrochimica Acta, vol. 188, pp. 218âĂŞ221, Jan. 2016.

[7] O. Bandman, “Coarse-Grained Parallelization of Cellular-Automata Simulation Algorithms”, Lecture Notes in Computer Science, vol. 4671, pp. 371-384, Sep. 2007.

[8] Gnuplot tutorial #2, Physics 209, http://www.phas.ubc.ca/ phys209/files/gnuplot_tutorial2.pdf.

[9] P. Argyrakis, R. Kopelman and K. Lindenberg, “Diffusion limited A+B=0 reactions: The hierarchy of non-classical regimes for random initial conditions”, Chemical Physics, vol. 177, issue 3, pp. 693-707, Dec. 1993.

Final Updated DSP Filter Calculation for a Digital Doppler Velocity Flow Meter

Daniel L. Garcia
Kennesaw State University
1100 S. Marietta Parkway
Marietta, GA 30060-2896, USA
678-925-9672
dgarci38@students.kennesaw.edu

Daren R. Wilcox
Kennesaw State University
1100 South Marietta Parkway
Marietta, Georgia 30060-2896, USA
678-915-7269
dwilcox@spsu.edu

Introduction

The goal of this article is to provide the final results for the proof of concept that digital signal processing has progressed to the point of equivalence to traditional analog Doppler flow meter designs. This article is a continuation of articles CSC3521 [1] and CSC3102 [2] published previously at this conference. The goal of this article is to show the final peripheral schematic, some of the key software code, and the final testing results from the microcontroller calculating the same test data.

Categories and Subject Descriptor

Proof of Concept for a Digital Ultrasonic Doppler Liquid Velocity Flow Meter Updated

General Terms

Digital Ultrasonic Doppler Liquid Velocity Flow Meter

Keywords

Doppler Liquid Flow Meter, Doppler Effect, Liquid Doppler Effect Formula

Background

The ability to read the speed of liquids flowing through a pipe without breaking the pipe wall is extremely coveted. Using the Doppler Effect, a close approximation (typically within 2%) can be calculated depending upon some simple prerequisites which can be found in the original article CSC3521 [1].

The following publication in the series formulated an equation for the conversion from the Doppler shift frequency to meters per second(MPS). The final equation is given below:

$$V_{mps} = \frac{medium\ SS_{mps} * \Delta f}{(f_0 - \Delta f) * \cos \emptyset°}$$

where:

- Medium SS=sound speed of the liquid in mps
- Δf=the delta frequency shift in Hz
- f_0=the transmission frequency in Hz
- Ø°=the angle of the crystals.

In that same paper, an addition $1/f^3$ filter was included to give added accuracy in the lower frequency region (less than 60Hz down to approximately 30Hz).

$$\frac{1}{(\max \text{Frequency})^3}$$ [3].

According to Dr. Theodore Grosch, Dr. Wojciech Klimkiewicz, Dr. Peter Moosbrugger, and Dr. Lynn Carpenter [3], this filter will approximate the naturally occurring noise in the low frequency region and thereby flatten out the increasing amplitude noise created by the carrier signal near the low end frequencies.

The goals of this publication is to present the hardware used in the final

experiment, to review some of the key software code used in the microcontroller, and to compare the microcontroller's results with MATLab's [4] results for the same data. This comparison will reveal that the microcontroller is calculating similar results to MATLab [4] in near real time (about 1 second delayed).

Hardware Schematic

The goal of this preliminary prototype design was to have a minimal amount of analog hardware filters. As a result, only second order analog op-amp filters were used. Below is the peripheral components hardware schematic:

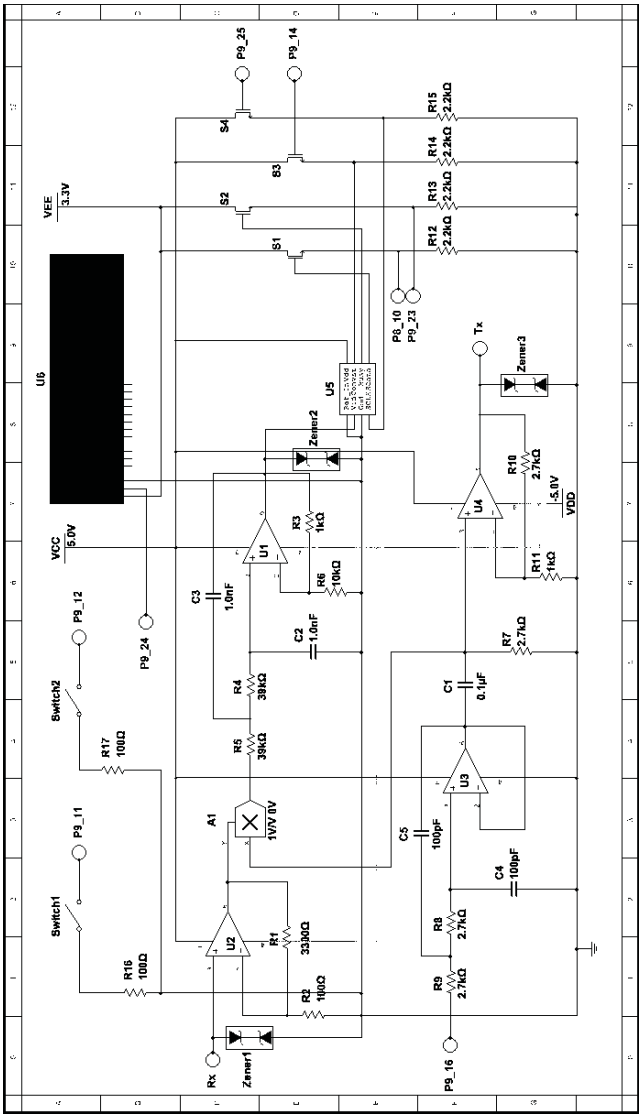

Each of the circular icons indicates a connection to either the microcontroller pins or the external transducers (which makes contact with the pipe).

Key C/C++ Code

The code which makes this version of a noninvasive Doppler velocity meter possible is the Fast Fourier Transform (FFT) which was derived from the book, "*Numerical Recipes in C publication - Second Edition - (Cambridge University Press)* [5]." (The full code used with modifications can be seen under the Appendix section of this article). The goal of this code is to convert the sampled data into the Frequency-Domain.

Next, a separate function then detects which frequency has the greatest amplitude and, finally, calculates the velocity using the formula determined in the last article (CSC3102) [2]. A full unmodified version of the code used can be requested from Southern Polytechnic State University Library in Marietta, Georgia. The title is "Results of Research and Development of Digital Signal Processing Filters and Doppler Calculations for a Non-Invasive Liquid Velocity Flow Meter," Prepared by Daniel L. Garcia and supervised by Professor Wilcox.

Micro Controller Results (Plots and Graphs)

The final testing step was to determine if the functions and hardware created/modified would return similar results to the originally recorded testing values. (The original data was recorded from approximately 20 seconds of audio samples at each frequency. Thus, a random start location for the sampled data was taken and stored into the microcontroller at a length of 4096 data points, and then ran

through the code.) The results from the microcontroller test were then re-written back into MATLab and graphed. The copied data was also stored into MATLab and ran through MATLab's FFT as a comparison. This was also graphed. Finally, the original complete sample recording was FFT and graphed. The following are the results of each test displayed side by side in order to accomplish a graphical comparison:

- 4.6fps Test 1 Data Comparison:

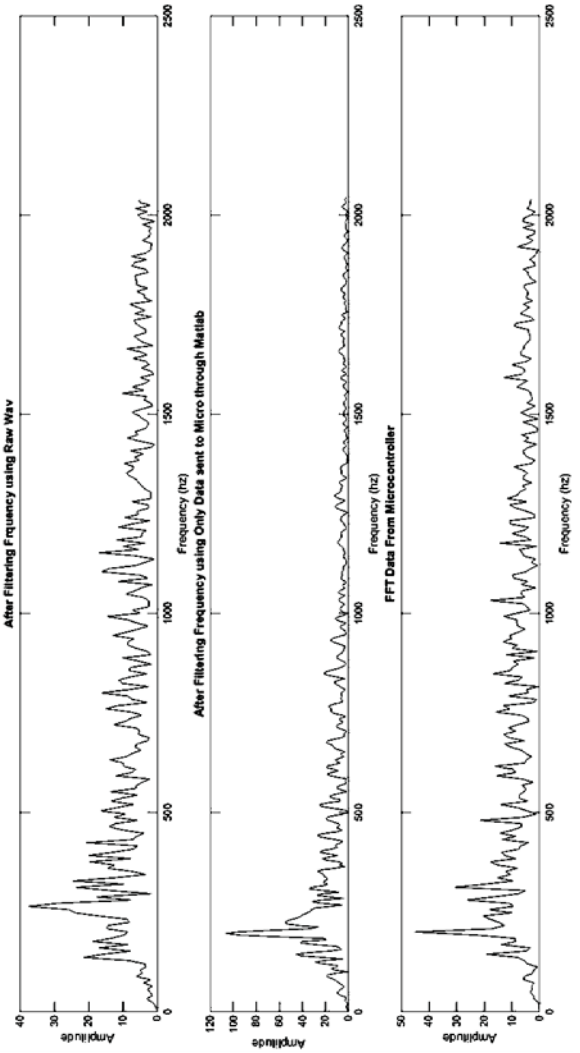

- 5.5fps Test 1 Data Comparison:

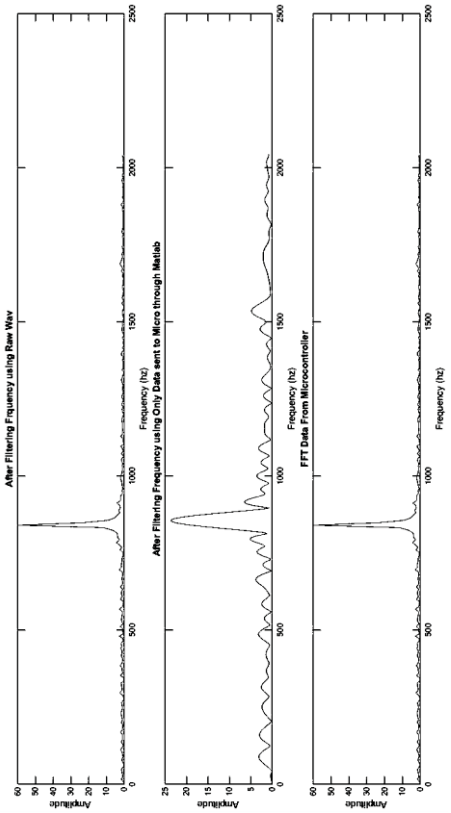

- 1.15fps Test 1 Data Comparison:

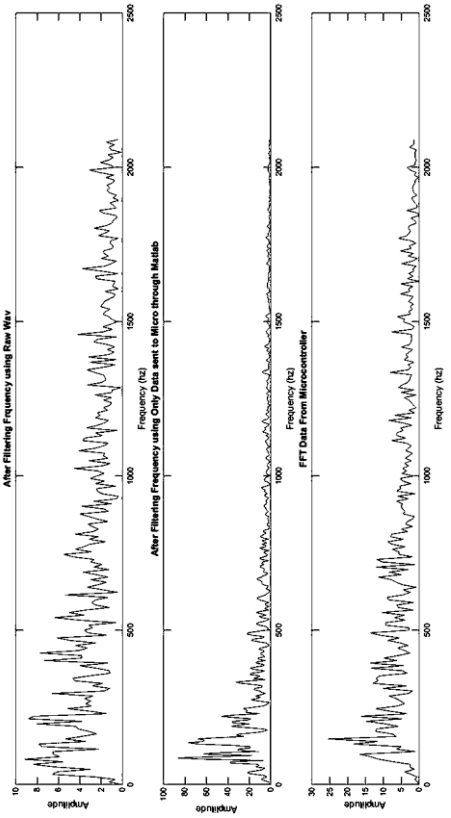

- 6.5fps Test 1 Data Comparison:

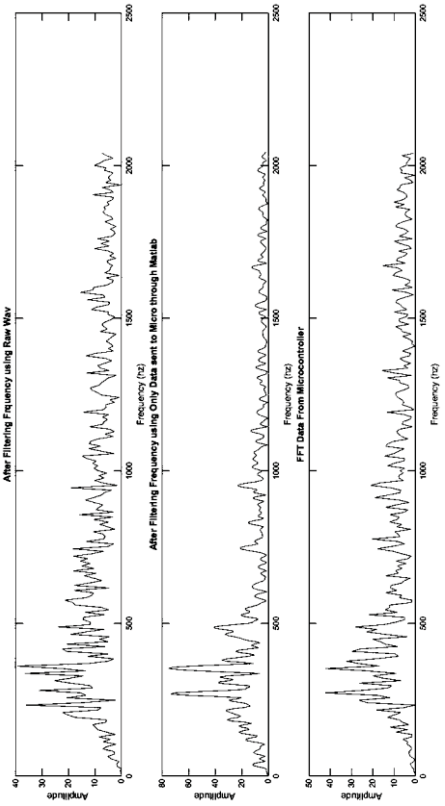

- 7fps Test 1 Data Comparison:

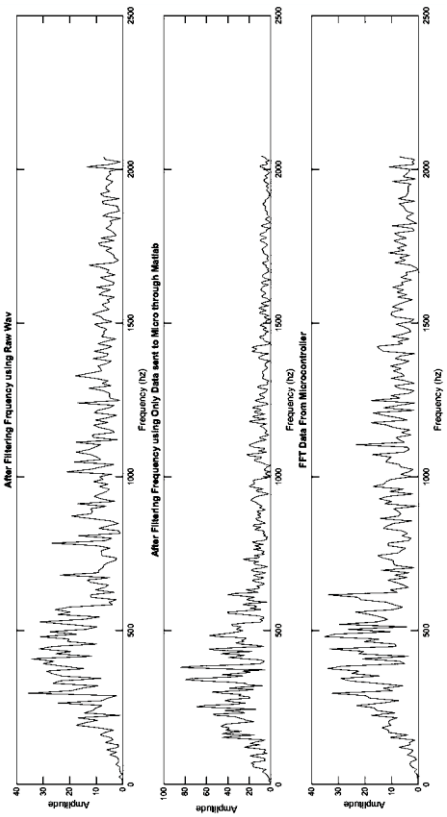

- 8fps Test 1 Data Comparison:

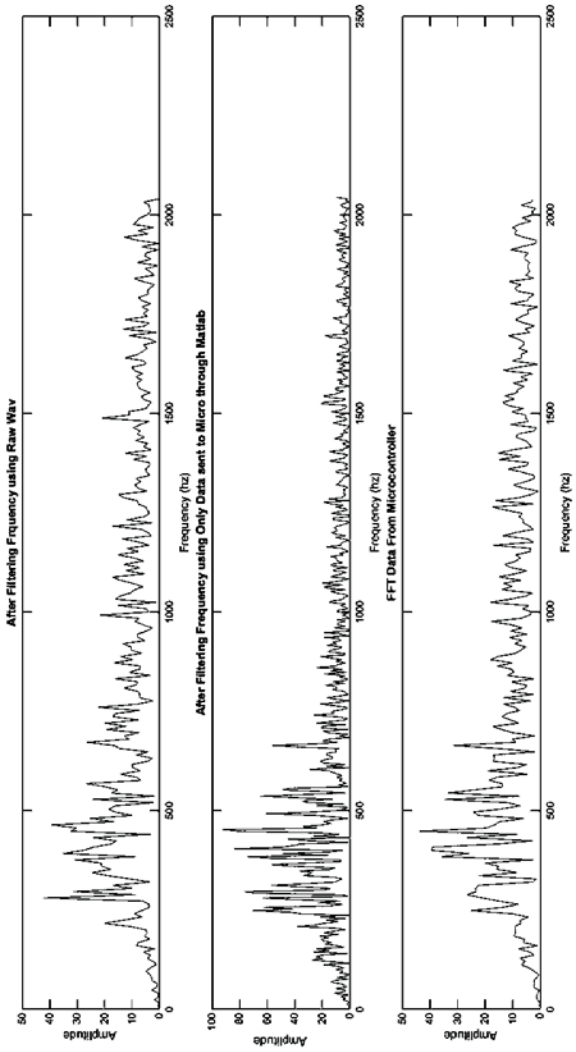

All results are similar in overall appearance and peak locations. There are some noticeable variations with the original data. This is primarily because of how MATLab calculates its FFT using short time processing when the sample size is smaller or larger than the conversion size. The micro-controller's version of the FFT does not calculate the FFT using this feature.

Conclusion

The theory that microcontrollers have progressed to the point that the liquid velocity could be calculated in near real-time with a

minimal of hardware/analog components has been proven to my satisfaction. Data recordings of the high frequency Doppler shift converted down to the low frequency range through an analog multiplier circuit (similar to AM radio systems), then processed to the frequency-domain through the microcontroller reveal similar results to MATLab's analysis of the same data. An estimated time of conversion is about one second for the capturing of the data samples and less than a quarter of a second for the conversion process to the calculation of velocity in mps. The total time for the acquisition, conversion, calculation and, ultimately, displaying the results on the LCD screen should take less than approximately 1.5 seconds. The conclusion is that a near real-time system is possible with a minimal of hardware/analog components.

Appendix

MATLab Code Sample [4]

```
NameOfFile=['APPROX 2FPS.WAV'];
[y,fs,nBits]=wavread(NameOfFile);

Lfft=2048;

Nth=10;
Hpth=3;
wl=2500/fs;

%create Butterworth low pass filter
[numl, denl]=butter(Nth,wl,'low');
[irl, time]=impz(numl,denl,Lfft);

%create 1/max^3 high pass filter
[numh, denh]= butter(HPth,wl^3,'high');
[irh, time]=impz(numh,denh,Lfft);

%convoluting filter w/ signal in
%frequency-domain
Y=abs( fft( y, Lfft ));
IRl=fft( irl, Lfft);
IRh=fft( irh, Lfft);

YC=Y.*IRh;
YC=IRl.*YC;
```

FFT() Function from Numerical Recipes [5]

```
void fft(double data[], int nn, int isign)
{
    int n, mmax, m, j, istep, i;
    double wtemp, wr, wpr, wpi, wi, theta;
    double tempr, tempi;

    n = nn << 1;
    j = 1;
    for (i = 1; i < n; i += 2)
    {
       if (j > i)
       {
              tempr     =  data[j];
              data[j]   =  data[i];
              data[i]   =  tempr;
              tempr     =  data[j+1];
              data[j+1] =  data[i+1];
              data[i+1] =  tempr;
       }
```

```
        m = n >> 1;
        while (m >= 2 && j > m)
        {
               j -= m;
               m >>= 1;
        }
        j += m;
     }

     mmax = 2;
     while (n > mmax)
     {
        istep = 2*mmax;
        theta = TWOPI/(isign*mmax);
        wtemp = sin(0.5*theta);
        wpr = -2.0*wtemp*wtemp;
        wpi = sin(theta);
        wr = 1.0;
        wi = 0.0;

        for (m=1; m<mmax; m+= 2)
        {
               for (i=m;i<=n;i+=istep)
               {
j =i + mmax;
tempr = wr*data[j] - wi*data[j+1];
tempi = wr*data[j+1] + wi*data[j];
data[j] = data[i] - tempr;
data[j+1] = data[i+1] - tempi;
data[i] += tempr;
data[i+1] += tempi;
               }
wr = (wtemp = wr)*wpr - wi*wpi + wr;
wi = wi*wpr + wtemp*wpi + wi;
        }
        mmax = istep;
     }
}[5]
```

References and Citations

[1] Garcia, Daniel L. and Wilcox, Daren R. (2014, July) DSP Filter Calculation for a Digital Doppler Velocity Flow Meter. (CSC3521). *Las Vegas Nevada, USA: CSREA Press*, 21 July, 2014, ISBN: 1-60132-266-6.

[2] Garcia, Daniel L. and Wilcox, Daren R. (2016, July) DSP Filter Calculation for a Digital Doppler Velocity Flow Meter. (CSC3102). *Las Vegas Nevada, USA: CSREA Press*, 25 July, 2016.

[3] Theodore Grosch, Wojciech Klimkiewicz, Peter Moosbrugger, and Lynn Carpenter, "A 24 GHz FM/CW automotive radar designed for collision warning," *SPIE International Symposium on Photonic Sensors and Controls for Commercial Applications*, 13 October- 4 November 1994, Boston MA.

[4] MATLab, 2016, http://www.mathworks.com, Copyright © 1994-2016 The MathWorks, Inc. Reprinted with Permission.

[5] Press, William H.; Teukolsky, Saul A.; Vetterling, William T.; Flannery, Brian P. (1986). Numerical Recipes: The Art of Scientific Computing. New York: Cambridge University Press. p. xi. ISBN: 0-521-30811-9. [Retrieved on August 18th, 2015] Retrieved from http://apps.nrbook.com/c/index.html

Unsolved Problems in Computational Science: II Computation in Pattern Avoidance of Lattice Paths

Shanzhen Gao, Keh-Hsun Chen
Department of Computer Science, College of Computing and Informatics
University of North Carolina at Charlotte, Charlotte, NC 28223, USA
Email: sgao3@uncc.edu, chen@uncc.edu

***Abstract*—In our "Unsolved Problems in Computational Science", we will talk about some interesting open problems in computational science. These problems are related to number theory, geometry theory, combinatorics, graph theory, linear algebra and group theory. They are easy to state and understand although they are very difficult to be solved by researchers in mathematics or computer science. It seems to us that it is very challenging to find suitable mathematical methods or efficient algorithms to deal with them.**

In this paper, we will discuss some enumerative problems on pattern avoidance in lattice paths. And many closed formulas, integer sequences, generating functions, and open problems are posted.

Keywords: Lattice path, pattern avoidance, generating function, closed formula, integer sequence

I. Introduction, Notations and Preliminaries

Notations:

East step: E or $\rightarrow$ or $(1,0)$, or x-step

You can see more in the table below:

$(0,1)$	$(1,0)$	$(1,1)$	$(0,-1)$
$\uparrow$	$\rightarrow$	$\nearrow$	$\downarrow$
N	E	NE	S

$(-1,0)$	$(-1,-1)$	$(-1,1)$	$(1,-1)$
$\leftarrow$	$\swarrow$	$\nwarrow$	$\searrow$
W	SW	NW	SE

$\uparrow^{\geq k}$: k or more consecutive $\uparrow$ steps

$\uparrow^{=k}$: k consecutive $\uparrow$ steps

avoiding $\uparrow^{\geq k}$: no k or more than k consecutive $\uparrow$ steps

avoiding $\uparrow^{=k}$: no k consecutive $\uparrow$ steps, but can have more than or less than k consecutive $\uparrow$ steps

$\lfloor x \rfloor$: the largest integer not greater than x, $floor(x)$

$\lceil x \rceil$: is the smallest integer not less than x, $ceiling(x)$

$[x^n]f(x)$ denotes the coefficient of x^n in the power series expansion of a function $f(x)$.

$[x^m y^n]f(x,y)$ denotes the coefficient of $x^m y^n$ in the power series expansion of a function $f(x,y)$.

$\binom{n}{r}$, the number of combinations of n things r at a time.

$$\binom{n}{r} = \frac{n!}{(n-r)!r!} = \binom{n}{n-r} = \binom{n-1}{r-1} + \binom{n-1}{r}$$

$$\binom{-n}{r} = (-1)^r \binom{n+r-1}{r}$$

A lattice path [8] is a path from the lattice point (x_1, y_1) to the lattice point (x_2, y_2), $x_1 \leq x_2$, $y_1 \leq y_2$, we mean a directed path from (x_1, y_1) to (x_2, y_2) which passes through lattice points with movements parallel to the positive direction of either axis. Here, we refer to two types steps, $x-$steps and $y-$steps, where an x (y)$-$step is a directed line segment parallel to the x (y) axis going right (up) joining two neighboring points. For counting purposes we may, without loss of generality, consider lattice paths from the origin to (m,n) and observe that each such path is characterized by having exactly m horizontal steps and n vertical steps. If we denote by $f(m,n)$ the number of paths from $(0,0)$ to (m,n), elementary reasoning gives the results

$$f(m,n) = \binom{m+n}{n}.$$

Lattice paths are encountered in a natural way in various problems, e.g., ballot problems [7], compositions, random walks, fluctuations, queues, and the tennis ball problem.

The number of lattice paths from the origin to (m,n), $m > n+t$, not touching the line $x = y+t$, where t is a nonzero integer satisfies [5]

$$\binom{m+n}{n} - \binom{m+n}{m-t}.$$

The number of lattice paths of length n starting from the origin that are below the line $y = x+t$, where t is a positive integer satisfies

$$\sum_{i=\max\{\lfloor 1+n/2 \rfloor, t\}}^{n} \left(\binom{n}{n-i} - \binom{n}{i+t}\right).$$

When $t = 0$, the paths have to touch the line $x = y$ at the origin, and therefore the number paths from the origin to (m,n) that do not touch the line $x = y$ except at the origin is given by

$$\frac{m-n}{m+n}\binom{m+n}{n}.$$

The number of lattice paths of length n starting from the origin that are below the line $x = y$ except at the origin is given by

$$\sum_{i=\lfloor 1+n/2 \rfloor}^{n} \frac{2i-n}{n}\binom{n}{n-i}.$$

The number of lattice paths from (r, s) to (m, n) that never rise above the line $y = x$ is [1]

$$\binom{n+m-r-s}{m-r} - \binom{n+m-r-s}{m-s+1}.$$

Then the number of lattice paths from $(0, 0)$ to (m, n) that never rise above the line $y = x$ is

$$\binom{n+m}{m} - \binom{n+m}{m+1}.$$

The number of n-step lattice paths starting from $(0, 0)$ that never rise above the line $y = x$ is

$$\sum_{i=\lceil n/2 \rceil}^{n} \frac{n!(2i+1-n)}{(i+1)!(n-i)!} = \binom{n}{\lfloor n/2 \rfloor}.$$

The number of paths from $(0, 0)$ to (n, n) that never rise above the line $y = x$ is the m-th Catalan number, denoted by C_n, and define $C_0 = 1$.

$$\begin{aligned} C_n &= \frac{1}{n+1}\binom{2n}{n} \\ &= \binom{2n}{n} - \binom{2n}{n+1} \\ &= \sum_{i=0}^{n} \binom{n}{i}^2 \end{aligned}$$

with generating function

$$\frac{1-\sqrt{1-4x}}{2x}.$$

Also,

$$\begin{aligned} C_{n+1} &= \sum_{i=0}^{n} C_i C_{n-1} \\ &= \frac{2(2n+1)}{n+2} C_n. \end{aligned}$$

The follow table is the number of lattice path from $(0, 0)$ to (m, n) and weakly above the line $y = x$:

$n = 8$	1	8	35	110	275	572
$n = 7$	1	7	27	75	165	297
$n = 6$	1	6	20	48	90	132
$n = 5$	1	5	14	28	42	42
$n = 4$	1	4	9	14	14	
$n = 3$	1	3	5	5		
$n = 2$	1	2	2			
$n = 1$	1	1				
$n = 0$	1					
	$m = 0$	$m = 1$	$m = 2$	$m = 3$	$m = 4$	$m = 5$

The numbers on the diagonal are the Catalan numbers.

We can see that the sum of the numbers on the n-th slope -1 line is $\binom{n}{\lceil n/2 \rceil}$:

$$1, 2, 3, 6, 10, 20, 35, 70, 126, 252, 462, ...$$

It is the number of n-step lattice paths starting from $(0, 0)$ that never rise above the line $y = x$.

The number of ways of putting n like objects into r different cells is [10]

$$\binom{n+r-1}{n} = \binom{n+r-1}{r-1}.$$

It is also the number of nonnegative integer solutions to the equation

$$\sum_{i=1}^{r} x_i = n.$$

The above number also equals

$$\begin{aligned} &[x^n](1 + x + x^2 + x^3 + ...)^r \\ &= [x^n](\frac{1}{1-x})^r \\ &= [x^n](1-x)^{-r} \\ &= [x^n]\sum_{i\geq 0}\binom{-r}{i}(-1)^i x^i \\ &= [x^n]\sum_{i\geq 0}(-1)^i\binom{i+r-1}{i}(-1)^i x^i \\ &= \binom{n+r-1}{n}. \end{aligned}$$

The number of ways of putting n like objects into r different cells with no cell is empty is

$$\binom{n-1}{r-1}.$$

It is also the the number of positive integer solutions to the equation

$$\sum_{i=1}^{r} x_i = n.$$

The above number also equals

$$\begin{aligned} &[x^n](x + x^2 + x^3 + ...)^r \\ &= [x^n](\frac{x}{1-x})^r \\ &= [x^n]x^r(1-x)^{-r} \\ &= [x^{n-r}]\sum_{i\geq 0}\binom{-r}{i}(-1)^i x^i \\ &= [x^{n-r}]\sum_{i\geq 0}(-1)^i\binom{i+r-1}{i}(-1)^i x^i \\ &= \binom{n-1}{n-r} = \binom{n-1}{r-1}. \end{aligned}$$

If p is a prime, then $\binom{p}{i}$ is divisible by p for $1 \leq i \leq p-1$.

Fibonacci number: F_n is defined as $F_0 = 0$, $F_1 = 1$, $F_n = F_{n-2} + F_{n-1}$ for $n \geq 2$. The generating function is

$$\frac{1}{1-x-x^2}.$$

Definition 1. *A B-Sheffer sequence is a sequence of polynomials $(p_i)_{i\in\mathbb{N}_0}$ such that $\deg p_i = i$, $Bp_i = p_{i-1}$, and $p_0 \neq 0$,*

associated with an operator B that can be written as a power series of order 1 in the derivative operator, $\mathcal{D}$. If a B-Sheffer sequence has the initial value $p_n(0) = \delta_{0,n}$, then it is a B-basic sequence. [9]

II. Main Results

Theorem 2. *The number of lattice paths avoiding $\uparrow^{\geq 2}$, from $(0,0)$ to (m,n) is*

$$\binom{m+1}{n}.$$

Proof: The m East steps provide $m+1$ positions (we can say $m+1$ different cells) for n North steps to be inserted with each cell containing at most one element (North step). Then there are $\binom{m+1}{n}$ ways to choose n cells. ■

Corollary 3. *The number of lattice paths from $(0,0)$ to $(ns+1, nt-1)$, avoiding $\uparrow^{\geq 2}$is*

$$\binom{ns+2}{nt-1}.$$

Corollary 4. *The number of n-step paths with east and north steps and with two consecutive north steps forbidden is equal to*

$$\sum_{i=0}^{\lceil n/2 \rceil} \binom{n+1-i}{i} = F_{n+2}.$$

Theorem 5. *The number of lattice paths from $(0,0)$ to (m,n) avoiding $\uparrow^{\geq 3}$is*

$$\sum_{i=0}^{\lfloor n/2 \rfloor} \binom{m+1}{n-i}\binom{n-i}{i}.$$

Proof: Without loss of generality, we assume that there are i copies of double North Steps, $n-2i$ copies of single North step in a lattice path from $(0,0)$ to (m,n) and avoiding $\uparrow^{\geq 3}$. It is clear that $0 \leq i \leq \lfloor n/2 \rfloor$. The m East steps provide $m+1$ positions (we can say $m+1$ different cells) for n North steps to be inserted with each cell containing at most one element ($\uparrow$ or $\uparrow^2$). There are $\binom{m+1}{n-i}$ ways to choose n cells for the i copies $\uparrow^2$ and $n-2i$ copies of $\uparrow$. We have $\binom{n-i}{i}$ ways to distribute the i copies $\uparrow^2$. ■

Corollary 6. *The number of lattice paths of length l, starting from $(0,0)$, avoiding $\uparrow^{\geq 3}$is*

$$\sum_{n=0}^{\lfloor 2(l+1)/3 \rfloor} \sum_{i=0}^{\lfloor n/2 \rfloor} \binom{l-n+1}{n-i}\binom{n-i}{i}.$$

Corollary 7. *The number of lattice paths from $(0,0)$ to $(ns+1, nt-1)$ avoiding $\uparrow^{\geq 3}$is*

$$\sum_{i=0}^{\lfloor (nt-1)/2 \rfloor} \binom{ns+2}{nt-1-i}\binom{nt-1-i}{i}.$$

Theorem 8. *Let $f(m,n)$ be the number of lattice paths from $(0,0)$ to (m,n) avoiding $\uparrow^{\geq k}$ and $\longrightarrow^{\geq k}$, taking steps from $\{\uparrow, \longrightarrow\}$. Then*

$$f(m,n) = f(m-1,n) + f(m,n-1) - f(m-k,n-1) - f(m-1,n-k) + f(m-k,n-k).$$

Theorem 9. *The number of lattice paths from $(0,0)$ to (m,n) avoiding $\uparrow^{\geq 2}$ and $\rightarrow^{\geq 3}$is*

$$\binom{n+1}{m-n-1} + 2\binom{n}{m-n} + \binom{n-1}{m-n+1}.$$

Corollary 10. *The number , say $f(n)$, of lattice paths of length l, starting from $(0,0)$, avoiding $\uparrow^{\geq 2}$ and $\rightarrow^{\geq 3}$is*

$$\sum_{m=\lceil (l+1)/2 \rceil}^{\lfloor 2(l+1)/3 \rfloor} \binom{l-m+1}{2m-l-1} + 2\sum_{m=\lceil l/2 \rceil}^{\lfloor 2l/3 \rfloor} \binom{l-m}{2m-l} + \sum_{m=\lceil (l-1)/2 \rceil}^{\lfloor 2(l-1)/3 \rfloor} \binom{l-m-1}{2m-l+1}).$$

$$f(n) = f(n-2) + f(n-3)$$
$$f(1) = 2,\ f(2) = 3,\ f(3) = 4.$$

The generating function is

$$\frac{1+2x+2x^2+x^3}{1-x^2-x^3}.$$

Theorem 11. *The generating function of the number of lattice paths from $(0,0)$ to (m,n) avoiding $\uparrow^{\geq i}$, $\rightarrow^{\geq j}$satisfies*

$$[x^m y^n] \frac{(\sum_{k=1}^{i} x^{k-1})(\sum_{k=1}^{j} y^{k-1})}{1-(\sum_{k=2}^{i} x^{k-1})(\sum_{k=2}^{j} y^{k-1})}.$$

Proof: Let $P(x,y)$ be the generating function of the number of lattice paths from $(0,0)$ to (m,n) avoiding $\uparrow^{\geq i}, \rightarrow^{\geq j}$.

$$P(x,y) = \sum_{s\geq 0}\sum_{t\geq 0} p(m,n)x^m y^n.$$

Case 1. The contribution of paths starting with s East steps and followed by t North steps ($0 \leq s \leq i-1$, $0 \leq t \leq j-1$) is

$$x^s y^t.$$

The total contribution for all possible s and t is

$$\left(1+x+x^2+...+x^{i-1}\right)\left(1+y+y^2+...+y^{j-1}\right) = (\sum_{k=1}^{i} x^{k-1})(\sum_{k=1}^{j} y^{k-1}).$$

Case 2. For the walks obtained by concatenating a path, u (for possible u) North steps, and then v ($1 \leq v \leq i-1$) East steps, the contribution is

$$y^u x^v P(x,y).$$

The total contribution for all possible u and v is

$$(y+y^2+...+y^{j-1})(x+x^2+...x^{i-1})P(x,y)$$
$$=(\sum_{k=2}^{i}x^{k-1})(\sum_{k=2}^{j}y^{k-1})P(x,y).$$

Adding these two contributions give the equation

$$P(x,y)=(\sum_{k=1}^{i}x^{k-1})(\sum_{k=1}^{j}y^{k-1})+(\sum_{k=2}^{i}x^{k-1})(\sum_{k=2}^{j}y^{k-1})P(x,y).$$

Therefore,

$$P(x,y)=\frac{(\sum_{k=1}^{i}x^{k-1})(\sum_{k=1}^{j}y^{k-1})}{1-(\sum_{k=2}^{i}x^{k-1})(\sum_{k=2}^{j}y^{k-1})}.$$

■

Theorem 12. *The number, say $f(m,n)$, of lattice paths from $(0,0)$ to (m,n) avoiding $\uparrow^{\geq 3}$and $\rightarrow^{\geq 3}$is*

$$2\sum_{i=m-n}^{\lfloor m/2\rfloor}\binom{m-i}{i}\binom{m-i}{n-m+i}$$
$$+\sum_{i=m-n-1}^{\lfloor m/2\rfloor}\binom{m-i}{i}\binom{m-i-1}{n-m+i+1}$$
$$+\sum_{i=m-n+1}^{\lfloor m/2\rfloor}\binom{m-i}{i}\binom{m-i+1}{n-m+i-1}.$$

The generating function of the above numbers is

$$\frac{\left(1+x+x^2\right)\left(1+y+y^2\right)}{1-xy(1+x+y+xy)}.$$

Also, for $m\geq n$,

$$f(m,n)=2\sum_{r=\lceil m/2\rceil}^{n}\binom{r}{m-r}\binom{r}{n-r}$$
$$+\sum_{r=\max\{\lceil (m-2)/2\rceil,\lceil n/2\rceil\}}^{\min\{m-1,n\}}\binom{r+1}{m-r-1}\binom{r}{n-r}$$
$$+\sum_{r=\lceil m/2\rceil}^{n-1}\binom{r}{m-r}\binom{r+1}{n-r-1}.$$

Example:

$$[x^my^n](\frac{\left(1+x+x^2\right)\left(1+y+y^2\right)}{1-xy(1+x+y+xy)})$$

counts the number of lattice paths from $(0,0)$ to (m,n) avoiding $\uparrow^{\geq 3}$and $\rightarrow^{\geq 3}$.

Proof: Now we prove the second formula of $f(m,n)$. We define a level-stretch (up-stretch), one or some unextendable continues level (north) steps.

Case 1. If there are r level stretches and r up stretches in a walk, then

$$\lceil m/2\rceil\leq r\leq n.$$

The generating function of this case is

$$2\sum_{r=\lceil m/2\rceil}^{n}(x+x^2)^r(y+y^2)^r.$$

$$[x^my^n]2\sum_{r=\lceil m/2\rceil}^{n}(x+x^2)^r(y+y^2)^r$$
$$=2[x^my^n]\sum_{r=\lceil m/2\rceil}^{n}(\sum_{i=0}^{r}\binom{r}{i}x^{2i}x^{r-i})(\sum_{j=0}^{r}\binom{r}{j}x^{2j}x^{r-j})$$
$$=2[x^my^n]\sum_{r=\lceil m/2\rceil}^{n}(\sum_{i=0}^{r}\binom{r}{i}x^{r+i})(\sum_{j=0}^{r}\binom{r}{j}x^{r+j})$$
$$=2\sum_{r=\lceil m/2\rceil}^{n}\binom{r}{m-r}\binom{r}{n-r}.$$

Case 2. If there are $r+1$ level stretches and r up stretches in a walk, then

$$\max\{\lceil (m-2)/2\rceil,\lceil n/2\rceil\}\leq r\leq\min\{m-1,n\}.$$

The generating function for this case is

$$\sum_{r=\max\{\lceil (m-2)/2\rceil,\lceil n/2\rceil\}}^{\min\{m-1,n\}}(x+x^2)^{r+1}(y+y^2)^r.$$

$$[x^my^n]\sum_{r=\max\{\lceil (m-2)/2\rceil,\lceil n/2\rceil\}}^{\min\{m-1,n\}}(x+x^2)^{r+1}(y+y^2)^r$$
$$=\sum_{r=\max\{\lceil (m-2)/2\rceil,\lceil n/2\rceil\}}^{\min\{m-1,n\}}\binom{r+1}{m-r-1}\binom{r}{n-r}.$$

Case 3. If there are r level stretches and $r+1$ up stretches in a walk, then

$$\lceil m/2\rceil\leq r\leq n.$$

The generating function for this case is

$$\sum_{r=\lceil m/2\rceil}^{n-1}(x+x^2)^r(y+y^2)^{r+1}.$$

$$[x^my^n]\sum_{r=\lceil m/2\rceil}^{n-1}(x+x^2)^r(y+y^2)^{r+1}$$
$$=\sum_{r=\lceil m/2\rceil}^{n-1}\binom{r}{m-r}\binom{r+1}{n-r-1}.$$

■

Corollary 13. *The number of lattice paths from* $(0,0)$ *to* (n,n) *avoiding* $\uparrow^{\geq 3}$*and* $\rightarrow^{\geq 3}$*is*

$$2\sum_{i=0}^{\lfloor n/2\rfloor}\binom{n-i}{i}\binom{n-i}{i}+2\sum_{j=1}^{\lfloor \frac{n}{2}\rfloor}\binom{n-j}{j}\binom{n-j+1}{j-1}.$$

Theorem 14. *The generating function for the number of lattice paths from* $(0,0)$ *to* (n,n) *avoiding* $\uparrow^{\geq 3}$*and* $\rightarrow^{\geq 3}$*, is*

$$\frac{(1-t)^2\sqrt{(1+t+t^2)(1-3t+t^2)}-(1-3t+t^2)(1+t^2)}{t^2(1-3t+t^2)}$$
$$=2t+6t^2+14t^3+34t^4+84t^5+208t^6+518t^7+\ldots.$$

A proof in detail of this theorem involves Finite Operator Calculus [6].

Proof: Let $f(m,n)$ be the number of paths from $(0,0)$ to (n,n) avoiding $\uparrow^k$ and $\longrightarrow^k$,taking steps from $\{\uparrow,\longrightarrow\}$. Then

$$f(m,n)=f(m-1,n)+f(m,n-1)-f(m-k,n-1)$$
$$-f(m-1,n-k)+f(m-k,n-k).$$

Using Finite Operator Calculus it can be shown that the basic sequence for this recursion for $k=3$ has the generating function

$$\sum_{n\geq 0}b_n(x)=2^{-x}\left(1+t-\sqrt{(t+1)(4t^2+t+1)}\right)^x$$

The initial values determine a Sheffer sequence, whose generating function at $x=0$ is the generating function in the Theorem.

$$f_n(m)=f_n(m-1)+f_{n-1}(m)-f_{n-3}(m-1)$$
$$-f_{n-4}(m-3)+f_{n-6}(m-3)$$
$$\nabla=B-E^{-1}B^3-E^{-3}B^4+E^{-3}B^6$$
$$E=\frac{1}{2}+\frac{1}{2}B-\frac{1}{2}\sqrt{1+2B+5B^2+4B^3}$$
$$\sum_{n\geq 0}b_n(x)=2^{-x}\left(1+t-\sqrt{(t+1)(4t^2+t+1)}\right)^x$$
$$=\phi(t)^x$$
$$\phi_1(t)^x=\sum_{n\geq 0}x\frac{b_n(n+x)}{n+x}t^n$$

$$f_n(n+x)=f_n(n+x-1)+f_{n-1}(n-1+x+1)-\ldots$$
$$E^{-1}Bf_n(n+x)=f_{n-1}(n-1+x)$$

with $f_n(n-1)-f_{n-3}(n-2)=0$ for all $n\geq 5$.

Let $\bar{B}=E^{-1}B$. Then

$$s_n(m)=s_n(m-1)+s_{n-1}(m+1)-s_{n-3}(m+2)$$
$$-s_{n-4}(m+1)+s_{n-6}(m+3)$$
$$\nabla=E^1\bar{B}-E^2\bar{B}^3-E^1\bar{B}^4+E^3\bar{B}^6$$
$$E^{-1}\nabla=\bar{B}\nabla+\left(E^{-1}\bar{B}-\bar{B}^4\right)\left(1-E^2\bar{B}^2\right)$$
$$\nabla=E^1\bar{B}\left(E^{-1}-\bar{B}^3\right)\left(1+E^1\bar{B}\right)=\tau(B)$$

$f_n(n-1)-f_{n-3}(n-2)=0$ for all $n\geq 5$

$g_{n+3}(n)-g_n(n-1)$
$f_4(3)-f_1(2)=1;\ f_3(2)-f_0(1)=-1;$
$f_2(1)-f_{-1}(0)=0;$
$f_1(0)=-1;\ f_0(-1)=1$
$L\langle f_n(n+x)\rangle=f_n(n-1)-f_{n-3}(n-3+1)$
$=Eval_{-1}-Eval_1\left(E^{-1}B\right)^3$
$\Rightarrow op(L)=E^{-1}-E\bar{B}$
$s_n(x)=f_n(n+x)=\sum_{l=0}^{n}\langle L|f_{n-l}\rangle\, op(L)^{-1}\bar{b}_l(x)$
$=op(L)^{-1}\bar{b}_n(x)-op(L)^{-1}\bar{b}_{n-1}(x)-op(L)^{-1}\bar{b}_{n-3}(x)$
$+op(L)^{-1}\bar{b}_{n-5}(x)$
$s(x,t)=\left(\frac{1}{2t^3}\left(-t^2+1-t-\sqrt{(t^2-3t+1)(t^2+t+1)}\right)\right)^x$
$\times\left(1-t-t^3+t^4\right)/$
$\left(\frac{1}{2t^3}\begin{pmatrix}-t^2+1-t\\ -\sqrt{(t^2-3t+1)(t^2+t+1)}\end{pmatrix}\right)^{-1}$
$-t^3\left(\frac{1}{2t^3}\left(-t^2+1-t-\sqrt{(t^2-3t+1)(t^2+t+1)}\right)\right)$
$(s(0,t)-1-t^2)/t^2)$ is the generating function. ■

Corollary 15. *The number of lattice paths from* $(0,0)$ *to* $((ns+1),(nt-1))$ *avoiding* $\uparrow^{\geq 3}$*and* $\rightarrow^{\geq 3}$*is*

$$2\sum_{i=n(s-t)+2}^{\lfloor (ns+1)/2\rfloor}\binom{ns+1-i}{i}\binom{ns+1-i}{nt-1-m+i}$$
$$+\sum_{i=n(s-t)+1}^{\lfloor (ns+1)/2\rfloor}\binom{ns+1-i}{i}\binom{ns-i}{n(t-s)-1+i}$$
$$\sum_{i=n(s-t)+3}^{\lfloor (ns+1)/2\rfloor}\binom{ns+1-i}{i}\binom{ns+1-i+1}{n(t-s)-3+i}$$

Example 16. *For* $m\leq 7$ *and* $n\leq 8$*, the number, say* $f(m,n)$*, of lattice paths from* $(0,0)$ *to* (m,n) *avoiding* $\uparrow^{\geq 3}$*and* $\rightarrow^{\geq 3}$*is as follows:*

$n=8$				1	15	87
$n=7$				4	30	114
$n=6$			1	10	43	113
$n=5$			3	16	45	84
$n=4$		1	6	18	34	45
$n=3$		2	7	14	18	16
$n=2$	1	3	6	7	6	3
$n=1$	1	2	3	2	1	
$n=0$		1	1			
	$m=0$	$m=1$	$m=2$	$m=3$	$m=4$	$m=5$

$$f(m,n)=f(m-1,n)+f(m,n-1)-f(m-3,n-1)$$
$$-f(m-1,n-3)+f(m-3,n-3).$$

$$f(6,6)=f(5,6)+f(6,51)-f(3,5)$$
$$-f(5,3)+f(3,3)$$
$$=113+113-16-16+14$$
$$=208.$$

Theorem 17. *The number of lattice path from* $(0,0)$ *to* (m,n) *avoiding* $\uparrow^{\geq 4}, \rightarrow^{\geq 4}$*is*

$$2\sum_{i=0}^{\lfloor n/3\rfloor}\sum_{j=0}^{\lfloor (n-3i)/2\rfloor}\binom{n-2i-j}{i}\binom{n-3i-j}{j}$$
$$\sum_{s=0}^{\min\{\lfloor n/3\rfloor,\lfloor\frac{2i+j}{2}\rfloor\}}\binom{n-2i-j}{s}\binom{n-2i-j-s}{2i+j-2s}$$
$$+2\sum_{i=0}^{\lfloor n/3\rfloor}\sum_{j=0}^{\lfloor (n-3i)/2\rfloor}\binom{n-2i-j}{i}\binom{n-3i-j}{j}$$
$$\sum_{s=0}^{\min\{\lfloor n/3\rfloor,\lfloor\frac{2i+j+1}{2}\rfloor\}}\binom{n-2i-j-1}{s}\binom{n-2i-j-s-1}{2i+j+1-2s}.$$

The above number equals

$$[x^m y^n](\frac{(1+x+x^2+x^3)(1+y+y^2+y^3)}{1-xy(1+y+y^2)(1+x^2+x)}).$$

Theorem 18. *Given two positive integers* n *and* r *and let* $p(n,r)$ *be the number of vectors* $(x_1, x_2, ..., x_r)$*, such that*

$$n=\sum_{i=1}^{r}x_i$$

x_i *is positive integer for* $i=1,2,...,r$*. Then*

$$p(n,r)=\binom{n-1}{r-1}.$$

Proof:

$$\begin{aligned}&[x^n](x+x^2+x^3+...)^r\\&=[x^n]\,x^r(1-x)^{-r}\\&=[x^n]\,x^r\sum_{i\geq 0}\binom{i+r-1}{i}x^i\\&=\binom{n-1}{r-1}.\end{aligned}$$

Remember $\binom{-n}{k}=(-1)^k\binom{n+k-1}{k}$. ■

Theorem 19. *Given three positive integers* n*,* r *and* k *and let* $p(n,r,k)$ *be the number of vectors* $(x_1, x_2, ..., x_r)$*, such that*

$$n=\sum_{i=1}^{r}x_i$$

x_i *is positive integer, and* $1\leq x_i\leq k$ *for* $i=1,2,...,r$*. Then*

$$p(n,r,k)=\sum_{h=0}^{\min\{r,\lfloor\frac{n-1}{k}\rfloor\}}(-1)^h\binom{n-kh-1}{r-1}\binom{r}{h}.$$

Example:
$p(3,3,1)=p(3,3,2)=1$: $(1,1,1)$
$p(3,2,2)=2$: $(1,2)$ and $(2,1)$
$p(4,3,2)=3$: $(1,1,2)$, $(1,2,1)$ and $(2,1,1)$
$p(n,r,k)-p(n,r,n-1)\geq 0$ for $0<n\leq r(k+1)/2$.

Proof:

$$\begin{aligned}&[x^n](x+x^2+x^3+...+x^k)^r\\&=\left[x^{n-r}\right](1+x+x^2+...+x^{k-1})^r\\&=\left[x^{n-r}\right]\frac{(1-x^k)^r}{(1-x)^r}\\&=\left[x^{n-r}\right](1-x^k)^r(1-x)^{-r}\\&=\left[x^{n-r}\right](\sum_{h\geq 0}(-1)^h\binom{r}{h}x^{kh})(\sum_{i\geq 0}\binom{i+r-1}{i}x^i)\\&=\sum_{h=0}^{\min\{r,\lfloor\frac{n-1}{k}\rfloor\}}(-1)^h\binom{n-kh-1}{r-1}\binom{r}{h}.\end{aligned}$$

■

Theorem 20. *Given four positive integers* n*,* r*,* k*, and* t*, and let* $p(n,r,k,t)$ *be the number of vectors* $(x_1, x_2, ..., x_r)$*, such that*

$$n=\sum_{i=1}^{r}x_i$$

x_i *is positive integer, and* $t\leq x_i\leq k$ *for* $i=1,2,...,r$*. Then*

$$\begin{aligned}p(n,r,k,t)&=p(n-(t-1)r,r,k-(t-1)\\&=\sum_{h=0}^{\min\{r,\lfloor\frac{n-rt+r-1}{k-t+1}\rfloor\}}(-1)^h\times\\&\binom{n-rt+r-hk+ht-h-1}{r-1}\binom{r}{h}.\end{aligned}$$

Example:
$p(3,3,1,1)=1$: $(1,1,1)$
$p(3,2,2,1)=2$: $(1,2)$ and $(2,1)$
$p(4,3,2,1)=3$: $(1,1,2)$, $(1,2,1)$ and $(2,1,1)$

Proof:

$$\begin{aligned}&[x^n](x^t+x^{t+1}+x^{t+2}+...+x^k)^r\\&=\left[x^{n-tr}\right](1+x+x^2+...+x^{k-t})^r\\&=\left[x^{n-tr}\right]\frac{(1-x^{k-r+1})^r}{(1-x)^r}\\&=\left[x^{n-tr}\right](1-x^{k-r+1})^r(1-x)^{-r}\\&=\left[x^{n-tr}\right](\sum_{h\geq 0}(-1)^h\binom{r}{h}x^{(k-r+1)h})(\sum_{i\geq 0}\binom{i+r-1}{i}x^i)\\&=\sum_{h=0}^{\min\{r,\lfloor\frac{n-rt+r-1}{k-t+1}\rfloor\}}(-1)^h\times\\&\binom{n-rt+r-hk+ht-h-1}{r-1}\binom{r}{h}.\end{aligned}$$

■

III. Open Problems

Problem 21. *How to find the number of lattice paths from* $(0,0)$ *to* (m,n) *avoiding* $\uparrow^{\geq i}, \rightarrow^{\geq j}$*, and weakly above the diagonal* $y=x$*. And how to find a good generating function for this problem?*

Problem 22. *How to find the number, say $f(m,n)$, of lattice path from $(0,0)$ to (m,n) avoiding $\uparrow^{\geq 3}$, $\longrightarrow^{\geq 3}$, and weakly above $y=x$? (This problem is a special case of the above problem: $i=j=3$)*

You can see some numbers of this problem:

$n=14$					
$n=13$					
$n=12$					
$n=11$					
$n=10$					1
$n=9$					5
$n=8$				1	14
$n=7$				4	25
$n=6$			1	9	29
$n=5$			3	12	20
$n=4$		1	5	9	8
$n=3$		2	4	4	
$n=2$	1	2	2		
$n=1$	1	1			
$n=0$					
	$m=0$	$m=1$	$m=2$	$m=3$	$m=4$

For $m+2 \leq n$,

$$f(m,n) = f(m-1,n) + f(m-1,n-1) + f(m-1,n-2) - f(m-3,n) - f(m-3,n-1) - f(m-3,n-2).$$

For $m+1=n$,

$$f(n,n+1) = f(n-1,n+1) + f(n-1,n) - f(n-3,n+1) - f(n-3,n).$$

For $m=n$,

$$f(n,n) = f(n-1,n) - f(n-3,n).$$

Example:

$$\begin{aligned} f(9,12) &= f(8,12) + f(8,11) + f(8,10) \\ &\quad - f(6,12) - f(6,11) - f(6,10) \\ &= 1023 + 1156 + 956 - 27 - 70 - 130 \\ &= 2098 \end{aligned}$$

$$\begin{aligned} f(6,7) &= f(5,7) + f(5,6) - f(3,7) - f(3,6) \\ &= 70 + 45 - 4 - 9 = 103 \end{aligned}$$

$$\begin{aligned} f(5,5) &= f(4,5) - f(2,5) \\ &= 20 - 3 = 17 \end{aligned}$$

(1) We can say the numbers on the first line with slope 2 are:

$$1, 1, 1, 1, 1, 1, 1, 1, ...$$

(2) The numbers on the second line with slope 2 are:

$$1, 2, 3, 4, 5, 6, 7, ..$$

(3) The numbers on the third line with slope 2 are:

$$0, 2, 5, 9, 14, 20, 27, 35, 44, 54, ...$$

$$\binom{n+1}{2} - 1, \text{ for } n \geq 2$$

(4) The numbers on the fourth line with slope 2 are:

$$0, 1, 4, 12, 25, 44, 70, 104, 147, 200...$$

$$f(n) = \frac{1}{6} n(n+5)(n-2), \text{ for } n \geq 3$$

$f(n+3)$ is the number in the sequence [11, A000297] which counts other things:

Some kind of partitions by P. Erdos, R. K. Guy and J. W. Moon [2].

Rooted trees by J. Riordan [10].

(5) The numbers on the fifth line with slope 2 are:

$$0, 0, 2, 9, 29, 67, 130, 226, 364, 554, 807, ...$$

$$\frac{1}{24}(n-2)(n^3+8n^2-9n-48), \text{ for } n \geq 4$$

(6) The numbers on the sixth line with slope 2 are:

$$0, 0, 0, 4, 20, 70, 176, 370, 693, ...$$

$$\frac{1}{120}(n-2)\left(n^4+12n^3-21n^2-232n+360\right), \text{ for } n \geq 5$$

(7) The numbers on the seventh line with slope 2 are:

$$0, 0, 0, 0, 8, 45, 168, 454, 1023, 2045, 3751, ...$$

$$\frac{1}{720} n\left(n^5+15n^4-65n^3-675n^2+3304n-3300\right), \text{ for } n \geq 6$$

References

[1] B. Bollobás, The Art of Mathematics: Coffee Time in Memphis, Cambridge University Press, (2006).

[2] P. Erdos, R. K. Guy and J. W. Moon, On refining partitions, J. London Math. Soc., **9** (1975), 565-570.

[3] J. Fallon, S. Gao, H. Niederhausen, A finite operator approach to the tennis ball problem, Congr. Numer. **184** (2007), 5-10

[4] J. Fallon, S. Gao, H. Niederhausen, Proof of a lattice paths conjecture connected to the tennis ball problem, Journal of Statistical Planning and Inference, **140** (2010), 2227–2229.opical Review) J. Phys. A **42** (2009), 323001.

[5] S. G. Mohanty, Lattice Path Counting and Applications, New York: Academic Press, (1979).

[6] H. Niederhausen, Finite Operator Calculus With Applications to Linear Recursions (Book)

[7] H. Niederhausen, The ballot problem with three candidates. European J. Combin. **4** (1983), 161–167.

[8] H. Niederhausen, Lattice path enumeration and umbral calculus, Advances in Combinatorial Methods and Applications (editor: N. Balakrishnan), Birkh¨auser Boston (1997).

[9] H. Niederhausen, Recursive initial value problems for Sheffer sequences, Discrete Mathematics, **204**,(1999), 319-327.

[10] John Riordan, An Introduction to Combinatorial Analysis (originally published: New York: John Wiley 1958), Dover Publications (2002).

[11] The Online Encyclopedia of Integer Sequences (2016), published electronically at http://oeis.org

SESSION

MODELING AND SIMULATION FRAMEWORKS

Chair(s)

Dr. Douglas D. Hodson
Dr. Michael R. Grimaila

ISBN: 1-60132-430-8, CSREA Press ©

Studying Decoy State Protocol Configurations in Quantum Key Distribution Systems

Logan O. Mailloux, Michael R. Grimaila,
Douglas D. Hodson, Ryan D. Engle
Air Force Institute of Technology
Department of Systems Engineering and Management
Wright-Patterson Air Force Base, Ohio 45433
Logan.Mailloux@afit.edu

Colin V. McLaughlin
Naval Research Laboratory
Washington, D.C. 20375

Gerald B. Baumgartner
Laboratory for Telecommunication Sciences
College Park, Maryland 20740

***Abstract*—In this work, decoy state enabled Quantum Key Distribution (QKD) system configurations are studied using a specialized modeling and simulation framework. QKD systems exploit the laws of quantum mechanics to generate unconditionally secure cryptographic keying material for use in high-security applications such as banking, government, and military environments. However, QKD systems have implementation non-idealities which can negatively impact system performance and security. Moreover, performance-security configuration tradeoffs are not fully understood nor have they been comprehensively studied. This article extends previous work and addresses these gaps by examining decoy state enabled QKD system configurations outside of typical operating regimes. The results of this study demonstrate that practically-oriented QKD systems can provide high quantum throughput (i.e., system performance) and ensure photon number splitting attacks are detected with high confidence (i.e., system security).**

Keywords—Quantum Key Distribution; Decoy State Protocol; Modeling & Simulation

I. Introduction

Quantum Key Distribution (QKD) is a complex cyber security technology which exploits the laws of quantum mechanics to generate unconditionally secure cryptographic keying material for use in high-security environments such as banking, government, and military environments. The genesis of QKD traces back to the late 1960s, when Stephen Wiesner first proposed the idea of encoding information on photons using two conjugate encoding bases [1]. In 1984, Charles Bennett and Gilles Brassard extended this idea by introducing the first QKD protocol, known as "BB84," to generate shared secret keying material between two geographically separated parties [2]. From its relatively unnoticed beginnings, QKD has emerged as an important development in the cyber security solution space with commercial offerings available from several venders across Asia, Europe, and North America [3].

However, these systems have implementation non-idealities and practical engineering limitations which can negatively impact system performance and security. Moreover, performance-security configuration trade-offs are not fully understood nor have they been comprehensively studied. To address these gaps, a specialized Modeling and Simulation (M&S) framework is used to study the security and performance of real-world QKD systems [4], [5]. This work extends previous work [6] and examines decoy state protocol configurations different from typical operating regimes. The results of this M&S study demonstrate that practically-oriented QKD systems can provide high quantum throughput (i.e., performance) and ensure Photon Number Splitting (PNS) attacks are detected with high confidence (i.e., security).

II. Quantum Key Distribution (QKD) Systems

Fig. 1 illustrates a notional QKD system architecture, where single photons – known as quantum bits or "qubits" – are encoded and transmitted between two parties to securely generate a shared cryptographic key K. The QKD system consists of a sender "Alice," a receiver "Bob," a quantum channel (i.e., an optical fiber or direct-line-of-sight path), and a classical channel (i.e., a conventional networked connection). Alice is shown with a laser source configured to prepare (generate and encode) single photon optical pulses, while Bob measures them using specialized Single Photon Detectors (SPDs).

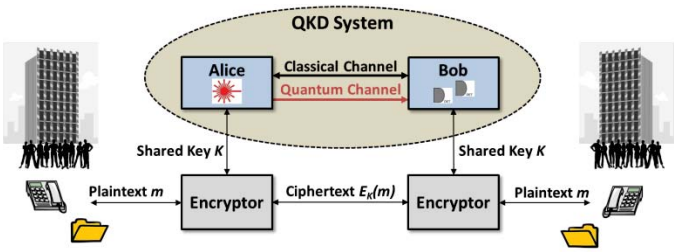

Fig. 1. QKD System Context Diagram. The sender "Alice" and receiver "Bob" generate shared secret key K for use in data encryption.

Typically, the QKD-generated shared key K is used to increase the security posture of traditional symmetric encryption algorithms such AES through frequent re-keying (i.e., reducing the time and information available for

cryptanalysis attempts). More ideally, QKD is often discussed as an enabler to the One-Time-Pad (OTP) – the only known encryption algorithm to achieve perfect secrecy [7], [8]. This is because QKD can uniquely generate unlimited amounts of unconditionally secure random keying material, making previously unrealistic OTP configurations possible. In this way, QKD enables unbreakable communication between two parties.

A. The BB84 QKD Protocol

While there are many competing QKD protocols, BB84 is relatively easy to understand and remains a popular implementation choice. As illustrated in Table I, BB84 is a prepare-and-measure QKD protocol where Alice prepares photons in one of four polarization states (e.g., $|\leftrightarrow\rangle$, $|\updownarrow\rangle$, $|\nearrow\rangle$, or $|\nwarrow\rangle$) according to a randomly selected basis ("rectilinear" shown as $\oplus$ or "diagonal" shown as $\otimes$) and bit value (0 or 1). Alice then transmits the encoded photons to Bob over the quantum channel, where he measures each photon using a randomly selected measurement basis ($\oplus$ or $\otimes$). If Alice and Bob's bases agree, the photon is read correctly with a high probability, otherwise a random result occurs.

TABLE I
EXAMPLE BB84 PROTOCOL

Alice Prepares			Bob Measures	
Encoding Basis	Bit	Prepared State	Decoding Basis	Result
$\oplus$	0	$\|\leftrightarrow\rangle$	$\oplus$	0
$\oplus$	1	$\|\updownarrow\rangle$	$\oplus$	1
$\oplus$	0	$\|\leftrightarrow\rangle$	$\otimes$	*random*
$\oplus$	1	$\|\updownarrow\rangle$	$\otimes$	*random*
$\otimes$	0	$\|\nearrow\rangle$	$\oplus$	*random*
$\otimes$	1	$\|\nwarrow\rangle$	$\oplus$	*random*
$\otimes$	0	$\|\nearrow\rangle$	$\otimes$	0
$\otimes$	1	$\|\nwarrow\rangle$	$\otimes$	1

The unconditionally secure nature of QKD is based on the inherent uncertainty of the measurement result when encoding and decoding photons with two conjugate bases as is the case with BB84 [9], [10]. Thus, whenever an eavesdropper "Eve" attempts to listen on the quantum channel, she must randomly select a measurement basis and will inevitably be wrong 50% of the time. Eve necessarily introduces detectable errors, which contribute to the system's Quantum Bit Error Rate (QBER). If the QBER exceeds the system's security threshold (e.g., QBER > 11% [11]), the QKD process is aborted as it is assumed an adversary is listening on the quantum channel.

B. Implementation Non-Idealities and System Vulnerabilities

BB84 security proofs assume several idealities, including perfect on-demand single photon sources, lossless quantum transmission, perfect transmitter-receiver basis alignment, and perfect single photon detection [2], [10]. However, these assumptions are not valid when building real-world QKD systems [12]. For example, reliable on-demand single photon sources are not currently available nor are they expected in the near term [13]. Therefore, most QKD systems attenuate classical laser pulses down from millions of photons to weak coherent pulses with a low Mean Photon Number (MPN) represented by a Poisson distribution [13]

$$P(n|\mu) = \frac{\mu^n e^{-\mu}}{n!} \quad (1)$$

where μ = MPN and n represents the number of photons in a pulse. For example, when $\mu = 0.1$, ~90.5% of the pulses have no photons, ~9.0% of the pulses have one photon, and ~0.5% of the pulses have two or more photons. These multiphoton pulses introduce a significant vulnerability, exposing information about the *unconditionally secure* key. For example, with an MPN of 0.5, as is often the case in decoy state QKD systems, nearly 25% of the pulses emitted by Alice are insecure multiphoton pulses. This implementation vulnerability has been subject of a number of practical and theoretical attacks, since the first QKD system [14].

C. Photon Number Splitting (PNS) Attacks

Fig. 2 provides a simplified depiction of Eve conducting a PNS attack against the QKD system (i.e., Alice and Bob). The powerful theoretical attack is designed to take advantage of this multiphoton vulnerability in order to obtain a full copy of Alice and Bob's shared secret key bits without introducing additional errors [15], [16]. In accordance with QKD security proofs, Eve is an all-powerful adversary limited only by the laws of quantum mechanics [11]. This means she is allowed to interfere with the quantum channel (thereby introducing losses and errors) and listen to the classical channel.

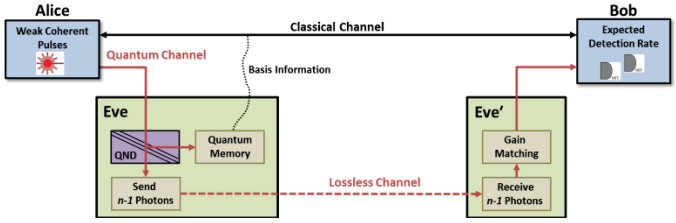

Fig. 2. The eavesdropper (Eve and Eve′) is shown conducting a Photon Number Splitting (PNS) attack against the QKD system (Alice and Bob).

In order to conduct the PNS attack, Eve replaces Alice and Bob's quantum channel with a lossless channel, requiring a geographically separated Eve′. For each weak coherent pulse Alice generates, Eve performs a Quantum Non-Demolition (QND) measurement to determine the number of photons n in each pulse without causing errors in the pulse's encoded state. If $n \leq 1$, Eve blocks the pulse and sends nothing to Bob. If $n \geq 2$, Eve splits one photon from the pulse and stores it in her quantum memory. She then sends the remaining $n-1$ photons to Bob via the lossless channel, typically achieved through quantum teleportation via entangled photon pairs [17]. Because of Eve's lossless channel, Eve′ must apply gain matching so as to not exceed Bob's expected detection rate to avoid obvious detection.

This process allows Eve to store a copy of every photon sent to Bob without introducing additional errors during quantum exchange. Once Alice and Bob announce their measurement basis information over the classical channel, Eve is then able to correctly measure her stored photons. In this manner, Eve is able to obtain a complete copy of Alice and Bob's *unconditionally secure* cryptographic key bits.

D. The Decoy State Protocol

In 2003, the decoy state protocol was introduced to detect PNS attacks [18]. It was quickly improved upon in [19], [20] and is now widely employed (see [6] for a comprehensive listing). In particular, the decoy state protocol is advantageous as it is relatively easy to implement (low cost), increases the system's distributed key rate (high performance), and provides the ability to detect PNS attacks (high security).

As shown in Table II, decoy state enabled QKD systems typically employ three states: 1. Signal, 2. Decoy, and 3. Vacuum [20]. In this configuration, the signal state facilitates increased key distribution rates and greater operational distances by using a higher MPN (i.e., 0.6 is greater than the value 0.1 typically used in non-decoy state protocols). The decoy state allows the system to detect PNS attacks through differential analysis between the signal and decoy states. Lastly, the vacuum state is used to characterize noise on the quantum channel (i.e. erroneous detections).

TABLE II
EXAMPLE DECOY STATE PROTOCOL CONFIGURATION

State	PURPOSE	MPN	Occurrence Percentage
Signal μ	The signal state is used to transmit pulses used for generating secret key.	0.6	70%
Decoy ν	The decoy state is used to detect unauthorized eavesdropping on the quantum channel through statistical differential with the signal state.	0.2	20%
Vacuum Y_0	The vacuum state is used to determine the "dark count" or noise level of the receiver's single photon detectors (i.e., when no photons are transmitted).	~0+	10%

The decoy state protocol extends the BB84 protocol by configuring Alice to randomly transmit signal, decoy, and vacuum states according to their prescribed occurrence percentages and respective MPNs. In order to maintain protocol integrity, each state must be identical (i.e., indistinguishable pulse shape, wavelength, duration, etc.) such that Eve cannot distinguish a decoy state from a signal or vacuum state. The only information available to Eve, which she obtains by making a QND measurement, is the number of photons $n = 0, 1, 2, ...$N in each pulse.

Through a slightly modified version of quantum exchange, the QKD system is able to detect PNS attacks by statistically identifying differences between the signal and decoy states, such as the efficiency-based security condition [21]

$$\eta^{signal} = \eta^{decoy}. \quad (2)$$

Under normal operational conditions (i.e., when no PNS attacks are occurring), the signal and decoy state efficiencies are the same for a given QKD architecture because the quantum channel efficiency is relatively fixed and not dependent on the state type (signal or decoy). Conversely, the PNS attack adversely impacts the decoy state more so than the signal state because of its lower MPN. Thus, an adversary is assumed to be conducting a PNS attack on the key distribution channel when $\eta^{\text{signal}} \neq \eta^{decoy}$.

While the decoy state protocol was introduced to detect PNS attacks, it has primarily been used to increase key generation rates without detailed consideration of its practical impact on performance or security. While the researcher's previous work [6] addresses the system's ability to detect PNS attacks in detail, this work extends those results beyond typical operating regimes and includes additional discussion regarding performance-security tradeoffs.

III. STUDYING DECOY STATE ENABLED QKD SYSTEMS

In this section, performance and security measures as they are used in this study are described. Note this paper is not a formal study of unconditionally secure key rates, which is already well studied in a number of research articles [11]. Instead, decoy state configurations are studied at a more rudimentary level, that is, performance is described by quantum throughput and security is described as the system's ability to detect PNS attacks.

In this study, the performance and security of the modeled decoy state QKD system is studied across four signal state MPNs. Specifically, the traditionally employed decoy state MPN of 0.5 [20] is compared to higher MPNs of 0.8, 1.0, and 1.2 as suggested by [22]. Additionally, the decoy state MPN is fixed at 0.1 as suggested in [20], while the decoy state protocol occurrence percentages for the signal, decoy, and vacuum states are set to 99%, 0.5%, and 0.5% based on previous work [6].

A. Measuring Implemtation Performance

QKD system performance is typically described as the unconditionally secure key rate R. However, in this study the system's quantum throughput is used as it provides a more direct accounting of the system's physical layer performance when comparing MPNs. That being said, the system's quantum throughput is closely related to the system's secret key rate, R, described as [19], [20]

$$R \leq q\{-Q_\mu f_{ER}(E_\mu)H_2(E_\mu)+Q_1[1-H_2(e_1)]\} * f_{PR} \quad (3)$$

where q is the protocol efficiency (i.e., 50% of system's detections are sifted out due to an incorrect measurement basis), $Q_\mu = \frac{Number\ of\ signal\ state\ detections}{Total\ number\ of\ sent\ signal\ state\ pulses}$ is the measured signal state gain, $E_\mu = 3\%$ is the signal state QBER,

$f_{ER}(E_\mu)$ is the efficiency of error reconciliation technique (e.g., 1.16 for error rates of ≤5% [23]), H_2 is the Shannon binary entropy calculation $H_2(x) = -xlog_2(x) - (1-x)log_2(1-x)$ [8], Q_1 is the estimated gain from single photon pulses emitted by Alice, e_1 is the estimated QBER for single photon pulses emitted by Alice, and $f_{PR} = 5$ Mhz is the system's modeled pulse rate. A more thorough treatment of this equation and its parameters is given in [5].

From Eq. (3), it is important to note the signal state gain Q_μ is directly measured during system operation, while the gain due to single photon pulses emitted by Alice Q_1 is merely bound. This is because practically-oriented QKD systems (i.e., systems which balance cost, performance, and security trades towards affordability) are unable to distinguish between a detection event due to a secure single photon pulse or an insecure multiphoton pulse – it is simply detected or not detected [11]. Thus, both the total measured quantum throughput (i.e., akin to Q_μ) and a worst case single-photon throughput based on Poissonian statistics (i.e., akin to Q_1) are considered for performance metrics.

B. Measuring Implementation Security

The QKD system's security is described as the likelihood of detecting PNS attacks (i.e., 0-100%) using a 99.9% prediction interval and the decoy state security condition as described in Eq. (2). For each of the four configurations considered (i.e., MPN = 0.5. 0.8, 1.0, and 1.2), simulations were conducted without and without PNS attacks for a total of eight treatments each with 1,000 simulation runs. A large number of runs are conducted to well-characterize the system's security posture and provide sufficient statistical evidence to detect PNS attacks with high confidence.

Additionally, regarding performance-security tradeoffs, it is of interest to understand the minimum number of decoy state detections required to detect PNS attacks with high confidence. This allows the decoy state configuration to be maximized for higher secret key rates. More specifically, the signal state occurrence percentage and MPN can be chosen to meet the minimum requirements to ensure PNS attacks are detected, thus, enabling maximum performance.

IV. Analysis of Results

A. Quantum Throughput

Fig. 3 illustrates the resulting quantum throughput for the four configurations considered (i.e., signal state MPN = 0.5, 0.8, 1.0, and 1.2) over an operational distance 50 km with 10 dB loss representative of telecom single mode fiber at 1550 nm wavelength [13]. Additionally, Bob's architecture induces ~4 dB of loss with 10% detection efficiency as is common in practically-oriented QKD systems.

As expected, the resulting quantum throughputs are linear in nature with decreasing improvement when accounting for the worst case single-photon throughput. While single-photon throughput grows with higher MPNs, QKD security proofs suggest an optimized signal state MPN of ~0.5 [20], [24] to maximize the number of single photon pulses and minimize the number of insecure multiphoton pulses. However, QKD developers wishing to increase system performance can select higher MPNs beyond this theoretical security limit to reduce the number of non-empty pulses as shown in Table III [25].

TABLE III
MPN Comparisons

MPN	Number of photons per pulse (Poissonian Distribution)			% of non-empty pulses	% of non-empty pulses that are single photon pulses
	0	1	≥2		
0.5	61%	30%	9%	39%	77%
0.8	45%	36%	19%	55%	65%
1.0	37%	37%	26%	63%	58%
1.2	30%	36%	34%	70%	52%

Note: when considering higher MPNs, it is important to remind the reader that the unconditionally secure nature of QKD requires that secret key only be generated from single photon pulses, despite the fact that the system cannot tell the difference between a secure single photon detection and an insecure multiphoton detection. Thus, information loss due to multiphoton pulses must be strictly accounted for and negated with advanced information theory techniques such as entropy estimation and privacy amplification [11].

B. Detecting Photon Number Splitting (PNS) Attacks

Fig 4. presents results of the decoy state configuration when the signal state MPN = 1.2 (MPNs of 0.5, 0.8, and 1.0 are not shown as the results are similar). The normal signal and decoy state efficiencies (i.e., without PNS attacks) are shown in blue and green. Additionally, the system's expected variation is captured by the 99.9% prediction interval based on the decoy state's measurements. The overlapping efficiencies, imply $\eta^{signal} = \eta^{decoy}$. Thus, the system is operating in a known secure state.

Conversely, when subject to PNS attacks the decoy state efficiency, shown in red, is outside the system's 99.9% prediction interval demonstrating the system is under attack (i.e., $\eta^{signal} \neq \eta^{decoy}$). This effect occurs because Eve's PNS attack blocks a disproportionate number of decoy state pulses due to its lower MPN, and thus, reduces the decoy state's calculated efficiency. In the four configurations considered at 50 km distances, the PNS attack was successfully detected with significant statistical confidence in all 4,000 trials (i.e., 100% detection). For example, in the worst case (i.e., when efficiencies are closest) the attack is detected with $P < 0.001$.

Lastly, Table IV provides an important finding regarding the minimum number of decoy state detections to reliably detect PNS attacks. From these results, we learn that a very small number of decoy state detections ≤14 is sufficient to detect PNS attacks with high confidence. More specifically, in all 1,000 PNS attacks, the decoy state efficiency is readily detectable as it is below the 99.9% lower bound of 0.00607.

TABLE IV
DECOY STATE DETECTIONS FOR HIGH PERFORMANCE CONFIGURATION
(99% SIGNAL STATES WITH MPN = 1.2, 0.5% DECOY STATES WITH MPN = 0.1)

Number of decoy states detected	Number of trials	Percentage of total	Average efficiency	Standard deviation
0	4	0%	0.00000	0
1	16	2%	0.00024	0.0000093
2	45	5%	0.00061	0.0000136
3	87	9%	0.00097	0.0000198
4	144	14%	0.00134	0.0000314
5	188	19%	0.00171	0.0000317
6	153	15%	0.00208	0.0000496
7	103	10%	0.00244	0.0000448
8	109	11%	0.00281	0.0000606
9	56	6%	0.00317	0.0000622
10	46	5%	0.00354	0.0000792
11	31	3%	0.00391	0.0000743
12	12	1%	0.00425	0.0000809
13	6	1%	0.00458	0.0001317
14	1	0%	0.00490	N/A

V. CONCLUSIONS

This work demonstrates how a specialized system-level M&S framework can be used to study complex cyber security technologies such as QKD. The results of this study shown that higher MPNs (i.e., MPNs of 1.0 – 1.2) can be employed by decoy state enabled QKD systems to provide increased single-photon throughput while ensuring PNS attacks are detected with high confidence. Additionally, these results aid cyber security specialists in understanding the QKD system's sensitivity to PNS attacks.

DISCLAIMER

The views expressed in this paper are those of the authors and do not reflect the official policy or position of the United States Air Force, the Department of Defense, or the U.S. Government.

ACKNOWLEDGMENT

This work was supported by the Laboratory for Telecommunication Sciences [grant number 5743400-304-6448]. This work was supported in part by a grant of computer time from the DoD High Performance Computing Modernization Program at the Air Force Research Laboratory, Wright-Patterson AFB, OH.

REFERENCES

[1] S. Wiesner, "Conjugate coding," *ACM Sigact News,* vol. 15, no. 1, pp. 78-88, 1983.

[2] C. H. Bennett and G. Brassard, "Quantum cryptography: public key distribution and coin tossing," in *Proceedings of IEEE International Conference on Computers, Systems and Signal Processing*, 1984.

[3] L. Oesterling, D. Hayford and G. Friend, "Comparison of commercial and next generation quantum key distribution: Technologies for secure communication of information," in *Homeland Security (HST), 2012 IEEE Conference on Technologies for*, 2012.

[4] L. O. Mailloux, J. D. Morris, M. R. Grimaila, D. D. Hodson, D. R. Jacques, J. M. Colombi, C. McLaughlin, R. Engle and J. Holes, "A modeling framework for studying quantum key distribution system implementation non-idealities," *IEEE Access,* pp. 110-130, 2015.

[5] L. O. Mailloux, R. D. Engle, M. R. Grimaila, D. D. Hodson and C. McLaughlin, "Modeling decoy state quantum key distribution systems," *Journal of Defense Model and Simulation,* vol. 12, no. 4, pp. 489-506, 2015.

[6] L. O. Mailloux, M. R. Grimaila, D. D. Hodson, R. D. Engle, C. V. McLaughlin and G. B. Baumgartner, "Optimizing Decoy State Enabled Quantum Key Distribution Systems to Maximize Quantum Throughput and Detect Photon Number Splitting Attacks with High Confidence," *IEEE/OSA Journal of Lightwave Technology.,* Submitted 2016.

[7] G. S. Vernam, "Cipher printing telegraph systems for secret wire and radio telegraphic communications," *American Institute of Electrical Engineers, Transactions of the,* vol. 45, pp. 295-301, 1926.

[8] C. E. Shannon, "Communication theory of secrecy systems," *Bell System Technical Journal,* vol. 28, pp. 656-715, 1949.

[9] D. Gottesman, H.-K. Lo, N. Lutkenhaus and J. Preskill, "Security of quantum key distribution with imperfect devices," in *Quant. Inf. Comput.*, 2004.

[10] R. Renner, N. Gisin and B. Kraus, "An information-theoretic security proof for QKD protocols," *Physical Review A,* vol. 72, no. 1, 012332, 2005.

[11] V. Scarani, H. Bechmann-Pasquinucci, N. J. Cerf, M. Dušek, N. Lütkenhaus and M. Peev, "The security of practical quantum key distribution," *Reviews of Modern Physics,* vol. 81, no. 3, pp. 1301-1350, 2009.

[12] V. Scarani and C. Kurtsiefer, "The black paper of quantum cryptography: real implementation problems," *arXiv:0906.4547v2,* 2009.

[13] N. Gisin, G. Ribordy, W. Tittel and H. Zbinden, "Quantum cryptography," *Reviews of Modern Physics,* vol. 74, no. 1, pp. 145-195, 2002.

[14] C. H. Bennett, F. Bessette, G. Brassard, L. Salvail and J. Smolin, "Experimental quantum cryptography," *Journal of Cryptology,* vol. 5, no. 1, pp. 3-28, 1992.

[15] G. Brassard, N. Lutkenhaus, T. Mor and B. C. Sanders, "Limitations on practical quantum cryptography," *Physical Review Letters,* vol. 85, no. 6, 1330, 2000.

[16] N. Lütkenhaus, "Security against individual attacks for realistic quantum key distribution," *Physical Review A,* vol. 61, no. 5, 052304, 2000.

[17] S. Loepp and W. K. Wootters, Protecting Information, New York: Cambridge University Press, 2006.

[18] W.-Y. Hwang, "Quantum key distribution with high loss: toward global secure communication," *Physical Review Letters,* vol. 91, no. 5, 057901, 2003.

[19] H.-K. Lo, X. Ma and K. Chen, "Decoy state quantum key distribution," *Physical Review Letters,* vol. 94, no. 3, 230504, 2005.

[20] X. Ma, B. Qi, Y. Zhao and H.-K. Lo, "Practical decoy state for quantum key distribution," *Physical Review,* vol. 72, no. 1, 012326, 2005.

[21] L. O. Mailloux, M. R. Grimaila, J. M. Colombi, D. D. Hodson, C. V. McLaughlin, R. D. Engle and G. Baumgartner, "Quantum key distribution: examination of decoy state enabled networks," *IEEE Communications Magazine,* Accepted for publication 2015.

[22] D. Pearson and C. Elliott, "On the optimal mean photon number for quantum cryptography," *quant-ph/0403065,* 2004.

[23] G. Brassard and L. Salvail, "Secret-key reconciliation by public discussion," *In Advances in Cryptology—EUROCRYPT'93,* pp. 410-423, 1994.

[24] J. W. Harrington, J. M. Ettinger, R. J. Hughes and J. E. Nordholt, "Enhancing practical security of quantum key distribution with a few decoy states," *arXiv,* pp. quant-ph/0503002, 2005.

[25] S. Wang, W. Chen, Z.-Q. Yin, H.-W. Li, D.-Y. He, Y.-H. Li, Z. Zhou and e. al., "Field and long-term demonstration of a wide area quantum key distribution network," *Optics Express,* vol. 22, no. 18, pp. 21739-21756, 2014.

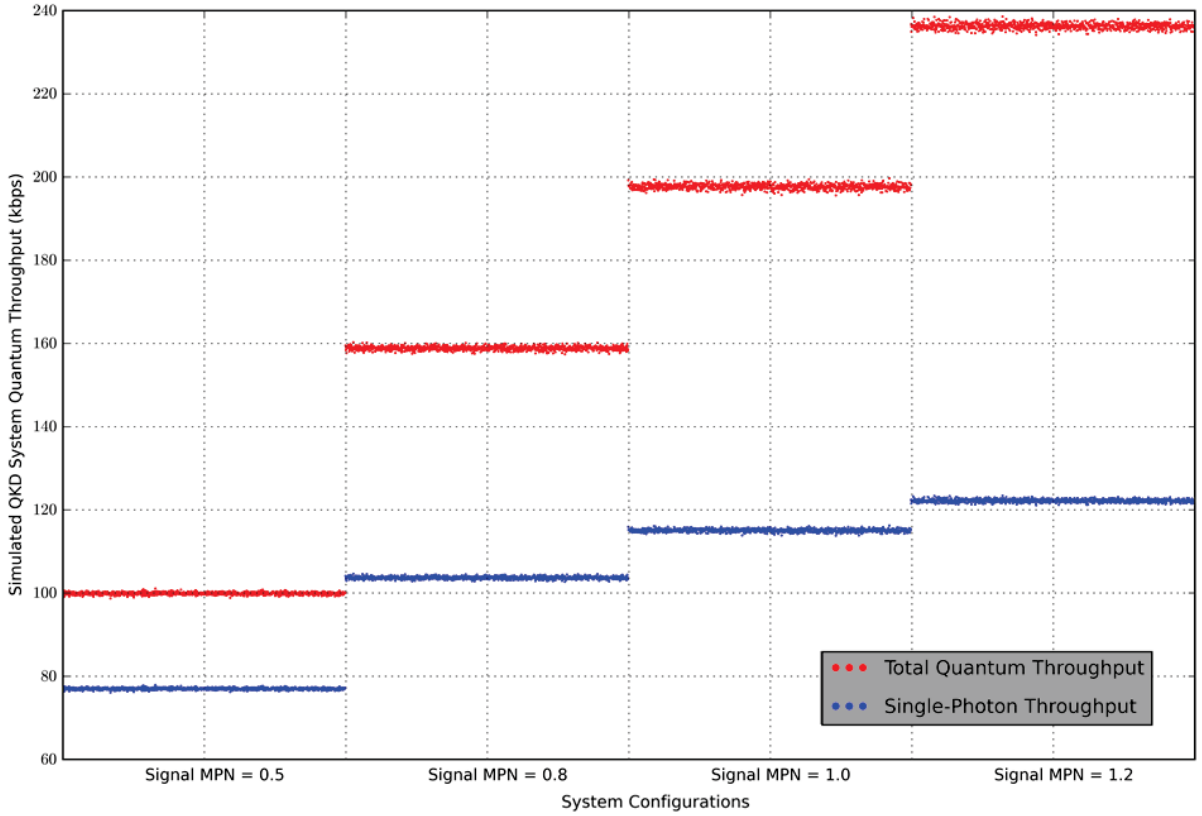

Figure 3. Quantum throughput for simulated QKD system configurations. For each configuration, 1,000 trials are conducted using an otherwise fixed architecture. As the quantum throughputs demonstrate, higher Mean Photon Numbers (MPNs) improve system performance.

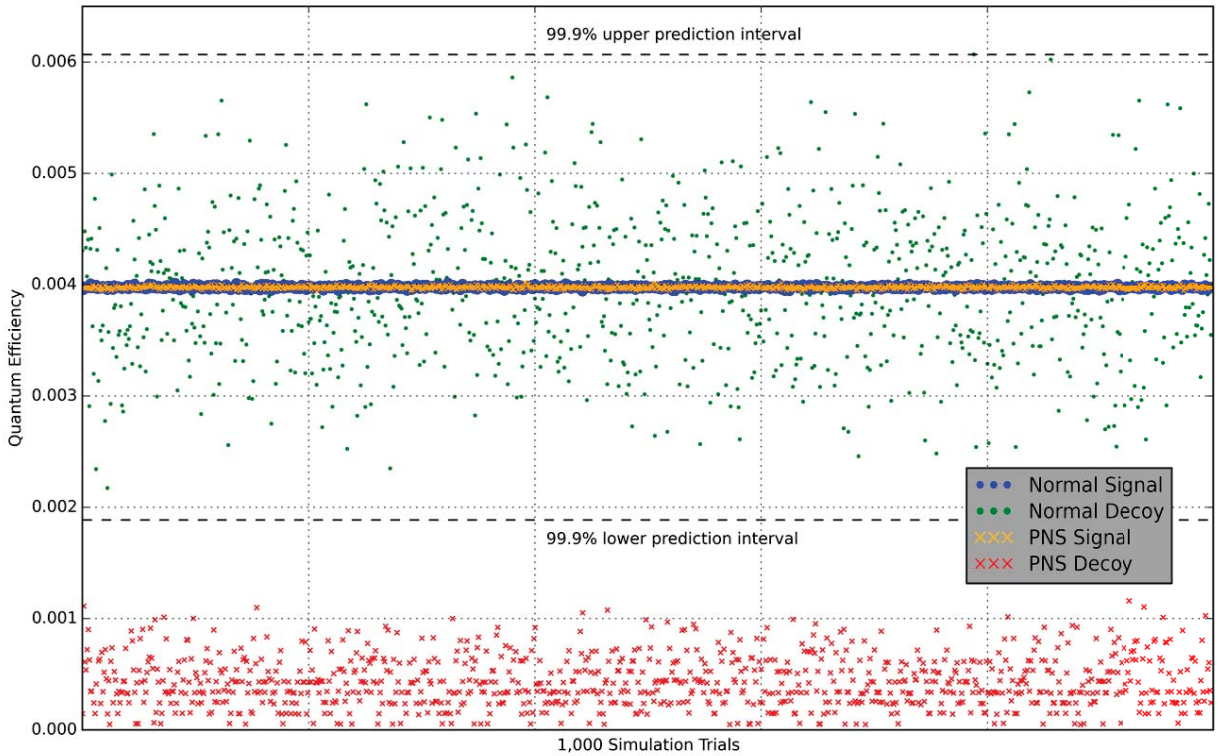

Figure 4. Detectability of the Photon Number Splitting (PNS) attack for the QKD systems configuration when the signal state MPN = 1.2. As demonstrated by the 99.9% prediction interval, the PNS attack is readily detectable.

Using a Systems Engineering Approach to Assess Operational Planning and Execution of Live, Virtual, Constructive Simulation Training Events

Andrew J. Roberts, Logan O. Mailloux, and Douglas D. Hodson
Air Force Institute of Technology
Wright-Patterson Air Force Base, Ohio
Email: {Andrew.Roberts; Logan.Mailloux; Douglas.Hodson} @afit.edu

***Abstract*—The Department of Defense (DoD) is actively pursuing the use of Live, Virtual, and Constructive (LVC) simulation to provide cost-effective training. This paper studies the planning and execution of a Command and Control (C2) LVC training event hosted by the Distributed Mission Operations Center (DMOC) in support of Air Combat Command's Weapons School curriculum. This training consists of operators from four C2 platforms responsible for managing a simulated battlespace with 100's of constructive entities (friendly, adversarial, and neutral) while integrating operations with space, cyberspace, and intelligence representatives. In this paper, the processes for planning and executing the C2 LVC event are captured and compared to the systems engineering technical processes described in the International Organization for Standardization 15288 standard. Lastly, the DMOC C2 LVC event planning and execution processes are decomposed and examined to gain insight, and offer suggestions for improving the effectiveness of LVC training opportunities.**

***Index Terms*—Live, Virtual, Constructive, Simulation, Command and Control, Training**

I. Introduction

Today's global security environment is increasingly unpredictable and the American Armed Forces must be prepared to respond to a variety of threats (e.g., the growth of ISIS, Chinese expansion in the South China Sea, the rise of Kim Jong-un in North Korea, and Russia's annexation of Ukraine) [1]. For this reason, military training which increasingly blends physical and virtual experiences to simulate contested environments is a top national level priority for the United States military [1]. Additionally, shrinking budgets and growing operational demands have created a situation where the military is continuously required to "do more with less" [2]. Previously, when the military faced similar budgetary issues it was argued that the most efficient way to "do more with less" was to improve Command and Control (C2) because the effective employment of C2 is a force multiplier and often the deciding factor in modern warfare [3], [4]. Thus, training of C2 personnel is of utmost importance and should focus on developing the C2 decision-making skills required to manage a complex battlespace [4], [3], [5]. However, these training opportunities are rare because they are difficult to organize, costly, subject to unpredictable environmental conditions, and pose significant risks to personnel and equipment [6], [7], [5], [8].

In this paper, we describe how recent advances in Live, Virtual, Constructive (LVC) simulation can help solve this training deficiency. More specifically, we study the planning and execution of a C2 LVC training event hosted by the Distributed Mission Operations Center (DMOC) in support of Air Combat Command's (ACC) Weapons School curriculum. Current LVC simulation environments enable training, familiarization, and rehearsal activities on not only the issues facing today's forces, but issues surrounding conflicts and technologies of the future. Previously these activities were either impossible or unfeasible due to finances, physical distance, public perception, intelligence sensitivities, or sheer scale [9], [10]. For example, it is now possible for individuals from geographically distributed locations, different warfighting commands, countries, and even operational domains (i.e., Air, Land, Sea, Space, and Cyberspace) to train together via more robust and realistic simulation environments [11], [12].

First, we provide a brief background which explains the applications and challenges associated with LVC simulations. Then, we define the DMOC approach for planning and executing a C2 LVC event and examine them using the Systems Engineering (SE) technical processes of ISO 15288 [13]. Next, the DMOC C2 LVC event planning and execution processes are decomposed into supporting activities. Finally, the C2 LVC training event is examined to gain insight and offer suggestions for improving the effectiveness of DoD training opportunities.

II. Background

Because C2 requires tacit and explicit knowledge, it must be both taught and developed [4], [3], [14]. For example, military members are often exposed to repeated stresses and dynamic decision making environments to create mental models that accelerate and improve decision-making [15], [14], [16]. In the past, these training scenarios largely consisted of "role-playing" highly scripted scenarios. For simple training scenarios with a limited number of participants, this may be sufficient; however, training C2 operators to effectively wage a large air campaign that integrates disparate services and coalition partners becomes exceedingly complicated and cost prohibitive [2], [5], [1]. To meet these needs the United States Air Force (USAF) and the Department of Defense (DoD) are

actively pursuing the use of LVC simulation to provide robust C2 operational training.

A. What is LVC?

Fig. 1 provides a common framework used in the DoD for distinguishing between the live, virtual, and constructive domains [17]. Live refers to warfighters operating their real-world equipment, virtual involves warfighters operating simulated systems (e.g., flight simulators), and constructive includes all of the software generated object representations required to create and enhance the simulated environment for a given scenario [2]. Applying this classification framework simplifies the classification of warfighting activities into the live, virtual, or constructive domains. LVC events often combine multiple domains [2], [18]. Additionally, LVC simulation often integrates both local and distributed participants into a single, seamless training scenario.

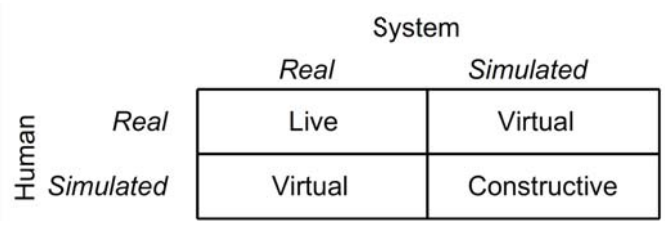

Fig. 1. Simulation Classification Framework [17].

B. LVC Benefits

Due to the multiple domains LVC technology is capable of integrating, it has numerous applications within both military and civilian environments. Fig. 2 denotes common LVC uses within the DoD [19], [10], [2], [18], [20]. Three main branches of LVC within the DoD are training, testing, and research and analysis. Within the past three decades, LVC training technology has grown to support training applications from one-on-one tactical level exercises to nation-on-nation wargaming simulations [10], [2], [21], [6]. Moreover, LVC is increasingly used to augment live operational training [5], [2]. For example, 5th generation fighters (e.g., F-22) currently utilize LVC training environments because live range availability and technical capabilities are unable to accommodate the full functionality of new weapon systems [22].

The LVC environment, also enables dynamic testing and experimentation which is not always possible at live test ranges [18], [9], [23]. For example, LVC environments can be used to test and experiment with network enabled weapons in a simulated congested environment [24], [25]. This helps to prevent exposing weapons and tactics to foreign intelligence collection while also simulating realistic demands for information in order to study system-of-system interactions. Likewise, in research and analysis applications, LVC technology enables strategy development and acquisition decisions based on simulated information and interactions that might need to be protected at higher classification levels. It is also apparent within the acquisition guidance of DoD Directive 5000.01, DoD Instruction 5000.02, and Chairman of the Joint Chiefs Staff Instruction (CJCSI) 3170.01G that the requirement for LVC, and more specifically Modeling & Simulation (M&S) within acquisition programs is necessary due to the interoperability and joint nature of modern warfare [23], [26], [20], [7].

Within the DoD, LVC technology has been shown to provide significant cost savings and additional training, testing, and experimentation opportunities [5], [2], [21]. It also minimizes risks to weapon systems, the environment, and operators [6]. Moreover, LVC has demonstrated the capability to enable scalable distributed training and collaboration events with options to provide secure environments for strategy development, research, and experiments that would otherwise be unattainable [19], [18], [2], [27]. For additional discussion of logical uses, see "Credible Uses of the DIS System [9]."

C. LVC Challenges

While the benefits of LVC training simulations are numerous, creating an effective virtual training environment that incorporates various C2 players into one scenario can be challenging. Most of the USAF C2 weapon systems in use today were developed decades ago and have antiquated training simulators (e.g., E-3 Sentry in 1977, and E-8 JSTARS in 1991) [28], [29]. They are under powered by today's standards and the software developed for them was never intended to be networked with other simulators or interface with vast libraries of constructive objects. Because these simulators were often designed to only satisfy specific training requirements, they require specialized gateways and software filters to enable basic interoperability [30]. Additionally, they were developed before information assurance became a concern, which causes significant accreditation issues. Furthermore, there are over a dozen competing software architectures for LVC simulators [31]. This creates significant interoperability problems when sharing or communicating simulation related data and attempting to maintain temporal consistency throughout the network [17]. While these legacy software and interoperability issues create challenges, recent LVC advancements are enabling more realistic simulation environments to be realized [2], [23], [31].

III. LVC Training Events

Within the Air Force, the 705th Combat Training Squadron, known as the Distributed Mission Operations Center (DMOC) is the premier unit for planning and executing campaign-level C2 LVC operational training [2], [32]. In addition to theater-wide training events, the DMOC hosts a number of smaller training events each year. Their method for planning and executing LVC training events has developed over several years and is tailored to enable rapid adaptation to customer needs [33]. This section systematically decomposes and examines the DMOC's planning and execution processes for routinely training operators in C2 warfare.

This paper's discussion of LVC training event processes and activities is strongly based on observations and interviews

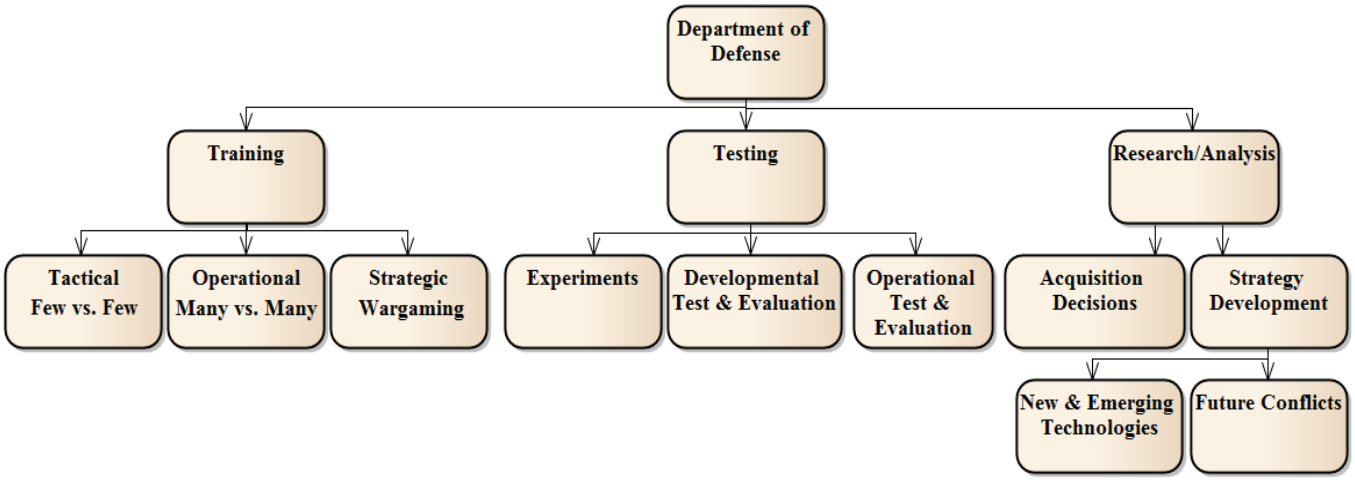

Fig. 2. LVC Applications within the DoD.

related to the DMOC processes for planning and executing a Weapons School C2 LVC training event. This is a medium sized LVC event with approximately 30 trainees and 20 support personnel responsible for directly executing the event. The trainees are USAF Weapons School students, supplemented with additional operators from Active, Guard, and Reserve units to fill mission critical roles and enhance the value of the event. The primary platform/mission sets involved are the E-3 Sentry (Airborne Warning and Control System-AWACS), E-8 Joint Surveillance Target Attack Radar System (JSTARS), Control and Reporting Center (CRC), RC-135 Rivet Joint. Intelligence and Space operators participate in a supporting role assisting the C2 decision makers throughout the exercise [34]. Of the 20 supporting personnel, about half are white force operators responsible for controlling $\geq$ 300 constructive entities, which represent enemy (red), friendly (blue), and non-combatant (gray) players. The remainder of the support personnel include Subject Matter Experts (SMEs), Weapon School instructors, exercise evaluators, and members of the technical troubleshooting and response teams that ensure proper execution of the training event. Participants and support personnel for this event were located both locally at the DMOC, Kirtland AFB, NM, and externally at Offutt AFB, NE.

While the focus of this analysis is on the planning and execution of a Weapons School C2 training event, the description and application of the DMOC process is nearly the same for larger more robust Distributed Mission Operations (DMO) training scenarios such as VIRTUAL FLAG (VF) [33], [32], [30], [8]. Upon initial inspection, the DMOC approach to planning and executing a training event appears similar to many project and program management approaches utilized by corporations and governments alike [13], [20], [35], [36]. In Fig. 3 the DMOC processes are defined and compared to the established SE technical processes of ISO 15288 for managing a complex system from cradle to grave [13]. Beginning with defining requirements and not ending until the completion of the disposal process, each ISO 15288 technical process defines activities that enable the DMOC to optimize project benefits and reduce risks introduced by technical and management decisions.

First, notice that the SE technical processes are very well aligned with the DMOC processes. As specified in ISO 15288, each of the DMOC processes is tailored as described in detail below in Fig. 4. Additionally, notice that many of the processes are executed in an iterative and co-dependent fashion; thus, not all of the processes are in numbered order. For example, the DMOC's Technical Planning process cannot begin before Resourcing has occurred. Given this constraint, the DMOC's annual budget has been modified to allocate funding for pre-planning activities associated with re-occurring events [30]. Alternatively, if the event is new and not considered in the budget, funding for the planning process will need to be agreed upon and allocated before proceeding with formal event planning and execution [32]. The following sections describe the DMOC processes as presented in the lower half of Fig. 3 and detailed in Fig. 4.

1.0 Requirements Gathering

The focus of this process is gathering all of the training requirements and objectives for effective training that meets stakeholder needs. This process contains three activities:

1.1 Pre-Planning: includes identifying potential stakeholders, developing a "10% plan" based on previous training events, and determining available training dates.

1.2 Planning Conference: involves representatives from all of the major stakeholders and provides an opportunity for each unit to express their training requirements and objectives. Also, a preliminary schedule is developed for progress meetings, milestones, scenario testing, simulator integration testing, travel, and training dates.

1.3 Establish Working Groups: typically a technical working group focused on developing the technical aspects of the

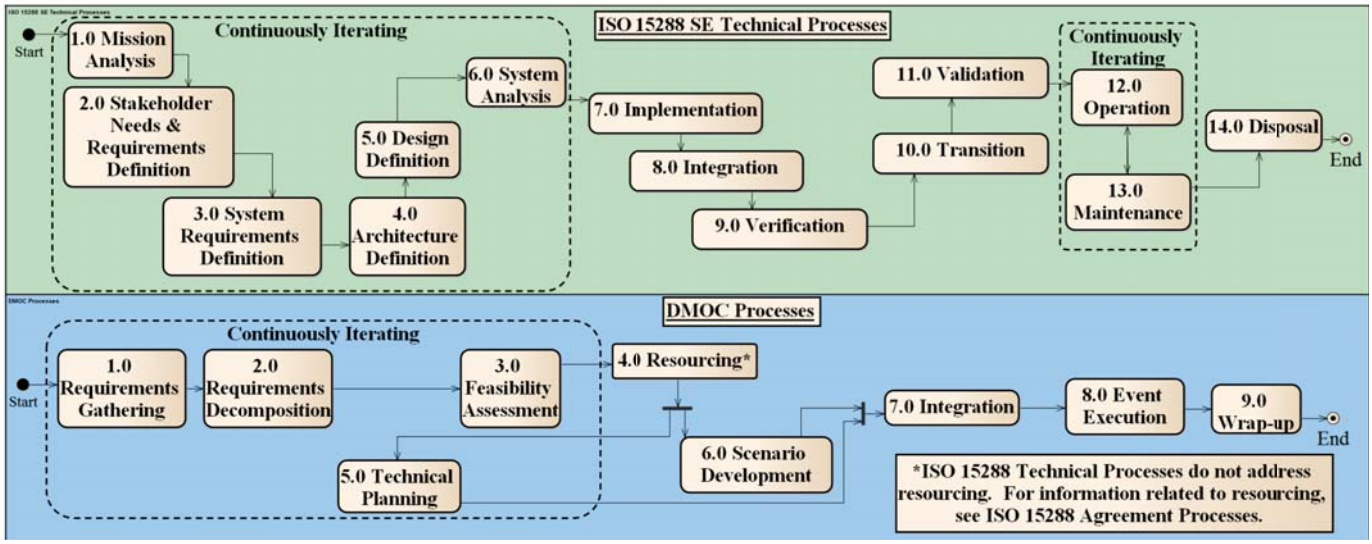

Fig. 3. DMOC Processes Mapped to ISO 15288 SE Technical Processes.

training scenario and an operations working group focused on operational training aspects and realistic scenario development. Other working groups may be created as necessary for atypical training events (e.g., integrating new simulators, mission types, or higher security classifications).

2.0 Requirements Decomposition

The goal of this process is translating user requirements into system specifications and estimating the resources necessary to support event execution. It is composed of two activities:

2.1 Develop Estimates: manning, schedule, technical, and cost estimates are developed and set as the baseline for event execution. This includes determining the number of servers, simulators, contractors, SMEs, white force, Inter-Service Agreements (ISAs), and days required to accomplish the training requirements.

2.2 Refine Scenario Scope: evaluates unit requirements and objectives provided by the planning conference, and reviews relevant Service, MAJCOM, and COCOM training expectations. With this information, training requirements are revisited and system specifications are defined. It also involves identifying constraints, such as limited bandwidth access, support personnel, or classification conflicts.

3.0 Feasibility Analysis

This process includes a series of assessments to determine if an event is feasible and results in a go/no-go decision where the DMOC Commander approves/disapproves the DMOC Directive–the authorization that allocates resources for the event. The feasibility analysis process involves three major activities:

3.1 Funding & Manpower Assessment: evaluates the DMOC's capability to support an event with required SMEs, contractors, and white force for the duration of the event.

3.2 Information Assurance Assessment: ensures the integrity of classified information required for the scenario (e.g., current weapon capabilities or operation plans). This activity is complicated by the addition of foreign players, visitors, or external network connections.

3.3 Technical Assessment: critically reviews DMOC technical capabilities and determines how to apply technical resources to support the training event.

4.0 Resourcing

This process ensures all resources required for successful event execution are in place or available. It is comprised of two major activities:

4.1 Gather Funds: any funds required for the simulation event are either allocated from the DMOC budget or gathered from participating units. The DMOC is resourced for recurring annual events. Additional events are typically one off, "pay to play" events [32].

4.2 Revise/Write Contract Documentation: required only when changes to support contracts or additional unbudgeted work is needed. Most events require some modification not originally accounted for but if the modification is small or simple enough, military or government personnel are able to adjust accordingly. However, if the required changes are too complicated, contracts might need to be modified to include additional work. Current contracts are not fee for service so each modification to manning requirements or after hour operations significantly increases the contracting workload [30], [8].

5.0 Technical Planning

This process involves developing and implementing the technical solutions necessary for network connectivity and simulator interfaces with internal and external participants. The two activities in this process are:

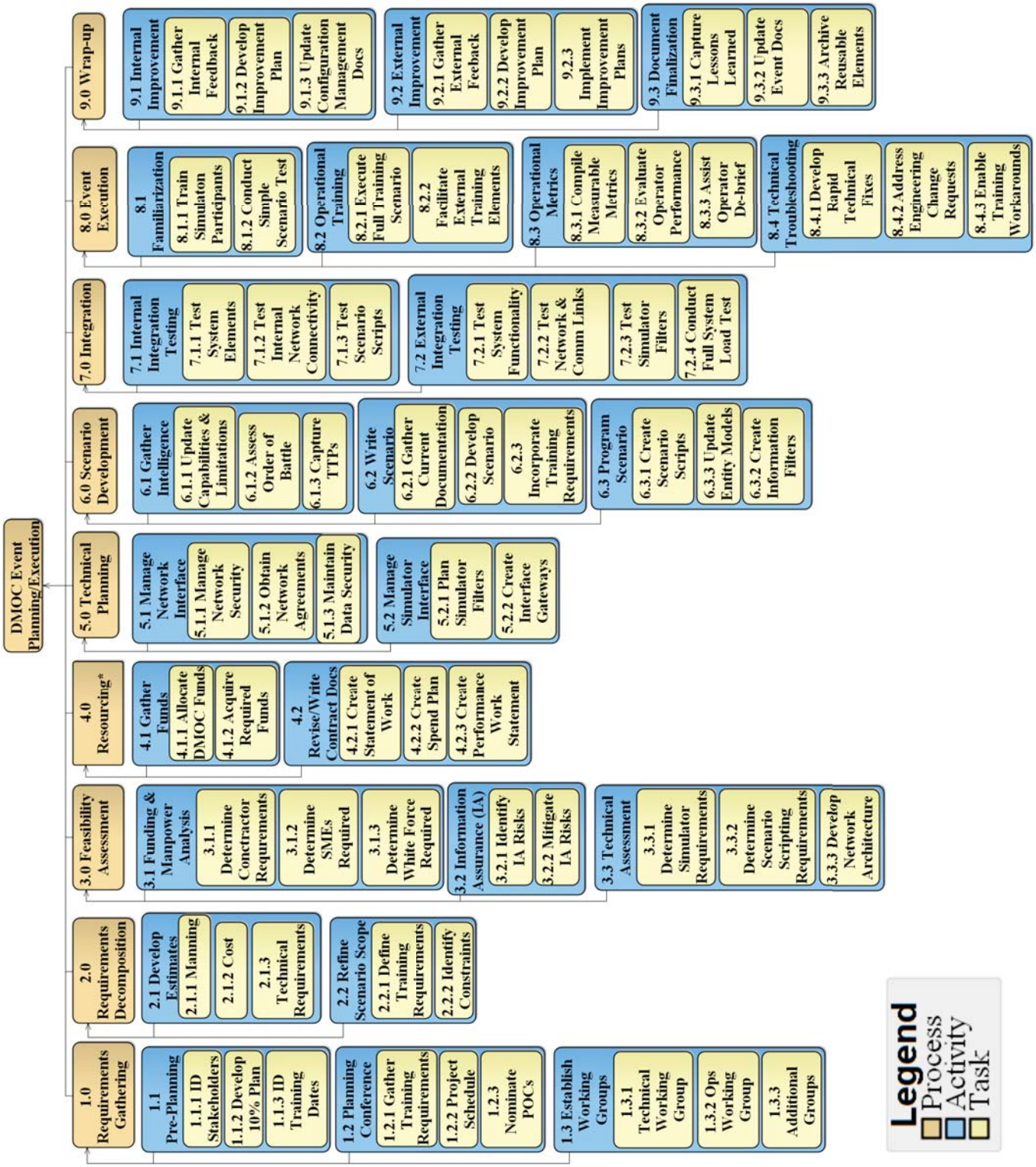

Fig. 4. DMOC Process Decomposition.

5.1 Manage Network Interface: ensures network access agreements for restricted networks, arrangements for sufficient bandwidth, and network security measures are complete and active for event execution. Also, this activity is responsible for creating and maintaining special hard-drives for restricted data and partitioning the network to prevent data leaks.

5.2 Manage Simulator Interface: involves creating and assessing software filters and gateways required to share simulation information within the training scenario.

6.0 Scenario Development

Within the DMOC, scenario development is mainly completed by SMEs and often scenarios developed for a particular customer or set of customers do not change drastically (i.e., Joint Kill Chain Event, Coalition VF, and WPS C2EW events, and they require only minor updates to constructive entity capabilities or the sequence of events). Done properly, the scenario is developed in sections of code that can be reused in later events while maintaining enough flexibility to be updated as required. This is accomplished largely through creating robust class, entity type, and behavior models within the environment generators. For example, classes of entities can have predetermined behaviors they execute when called into a scenario. Where an aircraft of a particular type associated with a particular country will default to a general set of programmed behaviors rather than requiring scripted flight patterns and responses for each entity in each scenario. It includes three major activities:

6.1 Gather Intelligence: an iterative activity that the intelligence personnel at the DMOC accomplish to ensure the most accurate capabilities and limitations, as well as current Tactics, Techniques, and Procedures (TTPs) of both red and blue forces are incorporated into the scenario.

6.2 Write Scenario: includes scouring the current and available real world documentation within an geographical area of interest and incorporating as much realism into the scenario plot or storyline as possible. At times the "realism" of a scenario is adjusted to create a challenging scenario capable of pushing the boundary of the trainee's knowledge and decision making faculties. Thus maximizing the value of the training experience.

6.3 Program Scenario: the technical side of turning the storylines into executable code or scripted entities and creating the constructive environment for the training event. Environment generators in use at the DMOC include a basic globe with relevant topographic information allowing the scenario to be based anywhere in the world with relative ease. With each new major world event, or strategic military focus (i.e., pivot to the pacific), training scenarios will shift and lead to new entities, reference waypoints, and detailed TTPs for use in subsequent scenarios.

7.0 Integration

This process ensures the simulation scenario can execute properly with realistic events in a stable DMO environment. It includes two major activities:

7.1 Internal Integration Test: ensure simulators and support equipment within the DMOC battlespace work properly. Each simulator and additional piece of support equipment is integrated and tested iteratively to troubleshoot any possible integration issues for equipment completely within the DMOC's control. Additionally an internal test of the scenario script is conducted to highlight any potential conflicts with simulators or the information being passed within the DMOC network.

7.2 External Integration Test: builds upon the internal testing and evaluates each connection to external customers, players, and support entities to ensure every aspect of the training event can be executed with minimal technical interference. Once each connection is established there is also a period of load testing to ensure appropriate bandwidth and detect additional interface issues prior to event execution.

8.0 Event Execution

Successful event execution is "delivering quality DMOC capabilities and training to warfighters while providing an event that makes them want to come back" [37]. This involves completing several major activities:

8.1 Familiarization: typically the first day of an event starts with a less complicated scenario to introduce the operators to the training simulation equipment. Because this is not considered the main training event, it offers an additional opportunity to find and/or fix any operational issues or errors and is considered the final phase of external integration.

8.2 Operational Training: formal execution of the training scenario with all players involved. Training can span several days and usually grows in difficulty. For instance, the Weapons School C2 training scenario consists of five fully scheduled days beginning at approximately 0600 and not ending for the students until approximately 2100. The scenario alternates between a "flying" day and a preparation/briefing day. Each "flying" day introduces progressively more complex scenarios involving larger numbers of constructive entities, including red, blue, and gray forces, increasingly difficult priority balancing decisions, and requiring more rapid dynamic responses.

8.3 Collect Operational Metrics: begins approximately one week prior to event execution and involves a team of SMEs comparing the training elements required for each participant with elements built into the planned scenario. From these training requirement documents a list of measurable metrics are generated for use in evaluating trainee performance within the simulation. Collected metrics are used in daily debriefs, after-action reports, and aid analysis for training improvements in future events. Thus serving two purposes, increasing the value of the training for participants by highlighting lessons learned to the whole group and improving the quality of future events by exposing scenario strengths and weaknesses.

8.4 Technical Troubleshooting: completed iteratively throughout the event and is focused on quickly solving technical issues to enable event execution. Most minor technical issues are resolved on the spot by one of the technical SMEs. Larger, more complicated issues are routed through

an Engineering Change Request (ECR) system for in-depth analysis and solutions, as well as, progress tracking.

9.0 Wrap-up

The wrap-up process is aimed at gathering meaningful feedback from participants, both operators and white force as well as compiling any lessons learned internally. The three major activities within this process are:

9.1 Internal Improvement: captures lessons learned by DMOC facilitators, develops a "get well plan" for any major issues that could negatively impact future events, and updates event continuity binders within the DMOC.

9.2 External Improvement: gathers and tracks feedback from the training participants and associated units. Feedback can range from a formalized survey after a VIRTUAL FLAG (VF) to informal queries for feedback following the smaller warfighter focused events. More emphasis is placed on collecting feedback and making improvements to the VFs because the DMOC "owns" them from beginning to end. Other events are typically "owned" by external customers, even though they are executed within the DMOC battlespace.

9.3 Document Finalization: extracts all of the lessons learned and archives reusable event elements (software code, contract modifications, etc.) for potential use in future events.

As shown in Fig. 4, each of these activities is essential to the planning and execution of an LVC event. Moreover, each of the processes are tailored to focus on the DMOC mission of developing, integrating and delivering DMOC capabilities and training to warfighters.

IV. Observations

Surveys were gathered from twenty participants of the most recent Weapons School C2 training event in May 2016. Although the sample population is not large enough for strong statistical significance, the responses are considered in combination with the Researcher's observations and past after action reports.

Based on these inputs the primary area for improvement is reducing training detractors such as errant constructive entities, unrealistic weapon effects, and simulation events that might distract or frustrate a trainee to the point of reducing the training value. The DMOC works diligently within its sphere of influence to first, fix technical issues rapidly, second, minimize "SIMisims" (i.e., technical problems limited to the simulation environment), and lastly, ensure sufficient white force are available to maintain the integrity of the training.

First, technical shortfalls can be mitigated with sufficient development time. The DMOC is constantly adapting to changes throughout the planning and execution processes. For this reason, it is vital to establish requirements and a network baseline early to avoid costly rework. The DMOC's method for mitigating this issue early in the planning process, is to gather qualified representatives from each of the stakeholders to participate in the planning conference and working groups. This helps prevent many issues, but there is also a team of technical SMEs on call during an event to respond as required.

Second, to address SIMisims that might detract from the training experience, the DMOC scripts training scenarios and develops tools to avoid known issues. Other issues that occur more randomly include targets that do not die or respond appropriately to simulated stimuli and time variations within the simulation that affect the simulator synchronization. For these instances there are additional technical SMEs available to rectify any issues in real time, during event execution.

Lastly, for immediate improvement to LVC training, advances need to be made in controlling constructive entities. For instance, imagine a training scenario incorporating hundreds of constructive entities (fighters, tankers, helicopters, and ISR assets). As a white force controller, it your responsibility to control the maneuvers of several fighter formations and respond with correct radio communications when contacted by a C2 trainee. For maximum training value, trainees require a factually correct and timely response to any command or request for information without unreasonable delays. If they are asking for each member of your formation to respond to different threats with specific weapons each in a unique direction, one can quickly see how task intensive the scenario can get with insufficient numbers of white force. Even in the medium training simulation studied here, there were times that a white force individual would attempt to physically control and verbally respond on behalf of dozens of constructive entities. While the ability to instantiate large numbers of constructive entities (over 300 in this case) is one of the major benefits of operating in the LVC environment as it provides more realistic congested airspace for C2 trainees, training suffers when there are insufficient numbers of white force controllers to respond to C2 direction in a reasonable amount of time or the verbal response is worded incorrectly.

Constructive entity control may be improved by supplying a sufficient number of qualified white force (i.e., operational units, recently retired, or specially trained personnel). This is the easiest and most immediate option, but often requires additional personnel and resources from operational units; many of whom are already saturated with training and deployment requirements. Another method is developing adequate dynamic behavior to anticipate communication from C2 trainees. This has been attempted and has yet to provide entities that correctly and reliably respond to the many various commands a C2 trainee might attempt to employ [8], [32].

V. Conclusion

This work provides a basic understanding of the DMOC approach to planning and executing a medium scale C2 LVC training event and its relation to the SE technical processes contained in ISO 15288. First, the ISO 15288 SE technical processes were mapped to relevant DMOC processes. Then, the DMOC approach to planning and executing a C2 LVC training event was codified and explained in Sec. III. Next, insights and suggestions for improving LVC training effectiveness were provided.

Overall, the DMOC approach to planning and executing medium scale LVC training events is effective and represents

a tailored SE approach with emphasis on the production and execution of high quality C2 training. For immediate cost effective improvements to nearly every LVC training event, improvements need to be made to the control and response characteristics of constructive entities. Either through developing more intelligent behavior models, or increasing the number of white force personnel. Additionally, at a more strategic level, the technical issues of interfacing various simulators can be mitigated in the long run by mandating and enforcing a minimum interoperability standard and LVC architecture for new and updating simulators in order to enable gains to training efficiency on an attrition basis.

REFERENCES

[1] M. Dempsey, "National military strategy of the United States," *Washington, DC: US Government Printing Office*, p. 6, 2015.

[2] Deputy Chief of Staff, Operations, Plans, and Requirements, *United States Air Force Live Virtual Constructive Operational Training Flight Plan*, Headquarters, United States Air Force, Washington, DC, February 2013.

[3] T. P. Coakley, *Command and control for war and peace*. DIANE Publishing, 1992.

[4] *MCDP-6: Command and Control*, U.S. Marine Corps, 1996.

[5] *Air Force Basic Doctrine*, U.S. Air Force, 2015.

[6] J. Summers, "Simulation-based military training: An engineering approach to better addressing competing environmental, fiscal, and security concerns," *Journal of the Washington Academy of Sciences*, vol. 98, no. 1, pp. 9–30, 2012.

[7] *CJCSI 3170.01 G: Joint Capabilities Integration and Development System*, Chairman of the Joint Chiefs of Staff Instruction, 2009.

[8] D. E. Shepard, "Intelligence perspective," Interview, May 2016.

[9] J. A. Dewar, S. C. Bankes, J. S. Hodges, T. Lucas, and D. K. Saunders-Newton, "Credible uses of the distributed interactive simulation (DIS) system." DTIC Document, Tech. Rep., 1996.

[10] S. Singhal and M. Zyda, *Networked virtual environments: design and implementation*. ACM Press/Addison-Wesley Publishing Co., 1999.

[11] E. Smith, H. McIntyre, S. E. Gehr, M. Schurig, S. Symons, B. Schreiber, and W. Bennett Jr, "Evaluating the impacts of mission training via distributed simulation on live exercise performance: Results from the US/UK "Red Skies" study," DTIC Document, Tech. Rep., 2007.

[12] M. E. Smith, "Distributed mission training – how distributed should it be?" vol. 1, pp. 13–15, October 2003.

[13] S. Arnold, "International Standards Organisation ISO 15288 systems engineering—system life cycle processes," 2015.

[14] J. T. Sumida, *Inventing grand strategy and teaching command: the classic works of Alfred Thayer Mahan reconsidered*. Woodrow Wilson Center Press, 1999.

[15] K. A. Ericsson, R. T. Krampe, and C. Tesch-Römer, "The role of deliberate practice in the acquisition of expert performance." *Psychological review*, vol. 100, no. 3, p. 363, 1993.

[16] R. Smith, "The long history of gaming in military training," *Simulation & Gaming*, 2009.

[17] D. D. Hodson and R. O. Baldwin, "Characterizing, measuring, and validating the temporal consistency of live-virtual-constructive environments," *Simulation*, vol. 85, no. 10, pp. 671–682, 2009.

[18] D. D. Hodson and R. R. Hill, "The art and science of live, virtual, and constructive simulation for test and analysis," *The Journal of Defense Modeling and Simulation: Applications, Methodology, Technology*, vol. 11, no. 2, pp. 77–89, 2014.

[19] P. K. Davis, "Distributed interactive simulation in the evolution of DoD warfare modeling and simulation," *Proceedings of the IEEE*, vol. 83, no. 8, pp. 1138–1155, 1995.

[20] *DoDI 5000.02, Operation of the Defense Acquisition System*, DoD, 2015.

[21] R. Lechner and C. Huether, "Integrated live virtual constructive technologies applied to tactical aviation training," in *Interservice/Industry Training, Simulation and Education Conference (IITSEC)*, 2008.

[22] R. DeForest, "The Air Force Agency for Modeling and Simulation: Advancing modeling and simulation for the warfighter," *Journal of International Test and Evaluation Association*, vol. 30, no. 1, pp. 23–28, 2009.

[23] C. G. D. Colombi, John; Cobb, "Live-virtual-constructive capabilities for Air Force testing and training," *Journal of International Test and Evaluation Association*, vol. 33, no. 1, pp. 49–57, March 2012.

[24] W. J. Bezdek, J. Maleport, and R. Olshon, "Live, virtual & constructive simulation for real time rapid prototyping, experimentation and testing using network centric operations," in *AIAA Modeling and Simulation Technologies Conference and Exhibit, AIAA-2008-7090*, 2008.

[25] C. Caravello, S. Pearce, and J. Estep, "Net–enabled weapons test and evaluation using live, virtual, and constructive methods," in *2007 US Air Force T&E Days*, 2007, p. 1609.

[26] *DoDD 5000.01, The Defense Acquisition System*, DoD, 2008.

[27] A. Tolk *et al.*, *Engineering principles of combat modeling and distributed simulation*. Wiley Online Library, 2012.

[28] Public Affairs Office. (2015, September) E-3 Sentry (AWACS). Air Combat Command. [Online]. Available: http://www.af.mil/AboutUs/FactSheets/Display/tabid/224/Article/104504/e-3-sentry-awacs.aspx

[29] P. A. Office. (2015, September) E-8C Joint Stars. Air Combat Command. 115 Thompson St., Suite 210; Langley AFB, VA 23665-1987. [Online]. Available: http://www.af.mil/AboutUs/FactSheets/Display/tabid/224/Article/104507/e-8c-joint-stars.aspx

[30] V. Chen, "DMOC processes," Interview, February 2016.

[31] A. E. Henninger, D. Cutts, M. Loper, R. Lutz, R. Richbourg, R. Saunders, and S. Swenson, "Live virtual constructive architecture roadmap (LVCAR) final report," *US DoD, September*, 2008.

[32] C. R. Tranisi, "WFE planning and execution," Interview, May 2016.

[33] J. K. Hamm, "Virtual flag perspective," Interview, May 2016.

[34] A. C. C. Headquarters, *United States Air Force Weapons School: 8 WPS WS Integration Phase Manual*, 8th Weapons School, April 2016.

[35] H. Steyn, *Project Management for Engineering, Business, and Technology*. Routledge, 2012.

[36] S. Friedenthal, A. Moore, and R. Steiner, *A practical guide to SysML: the systems modeling language*. Morgan Kaufmann, 2014.

[37] N. M. Lang, "DMOC mission," Interview, 2016.